

## ABSTRACT

ALLEN, LUKE ROBERT. Observed Mesoscale Surface Air Pressure Waves and In-Cloud Characteristics in the Context of Winter Storm Structures. (Under the direction of Sandra Yuter).

Heavy snowfall over the large metro areas along the Northeast US Atlantic coast and in the Midwest US has significant societal impacts. Current numerical weather models have large uncertainties in forecasts of snowfall rate, duration, and timing. In this study, we use recent and unique observational data sets to address questions regarding the primary and recurrent processes responsible for snow mass increases in winter storms. By focusing on snow storms over mostly flat land, this study complements previous work on orographic and lake-effect snowfall. This work has two components which address 1) atmospheric gravity waves and 2) vertical air motions within winter storms.

To examine the occurrence of gravity waves during winter storms and their associations with radar observed structures, we analyzed data from the National Weather Service WSR-88D operational radar network in conjunction with networks of high-precision pressure sensors in the Toronto, ON, Canada and New York, NY, USA metropolitan areas. In 40 months (Jan 2020-Apr 2023) of data, we objectively identified 33 coherent and trackable pressure wave events with wave periods  $\leq 67$  min, wavelengths  $\leq 170$  km, and amplitudes  $\geq 0.45$  hPa. Ten of those pressure wave events were caused by either frontal or outflow boundary passages or a wake low. The 23 pressure wave events that were gravity waves all occurred during the months between December and May. We found a strong correlation between gravity wave amplitude and event duration. In the New York City and Toronto metro areas, gravity waves are rare during snow events. Only 6 gravity wave events co-occurred with surface snow at our two observing networks, compared to 79 snow events of at least 4 hour duration. While gravity waves and enhanced reflectivity bands may co-exist in some instances, evidence from the large sample size of storms indicates that this association is not commonplace.

We combined aircraft data from two field studies, the NSF Profiling of Winter Storms (PLOWS) and NASA Investigation of Microphysics and Precipitation for Atlantic Coast-Threatening Snowstorms (IMPACTS), which sampled storms in the Northeast and Midwest US to characterize the distributions of vertical velocity and updrafts. We used  $\sim 100$ -m resolution in situ measurements of in-cloud vertical air velocity taken during 42 research flights. Upward motions capable of lofting precipitation-sized ice ( $\geq 0.5 \text{ m s}^{-1}$ ) were often associated with cloud-top generating cells, while regions below generating cell layers typically had sparse updrafts. Vertical velocity  $\geq 0.5 \text{ m s}^{-1}$  only occurred in  $\sim 10\%$  of in-cloud measurements. We defined updrafts as envelopes of consecutive in-cloud measurements of vertical velocity  $\geq 0.5 \text{ m s}^{-1}$ . The up-

drafts  $\geq 0.5 \text{ m s}^{-1}$  we observed were usually narrow (median envelope lengths  $\sim 0.25 \text{ km}$ ) and 90% were  $< 1.2 \text{ km}$  across. In these storms, upward lofting of precipitation-size ice particles typically occurs on scales of a few 100 m rather than within mesoscale (25+ km) updrafts.

Our results provide important context for the temporal and spatial scales of ice microphysics processes. Current conceptual models of winter storms usually assume relatively continuous ice growth along snow particle trajectories. Our results suggest that ice growth is likely more episodic as particles have few opportunities to pass through conditions that would sustain relative humidity sufficient for vapor deposition and/or riming. Additionally, our findings can serve as benchmarks for users and developers of numerical models to assess whether the vertical air motions in winter storm simulations are being represented realistically.

© Copyright 2024 by Luke Robert Allen

All Rights Reserved

Observed Mesoscale Surface Air Pressure Waves and In-Cloud Characteristics in the Context of  
Winter Storm Structures

by  
Luke Robert Allen

A dissertation submitted to the Graduate Faculty of  
North Carolina State University  
in partial fulfillment of the  
requirements for the Degree of  
Doctor of Philosophy

Geospatial Analytics

Raleigh, North Carolina  
2024

APPROVED BY:

---

Matthew Parker

---

DelWayne Bohnenstiehl

---

Brian Colle

---

Sandra Yuter  
Chair of Advisory Committee

## ACKNOWLEDGEMENTS

I am most grateful to my advisor, Dr. Sandra Yuter, for her teaching and mentorship throughout both my undergraduate and Ph.D. studies. She has persistently challenged me and taught me to become a better scientist during my time at NC State. Without her mentorship, this work would not have been possible.

Thank you to the other members of the Environment Analytics group for their guidance, assistance, and general advice. Matthew Miller, Laura Tomkins, and Kevin Burris in particular have been tremendously helpful with their expertise in working with different data sets and discussions about the interpretation of our results. This work was highly dependent on the pressure sensors built and managed by Dr. Miller. Special thanks to Declan Crowe and Logan McLaurin for their help in processing various data sets and for helping to improve the clarity of my writing.

Thank you to each of my committee members, Dr. Matthew Parker, Dr. DelWayne Bohnenstiehl, and Dr. Brian Colle, for their time spent to serve on my committee, and for their valuable feedback and insights which have greatly improved this work. I also want to thank Dr. Colle's students and colleagues at Stony Brook University, including Erin Leghart, Phillip Yeh, and Nicholas Leonardo, for the helpful discussions and feedback on this work.

Thank you to the rest of the NASA IMPACTS team for their hard work in collecting, processing, and analyzing the data going toward important science. In particular, I want to thank Lee Thornhill and David Delene for their assistance in acquiring and interpreting the data used in this work. I am also thankful to NSF, NASA, ONR, and the Center for Geospatial Analytics (CGA) for their financial support. Thank you to the CGA for the opportunity provided by this unique program.

Finally, thank you to my father, Robert Allen, for his everlasting love and support in my academic and life journey.

# TABLE OF CONTENTS

<b>List of Tables</b> . . . . .	<b>vi</b>
<b>List of Figures</b> . . . . .	<b>viii</b>
<b>Chapter 1 INTRODUCTION</b> . . . . .	<b>1</b>
1.1 Motivation . . . . .	1
1.2 Definitions of key terms . . . . .	2
1.3 Background . . . . .	4
1.3.1 Reflectivity bands and gravity waves in winter storms . . . . .	5
1.3.2 Vertical air motions in winter storms . . . . .	6
1.4 Road map of this dissertation . . . . .	7
<b>Chapter 2 Objective identification of pressure wave events from networks of 1-Hz, high-precision sensors</b> . . . . .	<b>9</b>
2.1 Introduction . . . . .	10
2.2 Data . . . . .	13
2.2.1 Networks of pressure sensors . . . . .	13
2.2.2 Operational weather observations . . . . .	15
2.3 Methods . . . . .	17
2.3.1 Identifying wave events in a single sensor . . . . .	17
2.3.2 Matching corresponding wave events between multiple sensors . . . . .	21
2.3.3 Estimating wave phase velocity vector . . . . .	24
2.4 Pressure disturbance examples . . . . .	25
2.4.1 15-17 January 2022: Hunga Tonga-Hunga Ha’apai eruption and Lamb wave . . . . .	26
2.4.2 25 February 2022: Gravity wave train over Toronto . . . . .	28
2.4.3 4 February 2022: Outflow pressure jump and subsequent oscillations over Long Island . . . . .	31
2.4.4 15 November 2020: Cold front passage over Toronto . . . . .	33
2.4.5 14 September 2021: Wake low associated with a mesoscale convective system . . . . .	34
2.5 Discussion and Summary . . . . .	36
<b>Chapter 3 Objectively identified mesoscale surface air pressure waves in the context of winter storm environments and radar reflectivity features: a 3+ year analysis</b> . . . . .	<b>41</b>
3.1 Introduction . . . . .	43
3.1.1 Possible effects of gravity waves on cloud and precipitation processes . . . . .	44
3.1.2 Gravity waves in winter storm case studies . . . . .	46
3.1.3 Reflectivity bands and velocity waves in winter storms . . . . .	47
3.1.4 Objectives of this study . . . . .	48
3.2 Data and Methods . . . . .	48
3.2.1 Pressure sensor data . . . . .	48

3.2.2	ERA5 reanalysis data . . . . .	53
3.2.3	Radar data . . . . .	55
3.2.4	Surface stations and operational soundings . . . . .	55
3.3	Pressure wave characteristics and environmental context . . . . .	58
3.3.1	Gravity wave event characteristics . . . . .	58
3.4	Conclusions . . . . .	75
<b>Chapter 4</b>	<b>Background and methods for analysis of in situ observations of winter storm cloud properties . . . . .</b>	<b>79</b>
4.1	Background and motivation . . . . .	80
4.1.1	Vertical velocity, snow trajectories, and snow bands . . . . .	80
4.1.2	Remote sensing analyses of winter storm vertical velocities . . . . .	83
4.1.3	Goals of this study . . . . .	84
4.2	Data and methods . . . . .	85
4.2.1	In situ measurements of vertical velocity . . . . .	85
4.2.2	Coordinated remote-sensing data from NASA ER-2 . . . . .	86
4.2.3	Cloud probe data and cloud definition . . . . .	86
4.2.4	Updraft envelope definition . . . . .	88
4.2.5	ERA5 reanalysis data and forcing/instability metrics . . . . .	90
4.2.6	Potential sampling biases with in situ aircraft data . . . . .	92
<b>Chapter 5</b>	<b>In-cloud vertical velocity characteristics in winter storms . . . . .</b>	<b>96</b>
5.1	Results . . . . .	96
5.1.1	Vertical velocity measurements and context for individual flight legs . . . . .	96
5.1.2	Distributions of vertical velocity measurements . . . . .	99
5.1.3	Updraft envelope properties . . . . .	104
5.2	Modeled distributions of in-cloud vertical velocity in winter storms . . . . .	105
5.3	Observed in-cloud relative humidity distribution in winter storms . . . . .	107
5.4	Conclusions . . . . .	108
<b>Chapter 6</b>	<b>Conclusions . . . . .</b>	<b>111</b>
6.1	Summary of key findings . . . . .	111
6.2	Implications . . . . .	112
6.2.1	On gravity waves in winter storms . . . . .	112
6.2.2	On winter storm in-cloud vertical velocities . . . . .	113
6.3	Future work . . . . .	113
<b>References</b>	<b>. . . . .</b>	<b>116</b>
<b>APPENDIX</b>	<b>. . . . .</b>	<b>131</b>
Appendix A	ERA5 forcing and instability metrics for selected P-3 flight legs during IMPACTS . . . . .	132

## LIST OF TABLES

Table 1.1	Definitions of key meteorological terms used in this dissertation. . . . .	2
Table 1.2	Definitions of key wave-related terms used in this dissertation. . . . .	3
Table 2.1	Summary of 5 wave events associated with the Hunga Tonga-Hunga Ha’apai eruption Lamb waves in January 2022. Wave events were subset to those with mean cross-correlation above 0.75, modeled delay time RMSE below 90 s, and modeled delay time NRMSE below 0.1. The start times shown are the earliest among sensors which captured a given event, and end times shown are the latest among sensors which captured a given event. Center wave periods and amplitudes are averaged across the sensors which captured a given event. The first 3 events shown [Outbound (i), (ii), and (iii)] are events associated with the initial outbound set of Lamb waves, and the last 2 events shown [Rebound (i) and (ii)] are events associated with the initial rebound set of Lamb waves. . . . .	27
Table 3.1	Properties of pressure waves presented in this study (indicated in <b>bold</b> ) and in some prior studies and meta-analyses in the literature. Rows are in ascending order by minimum wavelength. Information in cells indicated with * were inferred from figures in the associated paper (not directly stated), and the cell indicated with ** was inferred from the wavelength and phase speed range for that paper. . . . .	44
Table 3.2	Properties of the 33 pressure wave events detected over the 40 month analysis period. The leftmost column is an index column. In the location column, TOR indicates the Toronto sensor network, and NY indicates the New York and Long Island sensor network. The wave period and amplitude are averaged among sensors which detected a given event. Phase direction is shown in degrees clockwise from northward (e.g., 90 degrees indicates a wave propagating west to east). Rows in <b>bold</b> indicate gravity wave events. . . . .	53
Table 3.3	Environmental context for the 23 gravity wave events detected over the 40 month analysis period. The leftmost column is an index column, aligned with the index column in Table 3.2. Here, the position of wave events relative to the low and to air mass boundaries was determined based on manual analysis of $\theta_e$ and MSLP maps derived from ERA5 data at the center time of the event (Fig. 3.8). If no air mass boundary could be discerned near Toronto or New York for an event, then we consider it "Unclear" whether that event occurred in the cold sector or warm sector. Events 25 and 30 occurred roughly 2000 km or more to the east of the nearest cyclone, as indicated in the table and the text. . . . .	64

Table 3.4	Radar and precipitation context for the 23 gravity wave events detected during our 40 month analysis period. The leftmost column is an index column, aligned with the index column in Table 3.2. The presence of surface snow was determined using the nearest available ASOS data (CYYZ or KJFK). Echo, reflectivity bands, and Doppler velocity waves are considered "present" when they exist anywhere within the range of the 0.5° scan for the nearest NEXRAD radar (KBUF or KOKX). Reflectivity bands and Doppler velocity waves are considered "collocated" when they are located directly above pressure sensors and their movement is consistent with the gravity wave phase velocity. . . . .	71
Table 3.5	Hours with and without gravity wave events subdivided by ASOS precipitation data during the November to May months between January 2020 and April 2023. Precipitation is determined to be present when there was $\geq 0.1 \text{ mm hr}^{-1}$ liquid equivalent precipitation was recorded at Toronto (CYTZ precipitation type and CXTO precipitation amount) and at New York (KJFK precipitation type and amount). Hours with either only snow or a mixture of precipitation types containing snow are included under hours with snow. . . . .	73

## LIST OF FIGURES

Figure 1.1	(Figure 2 from McMurdie et al. 2022). An example plot of radar reflectivity factor (dBZ) illustrating narrow regions of high reflectivity associated with the primary snowband and multibands. Potential mechanisms contributing to snowband formation and maintenance are indicated on the figure. . . . .	4
Figure 1.2	<b>(a)</b> Contours of relative humidity with respect to ice ( $RH_{ice}$ ) and with respect to liquid water ( $RH_{water}$ ) as a function of temperature and water vapor mixing ratio, assuming a standard atmosphere temperature-pressure relationship (corresponding pressure values on right axis). RH values are contoured at 20% intervals, with the 100% contour dashed. <b>(b)</b> The temperature difference between the 100% $RH_{ice}$ and 100% $RH_{water}$ contours at each water vapor mixing ratio. . . . .	6
Figure 2.1	Locations of pressure sensor networks. <b>(a)</b> US northeast regional map with the locations of the Toronto, New York City and Long Island, and Raleigh networks indicated. Detailed maps of sensor locations in <b>(b)</b> Toronto, <b>(c)</b> New York and Long Island, and <b>(d)</b> Raleigh. . . . .	14
Figure 2.2	The maximum pressure perturbation $p'_{max}$ (hPa) contoured and colored, according to Eq. 2.2 at an air density $\rho_0$ of $1.225 \text{ kg m}^{-3}$ . $p'_{max}$ is a function of the maximum velocity perturbation $u'_{max}$ ( $\text{m s}^{-1}$ ) and absolute value of the difference between the wave phase speed and background wind speed $ c - u_0 $ ( $\text{m s}^{-1}$ ). In panel <b>(a)</b> , $u'_{max}$ and $ c - u_0 $ up to $15 \text{ m s}^{-1}$ are shown. In panel <b>(b)</b> , $u'_{max}$ and $ c - u_0 $ up to $3 \text{ m s}^{-1}$ are shown. The color scales differ in panels <b>(a)</b> and <b>(b)</b> . . . . .	16
Figure 2.3	Steps in process of identifying an event corresponding to a gravity wave train passage on 23 Feb 2023 in sensor 25. <b>(a)</b> Original 1-second pressure time series. <b>(b)</b> The 10 s moving average of the pressure time series, with every 10th point kept. <b>(c)</b> Wavelet power corresponding to the pressure time series in panel <b>(b)</b> . <b>(d)</b> Wavelet power normalized by the mean for each wave period corresponding to the pressure trace, with contours for values of 5 (dashed) and 10 (solid). The event region corresponding to the wave described in the text is outlined in magenta in panel <b>(d)</b> . <b>(e)</b> Time series of the extracted wave event. Wave periods in panels <b>(c)</b> and <b>(d)</b> are shown on a logarithmic scale. All times are UTC. . . . .	18
Figure 2.4	Mean wavelet power as a function of wave period across the entire data set (purple curve) and for the individual sensor networks around Toronto, ON, Canada (blue); New York City and Long Island, NY (red); and Raleigh, NC (yellow). . . . .	19

Figure 2.5	(a) Part of the synthetic time series of pressure data (blue) with an extracted wave event (black). This synthetic wave event had a wave period of 2 min and amplitude of $\pm 0.0464$ hPa. (b) The wavelet power corresponding to the time series shown in (a). The dashed and solid contours indicate where the wavelet power is 5 times and 10 times the mean wavelet power for a given wave period, respectively. (c) The synthetic wave events which were detected (blue filled circles) and undetected (red X symbols) using our methodology with a $K$ value of 10, as a function of their wave period and amplitude. . . . .	20
Figure 2.6	Extracted waveforms corresponding to the gravity wave train on 23 Feb, 2023 for sensors 25 (a), 04 (b), 23 (c), 24 (d), and 34 (e). In (b), (c), (d), and (e), brown lines show the extracted wave event with no time shift, and black lines show the extracted wave event shifted in time according to the peak cross-correlation with the extracted wave event time series for the event in sensor 25 (time shift and correlation coefficients are shown in subplot titles). All times are UTC. . . . .	22
Figure 2.7	Pressure traces and extracted waveforms for two events associated with the Lamb waves caused by the Hunga Tonga-Hunga Ta’apai eruption on 15 Jan 2022. Extracted waveforms (black lines) are overlaid on the total pressure time series (blue lines). (a) the Outbound (ii) wave event propagating from Tonga toward the antipode location in Algeria in Sensor 02 (Table 2.1, column 3). (b) the Rebound (ii) wave event propagating from the antipode location to Tonga in Sensor 18 (Table 2.1, column 6). All times are UTC. . . . .	28
Figure 2.8	Pressure traces and extracted waveforms for the 25 Feb 2022 wave event in sensors (a) 04, (b) 24, (c) 26, and (d) 34. Extracted waveforms (black lines) are overlaid on the total pressure time series (blue lines). All times are UTC. Cross-correlations and lag times are indicated relative to sensor 04. Cross-correlations are computed for each variation of pairs of sensors (not shown). . . . .	29
Figure 2.9	Upper air sounding data from Buffalo, NY, valid for 1200 UTC 25 Feb 2022. (a) Dry bulb temperature (blue), dew point (orange), wet bulb temperature (green), and frost point (red) profiles (all in $^{\circ}\text{C}$ ). (b) Equivalent saturation potential temperature ( $\theta_e^*$ ) profile (black line, K) overlaid on the vertical gradient in $\theta_e^*$ ( $\text{K km}^{-1}$ ). Positive values (blue) of the vertical gradient in $\theta_e^*$ indicate absolute stability, while negative values (red) indicate conditional or absolute instability. (c) Horizontal wind profile (barbs, kts; colored according to wind speed). Annotation indicates the vertical extents of a ducting layer and a trapping layer according to the gravity wave duct criteria described by Lindzen and Tung (1976) and Koch and O’Handley (1997). . . . .	30
Figure 2.10	As in Fig. 2.8, but for the 04 Feb 2022 wave event in sensors (a) 21, (b) 22, (c) 11, (d) 14, and (e) 20, with cross-correlations and lag times indicated relative to sensors 21. Extracted waveforms (black lines) are overlaid on the total pressure time series (blue lines). . . . .	31

Figure 2.11	(a) Reflectivity and (b) Doppler velocity wave detection for NWS WSR-88D radar data from Upton, NY, at 0.5° tilt, at 1920 UTC on 4 Feb 2022. In (a), reflectivity values are shown in greyscale where there is likely enhancement due to melting (Tomkins et al. 2022). Filled blue circles indicate locations of pressure sensors which captured the wave event described in Sect. 2.4.3, and unfilled blue circles indicate locations of pressure sensors which did not capture the wave event. Filled green circle indicates location of Islip, NY, ASOS station (KISP). An animation of this figure showing the time sequence from 1541 to 2130 UTC is in Video supplement Animation-Figure-S2.02. . . . .	32
Figure 2.12	Time series of one-minute ASOS data from Islip, NY (KISP), on 4 February 2022. (a) Temperature (purple) dew point (red), and pressure (blue). (b) Wind speed (orange), wind gust speed (red), and wind direction in degrees clockwise from northerly (yellow). Wind direction is not plotted when it changes by more than 180° in consecutive observations (e.g., when crossing 0° or 360°) or when the wind speed is below 1.5 m s <sup>-1</sup> . All times are UTC. . . . .	33
Figure 2.13	As in Fig. 2.8, but for the 15 Nov 2020 wave event in sensors (a) 34, (b) 04, (c) 24, (d) 25, and (e) 25, with cross-correlations and lag times indicated relative to sensor 34. Extracted waveforms (black lines) are overlaid on the total pressure time series (blue lines). . . . .	34
Figure 2.14	Time series of one-minute ASOS data from Buffalo, NY (KBUF), on 15 November 2020. (a) Temperature (purple) dew point (red), and pressure (blue). (b) Wind speed (orange), wind gust speed (red), and wind direction in degrees clockwise from northerly (yellow). Wind direction is not plotted when it changes by more than 180° in consecutive observations (e.g., when crossing 0° or 360°) or when the wind speed is below 1.5 m s <sup>-1</sup> . All times are UTC. . . . .	35
Figure 2.15	As in Fig. 2.8, but for the 14 Sep 2021 wave event in sensors (a) 21, (b) 27, (c) 14, and (d) 18, with cross-correlations and lag times indicated relative to sensor 21. Extracted waveforms (black lines) are overlaid on the total pressure time series (blue lines). . . . .	36
Figure 2.16	Time series of one-minute ASOS data from Islip, NY (KISP), on 14 September 2021. (a) Temperature (purple) dew point (red), and pressure (blue). (b) Wind speed (orange), wind gust speed (red), and wind direction in degrees clockwise from northerly (yellow). Wind direction is not plotted when it changes by more than 180° in consecutive observations (e.g., when crossing 0° or 360°) or when the wind speed is below 1.5 m s <sup>-1</sup> . All times are UTC. . . . .	37

Figure 2.17	Maps of radar reflectivity at 0.5° tilt from the NWS WSR-88D radar in Upton, NY, on 14 September 2021. Reflectivity values in color show meteorological echo and those are shown in greyscale are likely non-meteorological echo such as insects and birds in this case (Tomkins et al. 2022). Filled blue circles indicate the locations of pressure sensors which captured the wave event described in Sect. 2.4.5, and unfilled blue circles indicate the locations of pressure sensors which did not capture the wave event. Filled green circle indicates the location of the Islip, NY, ASOS station (KISP). The sequence of images from (a) 0303 UTC, (b) 0323 UTC, (c) 0342 UTC, and (d) 0402 UTC shows the southeastward movement of region of convective cells > 40 dBZ from closer to further off the southern coast of Long Island. The wake low is inferred to be near the trailing edge of the weaker stratiform precipitation region behind (west of) the convective cells. The minimum pressure at KISP associated with the wake low occurred near the time of the scan shown in (c). An animated version of this figure, with Doppler velocity wave detection, is shown in Video supplement Animation-Figure-S2.03. . . . .	38
Figure 3.1	Possible chains of processes and outcomes for gravity waves to yield changes in cloudiness and precipitation. The sequence goes from top to bottom. Green rectangles indicate conditions or requirements, ovals indicate microphysical processes which result from the air motions associated with gravity waves, and downward-pointing pentagons indicate irreversible changes within air parcels resulting from the previous steps. For simplicity, sequences where air parcel temperatures cross the 0°C level altitude are not shown. . . . .	45
Figure 3.2	Maps of the pressure sensor, ASOS, and radar sites used in this study. <b>(a)</b> Locations of Toronto and New York City. <b>(b)</b> Pressure sensor sites in Toronto (filled circles) with the 3 ASOS sites (stars) and KBUF radar (maroon diamond). <b>(c)</b> Pressure sensor sites in New York and Long Island (filled circles) with JFK ASOS (black star) and KOKX radar (maroon diamond). . . . .	49
Figure 3.3	Timelines of when the pressure sensors in <b>(a)</b> Toronto and <b>(b)</b> New York and Long Island recorded pressure data between January 2020 and April 2023. . . . .	50

Figure 3.4	Event 19 (gravity wave event) maps of <b>(a)</b> reflectivity, <b>(b)</b> radial Doppler velocity, <b>(c)</b> detected features of enhanced reflectivity, and <b>(d)</b> Doppler velocity wave detection for KBUF at 05:54 UTC on 1 April 2023. Filled blue circles indicate the locations of pressure sensors in Toronto. In this example, gravity waves moved SW to NE while a NW-SE aligned linear region of enhanced reflectivity about 150 km long and 80 km wide extends from near the western edge of Lake Ontario. Several NW-SE aligned Doppler velocity waves could be tracked from SW to NE between Lake Erie and Lake Ontario. The greyscale regions in <b>(a)</b> and <b>(c)</b> likely contain mixed precipitation (reflectivity > 20 dBZ and dual-polarization correlation coefficient < 0.97). An animated version of this figure is available in the Video Supplement Animation-Figure-S3.01. . . . .	56
Figure 3.5	Characteristics of the 33 pressure wave events detected in New York (orange) and Toronto (green) between January 2020 and April 2023. <b>(a)</b> Bar chart of the number of pressure wave events by month. <b>(b)</b> Scatter plot of wave amplitude against wave period, with error bars indicating the range of wave periods where $W \geq 10 \langle  W(b, a)  \rangle_b$ , i.e., where there was a strong wave signal. <b>(c)</b> Radial scatter plot of the wave phase velocities (directions shown are in degrees clockwise from northbound). In panels <b>(b)</b> and <b>(c)</b> , gravity wave events are indicated by filled circles, and front, outflow, and wake low events are indicated by other shapes according to the legend. . . . .	59
Figure 3.6	Extracted pressure wave event (black, left axes) and total pressure (blue, right axes) time series for the 23 gravity wave events. The ordering and numbering of wave events matches that in Table 3.2. For each gravity wave event, data from only a single sensor are shown. That sensor was chosen to maximize its optimal cross-correlation values with extracted event traces from other sensors which captured a given gravity wave event. . . . .	60
Figure 3.7	Scatter plot of wave amplitude against event duration for the 23 gravity wave events. Green points represent gravity wave events in Toronto, and orange points represent events in New York and Long Island. . . . .	61
Figure 3.8	ERA5 2 m equivalent potential temperature maps for all of the detected gravity wave events, at the center time of each event. The ordering and numbering of events matches that in Table 3.2. MSLP is contoured in white every 5 hPa. In each panel, either New York or Toronto are shown by cyan points, depending on where the gravity wave event occurred. . . . .	65
Figure 3.9	ERA5 300 hPa wind speed maps for all of the detected gravity wave events, at the center time of each event. The ordering and numbering of events matches that in Table 3.2. 300 hPa geopotential height is contoured in black every 50 m. In each panel, either New York or Toronto are shown by cyan points, depending on where the gravity wave event occurred. . . . .	66

Figure 3.10	ERA5 300 hPa $\Delta$ NBE maps for all of the detected gravity wave events, at the center time of each event. The ordering and numbering of events matches that in Table 3.2. In each panel, either New York or Toronto are shown by magenta points, depending on where the gravity wave event occurred. . . . .	67
Figure 3.11	Cyclone track density (shading) for storms in the Northeast United States (NEUS) which brought at least 1 in of snowfall in a 24 hour period to at least two ASOS stations in the NEUS between 1996 and 2023. Cyclones were tracked using ERA5 data following the methodology of Crawford et al. (2021). . . . .	68
Figure 3.12	Air temperature inversion layers for soundings launched at KBUF for gravity wave events in Toronto, or at KOKX for gravity wave events in New York and Long Island, either during or within 2 hours of a gravity wave event. Inversion layers are colored according to the layer average lapse rate (darker colors indicate a stronger inversion). Event numbering matches that in Table 3.2. Two soundings were launched at KBUF during event 22. Events 2-22 were in Toronto and 24-30 were in NY. . . . .	69
Figure 3.13	As in Fig. 3.4, but for KOKX at 18:30 UTC on 18 February 2021, during event 28 (gravity wave event). In this example, an elongated enhanced reflectivity feature passed over the pressure sensor network from SW to NE during the wave event, which was inconsistent with the gravity wave phase direction (NW to SE). An animated version of this figure is available in the Video Supplement Animation-Figure-S3.02. . . . .	72
Figure 3.14	As in Fig. 3.4, but for KBUF at 19:30 UTC on 5 April 2023 during event 22 (gravity wave event). In this example, gravity waves moved from NW to SE while an elongated enhanced reflectivity feature is passing over the pressure sensors in Toronto from west to east. An animated version of this figure is available in the Video Supplement Animation-Figure-S3.03. . . . .	74
Figure 4.1	Fitch et al. (2021) (their Figure 6). Probability density function of estimates of fall speeds ( $v_p$ ) for sparsely rimed aggregates, moderately rimed particles, and graupel based on observations from a wind-shielded Multi-Angle Snowflake Camera in conditions of light horizontal wind speeds $U_{sfc}$ . . . . .	81
Figure 4.2	Lackmann and Thompson (2019) (their Figure 1) idealized conceptual model illustrating vertical cross-section of vertical air motions and snow water mixing ratios for snow storm structures a) with lofting and b) without lofting of precipitation-size ice. Relative snow mixing ratio shown in blue shading. Vertical velocity shown as dark red shading with contours labeled. In a) vertical velocity contour interval is $1 \text{ m s}^{-1}$ . Arrows show approximate vertical and horizontal length scales. Estimated aspect ratio of cross-section is 16:1. . . . .	82

Figure 4.3	P-3 in situ and ER-2 radar data from for a well-coordinated flight leg segment during the IMPACTS mission on 23 January 2023 from 1435 to 1445 UTC. In this flight leg, the P-3 flew through a layer of near cloud-top generating cells. <b>(a)</b> 2D-S total number concentration (logarithmic scale), the in-cloud threshold ( $10^{-3} \text{ cm}^{-3}$ ) is shown by a dashed horizontal line. <b>(b)</b> TAMMS vertical velocity. Dashed horizontal line at $0.5 \text{ m s}^{-1}$ indicates the updraft threshold definition. In-cloud updraft envelopes are indicated by purple shading. <b>(c)</b> CRS reflectivity. P-3 flight leg segments where the TAMMS vertical velocity $\geq 0.5 \text{ m s}^{-1}$ are indicated by black horizontal lines bounded by vertical bars. <b>(d)</b> CRS Doppler velocity, where positive values indicate upward motion. TAMMS vertical velocity is shown using colored points. Aspect ratio is 3:1 for panels <b>(c)</b> - <b>(d)</b> . . . . .	87
Figure 4.4	As in Fig. 4.3, but for a well-coordinated flight leg on 23 Jan 2023 from 1535 to 1546 UTC when the P-3 flew through the middle of the cloud layer, about 2 km below the cloud-top generating cells. . . . .	89
Figure 4.5	The location of 1000 randomly generated aircraft passes through an idealized spherical updraft, such that the likelihood of the aircraft passing through a given subregion of the cross-section is proportional to the area of that subregion. Cross-section through the center of the sphere in the $xz$ -plane where the aircraft is traveling in the $y$ -direction (shown by aircraft silhouette). Points are colored by the length of the aircraft's path through the sphere ( $L_{\text{updraft}}$ ), relative to the actual diameter of the sphere ( $D$ ). . . . .	93
Figure 4.6	Theoretical cumulative distribution function (CDF) of the measured length of an updraft ( $L_{\text{updraft}}$ ) by an aircraft randomly passing through a spherical updraft with diameter $D$ , relative to $D$ , according to Eq. 4.14. . . . .	94
Figure 5.1	<b>(a)</b> 2D Frontogenesis [ $\text{K (100 km)}^{-1} \text{ hr}^{-1}$ ], <b>(b)</b> $\text{Ri}_m$ (unitless), <b>(c)</b> $\frac{\partial \theta_e}{\partial z}$ ( $\text{K km}^{-1}$ ), <b>(d)</b> $\frac{\partial \theta_e^*}{\partial z}$ ( $\text{K km}^{-1}$ ), and <b>(e)</b> vertical velocity ( $\text{Pa s}^{-1}$ where upward motion is negative) obtained or calculated from ERA5 data along a cross-section corresponding to the flight leg shown in Fig. 4.3, in which the P-3 flew through a layer of cloud-top generating cells. In panels <b>(c)</b> and <b>(d)</b> , the zero contour is shown, and red shading indicates potential and conditional instability, respectively. In <b>(a)</b> - <b>(e)</b> , the P-3 flight level is indicated by a thin line, and observed in-cloud updrafts $\geq 0.5 \text{ m s}^{-1}$ are indicated by thick lines. Aspect ratio is 3:1. <b>(f)</b> Map of the flight leg (blue), MSLP (contoured in black every 5 hPa), and 700 hPa frontogenesis [shaded, $\text{K (100 km)}^{-1} \text{ hr}^{-1}$ ]. . . . .	97
Figure 5.2	As in Fig. 5.1, but for the flight leg shown in Fig. 4.4, in which the P-3 flew below a layer of cloud-top generating cells. . . . .	98
Figure 5.3	Top row: Maps of level flight legs in cloud with air temperature $< 0^\circ\text{C}$ sampled during <b>(a)</b> IMPACTS and <b>(b)</b> PLOWS. Bottom row: In-cloud vertical velocity measurements taken on level flight legs during IMPACTS and PLOWS, <b>(c)</b> probability density function (PDF) and <b>(d)</b> cumulative density function (CDF). . . . .	100

Figure 5.4	2D histogram of in situ vertical velocity against the P-3 distance below CRS echo top height for in-cloud samples with air temperature $< 0^{\circ}\text{C}$ during IMPACTS only. The number of points in each bin is normalized by the total number of samples taken at a given distance below echo top. Black dashed lines indicate the 10th, 50th, and 90th percentile of vertical velocity as a function of distance below echo top height. Vertical green dashed line is at $0.5 \text{ m s}^{-1}$ vertical velocity. . . . .	101
Figure 5.5	Histograms of in-cloud vertical velocity measurements taken on level flight legs at different temperature ranges, from colder temperatures at the top to warmer temperatures at the bottom, as indicated in subplot titles along with the sample size at each temperature range. Data are averaged over 1 s corresponding to about 100 m based on typical air speeds. Distributions from IMPACTS are shown in the left column, and distributions from PLOWS are shown in the right column. Temperature ranges were chosen to correspond with different ice growth modes (Huehlt et al. 2022). Overlays on each panel are as in Fig. 5.4. Gold lines show the distribution for all IMPACTS and PLOWS data in straight and level legs from Fig. 5.3c. . . . .	102
Figure 5.6	In-cloud level flight legs sampled during IMPACTS, shown in a Lagrangian framework relative to the low pressure center as determined using ERA5 data (Tomkins et al. 2024a). The origin of this figure represents the location of the low pressure center. . . . .	103
Figure 5.7	Distribution of in-cloud vertical velocity sampled during IMPACTS by cyclone quadrant. Overlays in each subplot are as in Fig. 5.5. . . . .	103
Figure 5.8	<b>(a)</b> 2-D histogram of updraft envelope mean vertical velocity against updraft envelope length, for IMPACTS and PLOWS combined. <b>(b)</b> The proportion of total upward mass flux contributed by updraft envelopes within 0.5-km length bins for IMPACTS and PLOWS separately. . . . .	105
Figure 5.9	Histograms of in-cloud vertical velocity, in terms of the proportion of data within each bin, for <b>(a)</b> IMPACTS, <b>(b)</b> PLOWS, and WRF simulations of <b>(c)</b> the 1-3 February 2016 case and <b>(d)</b> the 7 February 2020 case. In this figure, the data from IMPACTS and PLOWS are smoothed and subsampled to 20-second averages (based on typical airspeeds, approximately 2 km spatial scale). In each panel, the proportion of points where vertical velocity $\geq 0.5 \text{ m s}^{-1}$ is annotated in green, and the mean, 10th percentile, 50th percentile, and 90th percentile of the vertical velocity are shown using vertical lines as indicated by the legend. . . . .	106
Figure 5.10	2D histogram of $RH_{ice}$ against distance below echo top height for IMPACTS in-cloud samples with air temperature $< 0^{\circ}\text{C}$ . The number of points in each bin is normalized by the total number of samples taken at a given distance from echo top. Black dashed lines indicate the 10th, 50th, and 90th percentile of $RH_{ice}$ as a function of distance from echo top height. Vertical brown line is at 95% $RH_{ice}$ , and vertical blue line is at 105% $RH_{ice}$ . . . . .	108

Figure A.1	Cross-sections (3:1 aspect ratio) of <b>(a)</b> frontogenesis [ $\text{K (100 km)}^{-1} \text{ hr}^{-1}$ ], <b>(b)</b> moist Richardson number (unitless), <b>(c)</b> the vertical gradient in $\theta_e$ ( $\text{K km}^{-1}$ ), <b>(d)</b> the vertical gradient in $\theta_e^*$ ( $\text{K km}^{-1}$ ), and <b>(e)</b> vertical velocity ( $\text{Pa s}^{-1}$ , where negative values indicate upward motion) from ERA5 data along the P-3 flight leg from 21:47 to 22:19 UTC 05 February 2020. In <b>(a)</b> - <b>(e)</b> , the P-3 flight track is shown by thin black lines and in-cloud updraft observations $\geq 0.5 \text{ m s}^{-1}$ are shown by thicker black ( <b>(a)</b> and <b>(e)</b> ) or magenta ( <b>(b)</b> - <b>(d)</b> ) lines. <b>(f)</b> Map of the P-3 flight track (blue), with MSLP (black contours every 5 hPa) and 700 hPa frontogenesis [ $\text{K (100 km)}^{-1} \text{ hr}^{-1}$ ] from ERA5 data at the time corresponding to the cross-sections. <b>(g)</b> Histogram of in-cloud updraft envelope lengths for the flight leg shown. . . . .	133
Figure A.2	As in Fig. A.1, but for the P-3 flight leg from 16:17 UTC 07 February 2020 to 16:43 UTC 07 February 2020. . . . .	134
Figure A.3	As in Fig. A.1, but for the P-3 flight leg from 16:48 UTC 07 February 2020 to 17:17 UTC 07 February 2020. . . . .	135
Figure A.4	As in Fig. A.1, but for the P-3 flight leg from 19:32 UTC 18 February 2020 to 20:03 UTC 18 February 2020. . . . .	136
Figure A.5	As in Fig. A.1, but for the P-3 flight leg from 15:15 UTC 19 February 2022 to 15:47 UTC 19 February 2022. . . . .	137
Figure A.6	As in Fig. A.1, but for the P-3 flight leg from 17:24 UTC 19 February 2022 to 17:39 UTC 19 February 2022. . . . .	138
Figure A.7	As in Fig. A.1, but for the P-3 flight leg from 17:42 UTC 19 February 2022 to 17:57 UTC 19 February 2022. . . . .	139
Figure A.8	As in Fig. A.1, but for the P-3 flight leg from 21:41 UTC 19 January 2023 to 22:09 UTC 19 January 2023. . . . .	140
Figure A.9	As in Fig. A.1, but for the P-3 flight leg from 22:13 UTC 19 January 2023 to 22:47 UTC 19 January 2023. . . . .	141
Figure A.10	As in Fig. A.1, but for the P-3 flight leg from 23:17 UTC 19 January 2023 to 23:28 UTC 19 January 2023. . . . .	142
Figure A.11	As in Fig. A.1, but for the P-3 flight leg from 00:14 UTC 20 January 2023 to 00:26 UTC 20 January 2023. . . . .	143
Figure A.12	As in Fig. A.1, but for the P-3 flight leg from 00:31 UTC 20 January 2023 to 00:44 UTC 20 January 2023. . . . .	144
Figure A.13	As in Fig. A.1, but for the P-3 flight leg from 00:48 UTC 20 January 2023 to 01:01 UTC 20 January 2023. . . . .	145
Figure A.14	As in Fig. A.1, but for the P-3 flight leg from 13:59 UTC 23 January 2023 to 14:13 UTC 23 January 2023. . . . .	146
Figure A.15	As in Fig. A.1, but for the P-3 flight leg from 14:25 UTC 23 January 2023 to 14:32 UTC 23 January 2023. . . . .	147
Figure A.16	As in Fig. A.1, but for the P-3 flight leg from 14:34 UTC 23 January 2023 to 14:47 UTC 23 January 2023. . . . .	148
Figure A.17	As in Fig. A.1, but for the P-3 flight leg from 14:51 UTC 23 January 2023 to 15:24 UTC 23 January 2023. . . . .	149
Figure A.18	As in Fig. A.1, but for the P-3 flight leg from 16:02 UTC 23 January 2023 to 16:24 UTC 23 January 2023. . . . .	150

Figure A.19	As in Fig. A.1, but for the P-3 flight leg from 16:30 UTC 23 January 2023 to 16:49 UTC 23 January 2023. . . . .	151
Figure A.20	As in Fig. A.1, but for the P-3 flight leg from 17:58 UTC 16 February 2023 to 18:19 UTC 16 February 2023. . . . .	152
Figure A.21	As in Fig. A.1, but for the P-3 flight leg from 17:30 UTC 16 February 2023 to 17:52 UTC 16 February 2023. . . . .	153
Figure A.22	As in Fig. A.1, but for the P-3 flight leg from 18:26 UTC 16 February 2023 to 18:54 UTC 16 February 2023. . . . .	154
Figure A.23	As in Fig. A.1, but for the P-3 flight leg from 18:59 UTC 16 February 2023 to 19:24 UTC 16 February 2023. . . . .	155
Figure A.24	As in Fig. A.1, but for the P-3 flight leg from 19:31 UTC 16 February 2023 to 19:50 UTC 16 February 2023. . . . .	156
Figure A.25	As in Fig. A.1, but for the P-3 flight leg from 14:44 UTC 23 February 2023 to 15:11 UTC 23 February 2023. . . . .	157
Figure A.26	As in Fig. A.1, but for the P-3 flight leg from 10:58 UTC 28 February 2023 to 11:21 UTC 28 February 2023. . . . .	158

# CHAPTER

# 1

# INTRODUCTION

## **1.1 Motivation**

Heavy snow and winds associated with winter storms can have significant negative societal impacts, including power outages, roof failures, and closure of transportation systems. Twenty-four winter storms caused at least 1 billion USD in damage between 1980 and 2024 (NOAA National Centers for Environmental Information 2024). The northeast United States is especially vulnerable to the risks associated with winter storms due to the large population centers near the coast (e.g., Washington, D.C., Philadelphia, PA, New York, NY, and Boston, MA) and the regular occurrence of extratropical cyclones bringing snowfall to the region (Kocin and Uccellini 2004).

Forecasting the timing and location of heavy snowfall rates represents a challenge to operational meteorologists, and there is often large uncertainty in forecasts of snowfall accumulation (Novak et al. 2014). Numerical weather prediction models often have substantial error in their forecasts of snowfall intensity, timing, and location (e.g., Zhang et al. 2002; Radford et al. 2019; Connelly and Colle 2019; Fritz 2023). The representation of processes relevant to snow mass growth and shrinkage is a source of error in numerical weather models (Connelly and Colle 2019; McMurdie et al. 2022). This study addresses questions related to understanding which processes are primarily important to snow mass growth in most winter storms affecting flat-land

regions in the Northeast and Midwest United States.

## 1.2 Definitions of key terms

Table 1.1 defines key terms which are used throughout this dissertation and may be unfamiliar to non-meteorologist readers.

Table 1.1: Definitions of key meteorological terms used in this dissertation.

<b>Term</b>	<b>Definition</b>
<b>Radar reflectivity</b>	Measure of the energy received by a weather radar which is reflected back from scatterers, precipitation particles and non-meteorological targets, in a scanned volume. In rain, radar reflectivity is a function of the number and size of rain drops in a given volume, and higher reflectivity is typically associated with higher rain mass per unit volume. In snow, the different shapes and densities of snow particles means that the relationship between reflectivity and snow mass per unit volume is not monotonic.
<b>Enhanced reflectivity bands</b>	Narrow, linear horizontal regions where the radar reflectivity is higher than some "background" value. Bands can be identified objectively from scanning radar data following Tomkins et al. (2024b).
<b>Doppler velocity</b>	Measure of the component of velocity of scatterers along a radar beam. For radars scanning close to horizontal, the Doppler velocity is indicative of the horizontal wind. For radars scanning vertically, the Doppler velocity is the sum of vertical air motion and particle fall speeds.
<b>Doppler velocity wave</b>	Sets of banded features in radar Doppler velocity data. Doppler velocity waves can be identified from scanning radar data following Miller et al. (2022).
<b>Generating cells</b>	Overturning convective circulations commonly present near cloud top in winter storms. "Ice streamers" of enhanced reflectivity are often observed descending from generating cells.
<b>Frontogenesis</b>	The strengthening of the gradient of a scalar field (typically temperature or related) following an air parcel. Frontogenesis is associated with an air circulation in which there is upward motion on the warm side of a weather front.
<b>Relative humidity</b>	The proportion of the equilibrium (i.e., saturation) water vapor mixing ratio which is present in an air parcel. Relative humidity can be expressed either with respect to liquid water ( $RH_{water}$ ) or with respect to ice ( $RH_{ice}$ ). When air temperature $< 0^{\circ}\text{C}$ , $RH_{ice} > RH_{water}$ .
<b>Supersaturation</b>	A condition where $RH > 100\%$ , either with respect to liquid water or with respect to ice. If air is supersaturated with respect to ice, then ice particles grow by vapor deposition. If air is supersaturated with respect to liquid water, then water droplets grow by condensation.

Table 1.2 defines terms which are used mostly in Chapters 2 and 3 that relate to wave analysis.

Table 1.2: Definitions of key wave-related terms used in this dissertation.

<b>Term</b>	<b>Conventional symbol</b>	<b>Definition</b>
Wave period	$\tau$	For a fixed location, the amount of time from one wave peak (or trough) to the next. Inverse of wave frequency. Unit: s.
Wave frequency	$f$	For a fixed location, the number of wave peak (or trough) passages per unit time. Inverse of wave period. Units: $s^{-1}$ or Hz.
Wavelength	$\lambda$	The distance between wave peaks (or wave troughs). Product of wave period and phase speed. Unit: m.
Wave amplitude	A	The difference between the wave peak and trough values in hPa.
Event duration		The amount of time over which a detectable wave signal was present.
Wavelet power	$ W $	The absolute value of the wavelet transform output. Units: $\text{hPa}^2 \text{s}^{-1}$ (when applied to pressure in hPa).
Phase speed	$ \vec{c} $ or $c$	The distance traversed by a wave peak (or wave trough) per unit time. Product of wavelength and wave frequency. Units: $\text{m s}^{-1}$ .
Phase direction		The direction relative to north (where north is at 0 degree azimuth) in which the wave peaks/troughs are propagating. Unit: $^\circ$ .
Phase velocity	$\vec{c}$	Vector in xy-plane which has magnitude defined by the phase speed and direction defined by the phase direction. Units: $\text{m s}^{-1}$ .
Slowness vector	$\vec{s}$	Vector in xy-plane with components equal to the inverse of the phase velocity components. Points in phase direction. Units: $\text{s m}^{-1}$ .
Pressure wave		Detectable wave signals present in time series of pressure over at least 4 pressure sensors in a network.
Gravity wave / buoyancy wave		Waves attributed to the physical mechanism by which air parcels in a stable environment, when perturbed vertically, will oscillate about their original altitude.

### 1.3 Background

We will focus on *flat-land winter storms* to distinguish from orographically-forced or lake effect snow storms. Flat-land winter storms are usually forced by extratropical cyclones and associated air mass boundaries. Extratropical cyclones are characterized by minima in sea level pressure and sloped air mass boundaries (i.e., fronts) which separate warmer air from colder air. Frontal circulations, large-scale temperature advection, large-scale vorticity advection, and convective-scale instabilities near cloud top provide forcing for vertical air motion (e.g., Schultz et al. 2019). The effects of warm lakes and topography superimpose additional forcing on extratropical cyclones which are not important to snow events impacting the Northeast US coastal areas or most of the Midwest US. *In general, "winter storms" will refer to flat-land winter storms in this dissertation.*

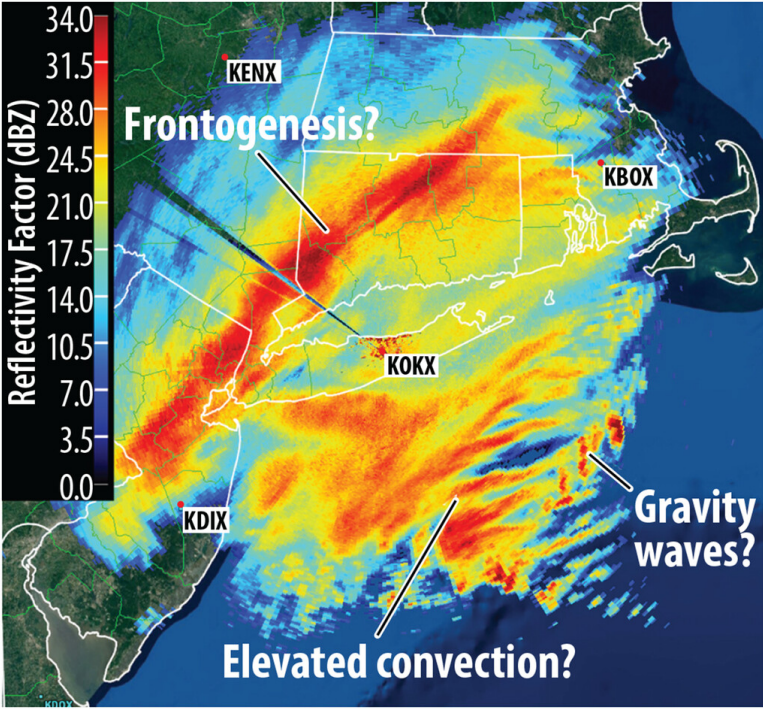


Figure 1.1: (Figure 2 from McMurdie et al. 2022). An example plot of radar reflectivity factor (dBZ) illustrating narrow regions of high reflectivity associated with the primary snowband and multibands. Potential mechanisms contributing to snowband formation and maintenance are indicated on the figure.

### 1.3.1 Reflectivity bands and gravity waves in winter storms

Previous work has focused on linear *bands* of enhanced radar reflectivity within winter storms, in which there were assumed to be higher snow rates (e.g., Novak et al. 2004, 2008, 2010; Hoban 2016; Ganetis et al. 2018; Leonardo and Colle 2024). These studies conventionally categorize bands as either primary (i.e., single) bands or as groups of multibands. Primary bands are  $\geq 200$  km in length, and Ganetis et al. (2018) found an association between primary bands and stronger frontogenesis. Multibands are groups of two or more bands parallel to each other,  $< 200$  km in length. In Fig. 1.1, a primary band spans from central New Jersey northeast to central Massachusetts. Two groups of multibands are present in Fig. 1.1, both southeast of Long Island: some are oriented west-east, and some are oriented north-south. There is no clear consensus on the physical process(es) and/or environmental condition(s) most important for multiband formation and maintenance, as the annotations of multibands in Fig. 1.1 indicate. More recent work has indicated that enhanced reflectivity features in flat-land winter storms rarely correspond to heavy surface snowfall rates. This is because snow mass does not have a direct relationship to reflectivity, and locally enhanced reflectivity features aloft can be "smeared" together at lower levels as snow falls toward the ground in environments with vertical wind shear (Tomkins 2024).

Hoban (2016) found that 64% of winter storms with multibands also contained *Doppler velocity waves*, which were detected using radar Doppler velocity data from operational National Weather Service radars (WSR-88Ds) (Miller et al. 2022). Hoban (2016) noted that the Doppler velocity waves did not always move in lockstep with multibands when both were present, but did not quantify how often this was the case. The Doppler velocity waves could result from convergence and divergence patterns associated with gravity waves, Kelvin-Helmholtz waves (Houser and Bluestein 2011), or flow anomalies associated with potential vorticity dipoles (Leonardo and Colle 2023).

The upward branches in gravity waves could yield increased snow mass by expanding and cooling air parcels, thereby lowering their saturation water vapor mixing ratio. The parcel water vapor mixing ratio remains constant for adiabatic processes (no phase changes or fluxes in/out of the parcel), so the RH of the parcel increases as it is lifted (upward movement in Fig. 1.2). If the parcel becomes supersaturated with respect to ice (crosses the 100%  $RH_{ice}$  contour in Fig. 1.2), ice particle growth by vapor deposition will occur. If the parcel become supersaturated with respect to liquid water (crosses the 100%  $RH_{water}$  contour in Fig. 1.2), liquid water droplets will form and could accrete on ice particles in a process called *riming*. Case study evidence exists of enhanced snow rates being associated with gravity waves (e.g., Bosart et al. 1998), but it is not known whether gravity waves are commonly associated with enhanced radar reflectivity or increased surface snowfall rates for flat-land winter storms.

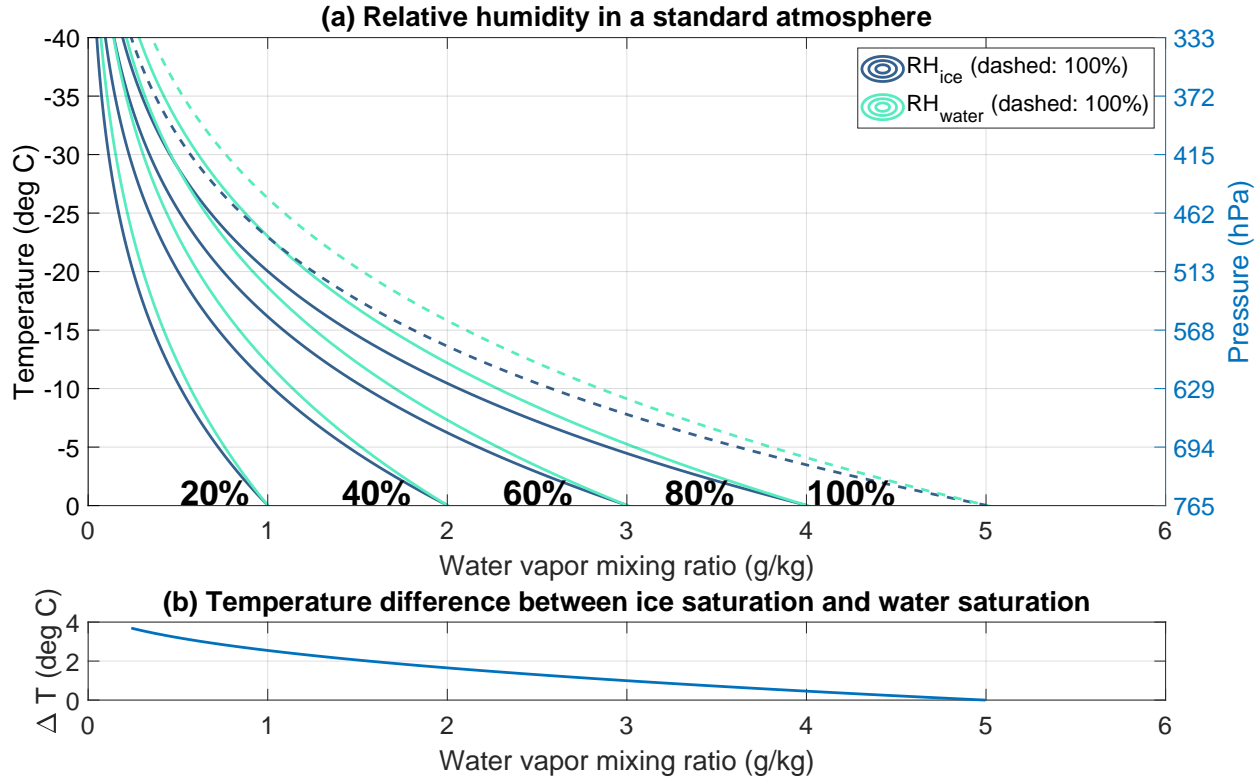


Figure 1.2: **(a)** Contours of relative humidity with respect to ice ( $RH_{ice}$ ) and with respect to liquid water ( $RH_{water}$ ) as a function of temperature and water vapor mixing ratio, assuming a standard atmosphere temperature-pressure relationship (corresponding pressure values on right axis). RH values are contoured at 20% intervals, with the 100% contour dashed. **(b)** The temperature difference between the 100%  $RH_{ice}$  and 100%  $RH_{water}$  contours at each water vapor mixing ratio.

### 1.3.2 Vertical air motions in winter storms

The in-cloud spatiotemporal distribution of vertical air velocity in winter storms is important to determining where and when ice mass increases and decreases may be occurring. As discussed in Sect. 1.3.1, upward motion cools and expands air parcels, raising their RH values (Fig. 1.2) and potentially leading to hydrometeor nucleation and growth. Conversely, downward motion heats and contracts air parcels, lowering their RH values and potentially leading to hydrometeor shrinkage.

It has been long recognized that the spatial distribution of surface precipitation is highly sensitive to the time between when a cloud particle reaches precipitation size and begins to fall and when it reaches the surface (e.g. Smith 1979; Colle and Mass 2000; Colle and Zeng 2004; Colle et al. 2005; Lackmann and Thompson 2019). If precipitation particles remain in cloud for more time, then there is more time for them to be horizontally advected. Horizontal

wind speeds in winter storms are typically 10x or more than the terminal fall speeds for snow ( $\sim 1 \text{ m s}^{-1}$ ). The duration of a precipitation-size particle within a storm is a function of its starting altitude where it first achieved precipitation size and the effective fall speed along its trajectory, where effective fall speed is the sum of terminal fall speed and vertical air motion. Updrafts will decrease effective fall speed while downdrafts will do the opposite.

Vertical velocity is spatial scale-variant, meaning that the spatial resolution over which vertical velocity is sampled will influence the resulting distribution of vertical velocity. Vertical air motions are generally weaker when averaging over larger horizontal areas. Remote-sensing analyses of vertical velocity in winter storms have sampled on resolutions of tens to hundreds of m (e.g., Crouse et al. 2007; Rosenow et al. 2014; Rauber et al. 2017; Oue et al. 2024), and airborne in situ instruments sample on similar horizontal resolutions. Rosenow et al. (2014), Keeler et al. (2016), and Rauber et al. (2017) found overturning air motions associated with cloud-top generating cells on horizontal scales as small as  $\sim 1 \text{ km}$ . In contrast, global operational forecast models typically have grid resolutions  $> 10 \text{ km}$  and some regional operational forecast models use grids of  $3 \text{ km}$ . Therefore, current numerical weather models do not resolve the small-scale variability in vertical air motions, including the cloud-top generating cells. Those small-scale vertical air motions will affect the ambient relative humidity and thus conditions for ice growth and shrinkage, which will not be fully represented in models with coarse grid spacing.

## 1.4 Road map of this dissertation

In this dissertation, we are broadly aiming to address the following knowledge gaps:

- how often gravity waves can be detected during flat-land winter storms in the Northeast United States and Southern Canada, and whether gravity waves can be linked to enhancements in radar reflectivity and/or waves in radar Doppler velocity
- the typical strength of vertical air motions and breadth of updrafts in winter storms as measured by in situ instruments, and whether those vertical air motions are capable of lofting precipitation-size ice particles over large spatial scales

In order to determine the presence of gravity waves, pressure sensor data are needed (Nappo 2002, Sect. 8.2). Chapters 2 and 3 describe our analysis of data from networks of high-precision pressure sensors. Chapter 2, which has been published in *Atmospheric Measurement Techniques*, focuses on the method for objectively identifying and extracting wave signals from the pressure data and the calculation of wave phase velocity. Examples of different types of

pressure waves with context are given in Chapter 2. In Chapter 3, to be submitted to *Atmospheric Chemistry and Physics*, we examine pressure wave events identified over 40 months of data. We use contextual data sets to determine which pressure wave events are gravity waves, and we determine whether the gravity wave events co-occurred with enhanced reflectivity bands and/or Doppler velocity waves. Chapter 3 concludes with a discussion on the implications of our results in the context of previous studies of gravity waves in winter storms.

Chapters 4 and 5 describe our analysis of in-cloud vertical air motions measured by in situ instruments. A distilled version of Chapters 4 and 5 will be submitted to either *Geophysical Research Letters* or *Journal of Geophysical Research: Atmospheres*. Chapter 4 motivates our analysis of in-cloud vertical air motions and describes the data and methods used in that analysis. Chapter 5 includes results and conclusions of our in-cloud vertical air motion analysis.

Finally, Chapter 6 contains a summary of the main conclusions of this dissertation and implications on the current conceptual model of flat-land winter storms. We also discuss potential avenues for future work.

## CHAPTER

# 2

# OBJECTIVE IDENTIFICATION OF PRESSURE WAVE EVENTS FROM NETWORKS OF 1-HZ, HIGH-PRECISION SENSORS

Published in Atmospheric Measurement Techniques in January 2024.

**Citation** Allen, Luke R., S. E. Yuter, M. A. Miller, L. M. Tomkins, 2024: Objective identification of pressure wave events from networks of 1 Hz, high-precision sensors. *Atmospheric Measurement Techniques*, **17**, 113-134. <https://doi.org/10.5194/amt-17-113-2024>

**Authors** Luke R. Allen<sup>1</sup>, Sandra E. Yuter<sup>1,2</sup>, Matthew A. Miller<sup>2</sup>, and Laura M. Tomkins<sup>1</sup>

<sup>1</sup>Center for Geospatial Analytics, North Carolina State University, Raleigh, NC, 27695, USA

<sup>2</sup>Department of Marine, Earth and Atmospheric Science, North Carolina State University, Raleigh, NC, 27695, USA

**Acknowledgements** The authors express their sincere appreciation to the pressure sensor hosts in Toronto, New York City metro area and Long Island, and Raleigh, including colleagues from Environment Canada, Stony Brook University, Columbia University, and friends, including

Jase Bernhardt, Drew Claybrook, Brian Colle, Daniel Horn, Daniel Michelson, Robert Pincus, Spencer Rhodes, Adam Sobel, David Stark, and Jeff Waldstreicher, who graciously agreed to plug in pressure sensors to their home internet. Figure 2.9 was made using code developed by Kevin Burris. The development and refinement of the methodology benefited from discussions with DelWayne Bohnenstiehl, Brian Colle, Brian Mapes, Matthew Parker, and Minghua Zhang.

This work was supported by the National Science Foundation (AGS-1905736), the National Aeronautics and Space Administration (80NSSC19K0354), the Office of Naval Research (N000142112116), and the Center for Geospatial Analytics at North Carolina State University.

**Abstract** Mesoscale pressure waves, including atmospheric gravity waves, outflow and frontal passages, and wake lows, are outputs of and can potentially modify clouds and precipitation. The vertical motions associated with these waves can modify the temperature and relative humidity of air parcels and thus yield potentially irreversible changes to the cloud and precipitation content of those parcels. A wavelet-based method for identifying and tracking these types of wave signals in time series data from networks of low-cost, high-precision (0.8-Pa noise floor, 1-Hz recording frequency) pressure sensors is demonstrated. Strong wavelet signals are identified using a wave period-dependent (i.e., frequency-dependent) threshold, then those signals are extracted by inverting the wavelet transform. Wave periods between 1 minute and 120 minutes were analyzed, a range which could capture acoustic, acoustic-gravity, and gravity wave modes. After extracting the signals from a network of pressure sensors, the cross-correlation function is used to estimate the time difference between the wave passage at each pressure sensor. From those time differences, the wave phase velocity vector is calculated using a least-squares fit. If the fitting error is sufficiently small (thresholds of RMSE < 90 s and NRMSE < 0.1 were used), then a wave event is considered robust and trackable. We present examples of tracked wave events, including a Lamb wave caused by the Hunga-Tonga volcanic eruption in January 2020, a gravity wave train, an outflow boundary passage, a frontal passage, and a cold front passage. The data and processing techniques presented here can have research applications in wave climatology and testing associations between waves and atmospheric phenomena.

## 2.1 Introduction

Gravity waves (i.e., buoyancy waves), which result from vertical perturbations of stably stratified fluid, are ubiquitous in the atmosphere and represent an important distributor of energy through the atmosphere (Fritts and Alexander 2003; Nappo 2002). The initial perturbations which generate gravity waves can have several sources, including but not limited to forced

flow over topography, deep convection, shear instability, adjustment of unbalanced flow, and nonlinear interaction between waves (Fritts and Alexander 2003). Within the troposphere, the vertical motions associated with gravity waves have been shown to influence cloud and precipitation processes. If parcels then reach saturation and produce precipitation which falls out, the changes to the parcel can be irreversible. Several studies have investigated the effects of gravity waves on marine stratocumulus. Allen et al. (2013) and Connolly et al. (2013) related gravity waves to changes in drizzle production within marine stratocumulus; specifically, enhanced condensation and collision-coalescence to form drizzle drops appeared to occur in the updrafts associated with gravity waves. Evidence also suggests a link between gravity waves and the rapid erosion of marine stratocumulus cloud decks (Yuter et al. 2018), perhaps because evaporation due to entrainment is enhanced as marine stratocumulus clouds are lifted by gravity waves (Connolly et al. 2013). Fovell et al. (2006) identified gravity waves as a potential trigger mechanism for deep moist convective cells. Case studies have linked gravity waves to snow bands, i.e., linear mesoscale enhancements in snowfall rate within winter storms (Bosart et al. 1998; Zhang et al. 2001; Gaffin et al. 2003), but it is unclear how often snow bands are associated with gravity waves.

To illustrate how the vertical motions associated with gravity waves could influence cloud microphysical properties, we use Fig. 1.2, which shows relative humidity with respect to ice ( $RH_{ice}$ ) and with respect to liquid water ( $RH_{water}$ ) as a function of temperature and water vapor mixing ratio for a standard atmosphere, as well as the temperature difference between 100%  $RH_{ice}$  and 100%  $RH_{water}$  for each water vapor mixing ratio. For temperatures below 0°C,  $RH_{ice} > RH_{water}$ . A lifted parcel would be cooled at a constant water vapor mixing ratio (move upward in Fig. 1.2) until it intersects the 100%  $RH_{ice}$  contour wherein vapor deposition would reduce the water vapor (further lifting would move upward and to the left in Fig. 1.2). If the parcel cools sufficiently to also intersect the 100%  $RH_{water}$  contour, supercooled water droplets would form in the parcel and riming would likely occur further depleting the available water vapor in the parcel. An up-and-down motion of an air parcel in a gravity wave that only crosses the 100%  $RH_{ice}$  contour yields ice mass changes that are reversible, i.e. the ice mass added by vapor deposition in the upward motion will be lost to sublimation in the downward motion.

In contrast, if the lifting of the parcel within a gravity wave starts at  $RH_{ice} \geq 100\%$  and intersects the 100%  $RH_{water}$  contour, the ice mass added by riming when ice particles collide with supercooled droplets is not reversible (i.e., there is no unriming process). For example, if an ice saturated parcel containing ice crystals (e.g., at -8.0°C and 2.96 gkg<sup>-1</sup> water vapor mixing ratio) is lifted and cooled to -9.7°C in a gravity wave (which requires roughly 190 m of lift assuming a 9°C km<sup>-1</sup> parcel lapse rate), it would become supersaturated with respect to water as well as with respect to ice. Water droplets would form in the parcel and the ice crystals

could potentially become rimed. If the parcel remains ice saturated when it descends in the gravity wave, the additional ice mass from the riming on the ice particle would not be removed. Ice mass added by riming can only be removed by sublimation in conditions where the parcel is subsaturated with respect to ice.

One way of distinguishing gravity waves from other wave phenomena such as Kelvin-Helmholtz waves is that gravity waves produce a surface pressure signal (Nappo 2002, Sect. 8.2), given that the stable layer in which they occur is adjacent or nearly adjacent to the surface. That said, several different phenomena can produce surface pressure disturbances on similar spatiotemporal scales to gravity waves, including but not limited to outflow boundary passages, convective wake lows (Johnson and Hamilton 1988), release of conditional symmetric instability (Gray et al. 2011), and Lamb waves generated by, e.g., distant volcanic eruptions (Matoza et al. 2022), large bolide impacts (ReVelle 2008), and thermonuclear explosions (Pierce and Posey 1971). Acoustic and acoustic-gravity waves can also produce pressure signals at shorter timescales. Such waves would include infrasound waves, which can be associated with, e.g., convective storms and strong flow over mountains (Coffer and Parker 2022; Bedard 1978).

Time series of surface pressure data have been analyzed to identify tropospheric wave events in previous studies (Kjelaas et al. 1974; Christie et al. 1978; Einaudi et al. 1989; Grivet-Talocia and Einaudi 1998; Grivet-Talocia et al. 1999; Koch and Saleeby 2001; de Groot-Hedlin et al. 2014). Kjelaas et al. (1974) and Christie et al. (1978) presented case studies of gravity wave events selected manually from time series pressure data. Grivet-Talocia and Einaudi (1998) and Grivet-Talocia et al. (1999) recorded data at 1/120 Hz (i.e., every 2 min) to identify wave periods longer than 30 min. Einaudi et al. (1989) used a network of microbarographs recording at 0.1 Hz (i.e., every 10 sec) placed within roughly 100 m of each other, which constrained the characteristics of disturbances which could be tracked through their network to waves with speeds up to 50 m s<sup>-1</sup>, and wave periods of 1-20 min. Koch and Saleeby (2001) used operational Automatic Surface Observing Systems (ASOS) data recorded at 1/300 Hz (i.e., every 5 min) which resolved wavelengths  $\geq 150$  km. While strong pressure disturbances including outflows and wake lows can be detected by ASOS pressure sensors logging data at 1 min intervals, the large spatial separation between operational weather stations, which are mostly located at airports, precludes determination of the associated wave speed and direction for mesoscale disturbances. de Groot-Hedlin et al. (2014) used 337 barometers deployed with the USArray Transportable Array, recording at 1 Hz (i.e., every 1 sec) frequency, to detect and track high-amplitude (roughly 3 hPa peak to trough) pressure waves associated with convective storms in the southern United States. The USArray Transportable Array barometers were spaced roughly 70 km apart, which might also preclude tracking of localized disturbances.

There is a scarcity of data for detecting and tracking pressure disturbances, including gravity

waves, on the meso- $\beta$  scale or meso- $\gamma$  scale (ranging from 2 km to 200 km). Pressure disturbances on those scales may be relevant to phenomena such as snow bands (e.g., McMurdie et al. 2022), trade wind cumulus (e.g., Seifert and Heus 2013), and bow echoes (e.g., Adams-Selin and Johnson 2010), which are active areas of research. We developed a measurement and analysis technique which will allow for questions regarding gravity waves on those scales to be addressed. To what degree and in what conditions information on gravity wave occurrence would be valuable in operational weather settings is yet to be determined.

This paper presents data from networks of internet appliance low-cost, high-precision air pressure sensors (i.e., microbarographs) and a methodology for objectively identifying mesoscale wave events and wave speed and direction. The methodology is intended to be used for post-processing in research applications, rather than for real-time or near-real-time detection of wave events. Similar low-cost sensor networks have been used for detection of seismic waves (Anthony et al. 2018) and for detecting infrasound waves to monitor fan rotation speeds in nuclear-reactor cooling towers (Eaton et al. 2022). The former network covered the area of Oklahoma, and the latter used networks covering the area of a single nuclear reactor. Our networks of pressure sensors are on the scale of a medium-to-large-sized city or metropolitan area.

Section 2.2 of this paper describes the pressure sensors used in this study and the data they provide. Section 2.3 describes the methodology for objectively identifying pressure waves from the pressure time traces. Section 2.4 provides five examples of events captured by the wave identification method. Finally, a summary and avenues for future work are discussed in Sect. 2.5.

## **2.2 Data**

### **2.2.1 Networks of pressure sensors**

Pressure sensors were placed in three separate networks: New York City metro area and Long Island, NY; Raleigh, NC; and Toronto, ON, Canada (Fig. 2.1). Each pressure sensor was either a Bosch BME280 (Bosch 2022) or a Bosch BMP388 (Bosch 2020) Adafruit breakout board connected to a Raspberry Pi Zero W single-board computer used to log the data. BME280 sensors measure pressure, temperature, and humidity. BMP388 sensors measure pressure and temperature. Each pressure sensor costs roughly 50-75 US Dollars, subject to changes in the cost of Raspberry Pi Zero W units. For context to another low-cost network concept, the Raspberry Shake 4D seismographs cost a few hundred dollars per unit (Anthony et al. 2018). The combined sensor and communications package is about the size of a deck of cards. Sensors

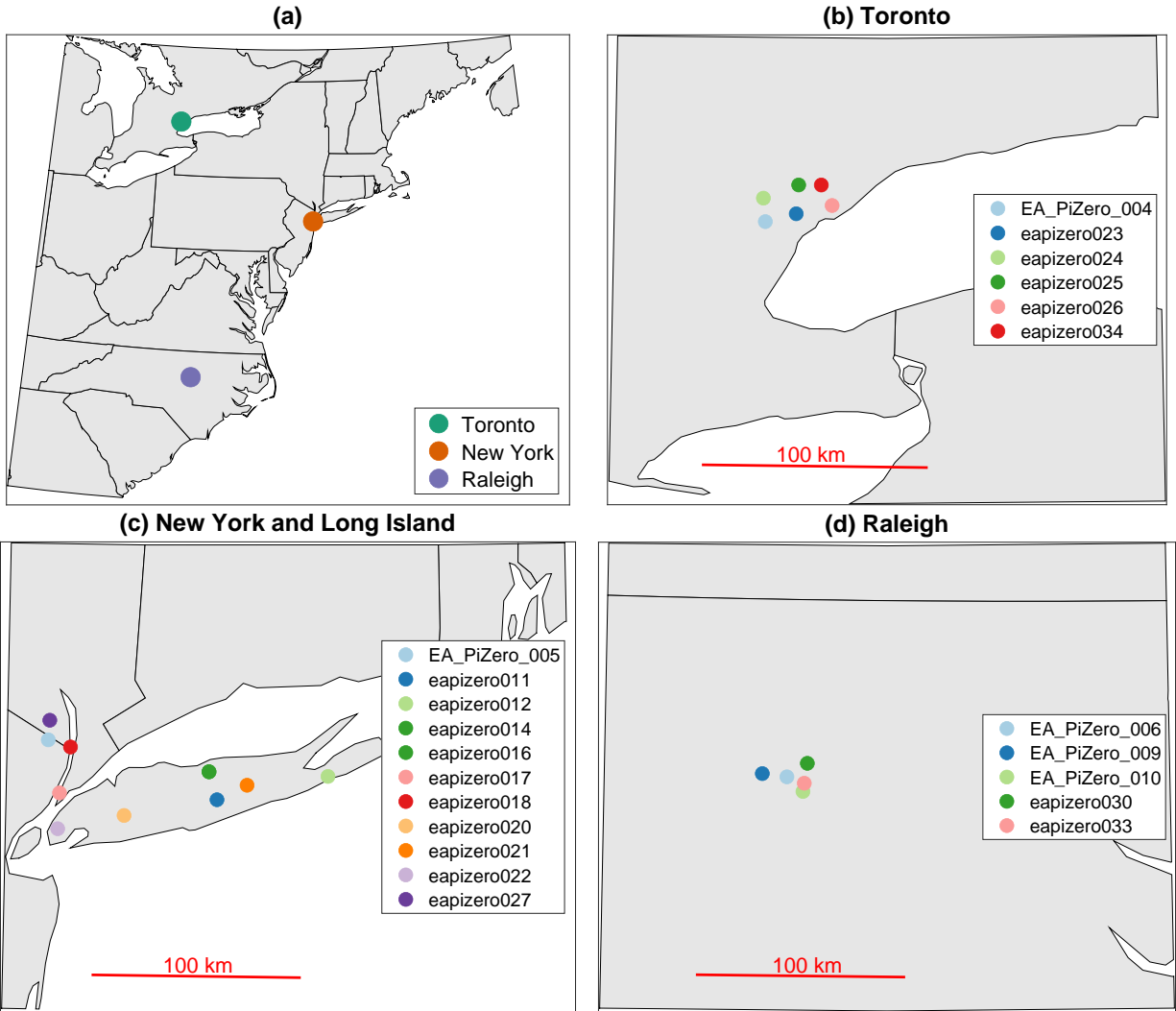


Figure 2.1: Locations of pressure sensor networks. **(a)** US northeast regional map with the locations of the Toronto, New York City and Long Island, and Raleigh networks indicated. Detailed maps of sensor locations in **(b)** Toronto, **(c)** New York and Long Island, and **(d)** Raleigh.

are connected to the internet and sync their data to a server at North Carolina State University. Initial testing of the sensors outdoors on patios, in sheltered locations such as garages, and indoors revealed pressure waves were well resolved in all locations, and it was best practice to place the sensors indoors to minimize wind contamination in pressure measurements. When active, each sensor records pressure at 1-second intervals with a roughly 0.8 Pa noise floor depending on ambient conditions. The sensors synchronize to network time upon startup. The wave extraction method only depends on relative pressure variations and is not sensitive to absolute or relative calibration.

To examine the properties of gravity waves which are detectable by these pressure sensors, we consider an internal gravity wave occurring in an environment with constant background wind  $u_0$ . The relationship between the pressure perturbation  $p'$  and the horizontal velocity perturbation  $u'$  associated with the wave is described by Nappo (2002):

$$p' = u' \rho_0 (c - u_0) \quad (2.1)$$

where  $\rho_0$  is the environmental air density and  $c$  is the phase speed of the gravity wave. From Eq. 2.1, the maximum pressure perturbation  $p'_{max}$  can therefore be related to the maximum horizontal velocity perturbation  $u'_{max}$  by:

$$p'_{max} = u'_{max} \rho_0 (|c - u_0|) \quad (2.2)$$

Figure 2.2 shows  $p'_{max}$  values according to Eq. 2.2 at an air density of  $1.225 \text{ kg m}^{-3}$  (standard air density at sea level; American Meteorological Society 2022) for  $u'_{max}$  and  $|c - u_0|$  values up to  $15 \text{ m s}^{-1}$ . In order to reliably detect a wave signal, the amplitude likely needs to be substantially larger than the noise floor.

## 2.2.2 Operational weather observations

For context, we compare extracted wave signals with available operational weather observations.

We use Automated Surface Observing Systems (ASOS; NOAA National Centers for Environmental Information 2021a) data including surface temperature, dew point, wind speed and direction, and additional pressure measurements coincident with wave events. ASOS data are recorded each minute. For wave events detected in New York and Long Island, we examined ASOS data from John F. Kennedy International Airport (KJFK) and Long Island MacArthur Airport (KISP). For wave events detected in Toronto, we examined ASOS data from Buffalo Niagara International Airport (KBUF) and Niagara Falls International Airport (KIAG).

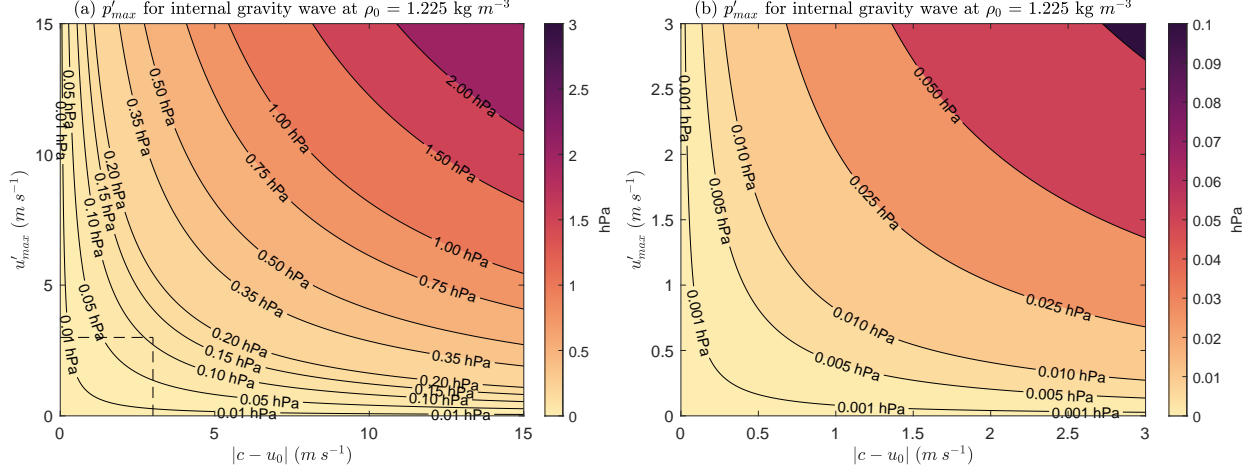


Figure 2.2: The maximum pressure perturbation  $p'_{max}$  (hPa) contoured and colored, according to Eq. 2.2 at an air density  $\rho_0$  of  $1.225 \text{ kg m}^{-3}$ .  $p'_{max}$  is a function of the maximum velocity perturbation  $u'_{max}$  ( $\text{m s}^{-1}$ ) and absolute value of the difference between the wave phase speed and background wind speed  $|c - u_0|$  ( $\text{m s}^{-1}$ ). In panel (a),  $u'_{max}$  and  $|c - u_0|$  up to  $15 \text{ m s}^{-1}$  are shown. In panel (b),  $u'_{max}$  and  $|c - u_0|$  up to  $3 \text{ m s}^{-1}$  are shown. The color scales differ in panels (a) and (b).

For one example case in Sect. 2.4.2, we show upper-air radiosonde data from a weather balloon launched in Buffalo, NY. We obtained data from the Integrated Global Radiosonde Archive (IGRA; NOAA National Centers for Environmental Information 2021b) and interpolated to a constant 100-meter resolution. The data include measurements of temperature, dew point, and winds, from which we calculated wet-bulb temperature, frost point, and saturation equivalent potential temperature ( $\theta_e^*$ ). Because radiosondes are typically launched every 12 hours at a limited number of locations, representative radiosonde data are not available for every case.

We use horizontal maps of data from the US National Weather Service (NWS) WSR-88D radars (NOAA National Weather Service Radar Operations Center 1991) to show storm features occurring coincident with wave events in Sect. 2.4.3 and Sect. 2.4.5. Radar reflectivities are processed following Tomkins et al. (2022) to indicate regions with mixed precipitation in the scan, by inferring that points with reflectivity above 20 dBZ and dual-polarization correlation coefficient below 0.97 have mixed precipitation. In maps of radar reflectivity, those regions with mixed precipitation are then shown in greyscale. Doppler velocity waves are extracted from radial velocity data following Miller et al. (2022), by calculating the difference in radial velocity from successive scans, converting those differences to a binary (positive/negative) field, and filtering out small objects in that binary field.

## 2.3 Methods

The methods outlined here for identifying wave events in the pressure time traces are adapted from the techniques used by Grivet-Talocia and Einaudi (1998) and Grivet-Talocia et al. (1999). The method uses wavelet transforms to identify wave events in time-wave period (or, equivalently, time-frequency) space. Wavelet transforms are preferable to Fourier transforms for the purpose of identifying transient waves which are localized in time (Torrence and Compo 1998). To illustrate the step-by-step procedure, an example corresponding to a gravity wave event on 23 February 2023 in the Toronto pressure network is described in detail.

### 2.3.1 Identifying wave events in a single sensor

The full pressure time series for a gravity wave event on 23 February 2023 captured by sensor 25 in Toronto is shown in Fig. 2.3a. As an initial pre-processing step, 10-second samples of pressure (i.e., averages of 10 pressure measurements) are used to smooth out noise and pressure perturbations due to high-frequency turbulent eddies in the data (Fig. 2.3b). Hereafter, time series labeled as total pressure are the 10-second subsamples of the original pressure measurements.

A wavelet transform  $W$  of a finite energy signal  $f(t)$  (a pressure time series in this study) can be defined as in (Grivet-Talocia and Einaudi 1998, their Eq. 1):

$$W(b, a) = \frac{1}{|a|} \int_{-\infty}^{\infty} f(t) \psi^*\left(\frac{t-b}{a}\right) dt \quad (2.3)$$

where  $a$  is the scale (related to the wave period), and  $b$  shifts the wavelet in time ( $t$ ).  $\psi^*$  represents the mother wavelet. An analytic Morse wavelet was used (e.g., Olhede and Walden 2002; Lilly and Olhede 2012) via the *cwt* function within MATLAB (Lilly 2021). In this study,  $W(b, a)$  will always refer to the wavelet transform of a pressure time series. The resulting wavelet transform is an array of complex values in time-scale space. The absolute value of the wavelet transform  $|W(b, a)|$  can be considered the wavelet power at a given time and scale. Figure 2.3c shows the wavelet power associated with the wave event at sensor 25 on 23 February 2023. In this study, wave periods between 1 minute and 120 minutes were analyzed, corresponding to expected periods for mesoscale disturbances.

To objectively identify wave event centers according to wavelet power, a scale-dependent (i.e., wave-period-dependent) threshold function  $A(a)$  is defined as the mean wavelet power across all available data for the sensor network by scale, multiplied by a constant  $K$ :

$$A(a) = K \langle |W(b, a)| \rangle_b \quad (2.4)$$

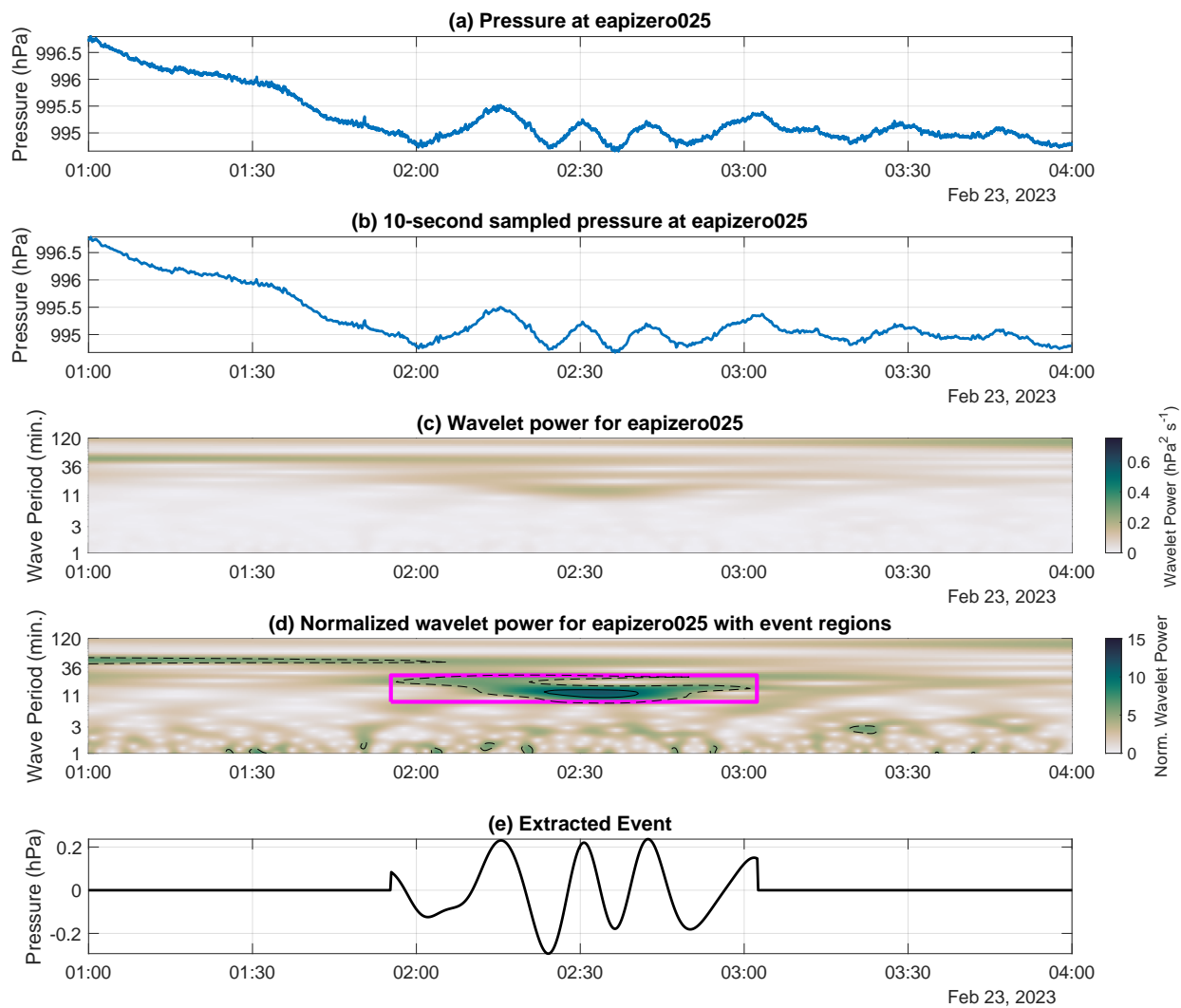


Figure 2.3: Steps in process of identifying an event corresponding to a gravity wave train passage on 23 Feb 2023 in sensor 25. **(a)** Original 1-second pressure time series. **(b)** The 10 s moving average of the pressure time series, with every 10th point kept. **(c)** Wavelet power corresponding to the pressure time series in panel **(b)**. **(d)** Wavelet power normalized by the mean for each wave period corresponding to the pressure trace, with contours for values of 5 (dashed) and 10 (solid). The event region corresponding to the wave described in the text is outlined in magenta in panel **(d)**. **(e)** Time series of the extracted wave event. Wave periods in panels **(c)** and **(d)** are shown on a logarithmic scale. All times are UTC.

A scale-dependent threshold  $K$  is necessary because the ‘background’ wavelet power for a pressure time series generally increases with scale (e.g., Canavero and Einaudi 1987). Grivet-Talocia and Einaudi (1998) and Grivet-Talocia et al. (1999) used 2 as an appropriate value for  $K$ . Lower values of  $K$  lead to more wave events being detected, which can include potential artifacts in the pressure time trace. For the present study, a  $K$  value of 10 was used to ensure that only the strongest wave signals were identified (solid contour in Fig. 2.3d). This threshold can be adjusted, and different applications may warrant different values of  $K$ . The mean wavelet power as a function of wave period is shown for each regional sensor network and for all networks combined in Fig. 2.4. Event centers were identified as local maxima in wavelet amplitude which exceed  $A(a)$ , which are located at  $(b_{max}, a_{max})$ . In Fig. 2.3, an event center is located within the solid contour. From the identified event centers, the first iterations of event regions ( $\Omega'$ ) were identified in time-scale space as connected regions where the wavelet power exceeds  $\frac{K}{2} \langle |W(b, a)| \rangle_b$ , i.e., half of the event center threshold. In Fig. 2.3d,  $\Omega'$  is represented by the region within a dashed contour which contains a solid contour.

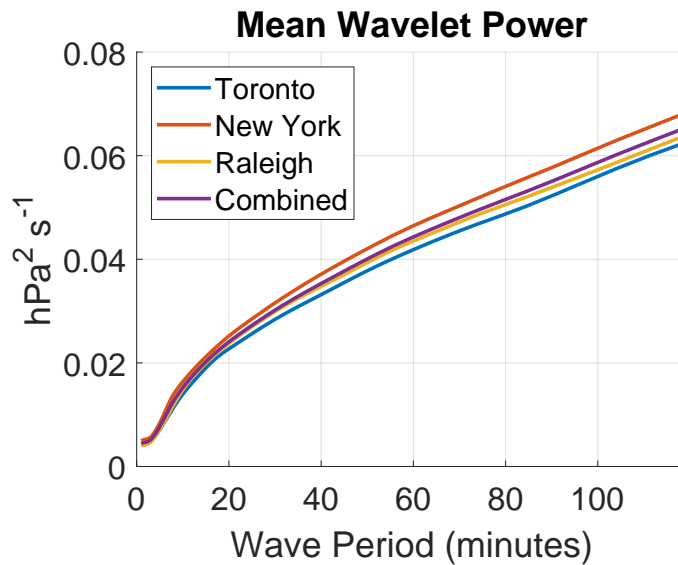


Figure 2.4: Mean wavelet power as a function of wave period across the entire data set (purple curve) and for the individual sensor networks around Toronto, ON, Canada (blue); New York City and Long Island, NY (red); and Raleigh, NC (yellow).

The watershed transform (Meyer 1994) was used to refine  $\Omega'$ . Watersheds (i.e., catchment basins) were identified in the negative wavelet power array  $-|W(b, a)|$ . Any watersheds within  $\Omega'$  whose period range was entirely outside the period range of the watershed containing the event center were removed from the event region  $\Omega'$ . This step was included to correct cases

where multiple "peaks" in wavelet power were present within  $\Omega'$  at different wave periods, with a "valley" in wavelet power in between where the wavelet power still exceeded  $\frac{K}{2} \langle |W(b, a)| \rangle_b$ , which likely represented distinct wave modes and should be considered separate wave events.

$\Omega'$  was extended to define the final event region  $\Omega$  for each event, first by taking the bounding box of  $\Omega'$  and then by extending the bounding box along the time axis in both directions until it reaches a local minimum in the wavelet amplitude to ensure that the entire signal of interest is contained in the event region. This could result in overlapping event regions. Figure 2.3d shows the wavelet power normalized by the mean wavelet power by scale ( $|W| / \langle |W| \rangle_b$ ) for the 23 February 2023 example in sensor 25, with the outline of the event region overlaid with the magenta box.

After defining the event region  $\Omega$ , the wave event trace could then be extracted (i.e., reconstructed) by inverting the wavelet transform function over the event region  $\Omega$ . Figure 2.3e shows the extracted wave event trace for the 23 February 2023 wave event in sensor 25. As in Grivet-Talocia and Einaudi (1998), wave events were identified and extracted one at a time, with the extracted wave event subtracted from the pressure trace and the wavelet transform recalculated at each iteration, until the absolute maximum of  $|W| / \langle |W| \rangle_b$  was less than  $K$  (i.e., until no more events are left to be found in the pressure time series).

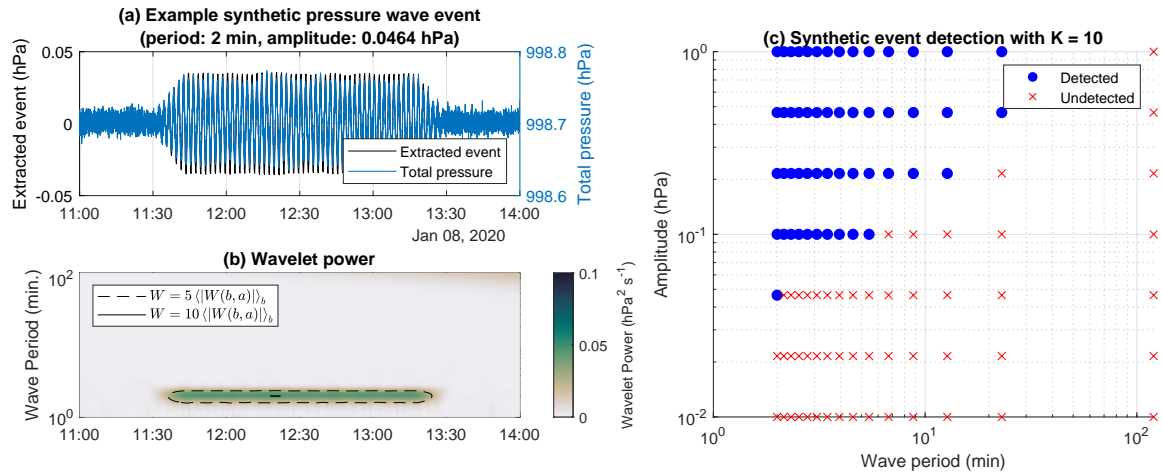


Figure 2.5: (a) Part of the synthetic time series of pressure data (blue) with an extracted wave event (black). This synthetic wave event had a wave period of 2 min and amplitude of  $\pm 0.0464$  hPa. (b) The wavelet power corresponding to the time series shown in (a). The dashed and solid contours indicate where the wavelet power is 5 times and 10 times the mean wavelet power for a given wave period, respectively. (c) The synthetic wave events which were detected (blue filled circles) and undetected (red X symbols) using our methodology with a  $K$  value of 10, as a function of their wave period and amplitude.

We tested the method of detecting wave events in a single sensor using synthetic pressure data. The synthetic time series of pressure is created by an initial constant pressure value (which is randomly chosen from a normal distribution with mean 1000 hPa and standard deviation 2 hPa). We then added normally distributed random noise centered on 0 with standard deviation equal to the noise floor (0.008 hPa). Finally, we added 105 pre-defined wave events, which consist of sine waves of period ranging from 2 min to 120 min and maximum amplitude ranging from  $\pm 0.01$  hPa to  $\pm 1$  hPa. Each set of sine waves lasts for 2 hours, with a 12 minute ramp-up and ramp-down period at the start and end of those 2 hours in which the amplitude increases and decreases linearly, respectively. One of these synthetic wave events is shown in Fig. 2.5a. Using the  $\langle |W(b, a)| \rangle_b$  values shown in Fig. 2.4 and a  $K$  value of 10, 52 of the 105 synthetic wave events were detected, with no false-positive event detections (Fig. 2.5c). The weakest detected synthetic wave event had an amplitude of  $\pm 0.0464$  hPa (or 0.0928 from peak to trough) and a wave period of 2 min (shown in Fig. 2.5a). Lower values of  $K$  do lead to more wave events being detected, with few false positives. The  $K = 2$  used by Grivet-Talocia and Einaudi (1998) results in 86 of the 105 wave events being detected with only one false positive. However, this exercise likely fails to capture the full extent of noise and the interference of many signals present in real pressure data. Lower values of  $K$  can result in more weak pressure wave events being detected, which may be "real" at a single sensor location, but these may then be erroneously paired with other weak pressure wave events at other sensor locations using the methods described in the proceeding sections. Therefore, we will use  $K = 10$  to detect and track pressure wave events across the networks of sensors.

### 2.3.2 Matching corresponding wave events between multiple sensors

Once wave events were identified for each sensor individually, the following steps were taken to identify coherent wave events across multiple sensors. For this purpose, the terms *primary sensor* (denoted by  $i$ ) and *secondary sensor* (denoted by  $j$ ) will be used to describe a pair of sensors for which events are identified and paired together.

For each event in the primary sensor pressure trace, events in the secondary sensor pressure trace that occurred within 2 hours of that primary sensor event (i.e., with a gap between the end of the event in one sensor and the start of the event in the other sensor not exceeding 2 hours) were considered "candidate" events to match with the primary sensor event. This 2 hour threshold is subjective, and it affects the range of speeds of wave events which can be detected. The threshold can be altered depending on the distances between pressure sensors and the desired application. For example, the largest distance between any two sensors in the three networks is that between sensors 012 and 027 (136 km apart, Fig. 2.1). A wave feature

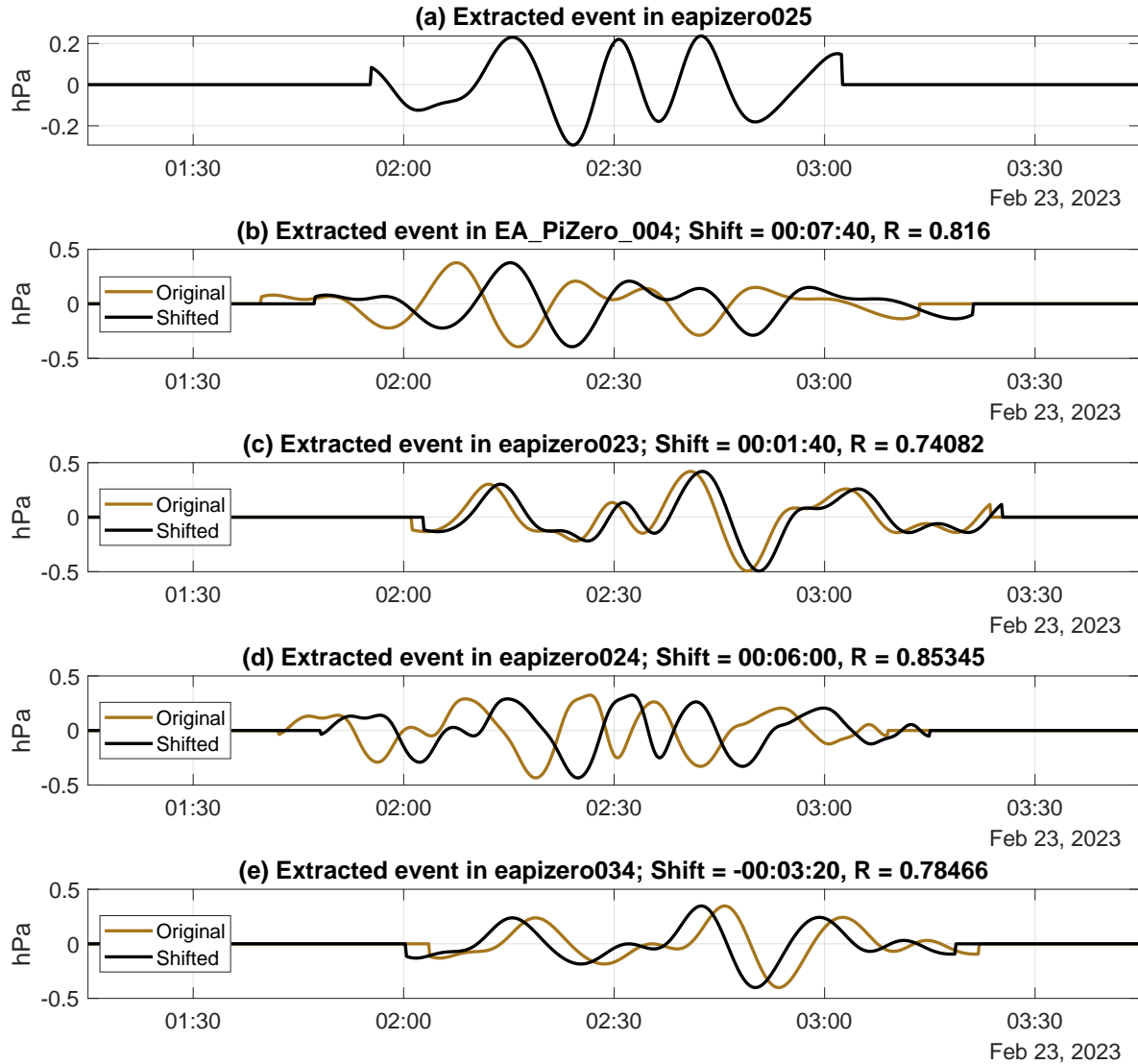


Figure 2.6: Extracted waveforms corresponding to the gravity wave train on 23 Feb, 2023 for sensors 25 (a), 04 (b), 23 (c), 24 (d), and 34 (e). In (b), (c), (d), and (e), brown lines show the extracted wave event with no time shift, and black lines show the extracted wave event shifted in time according to the peak cross-correlation with the extracted wave event time series for the event in sensor 25 (time shift and correlation coefficients are shown in subplot titles). All times are UTC.

propagating at  $18.9 \text{ m s}^{-1}$  would take 2 hours to propagate that distance. However, wave features propagating at an angle could be slower and propagate over both sensors within 2 hours, and as long as pressure sensors in between those two most distant sensors capture the event, the following processing technique will allow those sensors to bridge the gap even if the event takes longer than 2 hours to propagate across the distance between those sensors. Thus,  $18.9 \text{ m s}^{-1}$  is a conservative estimate of the minimum phase speed required for this methodology to track a wave event. Candidate matching events in the secondary sensor trace had to have a center period which was within the primary sensor event period range, and vice versa. Then, for each candidate matching event in the secondary sensor trace, the event waveforms are reconstructed by inverting the wavelet transform over the event region for both sensors. Figure 2.6 shows the extracted waveform for the 23 February 2023 event in sensor 25 and the same wave passage in sensors 04, 23, 24, and 34. The time lag estimate for the wave passage between sensors is  $\Delta t_{opt}$ , the time lag which maximizes the cross-correlation function  $C_{ij}(\Delta t)$ :

$$C_{ij}(\Delta t) = \frac{1}{\|p_i\| \|p_j\|} \int p_i(t) p_j(t + \Delta t) dt \quad (2.5)$$

where  $p_i(t)$  and  $p_j(t)$  are the extracted waveforms for the events in the primary and secondary sensor, respectively. The black lines and subfigure titles in Fig. 2.6 show the optimal shift in the extracted waveforms for sensors 04, 23, 24, and 34 to maximize  $C_{ij}$  to sensor 25 for the 23 February 2023 example. The match to the primary sensor event is the candidate event with the highest maximized cross-correlation to the primary sensor event. If the maximized cross-correlation exceeded 0.65, and the same pair of matched events results from switching the primary and secondary sensors (i.e., the event is matched two ways), the event from sensor  $i$  and the event from sensor  $j$  are paired together. Switching the primary and secondary sensors is necessary to avoid instances where multiple events in one sensor are matched with the same event in another sensor. This can occur, for example, when a set of waves manifests as one event in one sensor and multiple (separate) events in another sensor.

The process of matching events between sensors described above was repeated for each possible combination (within a sensor network) of primary and secondary sensors in order to obtain the full set of lag times between each pair of sensors which captured each event. In other words,  $N^2$  pairs of sensors, order-dependent, were analyzed, where  $N$  is the number of sensors in the network with data at a given time. Then, each event in each sensor was assigned an ID based on which other sensors had a matching event in order to track events across three or more sensors. This process required iterating through each sensor in a network. Each event in the first sensor was assigned a new (i.e., arbitrary) ID. For each subsequent sensor  $s_c$ , events with no two-way matches in any prior sensor were also given new IDs. If there were two-way

matches with an event in one or more prior sensor(s), the event in the sensor  $s_c$  would share the ID assigned to the matched event in the prior sensor. If there were multiple prior sensors with matched events and those events had different IDs, the ID associated with the higher maximized cross-correlation between the event traces was assigned to the event in sensor  $s_c$ . If this process results in multiple events in sensor  $s_c$  sharing the same event ID  $D$ , the event in sensor  $s_c$  associated with the highest maximized cross-correlation with any one prior sensor for an event with event ID  $D$  is assigned event ID  $D$ , and the previously outlined steps are repeated for the other event(s) in sensor  $s_c$ , with event ID  $D$  and associated sensors excluded.

The result of this process is a set of events with associated ID numbers for every sensor in the network. For a single sensor, each event has a unique ID. For each ID number that appeared in at least three sensors, the wave phase velocity vector was calculated using the set of lag times between each pair of sensors which captured the event.

### 2.3.3 Estimating wave phase velocity vector

Once sets of matched events were identified, the wave propagation velocities (two-dimensional vectors) could be estimated for events which occurred in three or more sensors. It is hypothesized for each wave event that a plane wave crosses the sensor network with slowness vector  $\vec{s} = (s_x, s_y)$ , where  $s_x$  and  $s_y$  are the inverses of the x- and y-components of the wave propagation vector (in  $\text{s m}^{-1}$ ), respectively.  $\vec{s}$  can be solved for from the following equation (Del Pezzo and Giudicepietro 2002):

$$\vec{t} = \vec{s} \cdot \Delta \mathbf{x} \quad (2.6)$$

where  $\vec{t}$  is the column vector of the  $\Delta t_{opt}$  values for each possible pair of sensors which captured the event, and  $\Delta \mathbf{x}$  is the two-column matrix of the x- and y-components of the distance vector between each pair of sensors which captured the event.  $\vec{t}$  and  $\Delta \mathbf{x}$  each have  $N_s(N_s - 1)/2$  rows, where  $N_s$  is the number of sensors which captured the event. Equation 2.6 can be considered an overdetermined system of  $N_s(N_s - 1)/2$  linear equations, as long as  $N_s \geq 3$ , and is solved for  $\vec{s}$  by a least squares approach represented by:

$$\vec{s} = (\Delta \mathbf{x}^T \Delta \mathbf{x})^{-1} \Delta \mathbf{x}^T \vec{t} \quad (2.7)$$

where superscript T indicates the transpose of a matrix (Del Pezzo and Giudicepietro 2002).

Once  $s_x$  and  $s_y$  are solved for, they can be inverted to obtain the wave phase velocity components,  $c_x$  and  $c_y$ , respectively. Additionally, the modeled delay times  $\vec{t}_m$  can be calculated by solving Eq. 2.6 for  $\vec{t}$ . From  $\vec{t}_m$ , we estimate the model error using root mean square error

(RMSE) and normalized root mean square error (NRMSE):

$$RMSE = \sqrt{\frac{\sum_{i=1}^{N_s(N_s-1)/2} (t_{m,i} - t_i)^2}{N_s(N_s-1)/2}} \quad (2.8)$$

$$NRMSE = \sqrt{\frac{\sum_{i=1}^{N_s(N_s-1)/2} (t_{m,i} - t_i)^2}{\sum_{i=1}^{N_s(N_s-1)/2} (t_i)^2}} \quad (2.9)$$

Events with sufficiently small RMSE and NRMSE in the modeled delay times can be considered "trackable" events in that there is higher confidence in the wave velocity estimates for those events. After processing multiple years of data from the Toronto and New York pressure sensor networks and analyzing the resulting RMSE and NRMSE distributions, it was found that a maximum RMSE threshold of 90 s and a maximum NRMSE threshold of 0.1 are reasonable to consider a wave event trackable.

Additionally, we require that wave events be captured by at least 4 sensors to be considered trackable. While the slowness vector and corresponding error metrics can be calculated for events captured by only 3 sensors, the calculation is less constrained because there are only 3 delay times  $\Delta t_{opt}$  in the calculation (compared to 6 delay times for events captured by 4 sensors, 10 delay times for events captured by 5 sensors, etc.). The result is that events captured by only 3 sensors can have small RMSE and NRMSE by chance much more easily than events captured by 4 or more sensors. For each robust and trackable wave event, the mean amplitude was calculated by averaging the difference between the maximum and minimum values in the extracted event trace for each sensor which captured the event. The center period for the event was calculated as the mean of the wave period corresponding to  $b_{max}$  for each sensor which captured the event.

## 2.4 Pressure disturbance examples

It is especially useful to have examples of wave events where other observational sources constrain the wave phase speed and direction. We discuss the following examples in this section, some of which have corroborating information on the wave phase speed and/or direction. The Lamb waves caused by the Hunga Tonga-Hunga Ha'apai volcanic eruption in January 2022 represent a case where the origin of the waves is known and the phase speed is known as a function of air temperature (Amores et al. 2022). A gravity wave train which passed over Toronto on 25 February 2022 occurred coincident with a surface cyclone 100 km distant but in local conditions of sparse radar echo. A wave event on 4 February 2022 is a case

associated with an outflow boundary clearly captured by Doppler radar data from the WSR-88D radar located in Upton, NY. In another example, waves coincided with a cold front which passed over Toronto on 15 November 2020. The cold front's associated narrow rain band and Doppler velocity wave (Miller et al. 2022) can be identified in WSR-88D radar data from Buffalo, NY. We also describe a wake low associated with a long-lived mesoscale convective system (MCS) which passed over Long Island on 14 September 2021. These events were each manually chosen after roughly 40 months of pressure data were processed. The gravity wave train on 25 February 2022 and cold front example on 15 November 2020 are not unusual; several other gravity wave trains and pressure jumps due to cold front passages were found. The other three example cases are atypical events, however. It is extremely rare to detect a pressure signal due to a volcanic eruption several thousand km away. While other outflow boundaries were found to produce detectable pressure waves, the case on 4 February 2022 was unusual in terms of the time of year when it occurred (most other pressure waves associated with outflow boundary passages occurred during the warm season) and the radar signature. The wake low detected on 14 September 2021 was the only wake low event detected by our pressure sensor network.

#### **2.4.1 15-17 January 2022: Hunga Tonga-Hunga Ha'apai eruption and Lamb wave**

On 14-15 January, 2022, large eruptions occurred at the Hunga Tonga volcano in the south Pacific Ocean which produced ash plumes reaching the mesosphere and a series of shock waves. A particularly violent, submarine eruption occurred at around 0400 UTC 15 January (Global Volcanism Program 2022). Satellite data suggest that the ash plume associated with this eruption reached as high as 57 km a.s.l. (Carr et al. 2022; Proud et al. 2022) and contained roughly 400 million kg of sulfur dioxide. Damaging tsunami waves due to the eruption were observed as far as Peru (Global Volcanism Program 2022). Subsequent analyses of the atmospheric pressure waves from the eruption have classified the pressure wave observed far from the source eruption as a Lamb wave (e.g., Amores et al. 2022). This Lamb wave has been the subject of several studies and media reports since the time of the eruption (e.g., Amores et al. 2022; Adam 2022; Burt 2022; Bhatia and Fountain 2022; Vergoz et al. 2022). The pressure signal associated with the Lamb wave was observed to circle the Earth several times with estimated phase speeds exceeding  $100 \text{ m s}^{-1}$  (Adam 2022; Burt 2022; Vergoz et al. 2022).

To identify and characterize the pressure waves from this event, we combined the three regional sensor networks (Fig. 2.1) to effectively create an array of 18 sensors which were active at the time of the Lamb wave passages. Table 2.1 summarizes events identified during this period which meet the robust event criteria outlined in the methods (captured by at

Table 2.1: Summary of 5 wave events associated with the Hunga Tonga-Hunga Ha’apai eruption Lamb waves in January 2022. Wave events were subset to those with mean cross-correlation above 0.75, modeled delay time RMSE below 90 s, and modeled delay time NRMSE below 0.1. The start times shown are the earliest among sensors which captured a given event, and end times shown are the latest among sensors which captured a given event. Center wave periods and amplitudes are averaged across the sensors which captured a given event. The first 3 events shown [Outbound (i), (ii), and (iii)] are events associated with the initial outbound set of Lamb waves, and the last 2 events shown [Rebound (i) and (ii)] are events associated with the initial rebound set of Lamb waves.

	Outbound			Rebound	
	(i)	(ii)	(iii)	(i)	(ii)
Event Start UTC	1509 1/15	1532 1/15	1606 1/15	0356 1/16	0652 1/16
Event End UTC	1631 1/15	1619 1/15	1714 1/15	0823 1/16	0729 1/16
Wave Period mm:ss	01:19	01:19	01:05	11:25	06:37
Mean Amplitude hPa	0.30	0.13	0.07	2.43	0.36
$N_{sensors}$	4	7	7	14	7
Mean Cross-Correlation	0.83	0.84	0.77	0.89	0.97
Phase Speed $m s^{-1}$	326.6	237.5	178.9	292.1	290.4
Phase Direction Degrees CW from N	64.2	93.1	56.8	261.9	262.0
RMSE s	1.04	25.19	74.19	17.90	8.21
NRMSE	0.015	0.023	0.035	0.014	0.043

least 4 sensors,  $RMSE \leq 90$  s, and  $NRMSE \leq 0.1$ ), in addition to having a mean optimal cross-correlation between the extracted event traces exceeding 0.75. The initial outbound (traveling from Tonga to the antipode location in Algeria) waves manifested as 3 separate detected events between 1509 and 1714 UTC 15 January, each with high wave frequencies (i.e., low wave periods barely over 1 minute) and low amplitudes (up to 0.3 hPa). The earliest, and strongest, of these events had a phase speed of  $326.6 m s^{-1}$  and direction of  $64.2^\circ$  (i.e., to the east-northeast). The subsequent rebound (traveling from the antipode location to Tonga) waves were detected as 2 separate events between 0356 and 0729 UTC 16 January. The rebound waves had a much higher amplitude (roughly 2.4 hPa) and lower wave frequency (i.e., longer wave periods on the order of roughly 10 minutes) than the outbound waves (Fig. 2.7). The earliest rebound wave

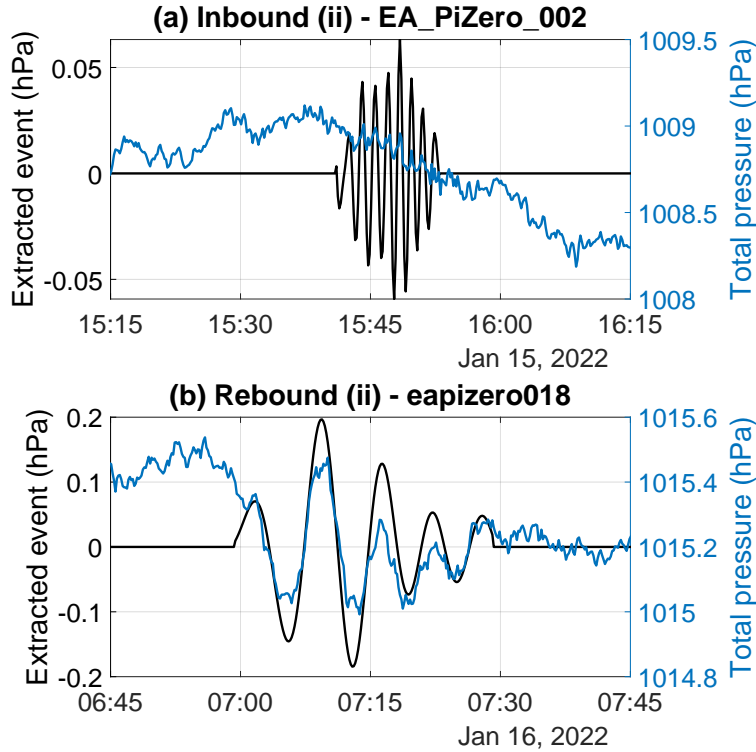


Figure 2.7: Pressure traces and extracted waveforms for two events associated with the Lamb waves caused by the Hunga Tonga-Hunga Ta’apai eruption on 15 Jan 2022. Extracted waveforms (black lines) are overlaid on the total pressure time series (blue lines). (a) the Outbound (ii) wave event propagating from Tonga toward the antipode location in Algeria in Sensor 02 (Table 2.1, column 3). (b) the Rebound (ii) wave event propagating from the antipode location to Tonga in Sensor 18 (Table 2.1, column 6). All times are UTC.

event had a phase speed of  $292.1 \text{ m s}^{-1}$  and direction of  $261.9^\circ$  (i.e., to the west-southwest). Our networks captured the initial outbound waves from Tonga to the antipode at Algeria [Outbound (i), (ii), and (iii) in Table 2.1] and the first rebound waves back from Algeria [Rebound (i) and (ii) in Table 2.1]. Subsequent reverberations of the Lamb waves were not trackable with our sensors and methods by the above criteria due to a combination of the low amplitudes, high frequency, and large phase speeds confounding the process of approximating delay times between sensors (an issue also described by Grivet-Talocia and Einaudi 1998).

#### 2.4.2 25 February 2022: Gravity wave train over Toronto

Four pressure sensors in Toronto were used to detect and track a series of pressure oscillations between 0816 and 1359 UTC on 25 February 2022, with a particularly large pressure peak near 1000 UTC (Fig. 2.8). The mean amplitude of the event across the 4 sensors was 2.1 hPa, and

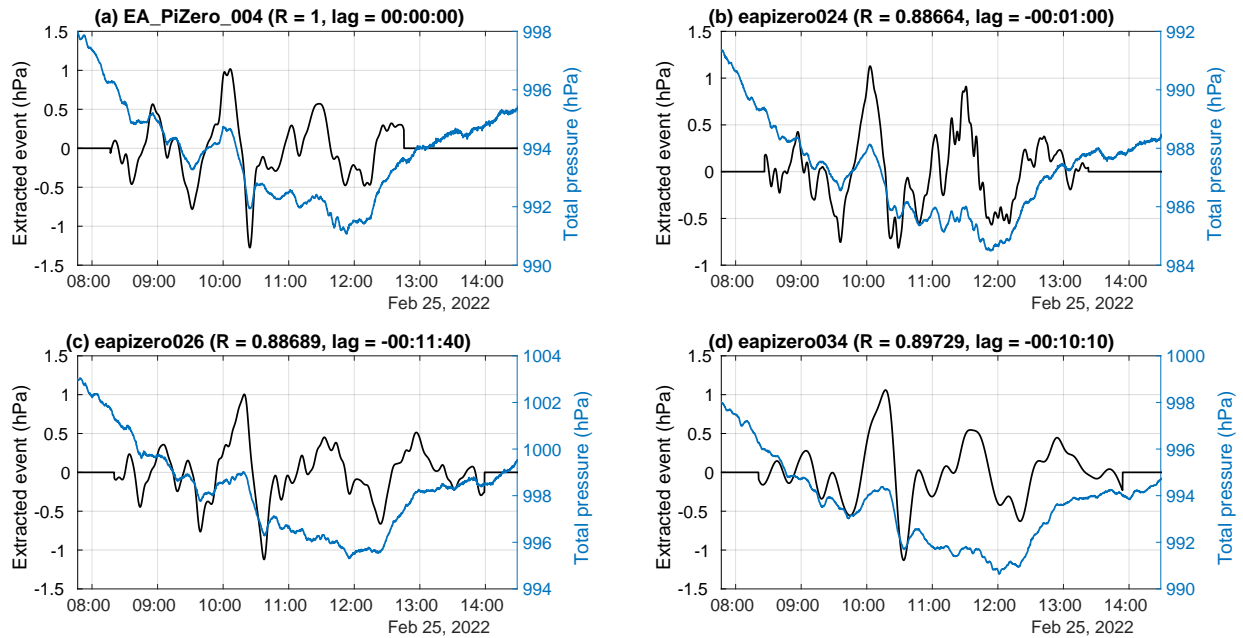


Figure 2.8: Pressure traces and extracted waveforms for the 25 Feb 2022 wave event in sensors (a) 04, (b) 24, (c) 26, and (d) 34. Extracted waveforms (black lines) are overlaid on the total pressure time series (blue lines). All times are UTC. Cross-correlations and lag times are indicated relative to sensor 04. Cross-correlations are computed for each variation of pairs of sensors (not shown).

the wave train was estimated to propagate at  $45.4 \text{ m s}^{-1}$  at  $73^\circ$  (i.e., to the east-northeast). The center wave period was 00:20:22. At this time a mature surface cyclone was located roughly 100 km to the south of Toronto. Linear bands of reflectivity were identified in WSR-88D radar data from Buffalo, NY, in the hours leading up to the detected pressure waves, but between 0900 UTC and 1200 UTC there was only sparse radar echo over the Toronto area. Between 1230 and 1430 UTC there was radar echo across the Toronto area, and a set of Doppler velocity waves was identified from the WSR-88D data using the methods in Miller et al. (2022). Those Doppler velocity waves appeared to propagate toward the northeast, in roughly the same direction as the detected pressure waves (Video supplement Animation-Figure-S2.01).

The nearest available sounding during the duration of the wave event appeared to indicate adequate environmental conditions for gravity wave ducting (Lindzen and Tung 1976; Koch and O’Handley 1997). The sounding from Buffalo, NY, valid at 1200 UTC on 25 Feb 2022, shows a temperature inversion roughly 2 km deep (Fig. 2.9), which serves as the "ducting layer" directly above a shallow boundary layer. A moist neutral or conditionally unstable layer (indicated by near-zero or negative values of the vertical gradient in equivalent saturation potential temperature) was above this inversion extending to around 4500 m MSL and serves as the

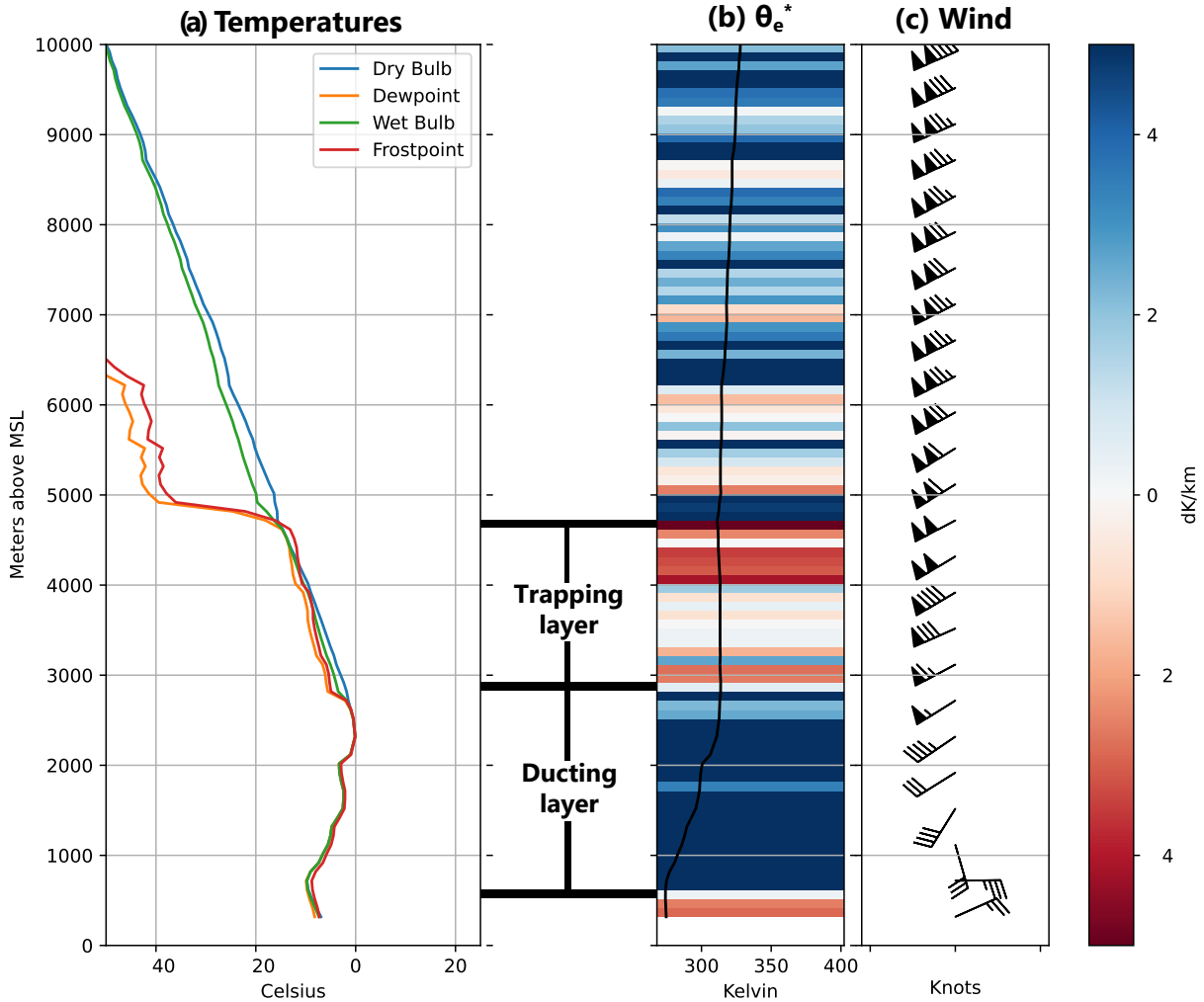


Figure 2.9: Upper air sounding data from Buffalo, NY, valid for 1200 UTC 25 Feb 2022. (a) Dry bulb temperature (blue), dew point (orange), wet bulb temperature (green), and frost point (red) profiles (all in  $^{\circ}C$ ). (b) Equivalent saturation potential temperature ( $\theta_e^*$ ) profile (black line, K) overlaid on the vertical gradient in  $\theta_e^*$  ( $K km^{-1}$ ). Positive values (blue) of the vertical gradient in  $\theta_e^*$  indicate absolute stability, while negative values (red) indicate conditional or absolute instability. (c) Horizontal wind profile (barbs, kts; colored according to wind speed). Annotation indicates the vertical extents of a ducting layer and a trapping layer according to the gravity wave duct criteria described by Lindzen and Tung (1976) and Koch and O’Handley (1997).

"trapping layer" in Fig. 2.9. The sharp change in stability between the inversion layer and conditionally unstable layer at roughly 2800 m MSL could serve as a reflector of gravity wave energy. The apparent presence of a gravity wave duct during the detected pressure wave event raises confidence that the pressure waves were gravity waves.

### 2.4.3 4 February 2022: Outflow pressure jump and subsequent oscillations over Long Island

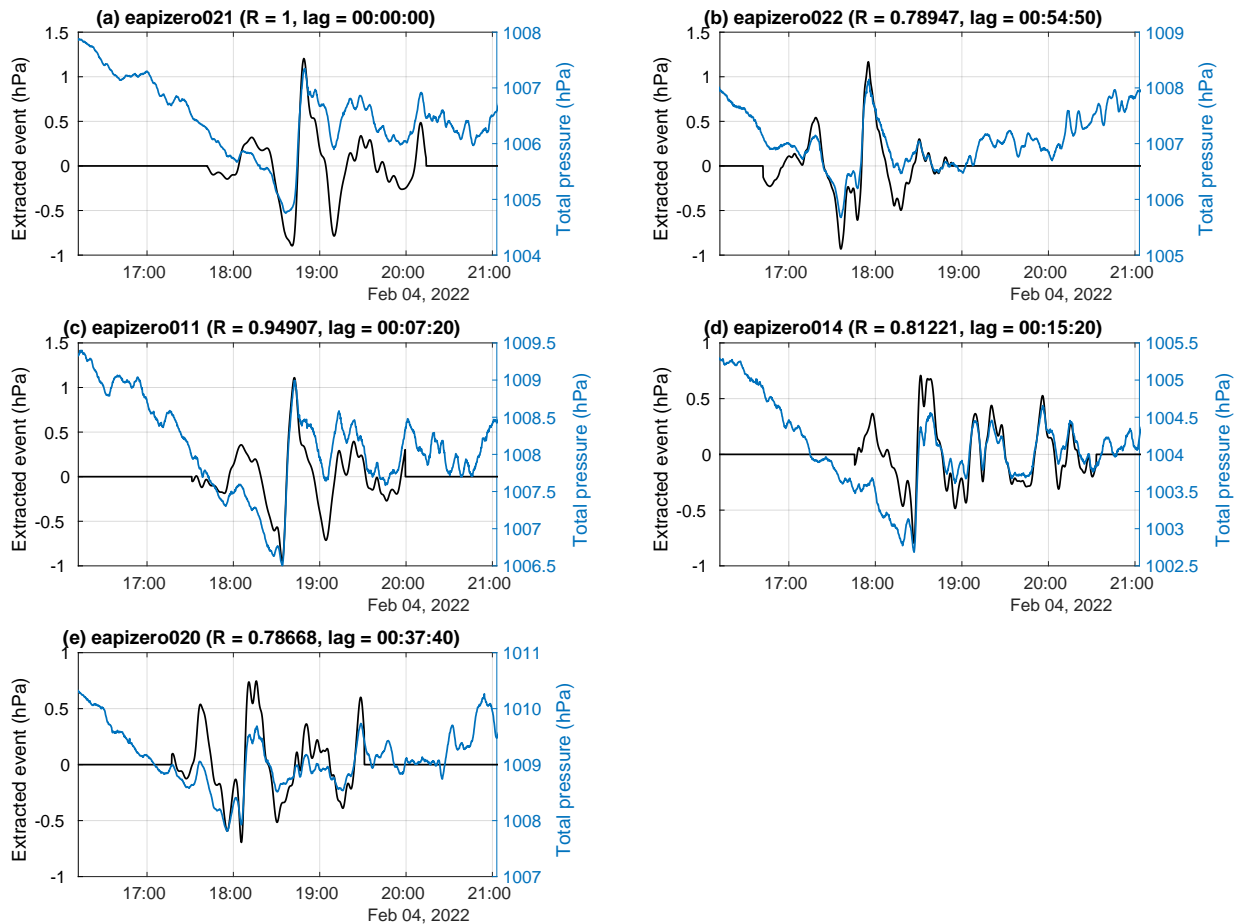


Figure 2.10: As in Fig. 2.8, but for the 04 Feb 2022 wave event in sensors (a) 21, (b) 22, (c) 11, (d) 14, and (e) 20, with cross-correlations and lag times indicated relative to sensors 21. Extracted waveforms (black lines) are overlaid on the total pressure time series (blue lines).

Between 1730 and 1900 UTC on 4 February 2022, an event with amplitude of roughly 1.8 hPa was detected by five pressure sensors in the New York City metro area and Long Island.

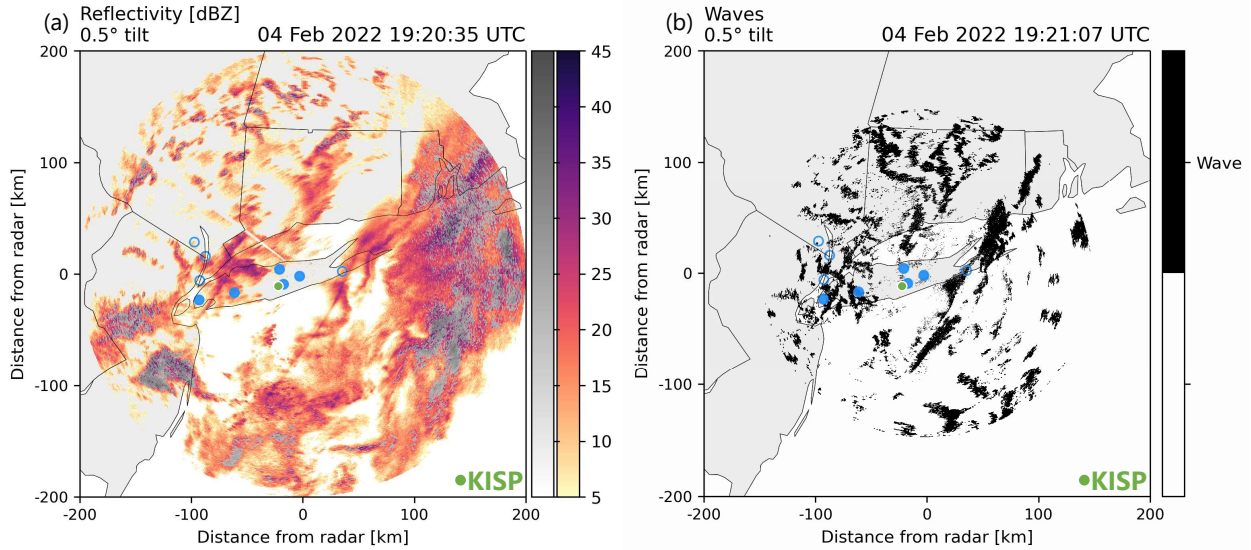


Figure 2.11: (a) Reflectivity and (b) Doppler velocity wave detection for NWS WSR-88D radar data from Upton, NY, at  $0.5^\circ$  tilt, at 1920 UTC on 4 Feb 2022. In (a), reflectivity values are shown in greyscale where there is likely enhancement due to melting (Tomkins et al. 2022). Filled blue circles indicate locations of pressure sensors which captured the wave event described in Sect. 2.4.3, and unfilled blue circles indicate locations of pressure sensors which did not capture the wave event. Filled green circle indicates location of Islip, NY, ASOS station (KISP). An animation of this figure showing the time sequence from 1541 to 2130 UTC is in Video supplement Animation-Figure-S2.02.

This event was a positive jump in pressure followed, to varying degrees in each sensor, by weak oscillations in the pressure trace (Fig. 2.10). Prior to the jump in pressure, there had been a decreasing trend in the pressure traces for several hours. At the same time, WSR-88D weather radar data from Upton, NY, showed widespread precipitation echo over Long Island. A wave feature was apparent in the Doppler radial velocity data, which could also be identified following the methods of Miller et al. (2022) (Fig. 2.11 and Video supplement Animation-Figure-S2.02). This wave event had a phase speed of  $21.1 \text{ m s}^{-1}$  and direction of  $118.2^\circ$  clockwise from north (i.e., southeastward). The values are consistent with the radar-detected Doppler velocity wave feature (Video supplement Animation-Figure-S2.02).

Operational one-minute Automated Surface Observing System (ASOS) data (Fig. 2.12a) also recorded a jump in the surface pressure of nearly 2 hPa. Near the time of this jump, there was also a peak in the wind speed and gusts, along with a brief shift in the wind direction from north-northeasterly to north-northwesterly (Fig. 2.12b). These features, along with the modest decrease in the temperature (Fig. 2.12a), are consistent with a convective outflow boundary (i.e., gust front). A "fine line" can be seen in WSR-88D reflectivity data at roughly the same location as the wave, which further suggests that a convective outflow was responsible for the

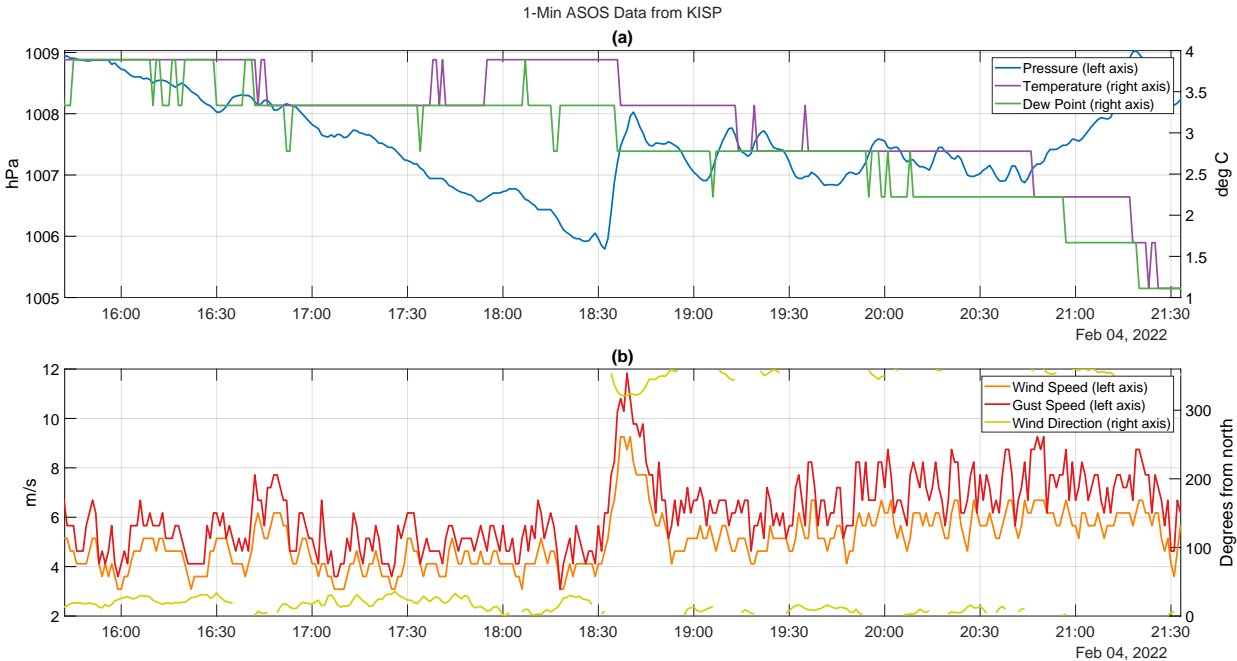


Figure 2.12: Time series of one-minute ASOS data from Islip, NY (KISP), on 4 February 2022. (a) Temperature (purple) dew point (red), and pressure (blue). (b) Wind speed (orange), wind gust speed (red), and wind direction in degrees clockwise from northerly (yellow). Wind direction is not plotted when it changes by more than  $180^\circ$  in consecutive observations (e.g., when crossing  $0^\circ$  or  $360^\circ$ ) or when the wind speed is below  $1.5 \text{ m s}^{-1}$ . All times are UTC.

pressure rise (Fig. 2.11 and Video supplement Animation-Figure-S2.02).

#### 2.4.4 15 November 2020: Cold front passage over Toronto

A robust and trackable wave event was detected by five pressure sensors in Toronto coincident with a cold front passage at roughly 2000 UTC on 15 November 2020. The pressure steadily dropped in the hours leading up to the frontal passage before abruptly rising 1-2 hPa as the cold air mass arrived. The pressure then dropped roughly 1 hPa about 30 min later. Some sensors recorded oscillations in the pressure trace embedded within the gradual pressure rise in the proceeding hours (Fig. 2.13). One-minute ASOS data from Buffalo, NY, also captured the pressure jump at roughly the same time as the temperature and dew point drop indicating the cold front passage (Fig. 2.14).

The pressure wave event for the cold front passage had an estimated phase speed of  $27.5 \text{ m s}^{-1}$  at  $65^\circ$  (i.e., to the east-northeast), a mean amplitude of 1.8 hPa, and a center wave period of 00:02:08. WSR-88D radar data from Buffalo, NY, show a narrow band of high reflectivity and

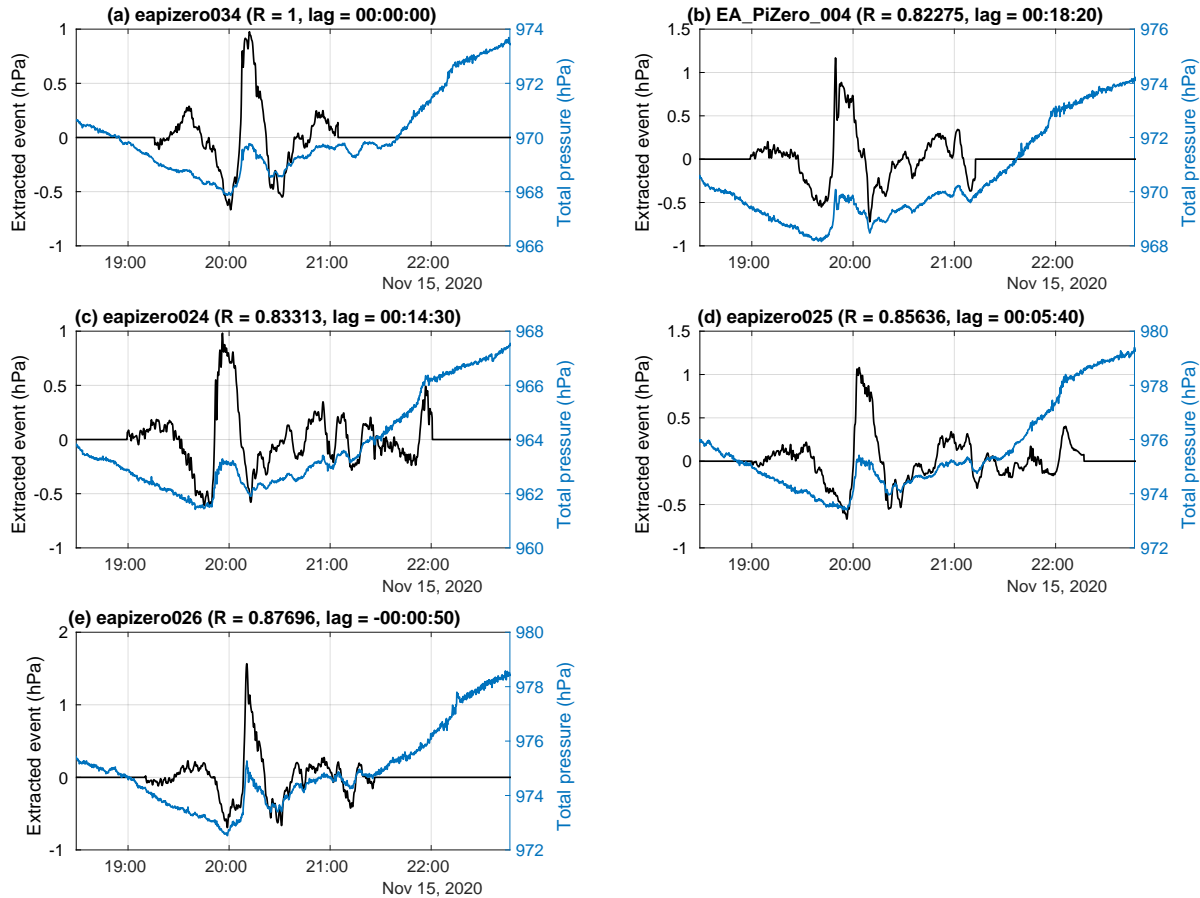


Figure 2.13: As in Fig. 2.8, but for the 15 Nov 2020 wave event in sensors (a) 34, (b) 04, (c) 24, (d) 25, and (e) 25, with cross-correlations and lag times indicated relative to sensor 34. Extracted waveforms (black lines) are overlaid on the total pressure time series (blue lines).

a Doppler velocity wave (identified following the methods in Miller et al. 2022) associated with the cold front advancing over Toronto at roughly 2000 UTC at a speed and direction consistent with the pressure wave (Video supplement Animation-Figure-S2.03).

## 2.4.5 14 September 2021: Wake low associated with a mesoscale convective system

Between 0300 and 0400 UTC on 14 September 2021, a pressure drop of roughly 5 hPa and subsequent recovery occurred at four of the pressure sensors in New York City metro area and Long Island network (Fig. 2.15). This was detected as a wave event with an estimated propagation speed of  $20.6 \text{ m s}^{-1}$  and propagation direction of  $67.5^\circ$  (i.e., to the east-northeast). ASOS data from Islip, NY (KISP; Fig. 2.16), and other stations in the area (not shown) also recorded the pressure minimum. This wave event occurred near the time of a mesoscale

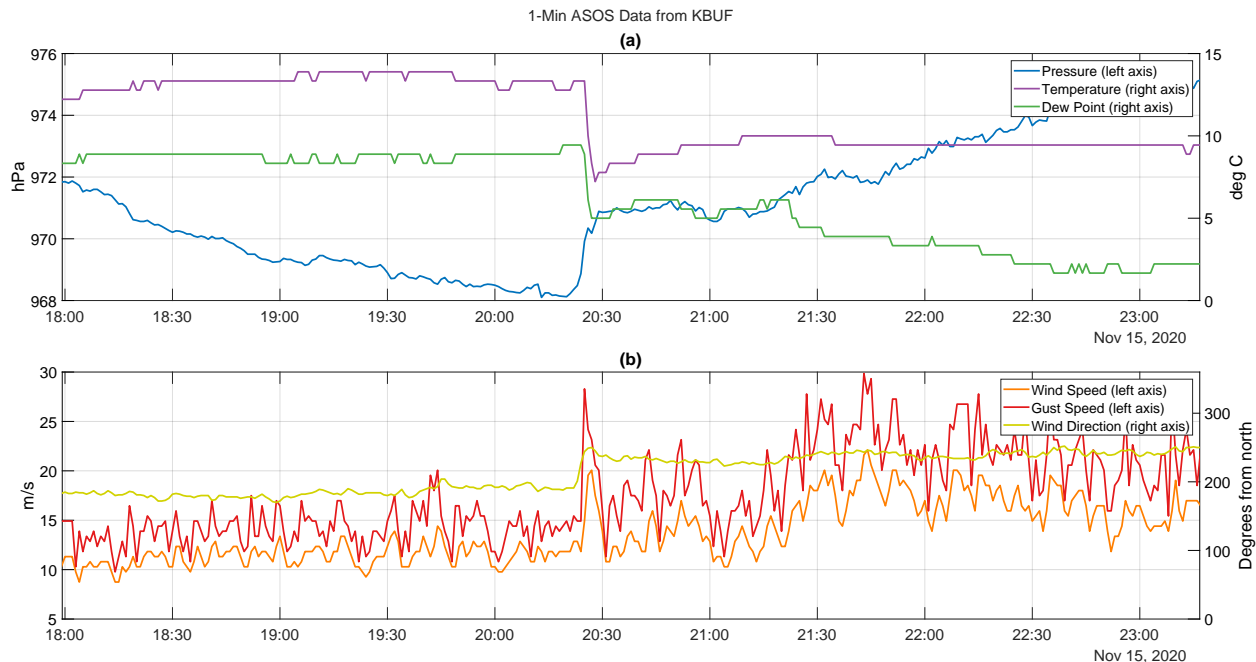


Figure 2.14: Time series of one-minute ASOS data from Buffalo, NY (KBUF), on 15 November 2020. (a) Temperature (purple) dew point (red), and pressure (blue). (b) Wind speed (orange), wind gust speed (red), and wind direction in degrees clockwise from northerly (yellow). Wind direction is not plotted when it changes by more than  $180^\circ$  in consecutive observations (e.g., when crossing  $0^\circ$  or  $360^\circ$ ) or when the wind speed is below  $1.5 \text{ m s}^{-1}$ . All times are UTC.

convective system (MCS) passage over Long Island as indicated by reflectivity data from the WSR-88D radar in Upton, NY (Fig. 2.17 and Video supplement Animation-Figure-S2.04). In addition to the precipitation echo associated with the MCS translating from northwest to southeast, there was also a stationary region of weak echo with low dual-polarization correlation coefficient (shown in greyscale following Tomkins et al. 2022) in the vicinity of the radar. The stationary weak echo was likely non-meteorological and due to either birds or insects. The precipitation echo appears to be entirely past KISP by 0342 UTC (Fig. 2.17c and Video supplement Animation-Figure-S2.04), which is roughly the same time as the minimum pressure at KISP (Fig. 2.16a).

This pressure minimum appears to be consistent with a *wake low*, associated with subsidence heating in the rear inflow jet (Markowski and Richardson 2010; Johnson and Hamilton 1988). The subsidence heating does not necessarily lead to warming at the surface, which was not observed in the ASOS data (Fig. 2.16a), but decreased air density aloft due to warming will still lead to a surface pressure decrease. Markowski and Richardson (2010) also note that a property of wake lows associated with a translating squall line is that the center of convergence

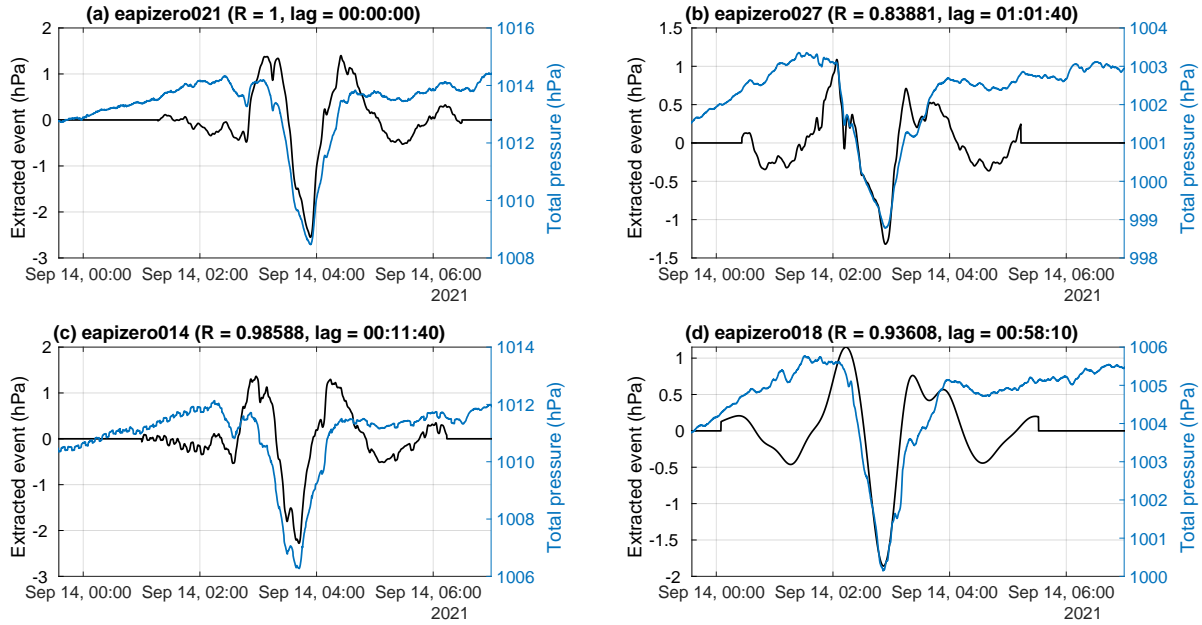


Figure 2.15: As in Fig. 2.8, but for the 14 Sep 2021 wave event in sensors (a) 21, (b) 27, (c) 14, and (d) 18, with cross-correlations and lag times indicated relative to sensor 21. Extracted waveforms (black lines) are overlaid on the total pressure time series (blue lines).

due to the wake low does not perfectly align with the center of the wake low. Rather, the convergence center slightly lags behind the wake low center. In the 14 September 2021 example, the ASOS time series data have a wind speed minimum co-occurring with a shift in the wind direction from near  $100^\circ$  (east-southeasterly) to near  $280^\circ$  (west-northwesterly) which can be interpreted as the convergence maximum (Fig. 2.16b). This convergence maximum occurs slightly after the pressure minimum associated with the wake low (Fig. 2.16a), consistent with the Markowski and Richardson (2010) description.

## 2.5 Discussion and Summary

In this study, a wavelet-based method was used to identify wave events in time series pressure data from networks of high precision sensors (0.8 Pa noise floor) recording the pressure every second. In addition to identifying wave events in each sensor individually, the delay times in wave passage among sensors in a given network were used to determine the direction of wave propagation and phase velocity. The methods shown are intended mainly for post-processing of pressure data for research applications, and not for real time, operational use. A benefit to this method is that it can be fully automated to detect wave events across many months of data, and we have made the processing code openly available (Allen and Miller 2023).

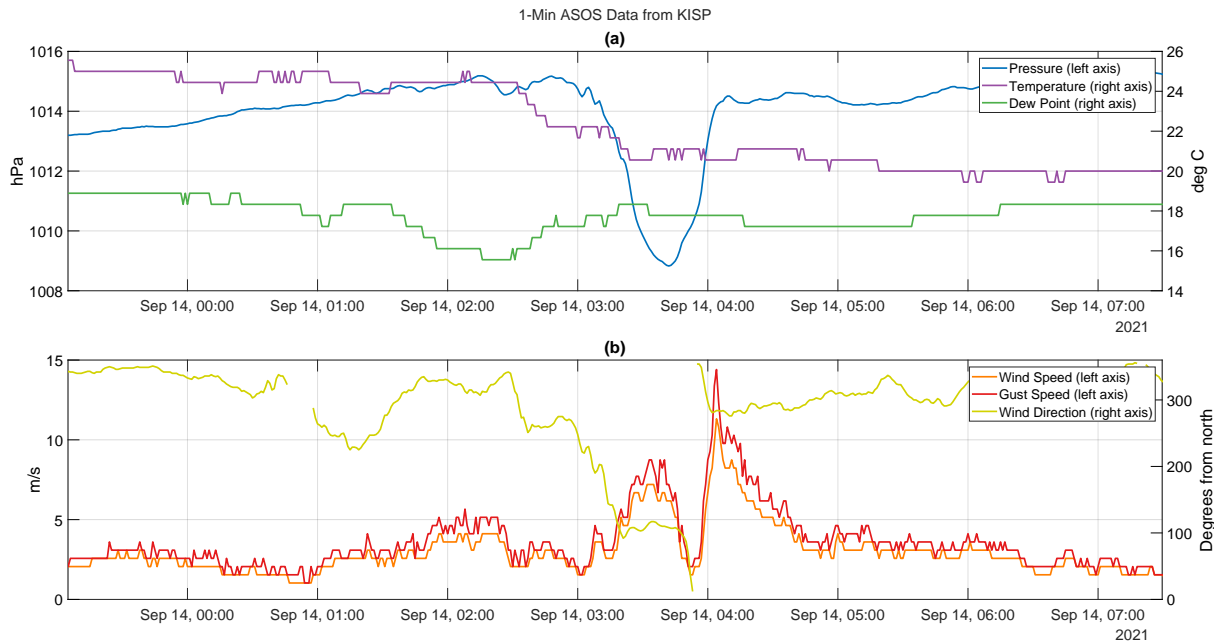


Figure 2.16: Time series of one-minute ASOS data from Islip, NY (KISP), on 14 September 2021. (a) Temperature (purple) dew point (red), and pressure (blue). (b) Wind speed (orange), wind gust speed (red), and wind direction in degrees clockwise from northerly (yellow). Wind direction is not plotted when it changes by more than  $180^\circ$  in consecutive observations (e.g., when crossing  $0^\circ$  or  $360^\circ$ ) or when the wind speed is below  $1.5 \text{ m s}^{-1}$ . All times are UTC.

Overall, the method was most successful at tracking pressure wave events with relatively large amplitudes (on the order of  $0.3 \text{ hPa}$  or more) and longer periods (i.e., lower frequencies; on the order of 5 minutes or more). Low-amplitude, high-frequency waves likely propagated across the sensor networks many times, but these waves were difficult to reconstruct, due to their wavelet signal being weaker, and to track, due to aliasing of the waveform conflating the time lag estimates between sensors. We use a rather strict criteria for detecting a wave event in a given sensor; the peak wavelet power must exceed 10 times the mean value for a given wave period (i.e.,  $K = 10$ ; eq. 2.4). Grivet-Talocia and Einaudi (1998) also used wavelet analysis to detect pressure waves with a scale dependent threshold; their  $K$  value was only 2. Therefore, many wave events detected using our criteria will be relatively high amplitude (on the order of  $1 \text{ hPa}$  or more), including most examples shown in Sect. 2.4. Depending on the desired application, this threshold and the other thresholds used in the wave detection can be adjusted.

Environmental factors can influence whether or not a given gravity wave is detected by our surface pressure sensors. Gravity waves aloft will not always produce a detectable pressure

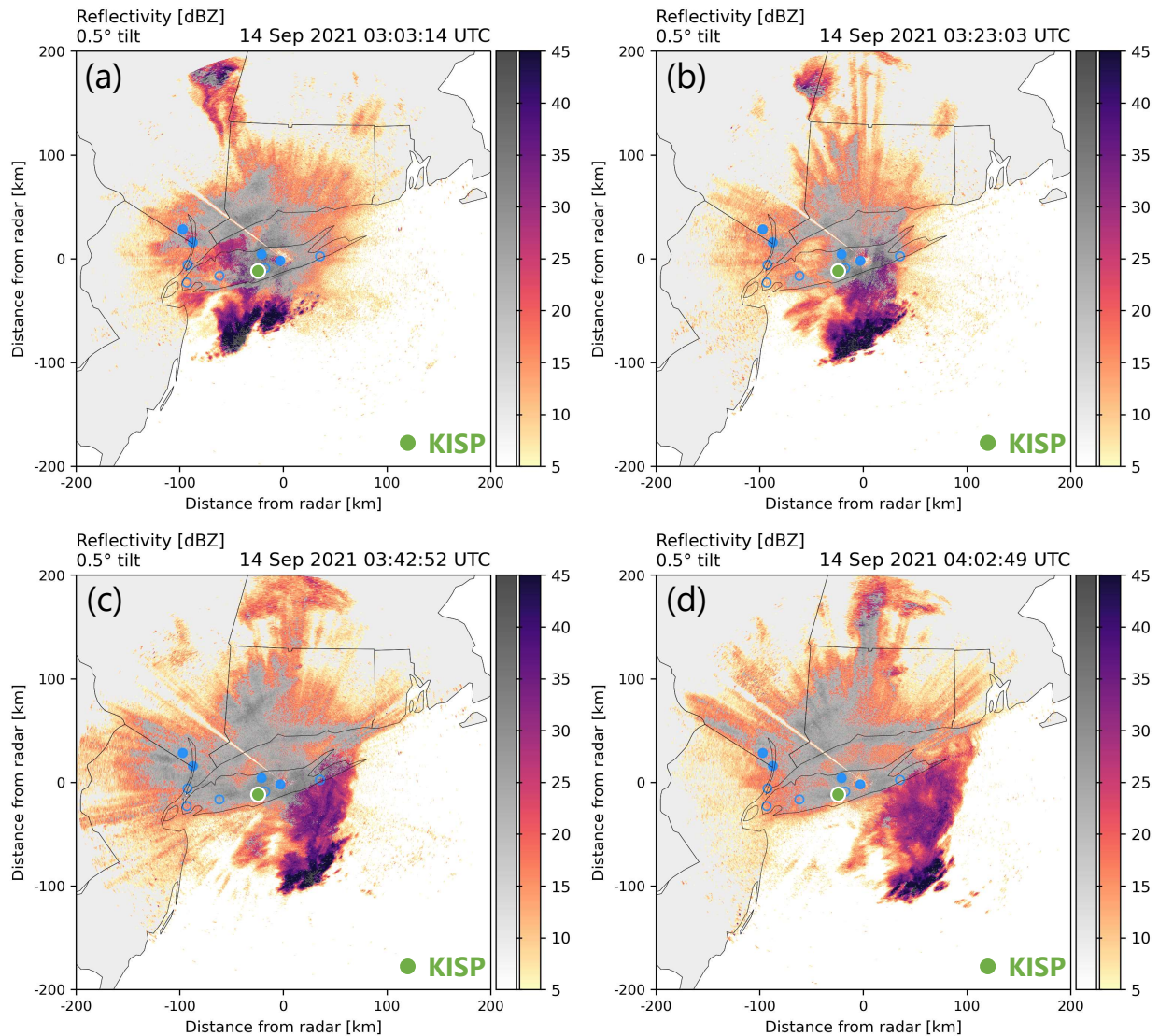


Figure 2.17: Maps of radar reflectivity at  $0.5^\circ$  tilt from the NWS WSR-88D radar in Upton, NY, on 14 September 2021. Reflectivity values in color show meteorological echo and those are shown in greyscale are likely non-meteorological echo such as insects and birds in this case (Tomkins et al. 2022). Filled blue circles indicate the locations of pressure sensors which captured the wave event described in Sect. 2.4.5, and unfilled blue circles indicate the locations of pressure sensors which did not capture the wave event. Filled green circle indicates the location of the Islip, NY, ASOS station (KISP). The sequence of images from (a) 0303 UTC, (b) 0323 UTC, (c) 0342 UTC, and (d) 0402 UTC shows the southeastward movement of region of convective cells  $> 40$  dBZ from closer to further off the southern coast of Long Island. The wake low is inferred to be near the trailing edge of the weaker stratiform precipitation region behind (west of) the convective cells. The minimum pressure at KISP associated with the wake low occurred near the time of the scan shown in (c). An animated version of this figure, with Doppler velocity wave detection, is shown in Video supplement Animation-Figure-S2.03.

signal at the surface, for example if the planetary boundary layer is neutral or unstable (e.g., Kjelaas et al. 1974). Another possible limitation is that in their current network deployments the pressure sensors are too far apart to track highly localized disturbances, particularly for the New York City/Long Island sensor network. Our method may not always properly track waves which are modified by local conditions (which may alter their amplitude, frequency, and/or phase velocity) as they propagate across the sensor network. Future work will examine data from networks of pressure sensors a few km to a few m apart and the degree to which signals associated with waves in shallow marine clouds are detectable with these sensors.

Deployment of networks of low-cost, high-precision sensors opens myriad opportunities for monitoring the direction and speed of gravity waves that have not been previously available with conventional pressure sensors on operational weather stations due to their longer measurement interval and larger station spacing. A forthcoming publication will describe a 3+ year climatology of wave events detected by the pressure sensors deployed in New York and Toronto and address hypotheses regarding the relationship between gravity waves and local enhancements in snowfall rate within winter storms (i.e., snow bands). There are observational case studies demonstrating this connection (e.g., Bosart et al. 1998; Gaffin et al. 2003), but a multi-year data set with continuously-monitoring pressure sensors in context of radar data will enable a more comprehensive examination of the co-occurrence, or lack thereof, of gravity waves with snow bands across many winter storms.

**Video supplement** All animations can be viewed at: [https://doi.org/10.5446/s\\_1476](https://doi.org/10.5446/s_1476). Individual animations can be viewed by following the DOI URL.

Animation-Figure-S2.01: Animated maps of (a) reflectivity and (b) Doppler velocity wave detection for NWS WSR-88D radar data from Buffalo, NY, at 0.5° tilt, from 0706 UTC to 1457 UTC on 25 Feb 2022. In (a), reflectivity values are shown in greyscale when there is likely enhancement due to melting (Tomkins et al. 2022). Filled blue circles indicate locations of pressure sensors which captured the wave event described in Sect. 2.4.2, and unfilled blue circles indicate locations of pressure sensors which did not capture the wave event. Title: 25 Feb 2022 KBUF Reflectivity and Doppler Velocity Waves. <https://doi.org/10.5446/62539> (Allen et al. 2023d).

Animation-Figure-S2.02: Animated maps of (a) reflectivity and (b) Doppler velocity wave detection for NWS WSR-88D radar data from Upton, NY, at 0.5° tilt, from 1541 UTC to 2129 UTC on 4 Feb 2022. In (a), reflectivity values are shown in greyscale when there is likely enhancement due to melting (Tomkins et al. 2022). Filled blue circles indicate locations of pressure sensors which captured the wave event described in Sect. 2.4.3, and unfilled blue circles indicate locations of pressure sensors which did not capture the wave event. Goes with Fig. 2.11. Title: 04

Feb 2022 KOKX Reflectivity and Doppler Velocity Waves. <https://doi.org/10.5446/62540> (Allen et al. 2023a).

Animation-Figure-S2.03: Animated maps of (a) reflectivity and (b) Doppler velocity wave detection for NWS WSR-88D radar data from Buffalo, NY, at 0.5° tilt, from 1805 UTC to 2324 UTC on 15 Nov 2020. In (a), reflectivity values are shown in greyscale when there is likely enhancement due to melting (Tomkins et al. 2022). Filled blue circles indicate locations of pressure sensors which captured the wave event described in Sect. 2.4.4, and unfilled blue circles indicate locations of pressure sensors which did not capture the wave event. Title: 15 Nov 2020 KBUF Reflectivity and Doppler Velocity Waves. <https://doi.org/10.5446/62541> (Allen et al. 2023c).

Animation-Figure-S2.04: Animated maps of (a) reflectivity and (b) Doppler velocity wave detection for NWS WSR-88D radar data from Upton, NY, at 0.5° tilt, from 0003 UTC to 0727 UTC on 14 Sep 2021. In (a), reflectivity values are shown in greyscale when there is likely enhancement due to melting (Tomkins et al. 2022). Filled blue circles indicate locations of pressure sensors which captured the wave event described in Sect. 2.4.5, and unfilled blue circles indicate locations of pressure sensors which did not capture the wave event. This animation goes with Fig. 2.17. Title: 14 Sep 2021 KOKX Reflectivity and Doppler Velocity Waves. <https://doi.org/10.5446/62542> (Allen et al. 2023b).

**Code and data availability** Data: The pressure time series data used throughout this publication can be found at <https://doi.org/10.5281/zenodo.8136536> (Miller and Allen 2023). The NWS NEXRAD Level-II data used in Figs. 2.11 and 2.17 can be accessed from the National Centers for Environmental Information (NCEI) at <https://www.ncei.noaa.gov/products/radar/next-generation-weather-radar> (NOAA National Weather Service Radar Operations Center 1991). The NWS ASOS surface station data used to create Figs. 2.12 and 2.16 can be accessed from NCEI at <https://www.ncei.noaa.gov/products/land-based-station/automated-surface-weather-observing-systems> (NOAA National Centers for Environmental Information 2021a). The radiosonde data used to create Fig. 2.9 can be accessed from NCEI at <https://www.ncei.noaa.gov/products/weather-balloon/integrated-global-radiosonde-archive> (NOAA National Centers for Environmental Information 2021b).

Code: The code used for processing the pressure time series data can be found at <https://doi.org/10.5281/zenodo.10150876> (Allen and Miller 2023).

## CHAPTER

### 3

# OBJECTIVELY IDENTIFIED MESOSCALE SURFACE AIR PRESSURE WAVES IN THE CONTEXT OF WINTER STORM ENVIRONMENTS AND RADAR REFLECTIVITY FEATURES: A 3+ YEAR ANALYSIS

This chapter will be submitted to *Atmospheric Chemistry and Physics*. This chapter builds on the work in Chapter 2, so the pressure wave detection methods described in Sect. 3.2.1 will be repetitive.

**Citation** Allen, Luke R., S. E. Yuter, M. A. Miller, L. M. Tomkins, 2024: Objectively identified mesoscale surface air pressure waves in the context of winter storm environments and radar reflectivity features: a 3+ year analysis. *Atmospheric Chemistry and Physics, in prep.*

**Authors** Luke R. Allen<sup>1</sup>, Sandra E. Yuter<sup>1,2</sup>, Matthew A. Miller<sup>2</sup>, and Laura M. Tomkins<sup>1,3</sup>

<sup>1</sup>Center for Geospatial Analytics, North Carolina State University, Raleigh, NC, 27695, USA

<sup>2</sup>Department of Marine, Earth and Atmospheric Science, North Carolina State University, Raleigh, NC, 27695, USA

<sup>3</sup>Current affiliation: Karen Clark and Company, Boston, MA, 02116, USA

**Acknowledgements** The authors express their sincere appreciation to the pressure sensor hosts in Toronto and the New York City metro area and Long Island, including colleagues from Environment Canada, Stony Brook University, Columbia University, and friends, including Jase Bernhardt, Drew Claybrook, Brian Colle, Daniel Horn, Daniel Michelson, Robert Pincus, Adam Sobel, David Stark, and Jeff Waldstreicher, who graciously agreed to plug in pressure sensors to their home internet. The development of the methodology, interpretation of the results, and visualizations benefited from discussions and correspondence with DelWayne Bohnenstiehl, Brian Colle, Declan Crowe, Brian Mapes, Logan McLaurin, Sonia Lasher-Trapp, Matthew Parker, James Ruppert, and Minghua Zhang.

This work was supported by the National Science Foundation (AGS-1905736), the National Aeronautics and Space Administration (80NSSC19K0354), the Office of Naval Research (N000142112116), and the Center for Geospatial Analytics at North Carolina State University.

**Abstract** Atmospheric gravity waves (i.e., buoyancy waves) can occur within stable layers when vertical oscillations are triggered by localized heating, flow over terrain, or imbalances in upper level flow. Case studies of winter storms have associated gravity waves with heavier surface snowfall, but the representativeness of those findings for settings without orographic precipitation has not been previously addressed.

To detect gravity waves, we deployed networks of high precision pressure sensors from January 2020 to April 2023 in and around Toronto, ON, Canada, and New York, NY, USA, two regions without strong topographic forcing. Pressure wave events were identified when at least 4 sensors in a network detected propagating pressure waves with wave periods  $\leq 67$  min, wavelengths  $\leq 170$  km, and amplitudes  $\geq 0.45$  hPa. We detected 33 pressure wave events across 40 months of data, of which 23 were gravity waves and the rest were frontal passages, outflow boundary passages, or a wake low.

Reanalysis model output and operational weather observations provided environmental context for each gravity wave event. Consistent with previous work, most gravity wave events occurred with strong upper-level flow imbalance to the south or west of their location. Of the 79 winter storms with snow that occurred over our 40 months of observations, only 6 had detectable gravity waves. For New York City, the typical offshore cyclone low center track means

the metro area is usually in a location where gravity waves are not expected to occur.

### **3.1 Introduction**

Atmospheric gravity waves (i.e., buoyancy waves) result from the forced perturbation of air parcels in a statically stable environment such that parcels oscillate about their original height with parcel buoyancy acting as the restoring force (Nappo 2002). Possible triggering mechanisms for gravity waves can include, but are not limited to, forced flow over topography, adjustment to imbalanced flow, and localized latent heating (Fritts and Alexander 2003). The resulting up and down motions can propagate outwards from the location of their originating triggering mechanism through stable layers, but do not yield net movement of fluid, nor do they necessarily follow the mean flow of the air through which they propagate.

Case studies of winter storms have associated gravity waves with heavier surface snowfall but the representativeness of these findings for settings without strong topographic forcing has not been systematically examined. It is the goal of this paper to remedy that gap with a comprehensive analysis of observed gravity waves based on 40 months of pressure sensor network data. The waves we present in this paper are propagating (i.e., not terrain-locked), moderate to high-amplitude (up to 5.5 hPa, in a similar range to Uccellini and Koch 1987), and have short to moderate wavelengths (up to 170 km) and wave periods (up to 67 min). The types of disturbances which were detected by our networks of pressure sensors included not only gravity waves, but also synoptic fronts, convective outflow boundaries, and a convective wake low. We will describe how we discerned those four types of disturbances from one another in Sects. 3.2.2-3.2.3. In order to keep terminology clear and consistent, and because different studies may use different conventions, Table 1.2 defines terms used in this paper related both to wave properties and the different types of waves.

Many observational studies have used pressure sensors to detect gravity wave signals (e.g., Christie et al. 1978; Kjelaas et al. 1974; Einaudi et al. 1989; Uccellini and Koch 1987; Bosart et al. 1998; Grivet-Talocia et al. 1999; Koch and Siedlarz 1999). In this study we use networks of high precision pressure sensors to detect and track gravity waves and analyze them in the context of radar-detected features in winter storms. Table 3.1 compares the properties of the waves presented in this paper to those in a selection of other papers in the literature. The spatial and time scales of pressure waves that we focus on, 3.5 to 170 km and 2 to 67 min overlap the larger end of the scales examined in previous work by Christie et al. (1978) and overlap the smaller end of the scales examined by Grivet-Talocia et al. (1999) and Uccellini and Koch (1987).

Table 3.1: Properties of pressure waves presented in this study (indicated in **bold**) and in some prior studies and meta-analyses in the literature. Rows are in ascending order by minimum wavelength. Information in cells indicated with \* were inferred from figures in the associated paper (not directly stated), and the cell indicated with \*\* was inferred from the wavelength and phase speed range for that paper.

Paper	Detection method	Number of cases	Amplitudes	Wavelengths	Wave periods	Phase speeds	Event durations	Types of waves, geographic region
Christie et al. (1978)	Pressure sensors	99	0.05-1.1 hPa	0.4-30 km	*2-20 min	4-50 m s <sup>-1</sup>	*8 min - 2 h	Wave packets and solitary waves; Central Australia
Kjelaas et al. (1974)	Acoustic sounders / pressure sensors	3	50-120 m vertical displacement	1-6 km	3-12 min	5-10 m s <sup>-1</sup>	20-40 min	Wave packets; Haswell, Colorado
<b>This study</b>	<b>Pressure sensors</b>	<b>33</b>	<b>0.45-5.51 hPa</b>	<b>3.5-170 km</b>	<b>2-67 min</b>	<b>17-62 m s<sup>-1</sup></b>	<b>47 min - 20 h</b>	<b>Wave packets and solitary waves (inc fronts, outflow boundaries, wake low); New York and Toronto Metro areas</b>
Grivet-Talocia et al. (1999)	Pressure sensors	626	0.2-10 hPa	40-600 km (96% of cases)	0.5-6 h	5-65 m s <sup>-1</sup>	*hours to days	Wave packets and solitary waves (inc surface boundaries); Central Illinois
Uccellini and Koch (1987)	Pressure sensors	13	0.2-7.0 hPa	50-500 km	1-4 h	13-50 m s <sup>-1</sup>	9-33 h	Wave packets and solitary waves; Central and Eastern United States
Koch and Siedlarz (1999)	Pressure sensors	13	0.2-0.7 hPa	200-260 km (3 strongest cases)	1-6 h	19-9-27.9 m s <sup>-1</sup> (3 strongest cases)	15-38 h	Wave packets and solitary waves; Central United States
Bosart et al. (1998)	Pressure sensors	1	< 1 hPa strengthening to > 10 hPa	200-300 km	**1-3 h	30-40 m s <sup>-1</sup>	> 18 h	Wave packet with a strong solitary wave; Northeast United States

### 3.1.1 Possible effects of gravity waves on cloud and precipitation processes

Gravity waves can have noticeable effects on cloud and precipitation processes when they occur within the troposphere and under the right conditions. In marine stratocumulus, upward motions associated with gravity waves can yield enhancements in drizzle (Allen et al. 2013; Connolly et al. 2013). In the southeast Atlantic, satellite observations have revealed cases of marine stratocumulus cloud decks rapidly eroding, and this abrupt cloud-clearing appears to be related at least in part to gravity waves (Yuter et al. 2018; Tomkins et al. 2021). In deep convection, latent heating can trigger gravity waves of varying frequency which alter the pre-storm environment and lead to initiation of convection ahead of the existing line of storms, often referred to as "action at a distance" (Fovell et al. 2006; Adams-Selin 2020) and "gregarious convection" (Nicholls et al. 1991; Mapes 1993; McAnelly et al. 1997). There has been extensive work describing mechanisms whereby terrain-locked gravity waves can enhance clouds and precipitation (e.g., Gaffin et al. 2003; Colle 2004; Doyle and Durran 2007; Houze 2012, 2014;

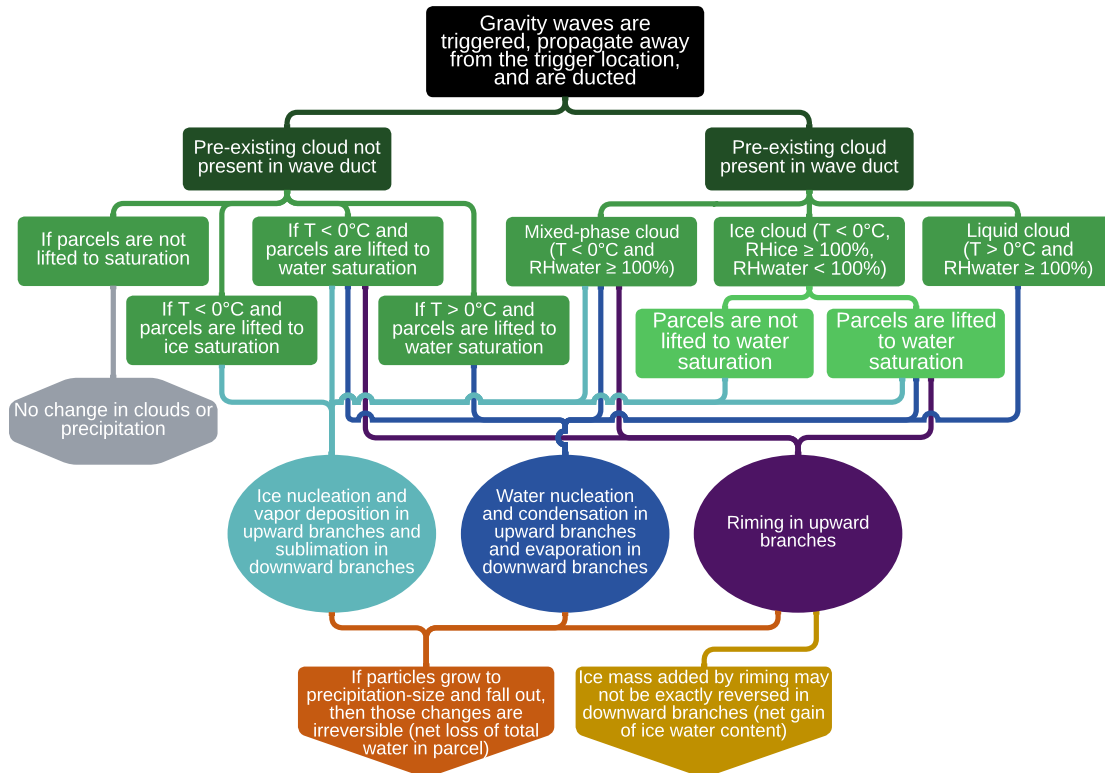


Figure 3.1: Possible chains of processes and outcomes for gravity waves to yield changes in cloudiness and precipitation. The sequence goes from top to bottom. Green rectangles indicate conditions or requirements, ovals indicate microphysical processes which result from the air motions associated with gravity waves, and downward-pointing pentagons indicate irreversible changes within air parcels resulting from the previous steps. For simplicity, sequences where air parcel temperatures cross the 0°C level altitude are not shown.

Kingsmill et al. 2016; Ma et al. 2023).

In order for gravity waves to modify clouds and precipitation, several processes have to occur within suitable conditions in sequence (Fig. 3.1). Gravity waves are first triggered, then the waves propagate away from their source location and may be ducted. If cloud is not already present in the wave duct, then the upward branches of the gravity waves must lift parcels to saturation, either with respect to ice (for air temperature < 0°C) or with respect to liquid water (for air temperature ≥ 0°C), in order for cloud to form. If conditions are saturated or supersaturated in the wave duct (either  $RH_{ice} \geq 100\%$  and/or  $RH_{water} \geq 100\%$ ), then enhanced vapor deposition and/or condensation can occur in the upward branches of gravity waves. If lifting associated with a gravity wave brings an ice or mixed phase cloud parcel to liquid water saturation, and riming then occurs, that rimed ice mass will not be removed unless  $RH_{ice}$

falls below 100% in the downward branch of the gravity wave and sublimation occurs. When net increases in particle mass due to gravity waves are sufficient to enlarge cloud particles to precipitation-size, the precipitation that falls out of the parcel results in a net loss of total water from the parcel which is not reversible (e.g., Allen et al. 2013).

### 3.1.2 Gravity waves in winter storm case studies

Previous case studies of gravity waves in winter storms include those that are close to the scale range targeted by this study (wavelengths  $\leq 170$  km and wave periods  $\leq 67$  min) and those that examined larger scale phenomena. Gaffin et al. (2003) described a heavy snowfall event where gravity waves generated by flow over terrain in the lee of the Smoky Mountains contributed to localized lifting. Bosart et al. (1998) presented a case of a very large-amplitude gravity wave (with a peak-to-trough pressure difference on the order of 10 hPa) associated with observed snowfall rates up to  $15 \text{ cm hr}^{-1}$  (this refers to snow depth, **not** liquid equivalent) in the northeastern United States on 4 January 1994. The gravity wave in this case propagated at roughly  $30\text{-}40 \text{ m s}^{-1}$  toward the northeast with a wavelength of 200-300 km (implying a wave period of roughly 1.4-2.8 h). Zhang et al. (2001) simulated the 4 January 1994 case presented by Bosart et al. (1998) using the National Center for Atmospheric Research/Pennsylvania State University Mesoscale Model 5. Their analysis of the simulated case indicated that geostrophic adjustment in the exit region of an upper-level jet streak initially triggered lower-amplitude gravity waves (roughly 1 hPa peak-to-trough), which merged and had a resonant interaction with an upper-level front leading to their nonlinear amplification. Zhang (2004) later generalized the term "geostrophic adjustment" as "balance adjustment" for curved flows as the trigger for gravity wave genesis. In the model results shown by Zhang et al. (2001), the upward motion associated with the interaction of the gravity wave and the upper-level front led to release of potential instability and a region of elevated convection, where heavy precipitation was produced in the simulation.

The conditions necessary for gravity wave generation by balance adjustment often exist in the strong baroclinic trough-ridge systems which produce winter storms. After gravity waves are generated aloft, their energy propagates upward and downward. If appropriate conditions exist, the waves can then be *ducted* or trapped within a cloud layer, allowing the waves to influence cloud processes (Ruppert et al. 2022). Lindzen and Tung (1976) described the theoretical conditions for an ideal wave duct: an absolutely stable ducting layer (where the environmental lapse rate  $<$  the moist adiabatic lapse rate) beneath a statically neutral or conditionally unstable reflecting layer (where the environmental lapse rate  $\geq$  the moist adiabatic lapse rate). Such lapse rate conditions are common ahead of a warm/stationary front or behind a cold front (e.g., Uccellini and Koch 1987).

### 3.1.3 Reflectivity bands and velocity waves in winter storms

Gravity waves have been previously suggested as the key mechanism yielding locally enhanced bands of radar reflectivity in snow and Doppler velocity waves. Detection of wave signals using an array of pressure sensors can help distinguish gravity waves from the other candidate processes (Nappo 2002, Sect. 8.2).

Linear regions of locally enhanced radar reflectivity (*bands*) are frequently observed in winter storms (e.g., Novak et al. 2004; Hoban 2016; Ganetis et al. 2018). These bands are conventionally categorized into two types: *primary band* and sets of *multibands*. Winter storms have been found to contain both a primary band and multibands, only a primary band, only multibands, or no bands at all (Hoban 2016; Ganetis et al. 2018). Primary bands are  $\geq 200$  km long, usually 30-70 km wide, occur as a single feature in reflectivity within a given storm, and have been associated with regions of strong frontogenesis along an occlusion (Novak et al. 2004; Baxter and Schumacher 2017; Ganetis et al. 2018). Multibands are  $< 200$  km long, usually 10-50 km wide, and occur in groups of two or more bands, which are often roughly evenly spaced (Hoban 2016; Ganetis et al. 2018). Given propagation speeds on the order of  $10\text{-}30\text{ m s}^{-1}$ , it can take enhanced reflectivity bands on the order of 5 min to 2 h to cross a given location.

Ganetis et al. (2018) found no robust correspondence between frontogenesis and the occurrence of multibands. Processes which may lead to multibands include gravity waves (Gaffin et al. 2003; Hoban 2016), Kelvin-Helmholtz waves (Houser and Bluestein 2011), shear-organized lines of cloud-top generating cells (Keeler et al. 2016, 2017), and convective cells elongated by flow anomalies resulting from potential vorticity dipoles (Leonardo and Colle 2023). A further complication in relating enhanced reflectivity in snow to heavy snowfall rates is that reflectivity can be increased by aggregation or partial melting of ice particles, which would not increase the associated snow mass. Additionally, localized reflectivity enhancements observed by radar a few km above the surface may not reach the surface (Tomkins 2024).

Hoban (2016) and Miller et al. (2022) identified waves in the Doppler velocities ("Doppler velocity waves") measured by National Weather Service NEXRAD radars (WSR-88Ds) in the Northeast United States during winter storms using the difference field between successive radar scans. Hoban (2016) analyzed 71 winter storms which contained multibands. Of those 71 storms with multibands, 50 also contained coherent sets of propagating Doppler velocity waves. If the sets of propagating parallel Doppler velocity bands have a surface pressure signal, they could be gravity waves. If not, other mechanisms such as Kelvin-Helmholtz waves are a more likely.

### **3.1.4 Objectives of this study**

In this study, we used high-precision surface pressure sensors to objectively identify pressure wave events over a 3+ year period, characterize the wave properties and their synoptic environments, and examine if the pressure waves are related to enhancements in radar reflectivity and coherent sets of Doppler velocity waves. Section 3.2 describes the pressure data and processing techniques to extract wave events, the reanalysis model output used to characterize the large scale environment, and the several types of observations used to identify enhanced reflectivity bands, Doppler velocity waves, temperature inversions, and surface snow rates. Section 3.3 describes the characteristics of pressure wave events and their environmental context. Section 3.3.1 puts the pressure waves into context of radar-detected features, including how often they were collocated and moving with enhanced reflectivity bands and/or Doppler velocity waves. Finally, Sect. 3.4 includes conclusions and discussion of the results with potential avenues for future work.

## **3.2 Data and Methods**

We used networks of pressure sensors in the Toronto, ON, Canada, and New York, NY, USA, metropolitan areas to detect wave events (Allen et al. 2024d, and Fig. 3.2), and we analyzed the context of those wave events using ERA5 reanalysis data (Hersbach et al. 2020), radiosonde data from the Integrated Global Radiosonde Archive (IGRA; NOAA National Centers for Environmental Information 2021b), surface weather data from Automated Surface Observing Systems (ASOS; NOAA National Centers for Environmental Information 2021a), and operational S-band radar data from US National Weather Service (NWS) WSR-88D radars (NEXRAD; NOAA National Weather Service Radar Operations Center 1991).

### **3.2.1 Pressure sensor data**

In numerical model output, gravity waves can be identified by analyzing the 3D gridded fields of pressure, geopotential height, wind, and temperature perturbation values. In observations, pressure sensor data are needed to definitively confirm the presence of gravity waves. We deployed high precision pressure sensor networks in the Toronto, ON, Canada, and New York, NY, USA, metropolitan areas over a three year period (sensor locations shown in Fig. 3.2). To minimize costs and hassle, these sensors were located in the homes and offices of our collaborators and automatically reported back to a server at North Carolina State University where the data were archived.

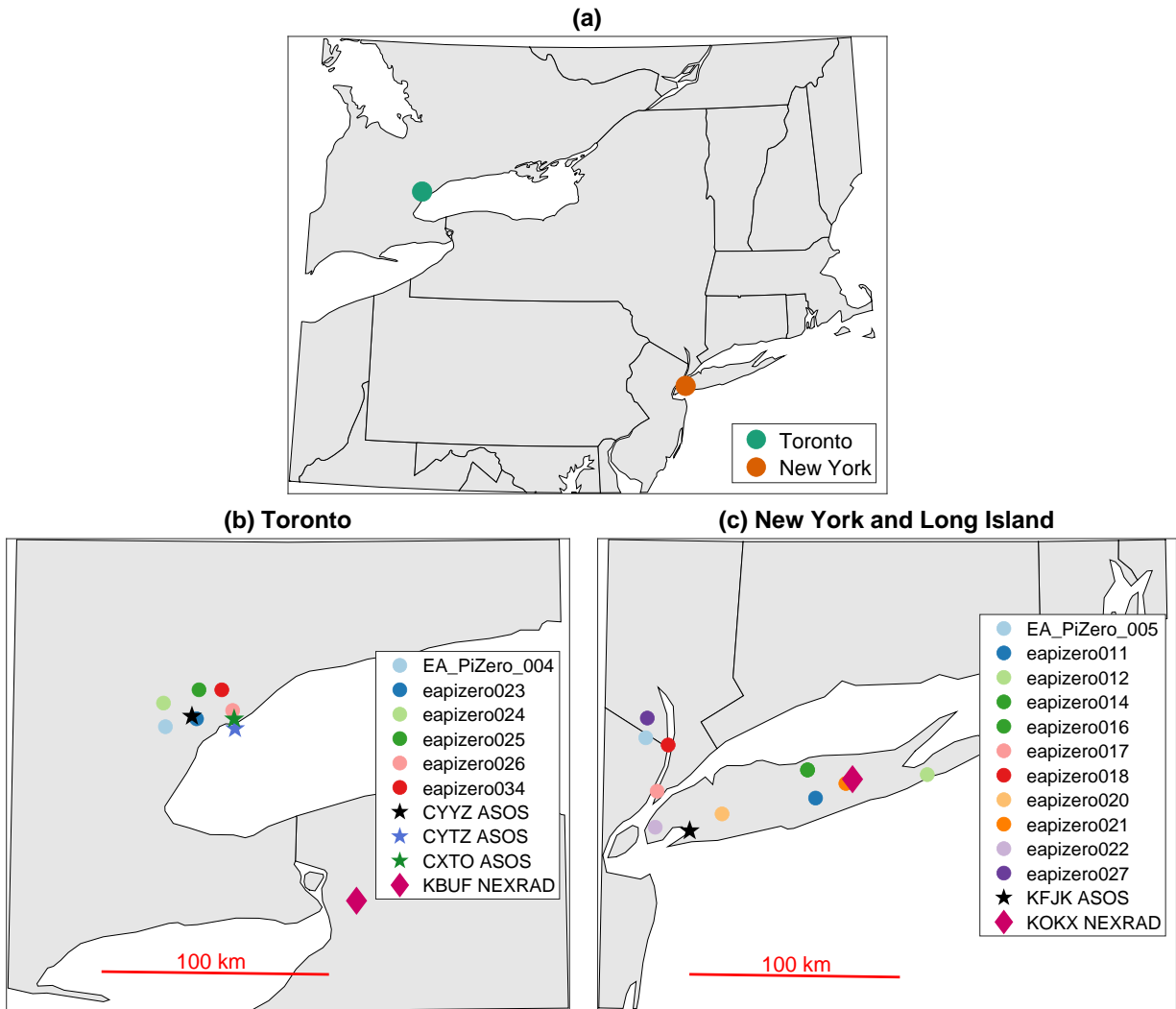


Figure 3.2: Maps of the pressure sensor, ASOS, and radar sites used in this study. **(a)** Locations of Toronto and New York City. **(b)** Pressure sensor sites in Toronto (filled circles) with the 3 ASOS sites (stars) and KBUF radar (maroon diamond). **(c)** Pressure sensor sites in New York and Long Island (filled circles) with KJFK ASOS (black star) and KOKX radar (maroon diamond).

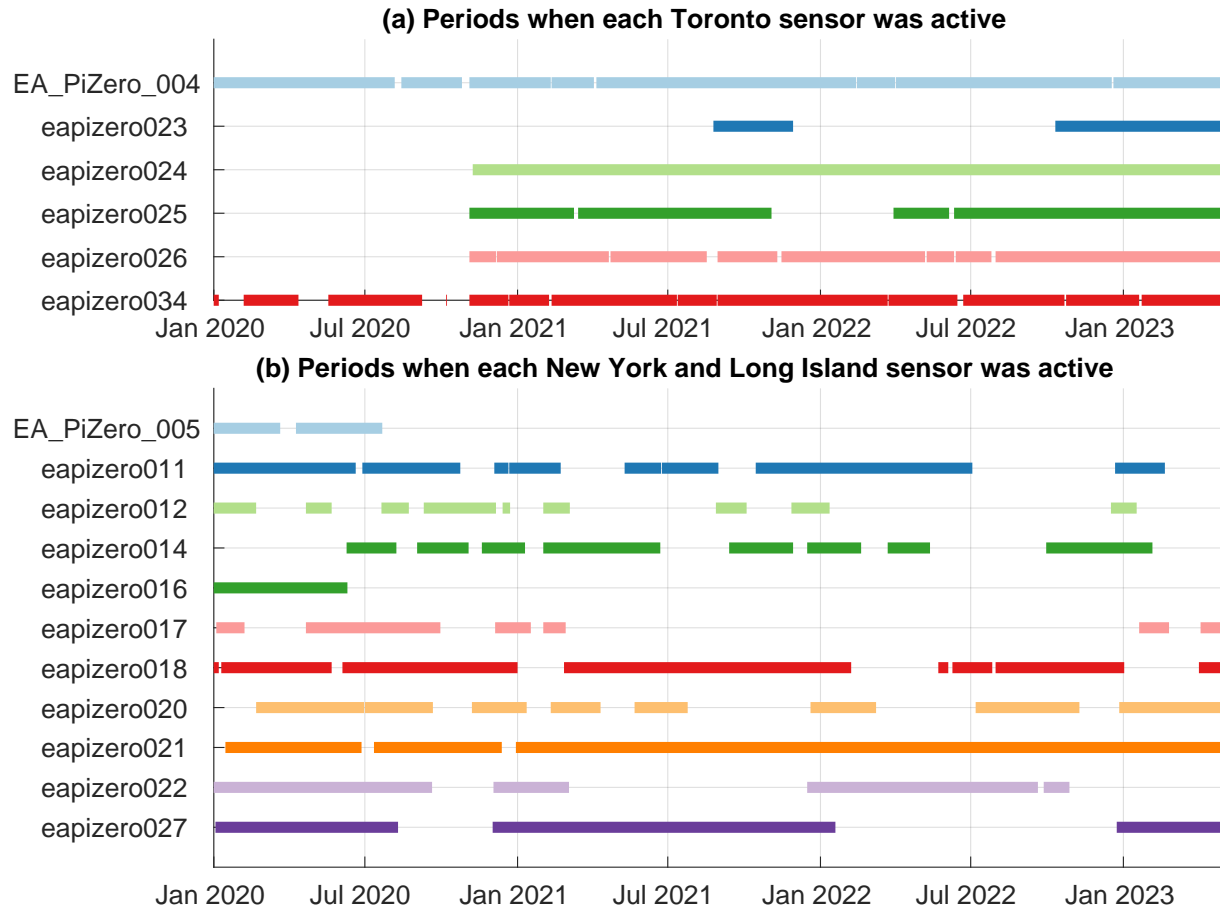


Figure 3.3: Timelines of when the pressure sensors in **(a)** Toronto and **(b)** New York and Long Island recorded pressure data between January 2020 and April 2023.

Each instrument utilized either a Bosch BME280 (Bosch 2022) or a Bosch BMP388 (Bosch 2020) pressure sensor, and the timestamps, data logging, and communications were handled by Raspberry Pi Zero single board computers (Allen et al. 2024d). Each sensor was placed indoors to minimize wind contamination in the pressure measurements. The noise floor of the sensors is roughly 0.8 Pa, depending on ambient conditions. The sensors continuously recorded pressure at 1-second intervals when possible, but power or internet outages occasionally caused gaps in the data record (Fig. 3.3). We analyzed data between January 2020 and April 2023. Most of the sensors in New York and Long Island were deployed prior to January 2020 while the sensors in Toronto were deployed starting in October 2020 (Fig. 3.3). Analysis subsequent to the deployment of the sensors suggests that the smaller spatial scale and more circular pattern of the Toronto network as compared to the larger spatial scale and more linear west-east arrangement of the sensors in New York likely makes the Toronto network better at detecting smaller amplitude pressure waves.

## Detection of wave events

Allen et al. (2024d) described the methods for detecting waves in the pressure sensor data in detail, which are summarized here. To smooth out artifacts and high-frequency pressure variations, we use 10-s samples of pressure in hPa (i.e., we take the 10-s moving average then use every 10th point of the smoothed time series). The detection method relies on a wavelet transform, a technique for identifying wave signals in time-wave period (or time-frequency) space, which is preferable to Fourier transforms for finding transient (i.e., time-localized) waves. We used an analytic morse wavelet (Olhede and Walden 2002; Lilly and Olhede 2012) and analyzed wave periods between 1 and 120 minutes to detect waves on similar temporal scales to enhanced reflectivity bands. The output of the wavelet transform is an array of complex values in time-scale space. The absolute value of those values is referred to as the wavelet *power* ( $|W(b, a)|$ , units  $\text{hPa}^2 \text{s}^{-1}$ ).

A scale-dependent threshold function  $A(a)$  was defined using the mean wavelet power across the full data set by scale, multiplied by a constant  $K$ :

$$A(a) = K \langle |W(b, a)| \rangle_b \quad (3.1)$$

To identify only the strongest wave signals, we used  $K = 10$ . Mean wavelet power increases with wave period (Allen et al. 2024d, Fig. 2.4). Wave events were then identified as peaks in the wavelet power which exceeded  $A(a)$ , along with their connected regions which exceeded  $\frac{A(a)}{2}$ . We refined these regions using the watershed transform to separate distinct signals at different wave periods, then took the bounding box to obtain the final event regions. The wavelet transform was then inverted over the final event region to extract the wave event trace (Allen et al. 2024d).

After wave event traces were extracted for each sensor individually, we identified coherent wave events across multiple sensors using the cross-correlation function  $C_{ij}(\Delta t)$ :

$$C_{ij}(\Delta t) = \frac{1}{\|p_i\| \|p_j\|} \int p_i(t) p_j(t + \Delta t) dt \quad (3.2)$$

where  $p_i(t)$  and  $p_j(t)$  are the extracted wave event traces for two sensors  $i$  and  $j$ . Events in pairs of sensors were matched together if the maximized  $C_{ij}(\Delta t)$  value exceeded 0.65, with the time between wave passages at the two sensors estimated by the corresponding time lag  $\Delta t_{opt}$  (in s). The cross-correlation function and associated  $\Delta t_{opt}$  values were calculated for each possible pair of sensors within a network, which produced a vector of time lags  $\vec{t}$  representing the time between wave passages at each pair of sensors which captured the event.

We then calculated the *slowness vector* using the time lags  $\vec{t}$  for each wave event. The

slowness vector is a two element vector  $\vec{s} = (s_x, s_y)$ , where  $s_x$  and  $s_y$  (in  $\text{s m}^{-1}$ ) are the inverses of the x- and y-components of the wave phase velocity,  $\frac{1}{c_x}$  and  $\frac{1}{c_y}$  (in  $\text{m s}^{-1}$ ), respectively. We solve for  $\vec{s}$  starting from the following equation (Del Pezzo and Giudicepietro 2002):

$$\vec{t} = \vec{s} \cdot \Delta \mathbf{x} \quad (3.3)$$

where  $\Delta \mathbf{x}$  is the two-column matrix of the x- and y-components of the distance vectors (in m) between each pair of sensors which captured the event. For events captured by at least 3 sensors, Eq. 3.3 represents an overdetermined system of linear equations, from which  $\vec{s}$  is estimated using a least-squares approach:

$$\vec{s} = (\Delta \mathbf{x}^T \Delta \mathbf{x})^{-1} \Delta \mathbf{x}^T \vec{t} \quad (3.4)$$

where superscript T indicates the transpose of a matrix (Del Pezzo and Giudicepietro 2002). The components of the slowness vector are then inverted to obtain the wave phase velocity vector  $\vec{c} = (c_x, c_y)$ . We assessed this phase velocity estimate by calculating the "modeled" delay times  $\vec{t}_m$  using Eq. 3.3 with the estimated slowness vector. We calculated the root mean square error (RMSE, in s) and normalized root mean square error (NRMSE, unitless) of the modeled delay times as follows:

$$RMSE = \sqrt{\frac{\sum_{i=1}^{N_s(N_s-1)/2} (t_{m,i} - t_i)^2}{N_s(N_s - 1)/2}} \quad (3.5)$$

$$NRMSE = \sqrt{\frac{\sum_{i=1}^{N_s(N_s-1)/2} (t_{m,i} - t_i)^2}{\sum_{i=1}^{N_s(N_s-1)/2} (t_i)^2}} \quad (3.6)$$

where  $N_s$  is the number of sensors which captured a given event.

To have reasonable confidence in the wave phase velocity estimate for a given event, we require the event to be captured by at least 4 sensors with RMSE below 90 s and NRMSE below 0.1, as discussed by Allen et al. (2024d). Additionally, the following results exclude any wave events found between 15 January and 18 January 2022, following the Hunga-Tonga volcanic eruption on 15 January 2022, which produced a Lamb wave with measurable pressure signals globally (Adam 2022; Burt 2022; Allen et al. 2024d). After applying those criteria, 33 total trackable pressure wave events were detected by the Toronto and New York pressure sensor networks between January 2020 and April 2023. Nineteen pressure wave events were detected by the Toronto pressure sensor network, and 14 were detected by the New York pressure sensor network (Table 3.2).

In general, pressure waves of amplitude above roughly 0.1 hPa could be detected in a

Table 3.2: Properties of the 33 pressure wave events detected over the 40 month analysis period. The leftmost column is an index column. In the location column, TOR indicates the Toronto sensor network, and NY indicates the New York and Long Island sensor network. The wave period and amplitude are averaged among sensors which detected a given event. Phase direction is shown in degrees clockwise from northward (e.g., 90 degrees indicates a wave propagating west to east). Rows in **bold** indicate gravity wave events.

	Event Start UTC	Event End UTC	Location	Event Type	$N_{sensors}$	Wave Period mm:ss	Mean Amp. hPa	Phase Speed $\text{ms}^{-1}$	Phase Dir. Degrees	Wavelength km
1	2020-11-15 1859	2020-11-15 2216	TOR	Front	5	02:08	1.83	27.5	65.2	3.5
2	<b>2020-12-25 0709</b>	<b>2020-12-25 1120</b>	<b>TOR</b>	<b>Gravity wave</b>	<b>4</b>	<b>26:33</b>	<b>1.69</b>	<b>48.7</b>	<b>29.6</b>	<b>77.6</b>
3	<b>2020-12-28 0437</b>	<b>2020-12-28 0525</b>	<b>TOR</b>	<b>Gravity wave</b>	<b>4</b>	<b>03:21</b>	<b>0.45</b>	<b>21.6</b>	<b>84.7</b>	<b>4.3</b>
4	<b>2021-02-18 1418</b>	<b>2021-02-18 1642</b>	<b>TOR</b>	<b>Gravity wave</b>	<b>4</b>	<b>04:53</b>	<b>0.89</b>	<b>62.0</b>	<b>64.6</b>	<b>18.2</b>
5	<b>2021-03-31 0543</b>	<b>2021-03-31 0642</b>	<b>TOR</b>	<b>Gravity wave</b>	<b>4</b>	<b>03:36</b>	<b>0.71</b>	<b>25.6</b>	<b>14.6</b>	<b>5.5</b>
6	<b>2021-04-28 1213</b>	<b>2021-04-28 1656</b>	<b>TOR</b>	<b>Gravity wave</b>	<b>4</b>	<b>04:34</b>	<b>2.73</b>	<b>29.6</b>	94.8	8.1
7	<b>2021-05-01 2140</b>	<b>2021-05-02 0051</b>	<b>TOR</b>	<b>Gravity wave</b>	<b>4</b>	<b>13:04</b>	<b>2.36</b>	<b>28.4</b>	<b>138.7</b>	<b>22.2</b>
8	2021-09-07 1931	2021-09-08 0528	TOR	Outflow	6	08:59	3.26	21.1	120.3	11.4
9	<b>2022-01-27 1415</b>	<b>2022-01-27 1533</b>	<b>TOR</b>	<b>Gravity wave</b>	<b>4</b>	<b>05:05</b>	<b>0.78</b>	<b>23.5</b>	<b>113.3</b>	<b>7.2</b>
10	<b>2022-02-25 0816</b>	<b>2022-02-25 1359</b>	<b>TOR</b>	<b>Gravity wave</b>	<b>4</b>	<b>20:22</b>	<b>2.14</b>	<b>45.4</b>	<b>72.8</b>	<b>55.5</b>
11	<b>2022-03-07 0352</b>	<b>2022-03-07 0630</b>	<b>TOR</b>	<b>Gravity wave</b>	<b>4</b>	<b>32:39</b>	<b>1.13</b>	<b>52.0</b>	<b>33.5</b>	<b>101.8</b>
12	<b>2022-03-07 1221</b>	<b>2022-03-07 2237</b>	<b>TOR</b>	<b>Gravity wave</b>	<b>4</b>	<b>55:42</b>	<b>3.09</b>	<b>50.7</b>	<b>90.3</b>	<b>169.4</b>
13	<b>2022-03-30 2118</b>	<b>2022-03-31 0133</b>	<b>TOR</b>	<b>Gravity wave</b>	<b>5</b>	<b>16:39</b>	<b>2.41</b>	<b>28.2</b>	<b>81.2</b>	<b>28.1</b>
14	<b>2022-05-21 1110</b>	<b>2022-05-21 1231</b>	<b>TOR</b>	<b>Gravity wave</b>	<b>4</b>	<b>05:51</b>	<b>0.81</b>	<b>30.6</b>	<b>104.3</b>	<b>10.7</b>
15	2022-05-21 1316	2022-05-21 22:47	TOR	Outflow	5	02:27	5.51	33.2	70.0	4.9
16	<b>2023-02-15 0550</b>	<b>2023-02-15 0749</b>	<b>TOR</b>	<b>Gravity wave</b>	<b>4</b>	<b>08:38</b>	<b>1.10</b>	<b>24.9</b>	<b>53.3</b>	<b>12.9</b>
17	<b>2023-02-19 1106</b>	<b>2023-02-19 1316</b>	<b>TOR</b>	<b>Gravity wave</b>	<b>5</b>	<b>03:23</b>	<b>1.20</b>	<b>29.0</b>	<b>68.8</b>	<b>5.9</b>
18	<b>2023-02-23 0139</b>	<b>2023-02-23 0323</b>	<b>TOR</b>	<b>Gravity wave</b>	<b>5</b>	<b>12:53</b>	<b>0.74</b>	<b>42.2</b>	<b>74.2</b>	<b>32.6</b>
19	<b>2023-04-01 0357</b>	<b>2023-04-01 0740</b>	<b>TOR</b>	<b>Gravity wave</b>	<b>6</b>	<b>21:21</b>	<b>1.33</b>	<b>37.9</b>	<b>48.9</b>	<b>48.5</b>
20	2023-04-01 0736	2023-04-01 1107	TOR	Front	6	07:35	1.63	36.8	56.1	16.8
21	2023-04-05 0745	2023-04-05 1401	TOR	Outflow	4	05:35	3.78	27.9	90.9	9.4
22	<b>2023-04-05 0809</b>	<b>2023-04-06 0400</b>	<b>TOR</b>	<b>Gravity wave</b>	<b>6</b>	<b>05:29</b>	<b>4.24</b>	<b>22.1</b>	<b>111.8</b>	<b>7.3</b>
23	2023-04-16 2250	2023-04-17 0206	TOR	Front	5	04:44	1.92	19.9	12.6	5.7
24	<b>2020-01-25 1544</b>	<b>2020-01-25 2254</b>	<b>NY</b>	<b>Gravity wave</b>	<b>4</b>	<b>09:49</b>	<b>2.87</b>	<b>18.7</b>	<b>52.9</b>	<b>11.0</b>
25	<b>2020-02-04 0824</b>	<b>2020-02-04 1200</b>	<b>NY</b>	<b>Gravity wave</b>	<b>4</b>	<b>16:31</b>	<b>1.48</b>	<b>17.2</b>	<b>179.4</b>	<b>17.0</b>
26	<b>2020-05-01 0435</b>	<b>2020-05-01 0939</b>	<b>NY</b>	<b>Gravity wave</b>	<b>5</b>	<b>30:02</b>	<b>2.43</b>	<b>19.4</b>	<b>64.3</b>	<b>34.9</b>
27	<b>2020-12-25 1629</b>	<b>2020-12-25 1952</b>	<b>NY</b>	<b>Gravity wave</b>	<b>4</b>	<b>04:32</b>	<b>1.18</b>	<b>47.3</b>	<b>39.7</b>	<b>12.9</b>
28	<b>2021-02-18 1556</b>	<b>2021-02-18 2247</b>	<b>NY</b>	<b>Gravity wave</b>	<b>6</b>	<b>60:28</b>	<b>2.25</b>	<b>32.7</b>	<b>114.6</b>	<b>118.7</b>
29	2021-09-14 0004	2021-09-14 0629	NY	Wake low	4	66:37	3.25	20.8	68.2	83.2
30	<b>2021-12-29 0755</b>	<b>2021-12-29 1258</b>	<b>NY</b>	<b>Gravity wave</b>	<b>6</b>	<b>11:55</b>	<b>1.92</b>	<b>33.5</b>	<b>130.2</b>	<b>24.0</b>
31	2022-02-04 1642	2022-02-04 2033	NY	Outflow	5	14:49	1.84	21.1	117.7	18.7
32	2022-02-18 1056	2022-02-18 1350	NY	Front	4	03:00	1.66	20.5	122.5	3.7
33	2022-03-08 0119	2022-03-08 0428	NY	Front	4	04:15	1.72	23.1	123.5	5.9

single sensor, depending on the wave period (shorter waves had a lower detection threshold). However, the waves with lower amplitudes (i.e., weaker signals) were more difficult to track across multiple sensors. As a result, each of the trackable pressure waves in this study had an amplitude of at least 0.45 hPa. Table 3.1 compares this amplitude to other studies in the literature, which found pressure waves between 0.05 and 10 hPa in amplitude.

### 3.2.2 ERA5 reanalysis data

We used hourly ERA5 reanalysis data (Hersbach et al. 2020) to characterize the large-scale environment near the surface and in the upper-troposphere during each wave event. ERA5 data are output to a global, 0.25 degree grid on constant pressure and height levels. From ERA5 data, we calculated equivalent potential temperature ( $\theta_e$ , in K) at 2 m above sea level and

analyzed the resulting maps for each pressure wave event to qualitatively determine where wave events occurred relative to surface air mass boundaries.  $\theta_e$  was calculated following the approximation provided by (Bolton 1980, their Eq. 43):

$$\theta_E = T_K \left( \frac{1000}{p} \right)^{0.2854(1-0.28*10^{-3}r)} * \exp\left[ \left( \frac{3.376}{T_L} - 0.00254 \right) * r(1 + 0.81 * 10^{-3}r) \right] \quad (3.7)$$

where  $T_K$  is the temperature in K,  $p$  is the air pressure in hPa, and  $r$  is the water vapor mixing ratio (unitless).  $T_L$  is the temperature at the lifting condensation level in K, approximated using Eq. 15 from Bolton (1980):

$$T_L = 56 + \frac{1}{\frac{1}{T_D - 56} + \frac{\ln(T_K/T_D)}{800}} \quad (3.8)$$

where  $T_D$  is the dew point temperature in K.

We analyzed maps of 300 hPa wind speed (in  $\text{m s}^{-1}$ ) and geopotential height (in m) for each pressure wave event to determine where they occurred relative to upper-level troughs, ridges, and jet streaks. To quantify upper-level flow imbalance, we calculated the residual of the nonlinear imbalance equation on a constant 300 hPa surface ( $\Delta NBE$  in  $\text{s}^{-2}$ ; Zhang et al. 2000; Ruppert et al. 2022):

$$\Delta NBE = 2J(u, v) - \beta u + f\zeta - \nabla^2 \phi \quad (3.9)$$

where  $J(u, v)$  is the Jacobian of the horizontal flow (Eq. 3.10),  $\beta$  ( $\text{s}^{-1} \text{m}^{-1}$ ) is the change in the Coriolis parameter  $f$  ( $\text{s}^{-1}$ ) with latitude,  $u$  ( $\text{m s}^{-1}$ ) is the zonal component of the flow,  $\zeta$  ( $\text{s}^{-1}$ ) is the vertical component of relative vorticity, and  $\phi$  ( $\text{m}^2 \text{s}^{-2}$ ) is the geopotential.

$$J(u, v) = \frac{\partial u}{\partial x} \frac{\partial v}{\partial y} - \frac{\partial u}{\partial y} \frac{\partial v}{\partial x} \quad (3.10)$$

Eq. 3.9 is obtained by scale analysis of the divergence tendency equation. Terms in the divergence tendency equation which contain the divergence, vertical velocity, and divergent components of horizontal velocity are dropped (Zhang et al. 2000). When the magnitude of  $\Delta NBE$  is large relative to "background" (e.g., in straight, zonal flow) values, gravity wave generation by balance adjustment may occur (James Ruppert, personal communication).

For each gravity wave event, we compared the location of the sensor network to the ERA5 mean sea level pressure (MSLP) patterns to determine where the detected waves occurred in a cyclone-relative framework. In some cases we were able to automatically track minima in ERA5 MSLP data (Tomkins et al. 2024a) using the algorithm described by Crawford et al. (2021). In the balance of cases we determined the cyclone location manually.

### 3.2.3 Radar data

We analyzed horizontal maps of reflectivity and radial velocity from the WSR-88D radars (NOAA National Weather Service Radar Operations Center 1991) in Buffalo, NY (KBUF), for pressure wave events in Toronto, and Upton, NY (KOKX), for pressure wave events in New York and Long Island. An example of these maps for the event on 1 April 2023 is shown in Fig. 3.4. In each case, we used the scan at the 0.5° elevation angle.

Reflectivity bands were identified as roughly linear features of high reflectivity relative to the "background" reflectivity, following Tomkins et al. (2024b). To find features of locally-enhanced reflectivity, we first calculate the background reflectivity as a windowed average in radii of 20 km. Grid points with reflectivity sufficiently exceeding that background average, or which have reflectivity  $\geq 35$  dBZ, are identified as features (Fig. 3.4c). When mapping the reflectivity and detected high reflectivity features, we "mute" regions with enhanced reflectivity likely due to melting and mixed precipitation (reflectivity  $> 20$  dBZ and correlation coefficient  $< 0.97$ ) by plotting in greyscale (Fig. 3.4a,c; Tomkins et al. 2022). In Fig. 3.4, enhanced reflectivity features were found throughout the coverage of the KBUF radar, but most notably there were linear features near the eastern edge of Lake Erie and extending southeastward.

We identified Doppler velocity waves following Miller et al. (2022). We first calculate the difference in radial velocity between successive NWS WSR-88D scans. That difference field is then converted to a binary field; i.e., positive values are converted to zeros, and negative values are converted to ones. Small objects are filtered out of the binary field. In Fig. 3.4d, Doppler velocity waves are detected across the radar domain, but most notably the wave extending from west-central Lake Ontario eastward then southward into New York State could be tracked as a coherent feature across several radar scans (Video supplement Animation-Figure-S3.01).

We analyzed the resulting sequences of maps for each wave event to determine whether any coherent bands or waves were present anywhere within the range of the radar. Additionally, if any bands or waves were present we assessed if they propagated directly over the pressure sensors at a velocity consistent with the estimated phase velocity of the pressure waves.

### 3.2.4 Surface stations and operational soundings

We used hourly ASOS data (NOAA National Centers for Environmental Information 2021a) to assess precipitation type and liquid water equivalent precipitation amount during each pressure wave event. We counted the METAR snow precipitation type and snow mixed with other precipitation types as "snow". We tabulated the total number of hours during our analysis period in which at least a 0.1 mm/hr of snowfall liquid water equivalent rate was measured. For New York, we were able to use data from John F. Kennedy International Airport (KJFK) to obtain

01 Apr 2023 05:54:15 UTC  
KBUF 0.5° tilt

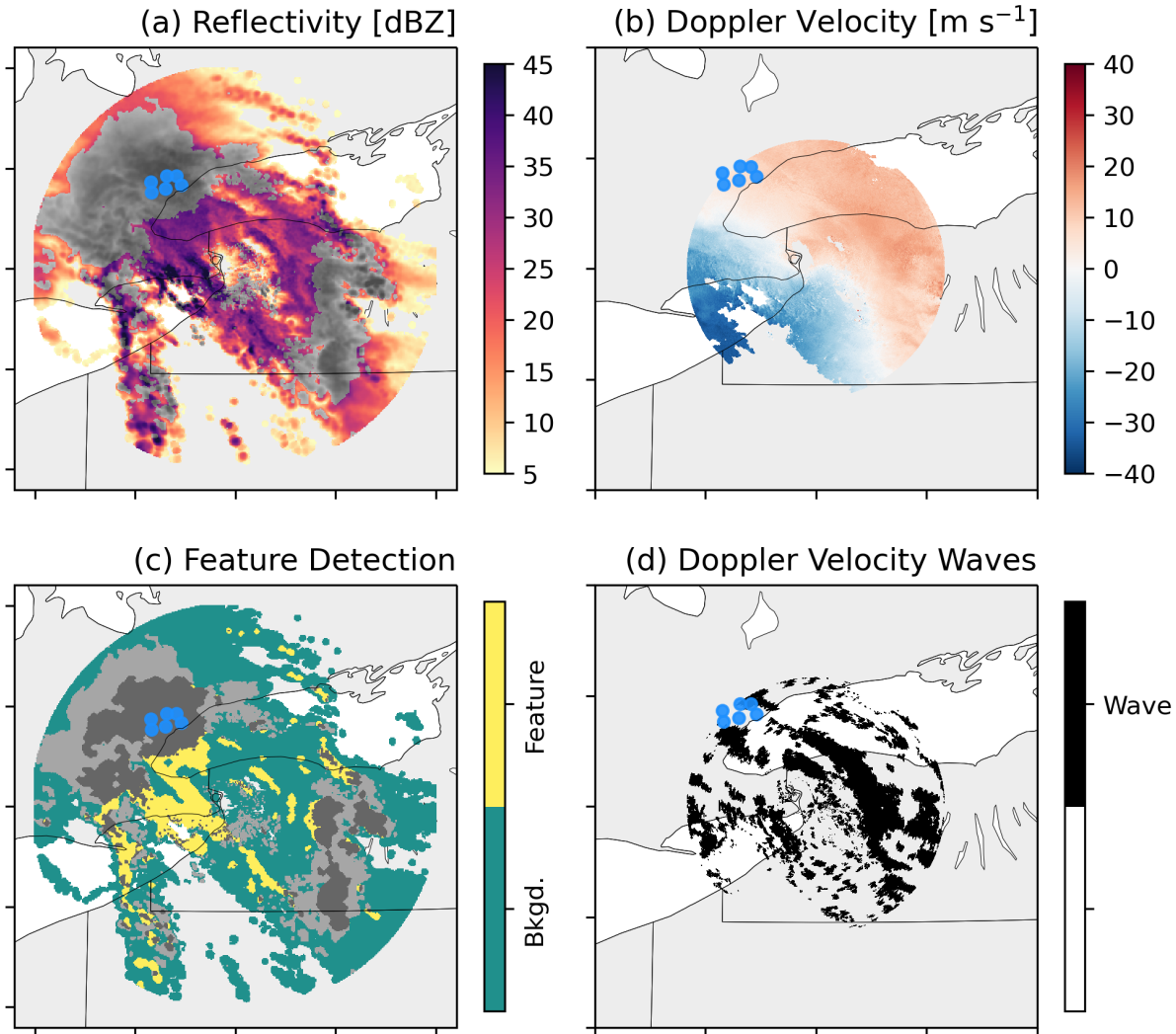


Figure 3.4: Event 19 (gravity wave event) maps of (a) reflectivity, (b) radial Doppler velocity, (c) detected features of enhanced reflectivity, and (d) Doppler velocity wave detection for KBUF at 05:54 UTC on 1 April 2023. Filled blue circles indicate the locations of pressure sensors in Toronto. In this example, gravity waves moved SW to NE while a NW-SE aligned linear region of enhanced reflectivity about 150 km long and 80 km wide extends from near the western edge of Lake Ontario. Several NW-SE aligned Doppler velocity waves could be tracked from SW to NE between Lake Erie and Lake Ontario. The greyscale regions in (a) and (c) likely contain mixed precipitation (reflectivity > 20 dBZ and dual-polarization correlation coefficient < 0.97). An animated version of this figure is available in the Video Supplement Animation-Figure-S3.01.

both precipitation type and snowfall intensity. As precipitation amounts at Toronto Pearson International Airport (CYYZ) were not available in the archived data, we used precipitation amount data from the Downtown Toronto (CXTO) ASOS, which does not record precipitation type, and precipitation type data from the Toronto City Airport (CYTZ) ASOS, which is closer to CXTO than CYYZ but does not record precipitation amount.

We used one-minute ASOS data to help determine whether each wave event was directly caused by the passage of a front or outflow boundary and its associated density and temperature change (e.g., when a sharp rise in pressure co-occurred with sharp drops in temperature and dew point). We also considered the radar and surface analysis maps when determining whether an event was directly caused by a front or outflow boundary passage. Examples of pressure wave events associated with a frontal passage and outflow boundary passage, along with contextual data, are shown in Sects. 2.4.3 and 2.4.4, respectively. In one case, a pressure wave event was caused by a convective wake low passage as indicated by the timing of the event relative to a mesoscale convective system passage (Allen et al. 2024d). Ideally, if we saw surface wind perturbations correlated with the pressure perturbations in one-minute ASOS data, then that would strongly suggest the pressure perturbations are associated with gravity waves. But, < 1-min surface wind data sets at the locations of the pressure sensor network sensors are not available. ERA5 and other reanalysis are too coarse in spatial and temporal scale to use for this purpose. We separated the front, outflow boundary, and wake low cases from the remaining cases, which we refer to as gravity wave events.

We analyzed upper-air radiosonde observations for gravity wave events with a nearby NWS weather balloon (Fig. 3.2) launched during a time window from 2 hours before the start of the wave event to 2 hours after the end of the wave event. For gravity wave events in the Toronto pressure sensor network, radiosonde data from Buffalo, NY (KBUF), were used, and for gravity wave events in the New York and Long Island pressure sensor network, radiosonde data from Upton, NY (KOKX), were used. We obtained the data from IGRA (NOAA National Centers for Environmental Information 2021b) and interpolated the data to a constant 100-meter vertical resolution. When sounding data were available, we determined whether an efficient wave duct was present (conditionally unstable layer above an absolutely stable layer; Lindzen and Tung 1976), as in Sect. 2.4.2 (Fig. 2.9), which added confidence that the pressure wave event was associated with gravity waves. For each sounding associated with a gravity wave event, we will determine whether a surface-adjacent temperature inversion was present or if any temperature inversions were present in the lowest 1 km above the surface. We identified temperature inversion layers as any observations where the temperature increased with increasing height.

### 3.3 Pressure wave characteristics and environmental context

Table 3.2 lists important attributes of all 33 pressure wave events, and it labels the events with numbers which will be referred to in the following text. No pressure wave events were detected between June and August (Fig. 3.5a). Five pressure wave events were solitary waves coincident with frontal passages, 4 pressure wave events were coincident with outflow boundary passages, 1 pressure wave event was caused by a wake low associated with a mesoscale convective system (Allen et al. 2024d), and the other 23 pressure wave events are considered gravity wave events (Fig. 3.5b,c).

There did not appear to be a strong relationship between wave period and wave amplitude for pressure wave events (Fig. 3.5b), which is somewhat surprising, given that the mean wavelet power generally increases with wave period for pressure (Canavero and Einaudi 1987; Grivet-Talocia and Einaudi 1998; Allen et al. 2024d). Individual pressure wave events (Fig. 3.5) may not follow the same pattern of increasing amplitude with increasing wave period as seen in longer-term mean values of wavelet power (Fig. 2.4). The pressure wave events are caused by atypical short-term pressure perturbations whereas the long-term mean wavelet power mainly consists of quiescent conditions, usually without sharp pressure changes. Figure 3.5b includes the range of wave periods where the wavelet power exceeded  $A(a)$  as error bars. From these error bars, it is apparent that nearly every pressure wave event had a strong wave signal at shorter wave periods ( $< 30$  min), while very few had a strong wave signal at longer wave periods ( $> 90$  min).

Every pressure wave event had an eastward component to its phase velocity (Fig. 3.5c). This result is similar to Grivet-Talocia et al. (1999), who found that 95% of pressure wave events in central Illinois had an eastward component to their phase velocities. Nineteen of the pressure wave events (58%) we detected had a northward component to their phase velocities, while 14 pressure wave events (42%) had a southward component to their phase velocities. Twenty out of 33 (61%) pressure wave events we detected had a phase speed between  $20 \text{ m s}^{-1}$  and  $35 \text{ m s}^{-1}$ , again similar to Grivet-Talocia et al. (1999).

#### 3.3.1 Gravity wave event characteristics

We will focus on the 23 gravity wave events to address their environmental and radar contexts with a focus on winter storms. All 23 gravity wave events occurred between December and May (Table 3.2). Figure 3.6 shows the extracted event and total pressure time series for a single sensor for each of those 23 gravity wave events. Most events consisted of multiple pressure oscillations. In some cases the amplitudes of those oscillations varied with time (e.g., events 2, 14, and 24), while in others the oscillations remained at a steady amplitude through the

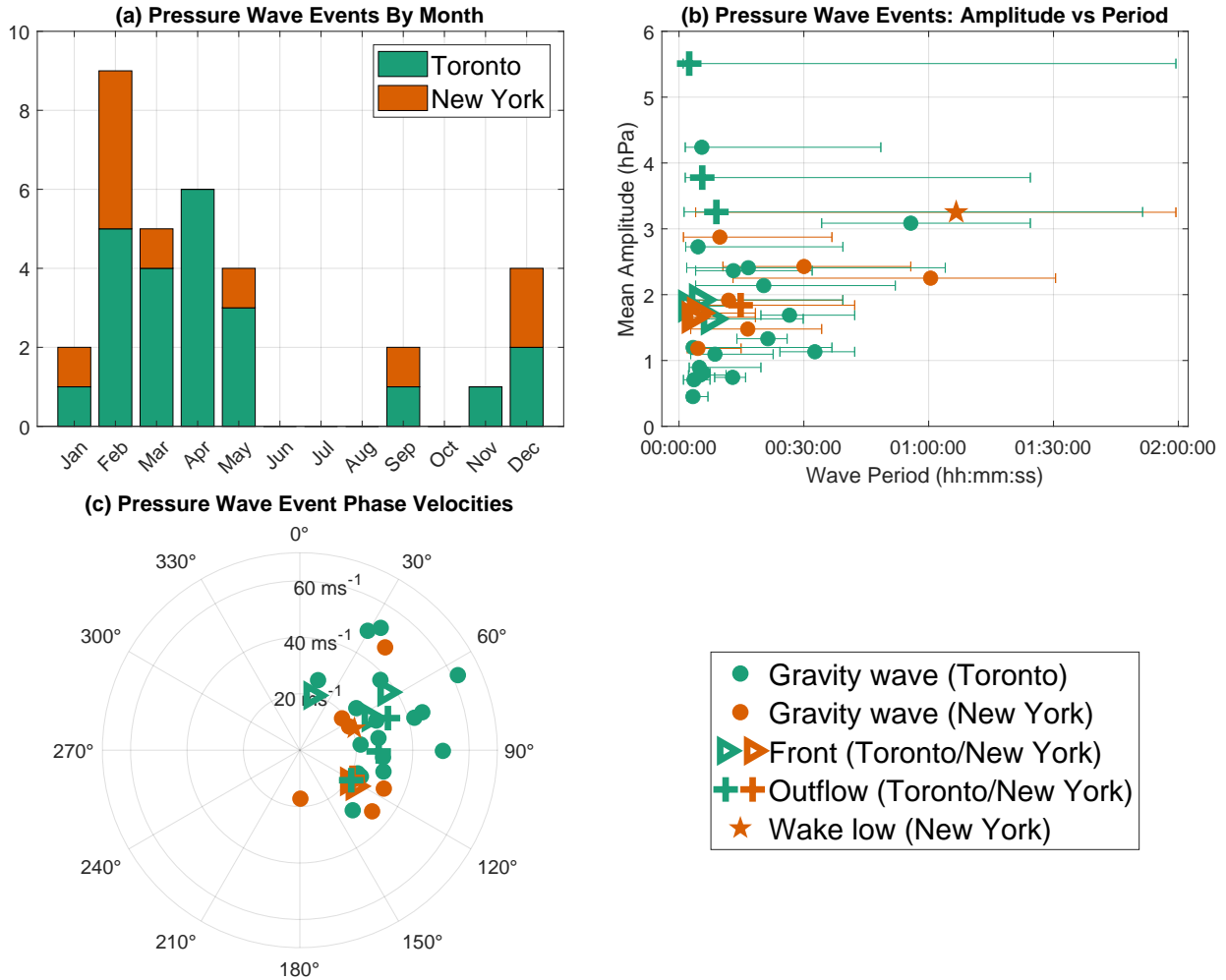


Figure 3.5: Characteristics of the 33 pressure wave events detected in New York (orange) and Toronto (green) between January 2020 and April 2023. **(a)** Bar chart of the number of pressure wave events by month. **(b)** Scatter plot of wave amplitude against wave period, with error bars indicating the range of wave periods where  $W \geq 10 \langle |W(b, a)| \rangle_b$ , i.e., where there was a strong wave signal. **(c)** Radial scatter plot of the wave phase velocities (directions shown are in degrees clockwise from northbound). In panels **(b)** and **(c)**, gravity wave events are indicated by filled circles, and front, outflow, and wake low events are indicated by other shapes according to the legend.

### Gravity wave event pressure traces

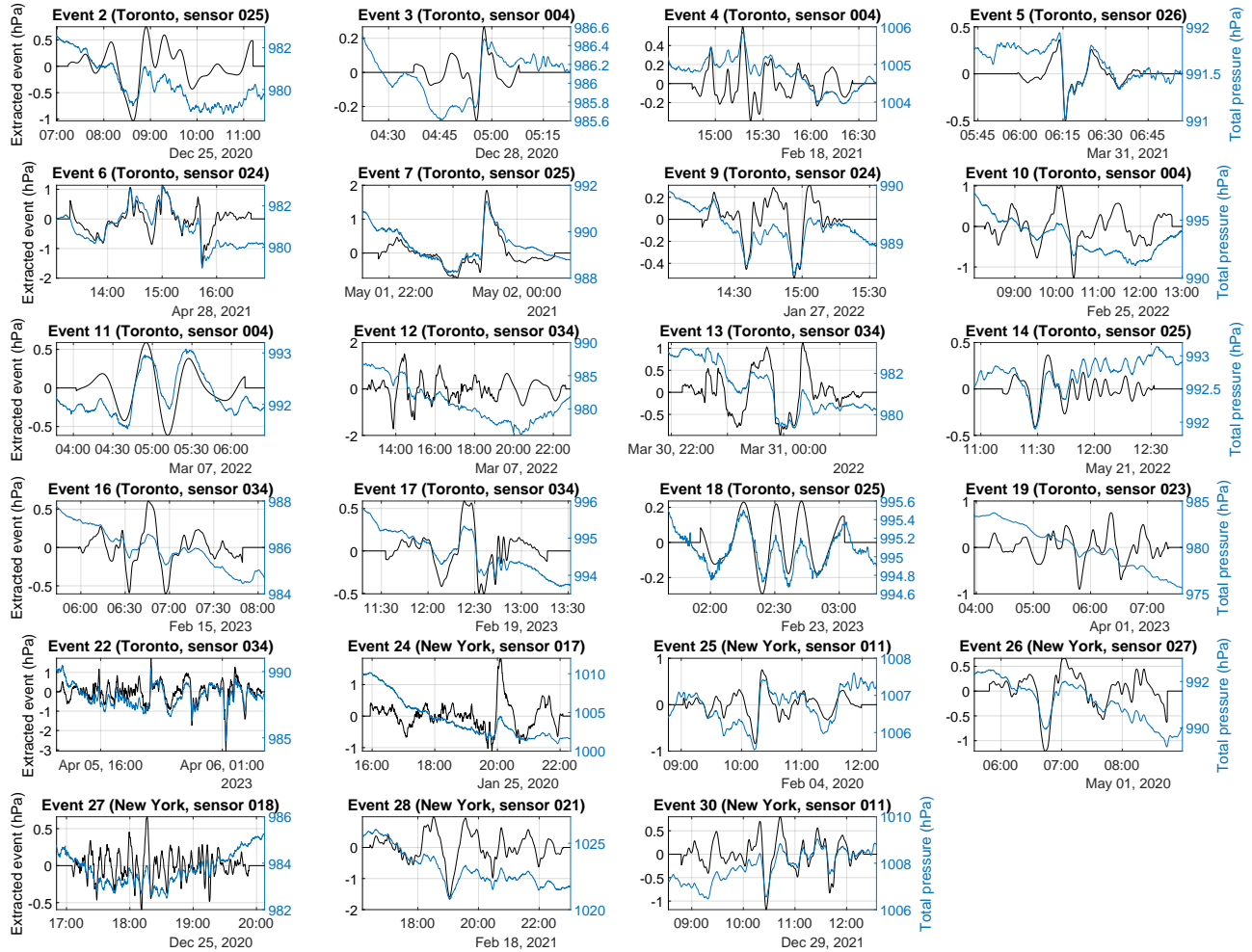


Figure 3.6: Extracted pressure wave event (black, left axes) and total pressure (blue, right axes) time series for the 23 gravity wave events. The ordering and numbering of wave events matches that in Table 3.2. For each gravity wave event, data from only a single sensor are shown. That sensor was chosen to maximize its optimal cross-correlation values with extracted event traces from other sensors which captured a given gravity wave event.

event (e.g., events 11 and 18). The gravity wave events had a wide range of durations, wave amplitudes, and wavelengths (Fig. 3.5). Event duration varied over a wide range. Event 5 was a solitary wave of depression with a duration of roughly 1 hour. Event 22 had a duration of nearly 20 hours.

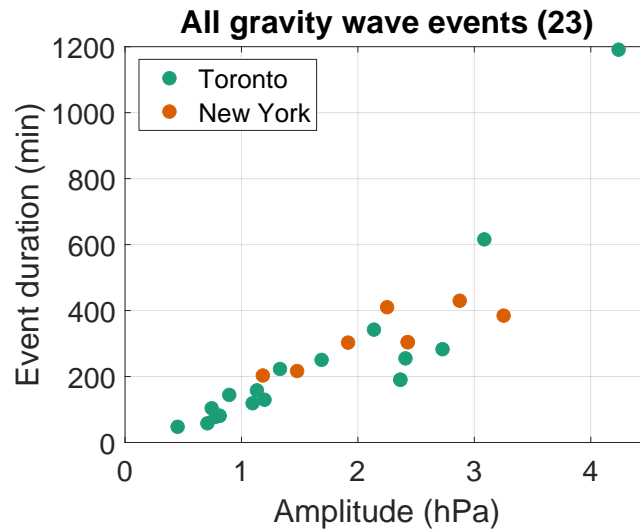


Figure 3.7: Scatter plot of wave amplitude against event duration for the 23 gravity wave events. Green points represent gravity wave events in Toronto, and orange points represent events in New York and Long Island.

For the 23 gravity wave events, a strong linear correlation between wave amplitude and event duration was found ( $R = 0.88$ ,  $p$ -value:  $3.2 \times 10^{-8}$ , Fig. 3.7). A simple linear regression suggests that a 1 hPa increase in amplitude corresponds roughly to a 170 min increase in event duration. It is possible that part of this correlation is due to the event extraction method. Testing on synthetic events with constant duration (not shown) showed that the higher-amplitude waves result in more residual wavelet signal extending beyond the given event duration. Given the large range of event durations over which this correlation holds, there is likely some physical meaning to the relationship. A similar relationship has been documented in seismic waves: higher-magnitude earthquakes tend to have longer durations (e.g., Trifunac and Brady 1975; Herrmann 1975), which can be explained by the stronger earthquakes propagating over larger areas of fault surfaces (e.g. Bonilla et al. 1984; Wells and Coppersmith 1994) and thus having larger source areas. This raises the question of whether higher-amplitude gravity waves have larger source areas, which is not possible to adequately answer with the data used in this study.

## Relating pressure perturbations to vertical parcel displacements for gravity waves

To give further context to the pressure perturbations associated with gravity waves, we can compute the vertical parcel perturbation for a case in which representative sounding data are available. The sounding launched at KBUF during Event 10 in Toronto on 25 February 2022 is useful for this as there is a clear gravity wave ducting layer in that example (Fig. 2.9). Equation 68-3 from Gossard and Hooke (1975) relates the pressure perturbation ( $P_0$  in Pa) to the vertical parcel displacement ( $\zeta_H$  in m) for a given gravity wave ducting layer depth ( $H$  in m):

$$\zeta_H = \frac{H}{\rho_s \left(\frac{\omega}{k}\right)^2} B P_0 \quad (3.11)$$

where  $\rho_s$  is the surface air density ( $1.225 \text{ kg m}^{-3}$  for this example),  $\omega$  is the intrinsic angular wave frequency (in  $\text{s}^{-1}$ ), and  $k$  is the horizontal wavenumber (in  $\text{m}^{-1}$ ).  $\omega$  and  $k$  are calculated by:

$$\omega = \frac{2\pi}{\tau} - u_0 k \quad (3.12)$$

$$k = \frac{2\pi}{\lambda} \quad (3.13)$$

where  $\tau$  is the wave period (1222 s for this example; Table 3.2),  $u_0$  is the mean wind speed within the wave duct ( $18.9 \text{ m s}^{-1}$  for this example), and  $\lambda$  is the wavelength (55.5 km for this example; Table 3.2). For this example,  $\omega = 0.003 \text{ s}^{-1}$  and  $k = 0.11 \text{ km}^{-1}$ . The calculation of  $B$  depends on the Brunt-Väisälä frequency ( $N$  in  $\text{s}^{-1}$ ). The wave duct is saturated for this example (Fig. 2.9), so we calculate the moist Brunt-Väisälä frequency  $N_m$  (Markowski and Richardson 2010, p. 42):

$$N_m = \sqrt{\frac{g}{\theta_{e0}} \frac{\Gamma_m}{\Gamma_d} \frac{\partial \theta_e}{\partial z}} \quad (3.14)$$

where  $g$  is the gravitational acceleration ( $\sim 9.81 \text{ m s}^{-2}$ ),  $\theta_{e0}$  is the mean equivalent potential temperature in the wave duct (294.7 K for this example),  $\Gamma_m$  is the moist adiabatic lapse rate in the wave duct ( $7.58 \text{ K km}^{-1}$  for this example),  $\Gamma_d$  is the dry adiabatic lapse rate ( $9.76 \text{ K km}^{-1}$ ), and  $\frac{\partial \theta_e}{\partial z}$  is the change in equivalent potential temperature with height in the wave duct ( $20.2 \text{ K km}^{-1}$  for this example). For this example,  $N_m = 0.023 \text{ s}^{-1}$ . We also need the vertical wavenumber  $n_1$  (in  $\text{m}^{-1}$ ) to calculate  $B$ .  $n_1$  is calculated by:

$$n_1 = k \sqrt{\frac{N_m^2}{\omega^2} - 1} \quad (3.15)$$

For this example,  $n_1 = 0.853 \text{ km}^{-1}$ . Since  $\omega < N_m$ ,  $B$  is calculated by (Gossard and Hooke 1975):

$$B = \frac{\sin(n_1 H)}{n_1 H} \quad (3.16)$$

For this example,  $B = 0.656$ . Finally, the peak-to-trough amplitude of the gravity wave was  $\sim 2 \text{ hPa}$  for Event 10 (Table 3.2), so we take half of that,  $1 \text{ hPa}$ , as the pressure perturbation  $P_0$ , so the vertical parcel displacement  $\zeta_H = 129 \text{ m}$  for this example. This result is on a similar order of magnitude to the vertical displacements reported by (Kjelaas et al. 1974, 50-120 m) and (Allen et al. 2013, 400 m).

### **Synoptic context for gravity wave events**

The synoptic environment setting for each of the 23 gravity wave events that occurred during our 40 months of analysis (Table 3.3) puts these events in context and permits comparisons to previous case studies and theoretical work. For each gravity wave event, we examined surface pressure and equivalent potential temperature (Fig. 3.8), 300 hPa geopotential heights and wind speeds (Fig. 3.9), and 300 hPa  $\Delta NBE$  (Fig. 3.10). For a gravity wave to be detected at the surface, there needs to be suitable conditions for the wave signal to reach the surface (e.g., there should ideally be no convective overturning in the boundary layer which would obscure the pressure signal due to the gravity wave).

Surface low center cyclone tracks for storms which produce snowfall in the Northeast United States are most common near the coast and over the Atlantic Ocean, to the east of New York City and Toronto (Fig. 3.11). As regards suitable near surface conditions for gravity waves, of the 23 gravity wave events in Toronto and New York during our 40-month analysis period, 13 (57%) occurred north or east of a surface low (events 3, 4, 10, 11, 12, 13, 16, 17, 18, 19, 22, 24, and 28), often on the cool side of warm or stationary fronts. Event 22 had such a long duration that it began when Toronto was on the cool side of a warm front and ended after the warm front had passed. Event 25 and 30 occurred very far (2000 km or more) to the east of a surface low and on the cool side of an air mass boundary. Event 2 occurred behind a cold front and to the west of a surface low. Event 6 occurred near a weak surface low and just on the cool side of an air mass boundary. Events 5, 9, and 27 occurred south of lows. Event 26 occurred near a weak air mass boundary with lows both to the north and the south.

Inversion layers at altitudes  $< 1 \text{ km}$  were found in all of the 12 gravity wave events when upper air soundings were launched either during or within 2 hours of the events (Figure 3.12). Event 22 had two radiosonde launches. Many of the inversion layers were only 100-200 m deep. Events 6, 17, 22, and 25 had an inversion layer adjacent to the surface. A near surface stable layer likely helps to maintain the coherence of the gravity wave signal across the network of

Table 3.3: Environmental context for the 23 gravity wave events detected over the 40 month analysis period. The leftmost column is an index column, aligned with the index column in Table 3.2. Here, the position of wave events relative to the low and to air mass boundaries was determined based on manual analysis of  $\theta_e$  and MSLP maps derived from ERA5 data at the center time of the event (Fig. 3.8). If no air mass boundary could be discerned near Toronto or New York for an event, then we consider it "Unclear" whether that event occurred in the cold sector or warm sector. Events 25 and 30 occurred roughly 2000 km or more to the east of the nearest cyclone, as indicated in the table and the text.

	Event start (UTC)	Warm/cold sector	Low-relative position	300 hPa context
2	2020-12-25 0709	Cold sector	West of low	Downstream of trough
3	2020-12-28 0437	Unclear	East of low	Downstream of trough
4	2021-02-18 1418	Cold sector	North of low	Downstream of trough
5	2021-03-31 0543	Warm sector	South of low	Downstream of trough
6	2021-04-28 1213	Cold sector	Low-adjacent	Near ridge axis
7	2021-05-01 2140	Unclear	No closed low	Upstream of trough
9	2022-01-27 1415	Unclear	South of low	Zonal flow
10	2022-02-25 0816	Cold sector	North of low	Downstream of trough
11	2022-03-07 0352	Cold sector	Northeast of low	Zonal flow
12	2022-03-07 1221	Cold sector	North of low	Downstream of trough
13	2022-03-30 2118	Cold sector	East of low	Near ridge axis
14	2022-05-21 1110	Warm sector	No closed low	Downstream of trough
16	2023-02-15 0550	Cold sector	East of low	Downstream of trough
17	2023-02-19 1106	Unclear	Southeast of low	Zonal flow
18	2023-02-23 0139	Cold sector	Northeast of low	Zonal flow
19	2023-04-01 0357	Cold sector	East of low	Near ridge axis
22	2023-04-05 0809	Warm sector	Southeast of low	Downstream of trough
24	2020-01-25 1544	Cold sector	Northeast of low	Downstream of trough
25	2020-02-04 0824	Cold sector	East of low (far)	Zonal flow
26	2020-05-01 0435	Cold sector	Between lows	Downstream of trough
27	2020-12-25 1629	Cold sector	South of low	Downstream of trough
28	2021-02-18 1556	Cold sector	North of low	Downstream of trough
30	2021-12-29 0755	Cold sector	East of low (far)	Zonal flow

### 2-meter $\theta_e$ and MSLP for gravity wave events

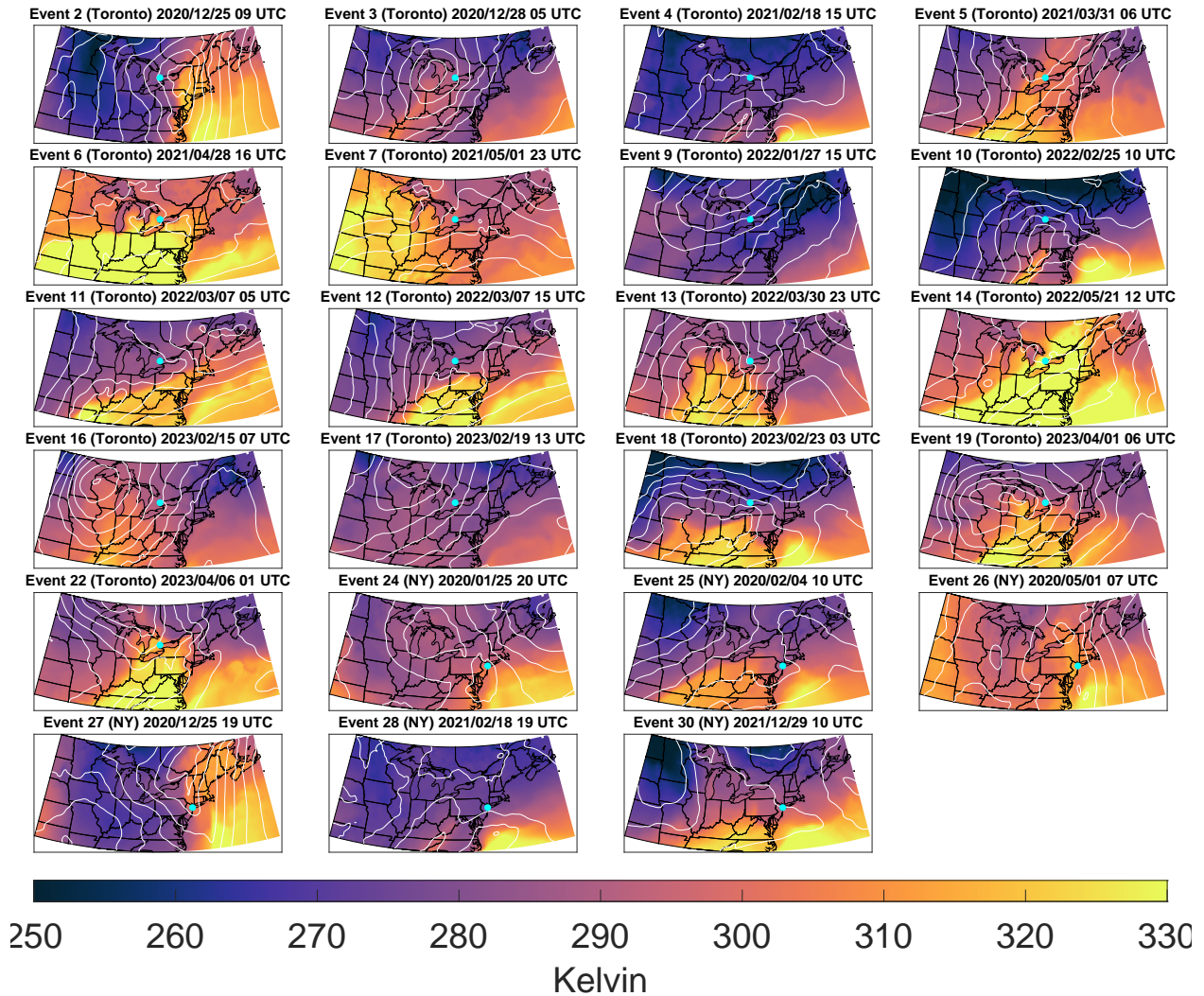


Figure 3.8: ERA5 2 m equivalent potential temperature maps for all of the detected gravity wave events, at the center time of each event. The ordering and numbering of events matches that in Table 3.2. MSLP is contoured in white every 5 hPa. In each panel, either New York or Toronto are shown by cyan points, depending on where the gravity wave event occurred.

### 300 hPa wind speed and geopotential height for gravity wave events

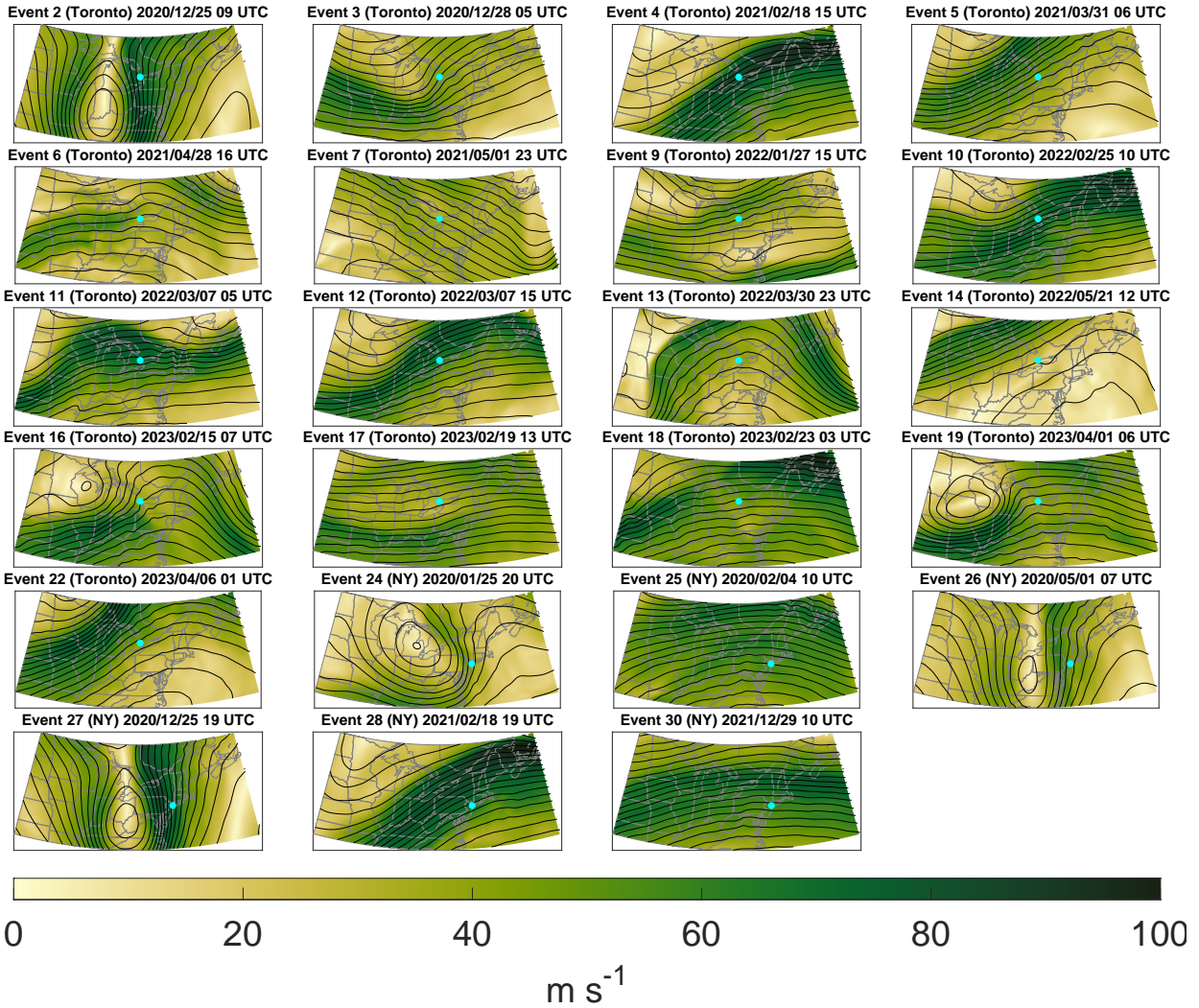


Figure 3.9: ERA5 300 hPa wind speed maps for all of the detected gravity wave events, at the center time of each event. The ordering and numbering of events matches that in Table 3.2. 300 hPa geopotential height is contoured in black every 50 m. In each panel, either New York or Toronto are shown by cyan points, depending on where the gravity wave event occurred.

### 300 hPa $\Delta$ NBE for all November-April wave events

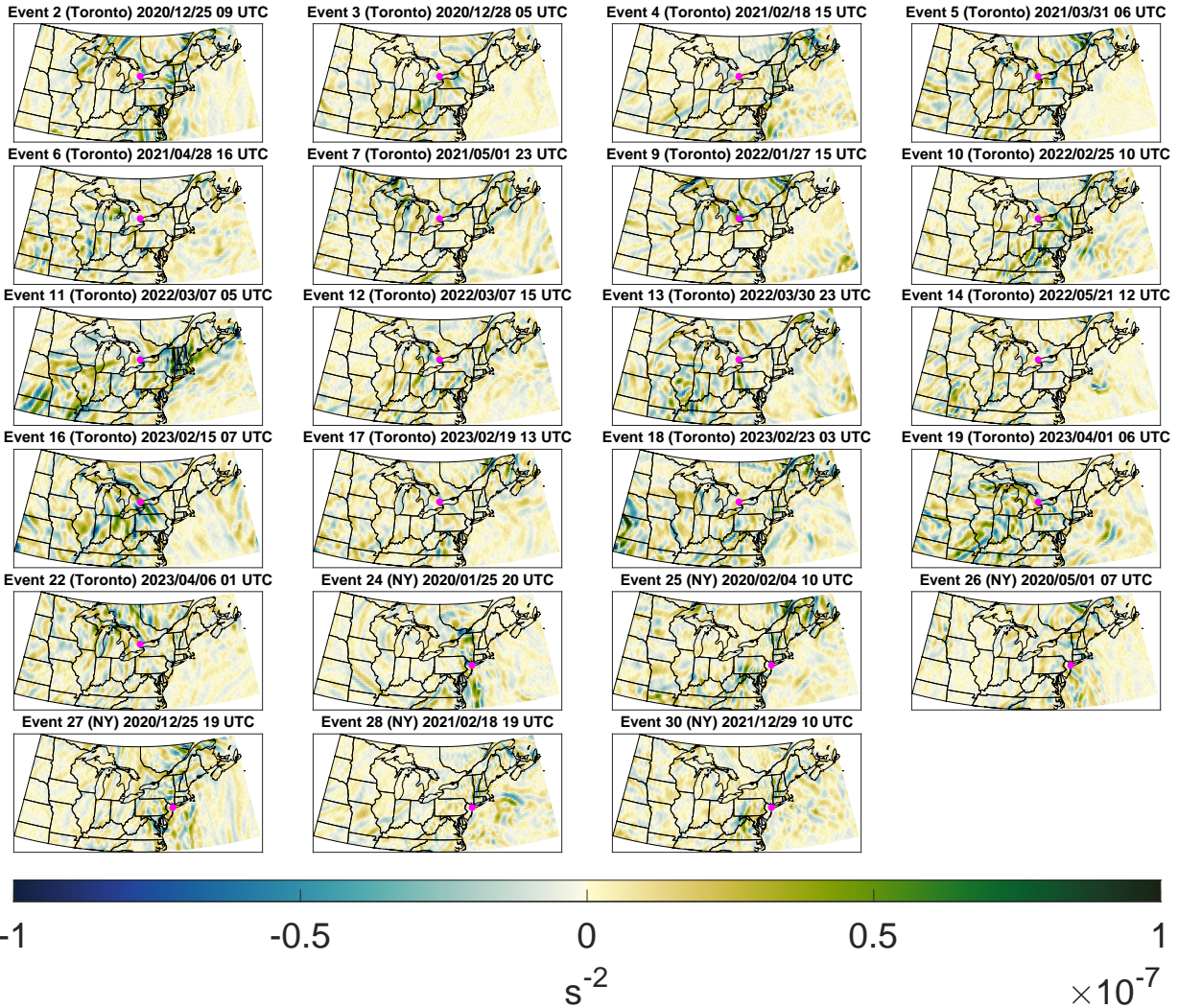


Figure 3.10: ERA5 300 hPa  $\Delta$ NBE maps for all of the detected gravity wave events, at the center time of each event. The ordering and numbering of events matches that in Table 3.2. In each panel, either New York or Toronto are shown by magenta points, depending on where the gravity wave event occurred.

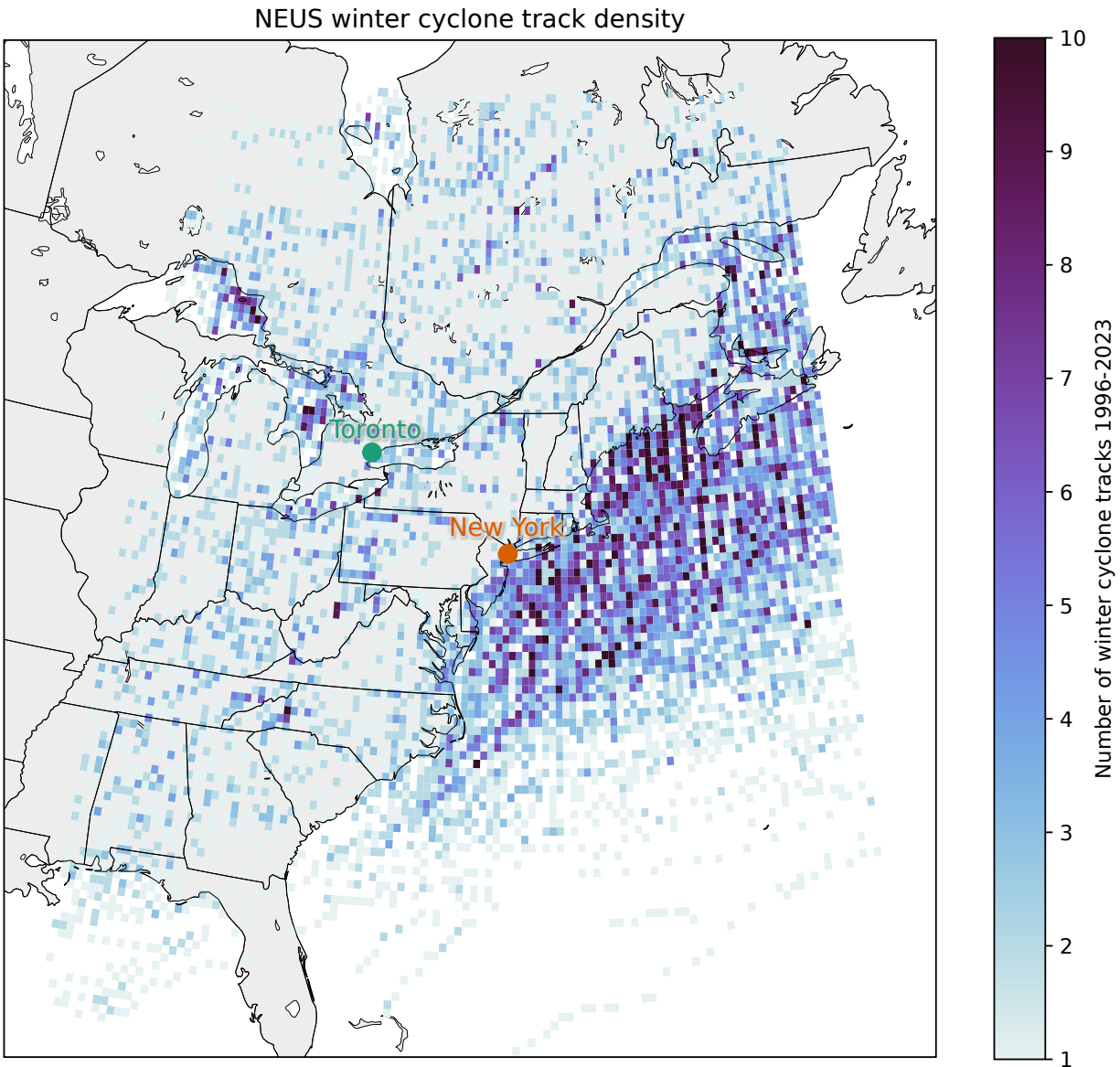


Figure 3.11: Cyclone track density (shading) for storms in the Northeast United States (NEUS) which brought at least 1 in of snowfall in a 24 hour period to at least two ASOS stations in the NEUS between 1996 and 2023. Cyclones were tracked using ERA5 data following the methodology of Crawford et al. (2021).

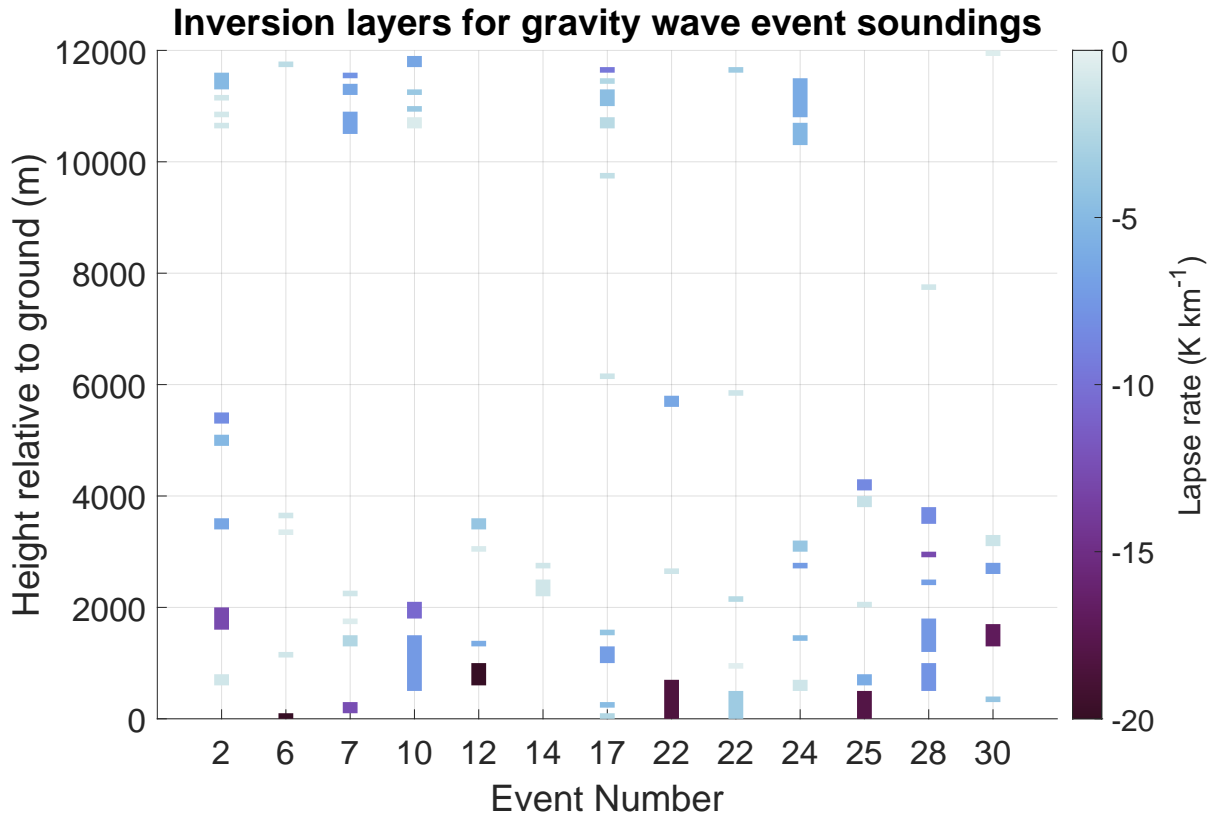


Figure 3.12: Air temperature inversion layers for soundings launched at KBUF for gravity wave events in Toronto, or at KOKX for gravity wave events in New York and Long Island, either during or within 2 hours of a gravity wave event. Inversion layers are colored according to the layer average lapse rate (darker colors indicate a stronger inversion). Event numbering matches that in Table 3.2. Two soundings were launched at KBUF during event 22. Events 2-22 were in Toronto and 24-30 were in NY.

sensors (Uccellini and Koch 1987). Unfortunately, coincident upper air soundings were not available for events 7 and 14 when gravity waves occurred with no closed surface low anywhere in the domain we analyzed (Fig. 3.8).

In terms of the large scale synoptic pattern aloft, 13 gravity wave events occurred downstream of 300 hPa troughs and upstream of 300 hPa ridges (Fig. 3.9, Table 3.3, events 2, 3, 4, 5, 10, 12, 14, 16, 22, 24, 26, 27, and 28), consistent with most gravity wave events shown by Uccellini and Koch (1987). Six others occurred in roughly zonal 300 hPa flow regimes (events 9, 11, 17, 18, 25, and 30), and 3 gravity wave events occurred below a 300 hPa ridge (events 6, 13, 19). One gravity wave event occurred upstream of a 300 hPa trough (event 7).

Regions with large magnitude  $\Delta NBE$ , regardless of sign, imply flow imbalance and the possibility of resulting gravity wave genesis. If gravity waves are triggered by flow imbalance at

300 hPa, they would not necessarily be observed on the ground directly beneath the trigger area as the wave signal must reach the lower troposphere to be observed, which might require the waves to propagate some distance vertically and horizontally. Eighteen of the 23 gravity wave events occurred with large 300 hPa flow imbalance to the south or west (events 2, 3, 5, 6, 7, 9, 10, 11, 13, 14, 16, 18, 19, 22, 24, 25, 27, and 30) (Fig. 3.10). Considering that many of the gravity wave events were observed to propagate from west to east (Fig. 3.5c and Table 3.2), it is plausible that many were triggered by flow imbalance aloft.

In general, previous studies (e.g., Uccellini and Koch 1987; Koch and Dorian 1988) often found mesoscale gravity waves east of surface lows and downstream of upper-level troughs. Our analysis of the 23 gravity wave events in the Toronto and New York metro areas between January 2020 and April 2023 largely agrees with those findings. In such cases, gravity waves may have been triggered by the balance adjustment mechanism described by Zhang et al. (2001). The gravity wave events associated with 300 hPa zonal flow with weak or no flow imbalance in the region were likely associated with different mechanisms, such as localized latent heating or interactions between waves propagating from farther afield (Fritts and Alexander 2003). However, with the available observations and reanalysis data, it is not possible to determine the gravity wave trigger mechanism with complete certainty.

### **Radar echo and precipitation type context for gravity waves**

NWS WSR-88D radar echo corresponds to precipitation-sized particles in the resolution volume. Only within regions with radar echo can enhanced reflectivity features and Doppler velocity waves be detected. Table 3.4 shows the radar echo characteristics and ASOS precipitation type context for each gravity wave event.

Eighteen (78%) of the 23 gravity wave events occurred with precipitation radar echo detected by the nearby WSR-88D in the 0.5° tilt. Only 6 of these cases (events 2, 4, 10, 12, 18, and 28) co-occurred with surface snow or mixtures including snow. Two of those cases with snow occurred with enhanced reflectivity bands within the radar range, but in neither case was the movement of the enhanced reflectivity bands consistent with the gravity wave phase velocity vector. For example, radar data during event 28 indicate there was an enhanced reflectivity feature passing over the pressure sensors, but the movement of the enhanced reflectivity feature (SW to NE) was not consistent with the phase direction of the gravity waves (NW to SE) (Fig. 3.13 and Video supplement Animation-Figure-S3.02).

Overall, gravity waves during surface snow were rare at our locations. Periods of snowfall at a rate of at least 0.1 mm hr<sup>-1</sup> (liquid equivalent) for at least 4 hours, with at most a one-hour gap without that rate of snowfall, occurred 59 times in Toronto and 20 times in New York during our analysis period. Fifty-one of those 59 snow storms in Toronto, and 16 of the 20 in New

Table 3.4: Radar and precipitation context for the 23 gravity wave events detected during our 40 month analysis period. The leftmost column is an index column, aligned with the index column in Table 3.2. The presence of surface snow was determined using the nearest available ASOS data (CYYZ or KJFK). Echo, reflectivity bands, and Doppler velocity waves are considered "present" when they exist anywhere within the range of the 0.5° scan for the nearest NEXRAD radar (KBUF or KOKX). Reflectivity bands and Doppler velocity waves are considered "collocated" when they are located directly above pressure sensors and their movement is consistent with the gravity wave phase velocity.

	Event Start	Echo Present	Surface Snow	Surface Rain	Reflectivity Band(s) Present	Reflectivity Band(s) Collocated	Doppler Velocity Wave(s) Present	Doppler Velocity Wave(s) Collocated
2	2020-12-25 0709	Yes	Yes	No	No	No	Yes	Yes
3	2020-12-28 0437	Yes	No	Yes	No	No	Yes	No
4	2021-02-18 1418	Yes	Yes	No	No	No	Yes	No
5	2021-03-31 0543	Yes	No	Yes	No	No	No	No
6	2021-04-28 1213	No	No	No	No	No	No	No
7	2021-05-01 2140	Yes	No	Yes	No	No	Yes	No
9	2022-01-27 1415	No	No	No	No	No	No	No
10	2022-02-25 0816	Yes	Yes	No	No	No	Yes	No
11	2022-03-07 0352	No	No	No	No	No	No	No
12	2022-03-07 1221	Yes	Yes	No	Yes	No	Yes	No
13	2022-03-30 2118	Yes	No	Yes	No	No	No	No
14	2022-05-21 1110	No	No	No	No	No	No	No
16	2023-02-15 0550	Yes	No	Yes	No	No	No	No
17	2023-02-19 1106	No	No	No	No	No	No	No
18	2023-02-23 0139	Yes	Yes	No	No	No	Yes	No
19	2023-04-01 0357	Yes	No	Yes	Yes	No	Yes	Yes
22	2023-04-05 0809	Yes	No	Yes	Yes	Yes	Yes	No
24	2020-01-25 1544	Yes	No	Yes	Yes	Yes	Yes	Yes
25	2020-02-04 0824	Yes	No	Yes	No	No	No	No
26	2020-05-01 0435	Yes	No	Yes	Yes	Yes	Yes	No
27	2020-12-25 1629	Yes	No	Yes	No	No	No	No
28	2021-02-18 1556	Yes	Yes	No	Yes	No	Yes	Yes
30	2021-12-29 0755	Yes	No	Yes	No	No	Yes	Yes
Total Yes		18	6	12	6	3	13	5

18 Feb 2021 18:33:06 UTC  
KOKX 0.5° tilt

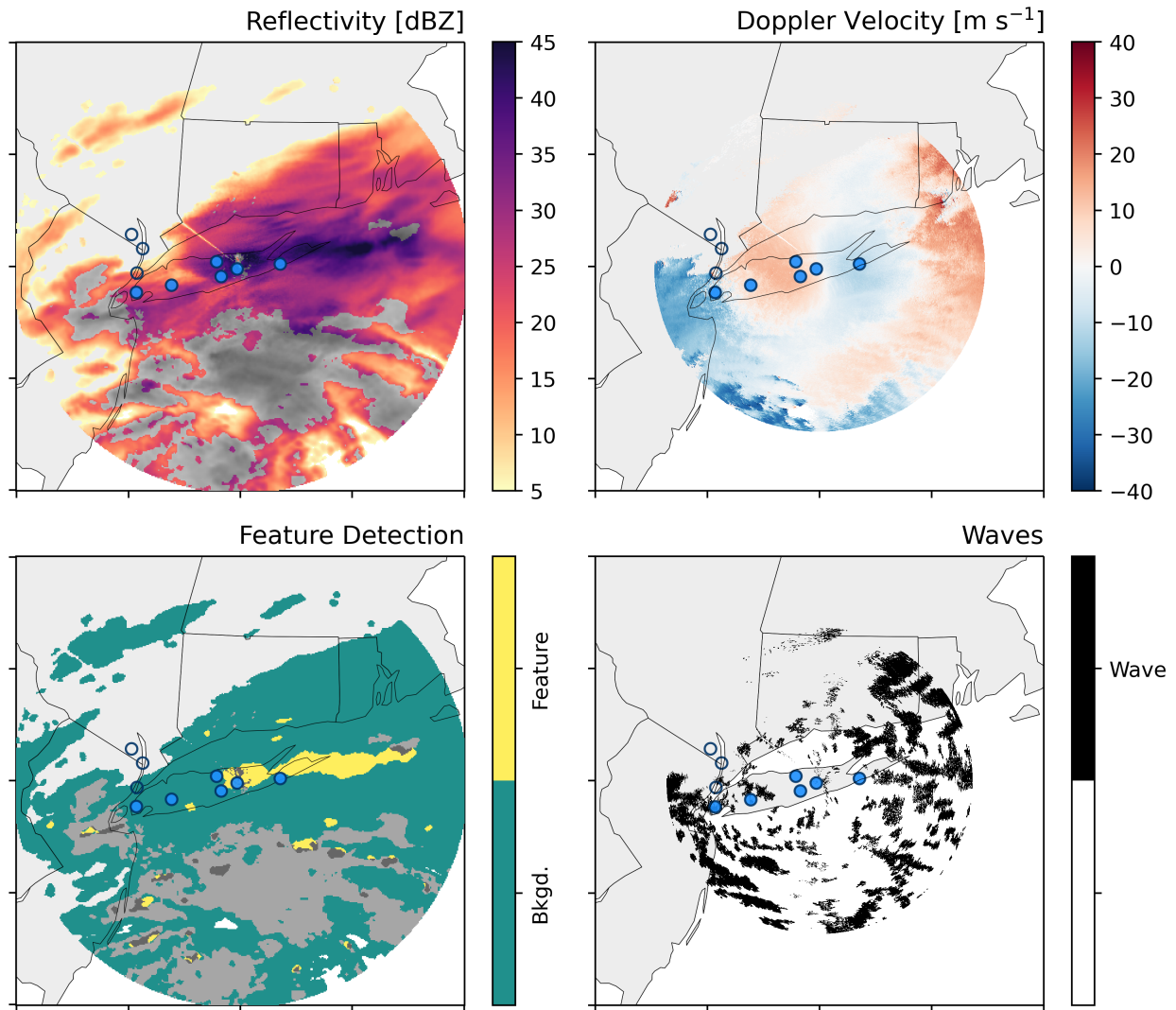


Figure 3.13: As in Fig. 3.4, but for KOKX at 18:30 UTC on 18 February 2021, during event 28 (gravity wave event). In this example, an elongated enhanced reflectivity feature passed over the pressure sensor network from SW to NE during the wave event, which was inconsistent with the gravity wave phase direction (NW to SE). An animated version of this figure is available in the Video Supplement Animation-Figure-S3.02.

Table 3.5: Hours with and without gravity wave events subdivided by ASOS precipitation data during the November to May months between January 2020 and April 2023. Precipitation is determined to be present when there was  $\geq 0.1 \text{ mm hr}^{-1}$  liquid equivalent precipitation was recorded at Toronto (CYTZ precipitation type and CXTO precipitation amount) and at New York (KJFK precipitation type and amount). Hours with either only snow or a mixture of precipitation types containing snow are included under hours with snow.

<b>Toronto</b>	Hours with snow	Hours with other precip	Hours with no precip	Total
Hours with gravity wave events	15	23	48	86
Hours without gravity wave events	445	1172	16214	17831
Total	460	1195	16262	17917
<b>New York</b>	Hours with snow	Hours with other precip	Hours with no precip	Total
Hours with gravity wave events	4	20	13	37
Hours without gravity wave events	130	1308	16538	17976
Total	134	1328	16551	18013

York, occurred between November and February, mostly before the peak in gravity wave events (February-May; Fig. 3.5a). In the Toronto area, there were 460 hours with at least  $0.1 \text{ mm hr}^{-1}$  (liquid-equivalent) of snow recorded. Of those, only 15 hours with snow were during a gravity wave event. In the New York area, snow was recorded for 134 hours of which only 4 occurred during gravity wave events (Table 3.5).

When surface rain was present, 3 gravity wave cases (events 22, 24, and 26) had enhanced reflectivity features collocated and moving at a velocity consistent with the pressure waves. During event 22, an elongated reflectivity feature crossed the pressure sensor network and appeared to move at a velocity consistent with the gravity wave phase velocity (Fig. 3.14, and Video supplement Animation-Figure-S3.03). The reflectivity band was an isolated feature lasting only 2 hours in a wave event which lasted nearly 20 hours. Event 24 occurred along with an occluded front which passed over the pressure sensor network at 20 UTC on 25 Jan 2020. We chose to categorize event 24 as a gravity wave rather than a "front" event because of the pressure oscillations observed in the hours before the occluded front passage (Fig. 3.6). During event 26, a narrow region of enhanced reflectivity on the trailing edge of a broader precipitation region passed over the pressure sensors in New York near the same time as a large pressure minimum (6:45 UTC on 1 May 2020; Fig. 3.6).

Depending on the spatial scale of gravity waves and the height and depth of the wave duct as well as their 3D position relative to the slanting WSR-88D scans, the transient convergence and divergence signals associated with the gravity wave's propagating upward and downward motions may or may not yield radar detectable Doppler velocity waves. Hence, we do not expect a 1:1 correspondence between detected gravity waves and detected Doppler velocity waves in the  $0.5^\circ$  elevation angle scan.

05 Apr 2023 19:30:05 UTC  
KBUF 0.5° tilt

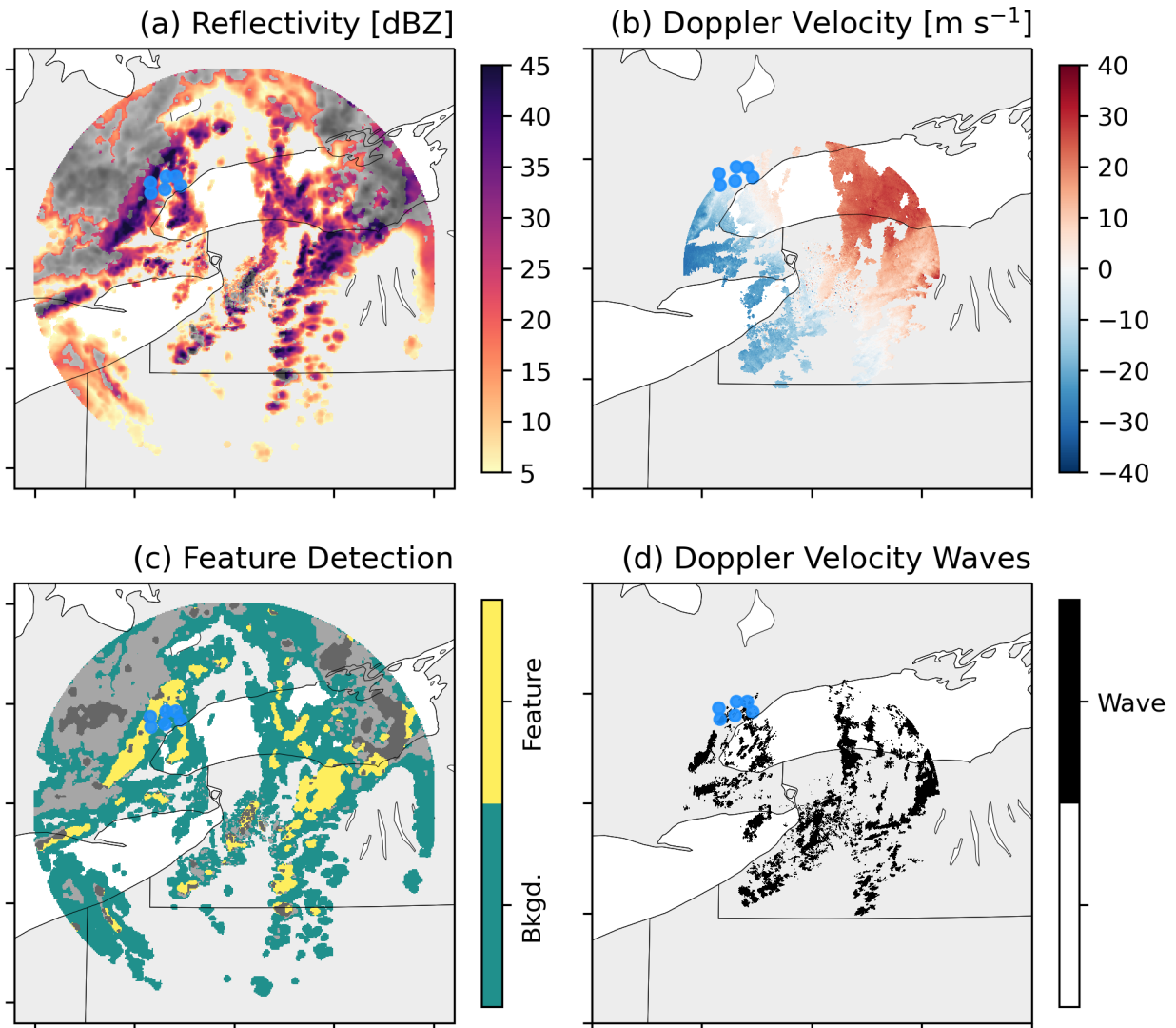


Figure 3.14: As in Fig. 3.4, but for KBUF at 19:30 UTC on 5 April 2023 during event 22 (gravity wave event). In this example, gravity waves moved from NW to SE while an elongated enhanced reflectivity feature is passing over the pressure sensors in Toronto from west to east. An animated version of this figure is available in the Video Supplement Animation-Figure-S3.03.

Thirteen gravity wave events of the 18 gravity waves with radar echo occurred with coherently moving Doppler velocity waves present anywhere within the range of the nearby WSR-88D radar. But, only five of these had Doppler velocity waves over the pressure sensors moving at a velocity consistent with the gravity wave phase velocity (Table 3.4). Based on this limited evidence, a subset of gravity waves may manifest a Doppler velocity wave signature. Figure 2.2 and Eq. 2.2 suggest that any gravity wave which produces a pressure perturbation  $\geq 0.5$  hPa should also produce a detectable velocity wave signal. The velocity waves may not appear in radar Doppler velocity data either because they are above or below the height of the radar beam, or because there is strong turbulence which obscures the signal associated with gravity waves. In Toronto, the KBUF radar beam is at a higher altitude than the KOKX radar beam is at over New York, and 3 of the 5 gravity wave events with corresponding Doppler velocity waves occurred in the New York pressure sensor network.

The Doppler velocity wave detection works best for waves which propagate less than half of their wavelength between successive radar scans (Miller et al. 2022), i.e., which have a wave period at least twice as long as the time between successive radar scans. Typical NEXRAD volume coverage patterns have a  $\sim 4$ -8 minute time between  $0.5^\circ$  elevation scans, and 12 of the 18 gravity wave events which co-occurred with radar echo had a wave period of 16:39 or less. Only 2 of those 12 gravity wave events were collocated with Doppler velocity waves which propagated at a velocity consistent with the gravity wave phase velocity. Of the 6 gravity wave events with a wave period longer than 16:39 that co-occurred with radar echo, 3 were collocated with Doppler velocity waves which propagated at a velocity consistent with the gravity wave phase velocity.

### 3.4 Conclusions

We deployed two air pressure sensor networks, one in Toronto, ON, Canada, and the other in the New York City area and Long Island, NY, USA, to study atmospheric gravity waves. In over 3 years of data, we objectively identified 33 pressure wave events which were observed by at least 4 pressure sensors and for which there was reasonable confidence in the estimate of the wave phase velocities. Our study examined wave amplitudes on the order of 0.5-5 hPa and wave periods on the order of 2-67 min. These spatial and temporal scales were chosen to align with the spatial and temporal scales of radar-observed enhanced reflectivity bands and Doppler velocity waves, both of which were surmised to potentially be related to gravity waves (Hoban 2016; Miller et al. 2022).

A few of our detected pressure wave events were associated with frontal passages (5), outflows (4), and a wake low (1), and the remaining 23 were gravity waves, 20 of which occurred

in the cool season between November and April. For context, there were 20 snow storms in the New York and 59 in the Toronto metropolitan areas over our 40 month observation period. While limited, the evidence we have suggests a both a lack of a common associations between reflectivity bands and gravity waves and between Doppler velocity waves and gravity waves. Just 6 of the gravity wave events co-occurred with any surface snowfall (including trace amounts). Only 2 of those 6 events had any enhanced reflectivity bands in the vicinity. The spatial wavelengths of the gravity waves and enhanced reflectivity bands were similar, but in all the cases with snow, the reflectivity bands were either not directly over the pressure sensors or not moving at a velocity consistent with the pressure waves (Table 3.4). A subset of our detectable gravity waves (5 of 18 gravity waves with radar echo in vicinity) may have manifested a detectable Doppler velocity wave signature in NEXRAD data but most did not.

While the observational and reanalysis output data used cannot confirm the cause of gravity wave genesis, most gravity wave events occurred with strong upper-level flow imbalance to the south or west of their location, suggesting that the mechanism of balance adjustment described by Zhang (2004) and Ruppert et al. (2022) may be relevant. The occurrence of several gravity waves downstream of an upper level trough, on the cool side of air mass boundaries, and with a temperature inversion in the lowest 1 km above ground level is consistent with the findings of Uccellini and Koch (1987).

We found a strong linear relationship between amplitude and event duration for the 23 atmospheric gravity wave events detected (Fig. 3.7). A potential explanation could be that parcels in gravity waves triggered by a larger initial perturbation might oscillate for a longer time before returning to an equilibrium state. Further exploration of the relationship between gravity wave amplitude and duration is a topic for future research. There may be an analogy to seismic waves in that higher-amplitude earthquakes tend to have longer durations because of the larger rupture area along the fault (Trifunac and Brady 1975; Herrmann 1975).

Satellite images of northeast US winter storms often show undulations in the overlying cirrus. These undulations may be either Kelvin-Helmholtz waves or gravity waves. Kelvin-Helmholtz waves on horizontal scales of  $\sim 3$  km could locally alter the cloud microphysical properties (Houser and Bluestein 2011). The surface pressure should reflect changes throughout the column of air, including gravity waves aloft. However, it is possible that gravity waves in the upper cloud layers with periods between 3 and 67 min do occur but have their surface pressure signals obfuscated by other perturbations. For example, if there is an unstable layer below the layer with the gravity waves, then the pressure wave amplitude at the surface would be reduced and obfuscated by pressure perturbations due to convective overturning (Kjelaas et al. 1974). Wind profiler data would help to resolve whether conditions for Kelvin-Helmholtz waves are present within the cirrus layer.

For the New York City area in particular, the low frequency of occurrence of gravity waves in winter storms is influenced in part by a sample bias related to the typical position of low pressure centers off-shore. The New York City metropolitan area and Long Island are usually in the northwest quadrant of the storm where gravity waves are not often found (Fig. 3.11). In both Toronto and New York, most snow storms  $\geq 4$  h in duration occurred between December and February, while most gravity waves were detected between February and May (Fig. 3.5a).

Whereas previous case study work examined heavy snow events that had gravity waves, we cast a broad net by putting out pressure sensor networks for an extended time period to see what we could "catch". Some of the previously studied winter storm gravity wave cases (e.g., Bosart et al. 1998) are clearly not representative of typical flat-land winter storms in the Northeast US, since of the 79 winter storms with snow that occurred over our 40 months of observations, only 6 had detectable gravity waves. It is well established that gravity waves can locally increase precipitation (e.g., Bosart et al. 1998; Gaffin et al. 2003; Colle 2004; Allen et al. 2013; Kingsmill et al. 2016). But, if gravity waves of a sufficient amplitude do not occur then they are irrelevant to locally increasing snow rates. Our findings suggest that gravity waves of amplitude  $\geq 0.5$  hPa are much less common in winter storms than reflectivity features on similar spatial and temporal scales, which are present in most winter storms (Hoban 2016; Ganetis et al. 2018).

**Video supplement** All animations can be viewed at: <https://av.tib.eu/series/1721/video+supplement+to+objectively+identified+mesoscale+surface+air+pressure+waves+in+the+context+of+winter+storm+environments+and+radar+reflectivity+features+a+3+year+analysis>. Individual animations can be viewed by following the DOI URL.

Animation-Figure-S3.01: Animated maps of **(a)** reflectivity, **(b)** Doppler velocity, **(c)** enhanced reflectivity feature detection and **(d)** Doppler velocity wave detection for NWS WSR-88D radar data from Buffalo, NY, at  $0.5^\circ$  tilt, from 04:00 UTC to 11:05 UTC on 1 April 2023. In **(a)** and **(c)**, values are shown in greyscale when there is likely enhancement due to melting (Tomkins et al. 2022). Filled blue circles indicate locations of pressure sensors which captured pressure wave event 15, and unfilled blue circles indicate locations of pressure sensors which did not capture the pressure wave event. This animation goes with Fig. 3.4. Title: 2023/04/01 KBUF radar 4-panel animation. <https://doi.org/10.5446/67635> (Allen et al. 2024b).

Animation-Figure-S3.02: Animated maps of **(a)** reflectivity, **(b)** Doppler velocity, **(c)** enhanced reflectivity feature detection and **(d)** Doppler velocity wave detection for NWS WSR-88D radar data from Upton, NY, at  $0.5^\circ$  tilt, from 15:59 UTC to 22:26 UTC on 18 February 2021. In **(a)** and **(c)**, values are shown in greyscale when there is likely enhancement due to melting

(Tomkins et al. 2022). Filled blue circles indicate locations of pressure sensors which captured pressure wave event 26, and unfilled blue circles indicate locations of pressure sensors which did not capture the pressure wave event. This animation goes with Fig. 3.13. Title: 2021/02/18 KOKX radar 4-panel animation. <https://doi.org/10.5446/67765> (Allen et al. 2024a).

Animation-Figure-S3.03: Animated maps of **(a)** reflectivity, **(b)** Doppler velocity, **(c)** enhanced reflectivity feature detection and **(d)** Doppler velocity wave detection for NWS WSR-88D radar data from Upton, NY, at 0.5° tilt, from 07:49 UTC on 5 April 2023 to 04:00 UTC on 6 April 2023. In **(a)** and **(c)**, values are shown in greyscale when there is likely enhancement due to melting (Tomkins et al. 2022). Filled blue circles indicate locations of pressure sensors which captured pressure wave event 18, and unfilled blue circles indicate locations of pressure sensors which did not capture the pressure wave event. This animation goes with Fig. 3.14. Title: 2023/04/05 KBUF radar 4-panel animation. <https://doi.org/10.5446/67633> (Allen et al. 2024c).

**Code and data availability** Data: The specific data shown in each figure can be found at <https://doi.org/10.5281/zenodo.11286349> (Allen 2024). The pressure time series data used throughout this publication can be found at <https://doi.org/10.5281/zenodo.8136536> (Miller and Allen 2023). The NWS NEXRAD Level-II data used in Figs. 3.4, 3.13 and 3.14 can be accessed from the National Centers for Environmental Information (NCEI) at <https://www.ncei.noaa.gov/products/radar/next-generation-weather-radar> (NOAA National Weather Service Radar Operations Center 1991). The one-minute ASOS data can be accessed from NCEI at <https://www.ncei.noaa.gov/products/land-based-station/automated-surface-weather-observing-systems> (NOAA National Centers for Environmental Information 2021a), and hourly ASOS data can be accessed from NCEP at <https://madis-data.ncep.noaa.gov/>. The radiosonde data used to create Fig. 3.12 can be accessed from NCEI at <https://www.ncei.noaa.gov/products/weather-balloon/integrated-global-rad> (NOAA National Centers for Environmental Information 2021b).

Code: The code used for processing the pressure time series data can be found at <https://doi.org/10.5281/zenodo.8087843> (Allen and Miller 2023).

## CHAPTER

# 4

# BACKGROUND AND METHODS FOR ANALYSIS OF IN SITU OBSERVATIONS OF WINTER STORM CLOUD PROPERTIES

We plan to submit a distilled version of material in this chapter and in Chapter 5 to either *Geophysical Research Letters* or the *Journal of Geophysical Research: Atmospheres*. The dissertation chapters include additional background, details on methods, and related results.

We analyzed in-cloud vertical velocities measured in situ by aircraft-mounted instruments. Our results provide important context for the temporal and spatial scales of ice microphysics processes as well as benchmarks for users and developers of numerical models to assess whether the vertical air motions in winter storm simulations are being represented realistically. Section 4.1 describes the general background and motivation for the in situ vertical velocity analysis. Section 4.1.2 describes previous remote sensing measurements of vertical air motions within winter storms. Section 4.2 describes our data sets in detail along with our analysis methods. In Chapter 5, we present the distributions of in-cloud vertical velocities sampled during IMPACTS and PLOWS including subsets within different temperature and altitudes, and we discuss conclusions and remaining questions. Previous work has examined aircraft in situ vertical air motions in deep convection (e.g. LeMone and Zipser 1980; Yang et al. 2016)

and orographic precipitation (Garvert et al. 2005). To our knowledge, this study is the first comprehensive analysis of in situ measurements of vertical velocity within flat-land winter storms (not orographic, not lake effect).

## 4.1 Background and motivation

The geographic distribution of surface snowfall accumulation is sensitive to the locations of ice mass increases and decreases within winter storms as well as to the trajectories of precipitation-size ice particles. Quantitative precipitation forecasts of snowfall accumulations have large uncertainties often of 100% or more (Novak et al. 2008, 2014, 2023; Greybush et al. 2017; National Weather Service 2018). Vertical air motions and relative humidity control where and when hydrometeors are nucleated, and grow and shrink in size. We examine a large sample size of aircraft in situ data from two recent winter storm field projects, the Investigation of Microphysics and Precipitation for Atlantic Coast-Threatening Snowstorms (IMPACTS, 2020-2023; McMurdie et al. 2022) and the Profiling of Winter Storms (PLOWs, 2009-2010; Rauber et al. 2014) field campaigns which obtained samples in the Northeast and Midwest United States. We analyze vertical air motions with respect to cloud probe and radar-observed structures to yield insights into where ice mass increases are more and less likely to occur within the storm structures and to scrutinize the realism of mesoscale regions of "snow lofting" proposed by Lackmann and Thompson (2019).

A key characteristic of vertical velocity within storms is that it is *spatial scale-variant*. Hence in order to be clearly interpreted, observed and modeled vertical velocities values need to be accompanied by their associated spatial scale. On synoptic ( $> \sim 2000$  km) and larger scales, the atmosphere is very close to hydrostatic balance, meaning that vertical air parcel accelerations are negligible. In winter storms, there might be gradual ascent on the order of a few  $\text{cm s}^{-1}$  when averaging along a warm conveyor belt (100+ km long; Browning 1971a). On convective and smaller scales ( $< \sim 10$  km), the atmosphere is usually not in hydrostatic balance (Markowski and Richardson 2010, p. 9 and Holton and Hakim 2013, p. 44). At these smaller scales, buoyancy, turbulence, and vertical pressure gradients can yield vertical motions of several  $\text{m s}^{-1}$  or more. At a given spatial scale, vertical air motions within winter storms, with the exception of orographic and lake effect snow storms, are usually weaker than those within deep convection.

### 4.1.1 Vertical velocity, snow trajectories, and snow bands

Since winds within precipitating storms were first measured by aircraft probes and Doppler radar it has been recognized that the spatial distribution of surface precipitation is highly

sensitive to the time between when a cloud particle reaches precipitation size and begins to fall and when it reaches the surface (e.g. Smith 1979; Colle and Mass 2000; Colle and Zeng 2004; Colle et al. 2005; Lackmann and Thompson 2019). Longer durations that hydrometeors are in cloud yield more time for horizontal advection. The duration a precipitation-size particle is within cloud has been called the cloud *delay time* and the *residence time* by different authors. We will use "residence time" in this document.

The residence time is a function of the starting altitude where the particle first grows to precipitation-size and starts to fall and the effective fall speeds of the particle along its trajectory. Effective fall speed is the sum of the terminal fall speed of the particle in still air at the relevant air pressure and the vertical air motion. Updrafts will decrease effective fall speed and increase residence time while downdrafts will do the opposite. When the upward air velocity exceeds the terminal fall velocity of precipitation-size hydrometeors, the hydrometeors are lofted upward, prolonging the time it takes for precipitation to fall out of cloud. When the timescale of snow falling to the surface is increased, the lengthening of the snow particle trajectory yields potentially more opportunities for particle growth and/or shrinkage processes to occur.

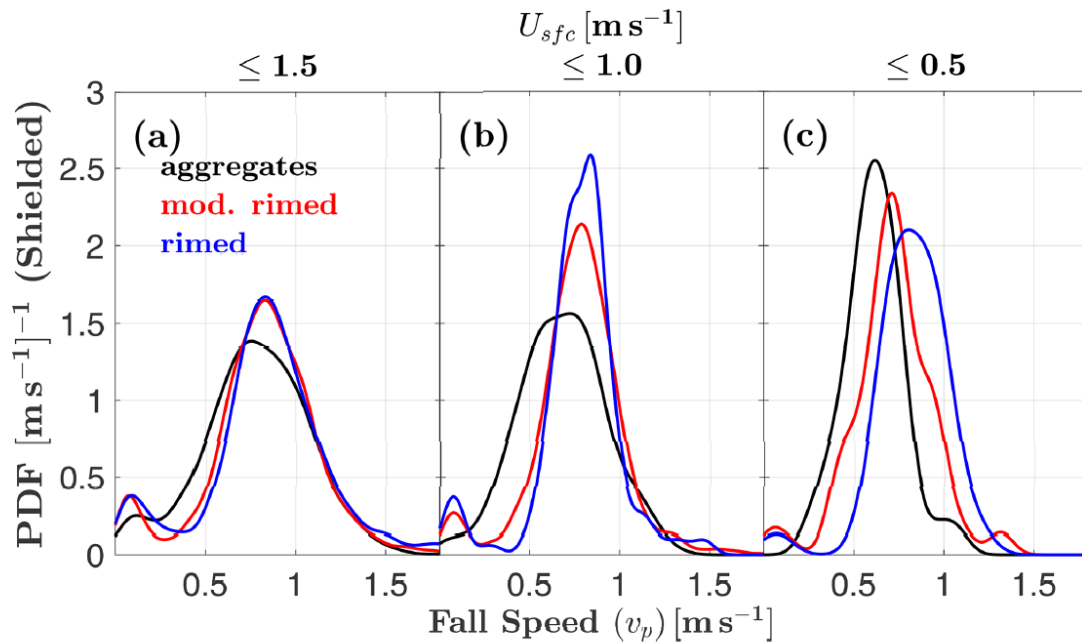


Figure 4.1: Fitch et al. (2021) (their Figure 6). Probability density function of estimates of fall speeds ( $v_p$ ) for sparsely rimed aggregates, moderately rimed particles, and graupel based on observations from a wind-shielded Multi-Angle Snowflake Camera in conditions of light horizontal wind speeds  $U_{sfc}$ .

Fitch et al. (2021) and Garrett and Yuter (2014) used a Multi-Angle Snowflake Camera (MASC) to measure the fall speed distributions of unrimed aggregates, rimed particles, and graupel. Fitch et al. (2021) additionally compared their MASC-measured fall speeds to the Doppler velocities measured by a vertically-pointing Ka-band radar. For aggregates, rimed particles, and graupel of maximum dimension between  $\sim 1$  and 8 mm diameter, fall speeds usually vary between about  $-0.5$  to  $1.5 \text{ m s}^{-1}$ , with the mode of the distribution between  $0.5$  and  $1 \text{ m s}^{-1}$ . The median fall speeds varied slightly dependent on surface wind speed and turbulence. Snow fall speed is only sensitive to particle size in nearly still air (Garrett and Yuter 2014). These high quality measurements show that upward air motions of at least  $0.5 \text{ m s}^{-1}$  are required to loft most precipitation-size ice particles.

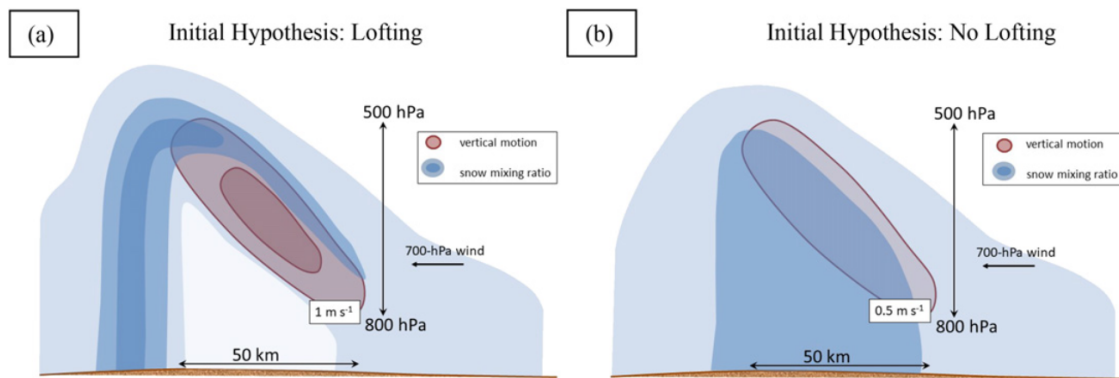


Figure 4.2: Lackmann and Thompson (2019) (their Figure 1) idealized conceptual model illustrating vertical cross-section of vertical air motions and snow water mixing ratios for snow storm structures a) with lofting and b) without lofting of precipitation-size ice. Relative snow mixing ratio shown in blue shading. Vertical velocity shown as dark red shading with contours labeled. In a) vertical velocity contour interval is  $1 \text{ m s}^{-1}$ . Arrows show approximate vertical and horizontal length scales. Estimated aspect ratio of cross-section is 16:1.

For a typical warm front sloped at a grade of  $1/300$  (Markowski and Richardson 2010, p. 122), the horizontal velocity of air impinging on that front would need to be at least  $150 \text{ m s}^{-1}$  in order for the mean vertical velocity caused by the upglide over the front surface to reach  $0.5 \text{ m s}^{-1}$ . Because such fast horizontal air velocities do not occur in the troposphere, some combination of frontogenetical circulation, buoyant accelerations, turbulence, and wave motions would be required to induce upward motion reaching  $0.5 \text{ m s}^{-1}$  in winter storms.

Lackmann and Thompson (2019) put forth a conceptual model advocating for the importance of lofting of precipitation-size ice particles over broad ( $\sim 25 \text{ km}$ ) horizontal scales (Fig. 4.2). The underpinning assumption of a prime importance of snow lofting to surface precipita-

tion is that regions with vertical motions exceeding  $0.5 \text{ m s}^{-1}$  over horizontal scales of 10s of km commonly exist in winter storms. Lackmann and Thompson (2019) stated, "Observational studies of winter cyclones document the occurrence of upward vertical air velocities in excess of  $1 \text{ m s}^{-1}$  in several storm-relative regions (e.g., Crounce et al. 2007; Rosenow et al. 2014; Rauber et al. 2017)." Lackmann and Thompson (2019) did not explicitly discuss the horizontal scale of updrafts. Rosenow et al. (2014) and Rauber et al. (2017) found updrafts that were generally up to 1-2 km in horizontal scale. Based on Figure 4.2a (Lackmann and Thompson 2019, their Fig. 1), observed updrafts  $\geq 0.5 \text{ m s}^{-1}$  on 20 to 25 km horizontal scales would commonly occur near snow bands. In contrast, the Novak et al. (2008) modeling study illustrated vertical velocities exceeding  $\sim 0.6 \text{ m s}^{-1}$  at horizontal scales of only a few km wide near a snow band. The naturally occurring horizontal scales of updraft envelopes capable of lofting snow can directly assessed with the aircraft measurements from IMPACTS and PLOWS. In this study, we will use those aircraft measurements to evaluate how commonly updrafts capable of lofting snow on horizontal scales of 10s of km occur in flat-land winter storms.

#### **4.1.2 Remote sensing analyses of winter storm vertical velocities**

Several winter field projects have used wind profilers and Doppler radars to estimate vertical air motions at horizontal scales from 10s of m to  $\sim 1$  km. Estimation of the vertical air motions from airborne and ground-based vertically-pointing sensors is complicated by the varying fall speeds of precipitation within the radar resolution volume (Gossard 1988, 1994; Gossard et al. 1990; Rosenow et al. 2014) and by airborne radar pointing angle errors (e.g., Rauber et al. 2017).

Crounce et al. (2007) used a ground-based 915-MHz wind profiler to sample vertical velocities in three winter storm cases. The profiler was positioned to measure bands of enhanced radar reflectivity on the north side of cyclones. The vertical resolution of the profiler was 105 m. The profiler had a half-power beamwidth of  $9^\circ$ , so the horizontal resolution at 2, 4, and 6 km altitudes was 310, 620, and 940 m, respectively. Crounce et al. (2007) analyzed vertical velocity derived from wind profiler data when enhanced reflectivity bands passed overhead. Within the 9 heavy reflectivity features (maxima in signal to noise ratio  $> 7$  dB) they sampled 1515 total data points. Their measured vertical velocities ranged from  $-4.3$  to  $6.7 \text{ m s}^{-1}$ , and 35% of their measured vertical velocities exceeded  $1 \text{ m s}^{-1}$  (Crounce et al. 2007, their Fig. 14). The overall mean vertical velocity in their measurements within precipitation bands was  $0.6 \text{ m s}^{-1}$ . Oue et al. (2024) used ground-based vertically-pointing Ka-band radar with a vertical gate spacing of 15 m to characterize updraft velocities. The radar half-power beamwidth was  $0.32^\circ$ , corresponding to a horizontal resolution at 2, 4, and 6 km altitudes of 11, 22, and 33 m, respectively. They found that updrafts, defined as upward Doppler velocity (*vertical air motion + particle fall*

*speed*)  $\geq 0.4 \text{ m s}^{-1}$ , were mostly  $< 20 \text{ s}$  in the time-height data, corresponding roughly to  $< 500 \text{ m}$  in horizontal scale, in four winter storm cases (Oue et al. 2024, their Fig. 5).

Rosenow et al. (2014) used airborne W-band radar data obtained by the NCAR C-130 aircraft to characterize vertical air motions in three Midwest United States winter storms, with a focus on the comma head region on the north side of the cyclone and on cloud-top generating cells. Their radar data had a 15 m vertical range gate spacing and a  $0.7^\circ$  beamwidth corresponding to a horizontal resolution at 2, 4, and 6 km distances from the aircraft of 24, 48, and 72 m, respectively. Within generating cells in the highest  $\sim 1.5 \text{ km}$  of cloud radar echo, they found maximum vertical motions between 1 and  $2 \text{ m s}^{-1}$  (Rosenow et al. 2014, their Figs. 8 and 10). Below the generating cells, they found much weaker vertical motions within updrafts, on the order of  $0.1\text{-}0.2 \text{ m s}^{-1}$  (Rosenow et al. 2014, their Figs. 8 and 10). Rosenow et al. (2014) also sampled discrete cells of elevated convection above a 1 km deep rain layer. The base of the elevated convection was  $\sim 4\text{-}5 \text{ km}$  below echo top, on the south side of the comma head region of the cyclone. Within the elevated convection, updrafts with peak velocities as strong as  $7 \text{ m s}^{-1}$  on 1 km horizontal scale were found (Rosenow et al. 2014, their Fig. 19). Rauber et al. (2017) used the HIAPER Cloud Radar, an airborne W-band radar, to sample a winter storm with heavy snow in the northeast United States. There were updrafts sampled in that case as strong as  $5 \text{ m s}^{-1}$  (when accounting for  $\sim 1 \text{ m s}^{-1}$  particle fall speeds) at 1 km horizontal scale and 1 km vertical scale associated with Kelvin-Helmholtz waves and generating cells (Rauber et al. 2017, their Fig. 10). The Kelvin-Helmholtz waves and generating cells were usually no more than 1-2 km wide.

### 4.1.3 Goals of this study

Several studies have quantitatively characterized the strengths and scales of vertical air motion in cumulus environments using in situ aircraft data (e.g., LeMone and Zipser 1980; Yang et al. 2016; Qin et al. 2023). Previous analyses of vertical air motions in winter storms have tended to utilize remote sensing data to examine small segments of storms (e.g., Rosenow et al. 2014; Rauber et al. 2017). Here, we are using in situ vertical velocity data from 42 research flights during the IMPACTS and PLOWS field campaigns to characterize the vertical air motions in flat-land winter storms. We will particularly focus on the portion of the storm with upward motion  $\geq 0.5 \text{ m s}^{-1}$ , including the horizontal scales of individual updrafts  $\geq 0.5 \text{ m s}^{-1}$ . We are aiming to address what strengths and horizontal scales of updrafts are common and recurrent in flat-land winter storms.

## 4.2 Data and methods

Our data come from the NASA Investigation of Microphysics and Precipitation for Atlantic Coast-Threatening Snowstorms (IMPACTS, 2020-2023; McMurdie et al. 2022) and the NSF Profiling of Winter Storms (PLOWs, 2009-2010; Rauber et al. 2014) field campaigns. IMPACTS and PLOWs conducted research flights into winter storms primarily in the Northeast and Midwest United States, respectively.

### 4.2.1 In situ measurements of vertical velocity

Vertical air motions measured in situ by aircraft probes are not affected by nearby precipitation fall speeds. The inertial navigation system (Barrick et al. 1996) and GPS are used to precisely measure the Earth-relative velocity of the aircraft. Horizontal spatial resolution of the in situ measurements is a function of sampling frequency and air speed. Vertical resolution of the probe is typically representative of a few meters.

During IMPACTS, the NASA Airborne Science Program's P-3 Orion was used to collect in situ measurements of cloud properties and ambient conditions on 40 total science flights in 2020, 2022, and 2023 (McMurdie et al. 2022). We used the subset of 30 IMPACTS flights that sampled surface snow-producing winter storms. The 3-D wind vector was measured in situ on the P-3 using the Turbulent Air Motion Measurement System (TAMMS), which is comprised of 5 pressure ports located on the nose of the aircraft which allow for the aircraft-relative flow to be determined, a high-resolution inertial and satellite navigation systems which measure the aircraft velocity relative to Earth, and a data logging system (Barrick et al. 1996). The TAMMS data acquired during IMPACTS are at 20 Hz frequency (i.e., measured every 0.05 s) with  $\pm 0.5 \text{ m s}^{-1}$  uncertainty in vertical velocity (Lee Thornhill, personal communication). For this analysis, we use 1 s samples of vertical velocity (i.e., averages of 20 vertical velocity measurements) to smooth out random noise in the data. Based on typical aircraft ground-relative speeds, 1 s corresponds to about 100 m spatial scale.

For PLOWs, the National Science Foundation/National Center for Atmospheric Research (NSF/NCAR) C-130 was equipped with both remote sensing and in situ instrumentation for 18 science flights in 2009-10 Rauber et al. (2014). We used data from the subset of 12 flights that sampled surface snow-producing winter storms. Similar to the TAMMS used in IMPACTS, the C-130 was equipped with a gust probe located on the radome of the aircraft and an inertial navigation system which provided measurements of the 3-D wind vector. The PLOWs data are archived at a 1 Hz. The 1 Hz measurements correspond to about 100 m spatial scale.

To analyze only the vertical velocity data which are most reliable, we define straight and level flight legs. Measurements during turns, ascents, and descents are excluded. We use the

same definition of straight and level flight legs for both IMPACTS and PLOWS. The aircraft (P-3 or C-130) must have a pitch angle between  $-2^\circ$  and  $2^\circ$  and a roll angle between  $-4^\circ$  and  $4^\circ$ . If there is a gap shorter than 5 s between any two straight and level flight legs, the two legs are joined together (i.e., the gap is also considered straight and level). We also exclude data from the transit flight legs between the aircraft base location and the targeted sampling region. In general, we will only analyze data sampled at air temperatures  $< 0^\circ\text{C}$ .

#### **4.2.2 Coordinated remote-sensing data from NASA ER-2**

For broader context to the in situ measurements made on the NASA P-3, we also use data from the NASA ER-2 flown during IMPACTS. The ER-2 was equipped with downward-pointing remote-sensing instrumentation with the goal of flying in coordination with (i.e., directly above) the P-3 (McMurdie et al. 2022; Heymsfield et al. 2024). We use data from the NASA Goddard Space Flight Center’s Cloud Radar System (CRS; McLinden et al. 2021), a W-band (94 GHz), polarimetric Doppler cloud radar on the ER-2. We use reflectivity and Doppler velocity data from the CRS during straight and level ER-2 flight legs when the ER-2 and P-3 were well-coordinated, defined by  $\leq 3$  km horizontal distance and  $\leq 5$  min time gap between the two aircraft. The edge of CRS echo (where reflectivity  $\sim -20$  dBZ) provides an estimate of the cloud boundary. When the P-3 and ER-2 were well-coordinated and the P-3 was within CRS echo, the P-3 distance from echo top was calculated as the vertical distance from the P-3 altitude to the nearest above altitude where CRS reflectivity  $< -20$  dBZ within the column.

#### **4.2.3 Cloud probe data and cloud definition**

For IMPACTS, we use data from the 2-Dimensional Stereo probe (2D-S; Lawson et al. 2006) and Cloud Droplet Probe (CDP; Lance et al. 2010) to determine when the P-3 was flying in cloud. The 2D-S detected cloud and precipitation particles 10-3000  $\mu\text{m}$  in diameter, and the CDP detected cloud particles 2-50  $\mu\text{m}$  in diameter (McMurdie et al. 2022). When either probe measured a total number concentration ( $N_T$ )  $\geq 10^{-3}$   $\text{cm}^{-3}$ , we consider the P-3 to have been in cloud at that time. In the example shown in Fig. 4.3, changes in the 2D-S total number concentration correspond to whether the P-3 was in regions just above cloud echo (at  $\sim 50$  km along the flight leg), higher reflectivity in cloud (at  $\sim 75$  km along the flight leg) and lower reflectivity in cloud (at  $\sim 115$  km along the flight leg).

From the NCAR C-130 during PLOWS, we use a combination of a CDP to detect cloud particles 2-50  $\mu\text{m}$  in diameter and data from the 2-Dimensional Optical Array Cloud Probe (2D-C; UCAR/NCAR - Earth Observing Laboratory 2024) to detect cloud particles 25-800  $\mu\text{m}$  in

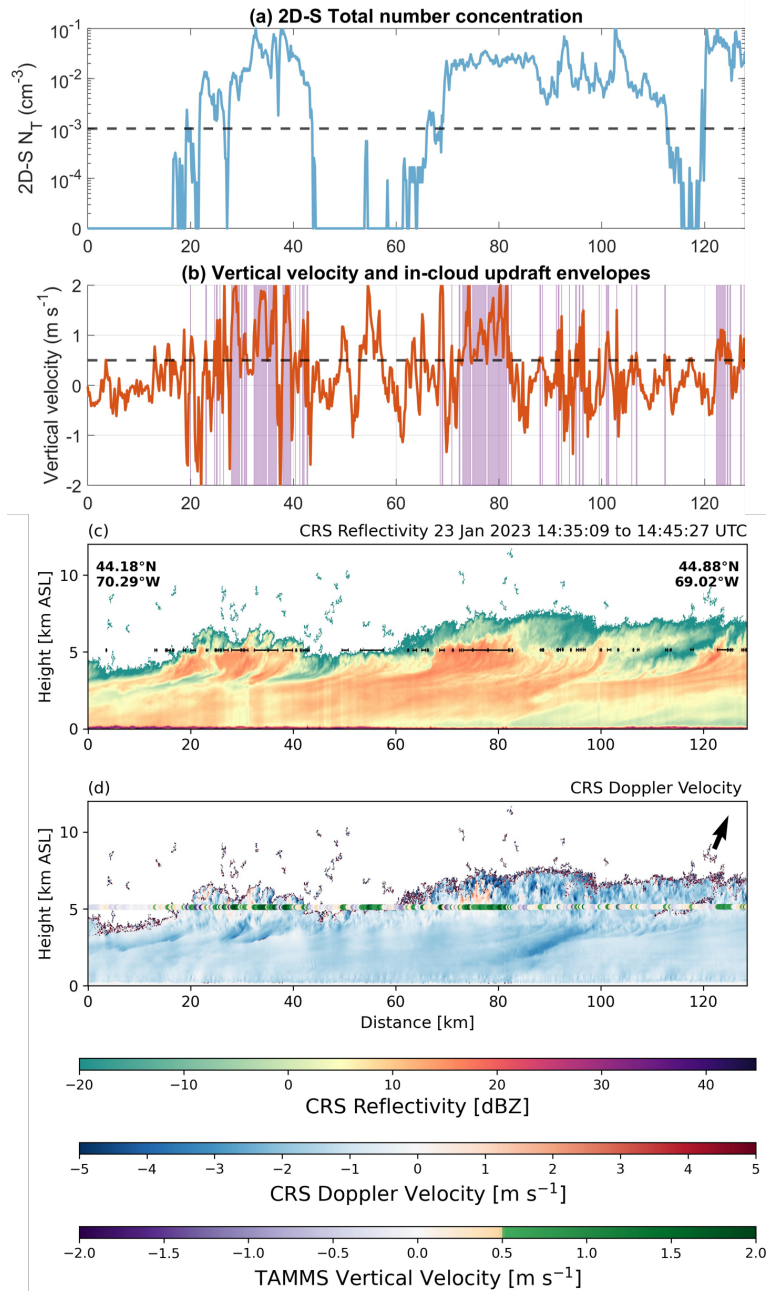


Figure 4.3: P-3 in situ and ER-2 radar data from for a well-coordinated flight leg segment during the IMPACTS mission on 23 January 2023 from 1435 to 1445 UTC. In this flight leg, the P-3 flew through a layer of near cloud-top generating cells. **(a)** 2D-S total number concentration (logarithmic scale), the in-cloud threshold ( $10^{-3} \text{ cm}^{-3}$ ) is shown by a dashed horizontal line. **(b)** TAMMS vertical velocity. Dashed horizontal line at  $0.5 \text{ m s}^{-1}$  indicates the updraft threshold definition. In-cloud updraft envelopes are indicated by purple shading. **(c)** CRS reflectivity. P-3 flight leg segments where the TAMMS vertical velocity  $\geq 0.5 \text{ m s}^{-1}$  are indicated by black horizontal lines bounded by vertical bars. **(d)** CRS Doppler velocity, where positive values indicate upward motion. TAMMS vertical velocity is shown using colored points. Aspect ratio is 3:1 for panels **(c)**-**(d)**.

diameter. Similar to IMPACTS, we consider the C-130 to have been in cloud when either the 2D-C or CDP measured  $N_T \geq 10^{-3} \text{ cm}^{-3}$ .

Across all the science flights during IMPACTS that we analyzed, there were 39.6 hours (142,614 1-second samples) of in-cloud vertical velocity data along 430 straight and level flight legs. For PLOWS, there were 22.8 hours (82,107 1-second samples) of in-cloud vertical velocity data along 779 straight and level flight legs.

#### 4.2.4 Updraft envelope definition

Prior studies of updrafts and downdrafts in convective clouds have defined and identified continuous envelopes of vertical velocities meeting given thresholds. For updrafts, LeMone and Zipser (1980) identified envelopes within the vertical velocity time series which continuously exceeded  $0 \text{ m s}^{-1}$  for  $\geq 500 \text{ m}$  and  $0.5 \text{ m s}^{-1}$  for  $\geq 1 \text{ s}$  (at least  $\sim 100 \text{ m}$ ). Yang et al. (2016) used a  $0.2 \text{ m s}^{-1}$  threshold to account for measurement uncertainty, and they removed the 500 m diameter requirement in order to capture smaller updrafts.

We use a similar method to Yang et al. (2016) to identify updraft envelopes, but we use a  $0.5 \text{ m s}^{-1}$  threshold for updrafts to account for measurement uncertainty. This threshold also represents a lower-end estimate for the terminal fall speed of precipitation size ice particles (Garrett and Yuter 2014; Fitch et al. 2021). While Yang et al. (2016) combined updraft envelopes that were separated by a distance  $\leq 50 \text{ m}$ , we skip this step because our data are at 1-second intervals (Yang et al. 2016's data were at 0.04-second intervals), and the P-3's typical ground speed was roughly  $100 \text{ m s}^{-1}$ . Fig. 4.4a-b is an example of updraft envelope identification for P-3 flight leg about 2 km below the cloud-top generating cells. This flight leg was entirely within cloud (2D-S total number concentration  $\geq 10^{-3} \text{ cm}^{-3}$ ). Eight updraft envelopes were identified.

For each updraft envelope, we compute the integrated upward mass flux ( $\phi_{upward}$  in  $\text{kg m}^{-1} \text{ s}^{-1}$ ) using Eq. 4.1:

$$\phi_{upward} = \rho \bar{w} L_{updraft} \quad (4.1)$$

where  $\rho$  ( $\text{kg m}^{-3}$ ) is the air density,  $\bar{w}$  ( $\text{m s}^{-1}$ ) is the mean vertical velocity within the updraft envelope, and  $L_{updraft}$  (m) is the length of the updraft envelope.  $\rho$  is calculated from the ideal gas law using the virtual temperature ( $T_v$  in K) using Eq. 4.2:

$$\rho = \frac{p}{R_d T_v} \quad (4.2)$$

where  $p$  (Pa) is the air pressure,  $R_d$  is the dry air gas constant ( $287 \text{ J kg}^{-1} \text{ K}^{-1}$ ).  $T_v$  is calculated

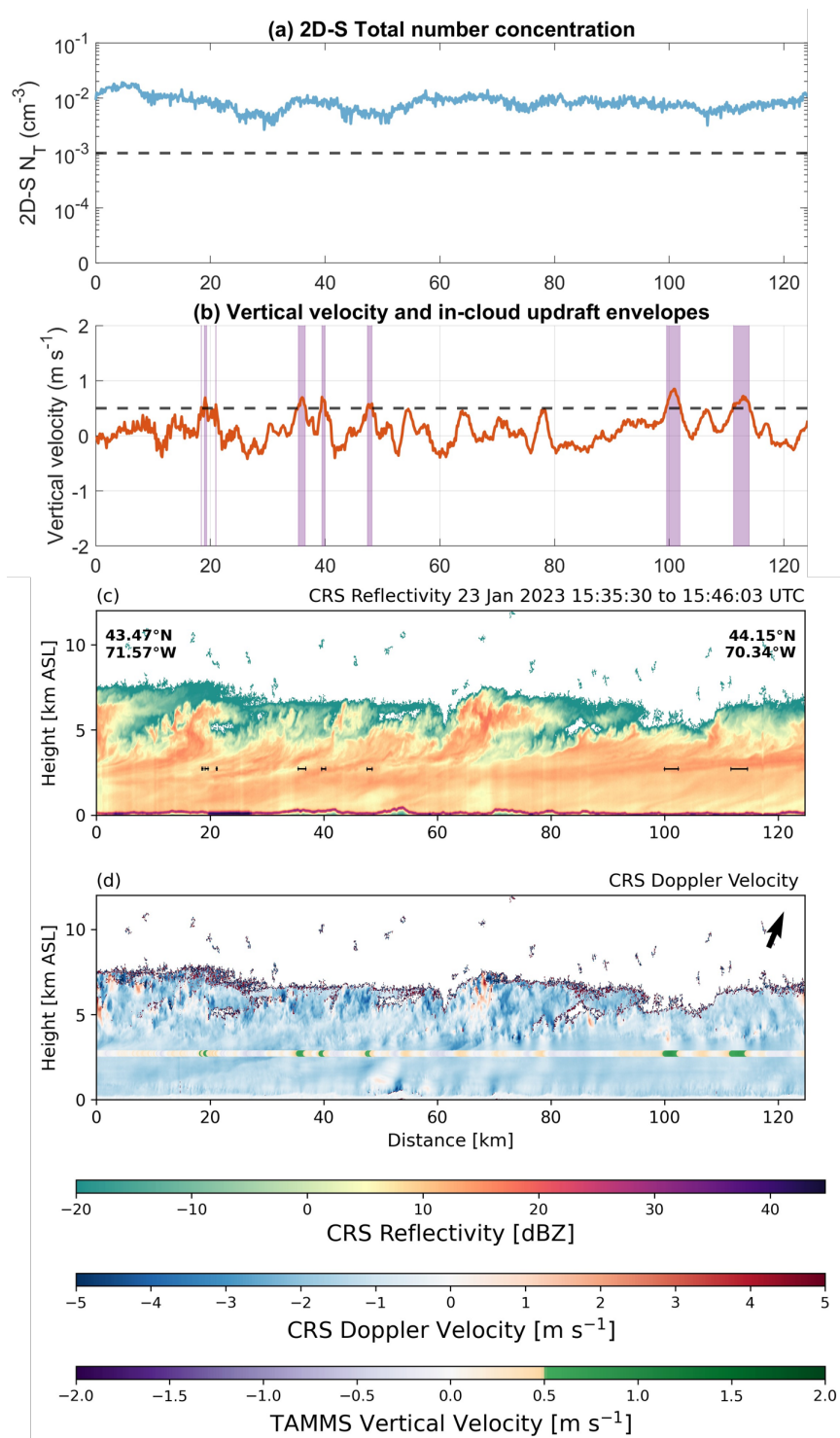


Figure 4.4: As in Fig. 4.3, but for a well-coordinated flight leg on 23 Jan 2023 from 1535 to 1546 UTC when the P-3 flew through the middle of the cloud layer, about 2 km below the cloud-top generating cells.

from the air temperature ( $T$  in K) and water vapor mixing ratio ( $q$ , unitless) using Eq. 4.3:

$$T_v = (1 + \varepsilon q)T \quad (4.3)$$

where  $\varepsilon$  is the ratio between the molecular mass of water and dry air ( $\sim 0.61$ ).

#### 4.2.5 ERA5 reanalysis data and forcing/instability metrics

We use ERA5 reanalysis data (Hersbach et al. 2020) to obtain the large-scale context for the in situ aircraft data. ERA5 data are output on a  $0.25^\circ$  grid globally at 1 h intervals. The data are available on either a single level (e.g., 2-meter temperature, 10-meter wind components; Hersbach et al. 2023b) or on pressure levels (e.g., 800 hPa temperature and wind components; Hersbach et al. 2023a).

To track surface lows, we used the algorithm from Crawford et al. (2021) with ERA5 mean sea level pressure (MSLP) data (Tomkins et al. 2024a). The low-relative position of the P-3 was calculated from the surface low tracks for each IMPACTS case.

We used ERA5 data to characterize different types of forcing and instability, including frontogenesis, Kelvin-Helmholtz instability, potential instability, and local and non-local conditional instability. Frontogenesis describes the rate at which the gradient of a scalar field, e.g. potential temperature ( $\theta$  in K), is changing with time in a parcel-following framework. We calculated 2D frontogenesis ( $F_{2D}$  in  $\text{K m}^{-1} \text{s}^{-1}$ ) following Novak et al. (2004), who used a simplified form of the equations from Miller (1948):

$$F_{2D} = \frac{1}{|\vec{\nabla}\theta|} \left[ -\frac{\partial\theta}{\partial x} \left( \frac{\partial u}{\partial x} \frac{\partial\theta}{\partial x} + \frac{\partial v}{\partial x} \frac{\partial\theta}{\partial y} \right) - \frac{\partial\theta}{\partial y} \left( \frac{\partial u}{\partial y} \frac{\partial\theta}{\partial x} + \frac{\partial v}{\partial y} \frac{\partial\theta}{\partial y} \right) \right] \quad (4.4)$$

where  $|\vec{\nabla}\theta|$  is the magnitude of the horizontal gradient of  $\theta$  ( $\text{K m}^{-1}$ ), and  $u$  and  $v$  are the zonal and meridional components of the flow (in  $\text{m s}^{-1}$ ), respectively. Positive frontogenesis is indicative of forcing for ascent associated with frontal circulations (Lackmann 2011, p. 140).

Kelvin-Helmholtz instability describes the presence of vertical shear instability within a statically stable layer. When shear instability is released, there is an extraction of energy from the mean flow. Initially, a thin layer of strong vertical wind shear (horizontal vorticity) is present, i.e., a "vortex sheet". Then, after the shear instability is released, there are discrete, roughly circular patches of vorticity. A necessary, but not sufficient, condition for Kelvin-Helmholtz instability to be present is the gradient Richardson Number (Ri, unitless) must be less than 0.25. Ri is the ratio between the squared Brunt-Väisälä frequency ( $N^2$  in  $\text{s}^{-2}$ ) and the square of the vertical gradient of the mean horizontal wind  $[(\frac{\partial \bar{u}}{\partial z})^2$  in  $\text{s}^{-2}$ ] (Markowski and Richardson

2010, pp. 58-66):

$$Ri_m = \frac{N_m^2}{\left(\frac{\partial \bar{u}}{\partial z}\right)^2} \quad (4.5)$$

Because our focus is on in-cloud conditions, we will calculate the moist Richardson number ( $Ri_m$ , unitless) using the moist Brunt–Väisälä frequency ( $N_m^2$ ). We calculate  $N_m^2$  using:

$$N_m^2 = \frac{g}{\bar{\theta}_e} \frac{\Gamma_m}{\Gamma_d} \frac{\partial \bar{\theta}_e}{\partial z} \quad (4.6)$$

where  $\bar{\theta}_e$  (K) is the equivalent potential temperature,  $\Gamma_m$  ( $\text{K m}^{-1}$ ) is the moist adiabatic lapse rate,  $\Gamma_d$  is the dry adiabatic lapse rate ( $9.8 \text{ K km}^{-1}$ ), and  $g$  is gravitational acceleration ( $9.81 \text{ m s}^{-1}$ ). We use the pseudoadiabatic lapse rate ( $\Gamma_{ps}$  in  $\text{K m}^{-1}$ ) to approximate  $\Gamma_m$  (American Meteorological Society 2024):

$$\Gamma_{ps} = g \frac{(1 + r_v) \left(1 + \frac{L_v r_v}{RT}\right)}{c_{pd} + r_v c_{pv} + \frac{L_v^2 r_v (\epsilon + r_v)}{RT_K^2}} \quad (4.7)$$

where  $r_v$  (unitless) is the water vapor mixing ratio,  $L_v$  is the latent heat of evaporation ( $2.501 \times 10^6 \text{ J kg}^{-1}$ ),  $R$  is the gas constant for dry air ( $287 \text{ J kg}^{-1} \text{ K}^{-1}$ ),  $T_K$  is the temperature in K,  $c_{pd}$  is the specific heat of dry air at constant pressure ( $1005.7 \text{ J kg}^{-1} \text{ K}^{-1}$ ),  $c_{pv}$  is the specific heat of water vapor at constant pressure ( $1860 \text{ J kg}^{-1} \text{ K}^{-1}$ ), and  $\epsilon$  is the ratio between the molecular mass of water and the molecular mass of dry air (0.61). We calculate  $\theta_e$  in K following Eq. 43 from Bolton (1980):

$$\theta_E = T_K \left(\frac{1000}{p}\right)^{0.2854(1-0.28*10^{-3}r_v)} * \exp\left[\left(\frac{3.376}{T_L} - 0.00254\right) * r_v (1 + 0.81 * 10^{-3} r_v)\right] \quad (4.8)$$

where  $p$  is the air pressure in hPa.  $T_L$  is the temperature at the lifting condensation level, approximated using Eq. 15 from Bolton (1980):

$$T_L = 56 + \frac{1}{\frac{1}{T_D - 56} + \frac{\ln(T_K/T_D)}{800}} \quad (4.9)$$

where  $T_D$  is the dew point temperature.  $T_K$ ,  $T_L$  and  $T_D$  are all in K.

Potential instability can occur where dry air is present over moist air and the layer of moist air is lifted. The lifted moist air cools at the moist adiabatic lapse rate and the lifted dry air above cools at the dry adiabatic lapse rate. This means that the dry air at the top of the layer will cool more quickly than the moist air at the bottom of the layer and thus the bottom of the layer will become warmer than the top of the layer. Potential instability is defined where  $\frac{\partial \theta_e}{\partial z} < 0$ .

The local environment is conditionally unstable if a saturated air parcel perturbed upward would gain a positive buoyant acceleration or alternately if a parcel perturbed downward would

gain a negative buoyant acceleration and thus accelerate away from its original altitude. Local conditional instability is present if the local environmental lapse rate ( $\Gamma$ ) is between the moist ( $\Gamma_m$ ) and dry ( $\Gamma_d$ ) adiabatic lapse rates. In effect, conditional instability is present where the vertical gradient of the saturation equivalent potential temperature ( $\theta_e^*$ ) is negative ( $\frac{\partial \theta_e^*}{\partial z} < 0$ ). We calculate  $\theta_e^*$  in the same way as  $\theta_e$ , except with the assumption that the air is saturated (i.e.,  $T_D = T_K = T_L$ ).

$$\theta_e^* = T_K \left( \frac{1000}{p} \right)^{0.2854(1-0.28*10^{-3}r_v)} * \exp\left[ \left( \frac{3.376}{T_K} - 0.00254 \right) * r_v (1 + 0.81 * 10^{-3} r_v) \right] \quad (4.10)$$

If local conditional instability is present, then non-local conditional instability may also be present over some depth (Stull 1993). As long as the parcel in a conditionally unstable environment remains warmer than the environment, once it is perturbed upward, it will continue to accelerate upward due to positive buoyancy. For a given altitude, there is non-local conditional instability to upward parcel motion if  $\theta_e^*$  is higher at any level below that altitude.

#### 4.2.6 Potential sampling biases with in situ aircraft data

With aircraft-mounted, in situ instruments, we are only able to sample along lines through the storms, representing a tiny portion of the total 3D storm volume. In practice, it is difficult for aircraft in situ data to comprehensively sample the 3D storm volume. PLOWS in particular and IMPACTS to a extent targeted regions where upward motions and ice growth were expected. Hence, their observed updraft distributions are *likely upper bounds on what would be present over the entire storm volume*. Winter storms over flat land with snow at the surface generally have weaker updrafts and turbulence than deep convection. For safety, regions with severe turbulence are avoided during research flight missions. Severe turbulence only occurred during one IMPACTS flight leg where strong Kelvin-Helmholtz waves were present over the Gulf of Maine (Matthew Miller, personal communication).

Measurements of updraft breadth by in situ instruments are subject to underestimation because the aircraft will usually not perfectly bisect an updraft. We can quantify this by considering an idealized case with a spherical updraft with diameter  $D$  and vertical velocity  $\geq 0.5 \text{ m s}^{-1}$ . We assume that the aircraft's path through this spherical updraft is a straight line which misses the center of the updraft by a distance  $h$ . The updraft breadth measured by the aircraft is the length of this straight line,  $L_{\text{updraft}}$ , which can be calculated as:

$$L_{\text{updraft}} = \sqrt{D^2 - 4h^2} \quad (4.11)$$

Then, we can calculate the distribution of measured updraft breadths for many random air-

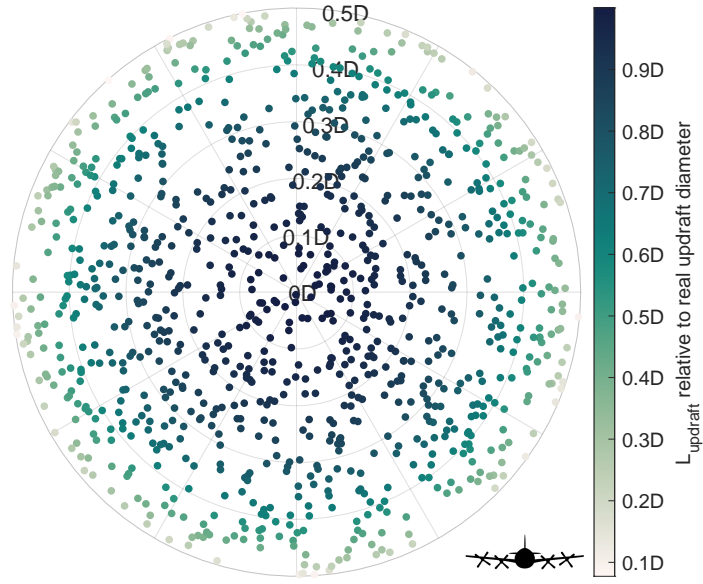


Figure 4.5: The location of 1000 randomly generated aircraft passes through an idealized spherical updraft, such that the likelihood of the aircraft passing through a given subregion of the cross-section is proportional to the area of that subregion. Cross-section through the center of the sphere in the  $xz$ -plane where the aircraft is traveling in the  $y$ -direction (shown by aircraft silhouette). Points are colored by the length of the aircraft's path through the sphere ( $L_{updraft}$ ), relative to the actual diameter of the sphere ( $D$ ).

craft passes through the updraft (Fig. 4.5). We assume that  $h$  is distributed such that within the cross-section of the spherical updraft which contains the sphere's center and is perpendicular to the aircraft path, the number of random aircraft passes within a region of the cross-section is proportional to the area of that region. In other words, the probability of the aircraft passing within a distance  $s$  of the sphere's center is:

$$P(h < s) = \frac{\pi s^2}{\pi(\frac{D}{2})^2} = \frac{4s^2}{D^2} \quad (4.12)$$

The cumulative distribution function (CDF) of  $L_{updraft}$  is  $P(L_{updraft} < \Lambda)$ , where  $\Lambda$  is the proportion of the actual updraft diameter in  $(0, D)$ . From Eq. 4.11, this can be rewritten as  $P(\sqrt{D^2 - 4h^2} < \Lambda)$ . Rearranging this gives:

$$P(L_{updraft} < \Lambda) = 1 - P\left(h < \frac{\sqrt{D^2 - \Lambda^2}}{2}\right) \quad (4.13)$$

After substituting Eq. 4.12 into Eq. 4.13 and simplifying:

$$P(L_{\text{updraft}} < \Lambda) = 1 - \frac{4\left(\frac{\sqrt{D^2 - \Lambda^2}}{2}\right)^2}{D^2} = \left(\frac{\Lambda}{D}\right)^2 \quad (4.14)$$

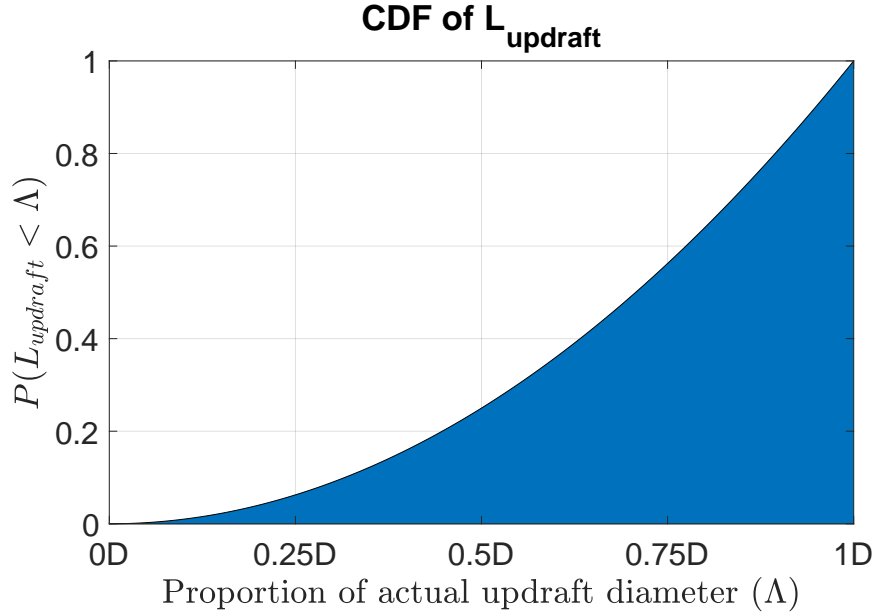


Figure 4.6: Theoretical cumulative distribution function (CDF) of the measured length of an updraft ( $L_{\text{updraft}}$ ) by an aircraft randomly passing through a spherical updraft with diameter  $D$ , relative to  $D$ , according to Eq. 4.14.

This means that using aircraft in situ data, the probability of measuring an updraft breadth smaller than some proportion of  $D$  is equal to the square of that proportion. For example, if an actual updraft is 1 km across, then 25% of random aircraft passes through that 1 km updraft will measure the updraft to be  $< 0.5$  km across. Similarly, since  $0.7^2 = .49$ , then 49% of random aircraft passes will measure that 1 km updraft to be  $< 0.7$  km across.

To calculate the probability density function (PDF) of  $L_{\text{updraft}}$ , we differentiate the CDF with respect to  $\Lambda$ :

$$PDF(L_{\text{updraft}}) = \frac{d[P(L_{\text{updraft}} < \Lambda)]}{d\Lambda} = \frac{2\Lambda}{D^2} \quad (4.15)$$

In reality, the regions where vertical velocity  $\geq 0.5 \text{ m s}^{-1}$  in winter storms will be irregularly shaped. Analytically calculating the distribution of  $L_{\text{updraft}}$  for an irregularly shaped updraft

region would be impractical, if not impossible. A sphere is a convenient shape for these calculations as it is rotationally symmetrical, and is likely a reasonable approximation for cloud-top generating cells. One could imagine an oblong updraft region associated with Kelvin-Helmholtz waves. For an oblong shape, the aircraft would be more likely to measure an updraft breadth longer than the minor axis but shorter than the major axis.

The updraft envelopes identified from in situ data following Sect. 4.2.4 will all represent *underestimates* of the real horizontal breadth of updrafts. Assuming spherical updraft shapes, then 25% of the measured updraft envelope lengths will be below half the actual updraft breadth (Fig. 4.6). If one doubled the length of each of the measured updraft envelope lengths, then it would overestimate the actual updraft breadth for 75% of the updrafts. If one multiplied the length of the measured updraft envelope by 3.2, then it would overestimate the actual updraft for 90% of the updrafts. As a rough rule of thumb, multiplying the breadth by 3.2 will overcompensate for underestimates of updraft breadth because the aircraft did not exactly bisect an updraft.

## CHAPTER

# 5

# IN-CLOUD VERTICAL VELOCITY CHARACTERISTICS IN WINTER STORMS

## 5.1 Results

### 5.1.1 Vertical velocity measurements and context for individual flight legs

Representative flight legs within and below generating cells for conditions with snow at the surface highlight key differences in the vertical velocity structures and large scale instabilities. For the IMPACTS flight leg on 23 January 2023 1435-1445 UTC, cloud top varied between 5 to 7 km altitude (Fig. 4.3). As the aircraft flew in and out of cloud at 5 km altitude, cloud particle concentrations varied from near zero outside of cloud to  $10^{-1} \text{ cm}^{-3}$  in cloud. Updraft envelopes were frequent and narrow in regions with generating cells with upward motion  $\geq 0.5 \text{ m s}^{-1}$  being broken up by intermittent measurements  $< 0.5 \text{ m s}^{-1}$  (around 20-40 km, 70-80 km, and 125 km along leg distance). The horizontal scales of updrafts near  $2 \text{ m s}^{-1}$  were only a few hundred meters. Based on ERA5 reanalysis (Fig. 5.1a), there was negative frontogenesis (i.e., frontolysis) present at the P-3 flight level. Much of the flight leg was through a region where  $Ri_m < 0.25$ , meaning that Kelvin-Helmholtz instability may have been present (Fig. 5.1b). There was also weak local potential and conditional instability at or just above the P-3 flight level

ERA5 (01/23 15 UTC) cross-section along P-3 flight leg at 2023/01/23 14:35-14:47 UTC

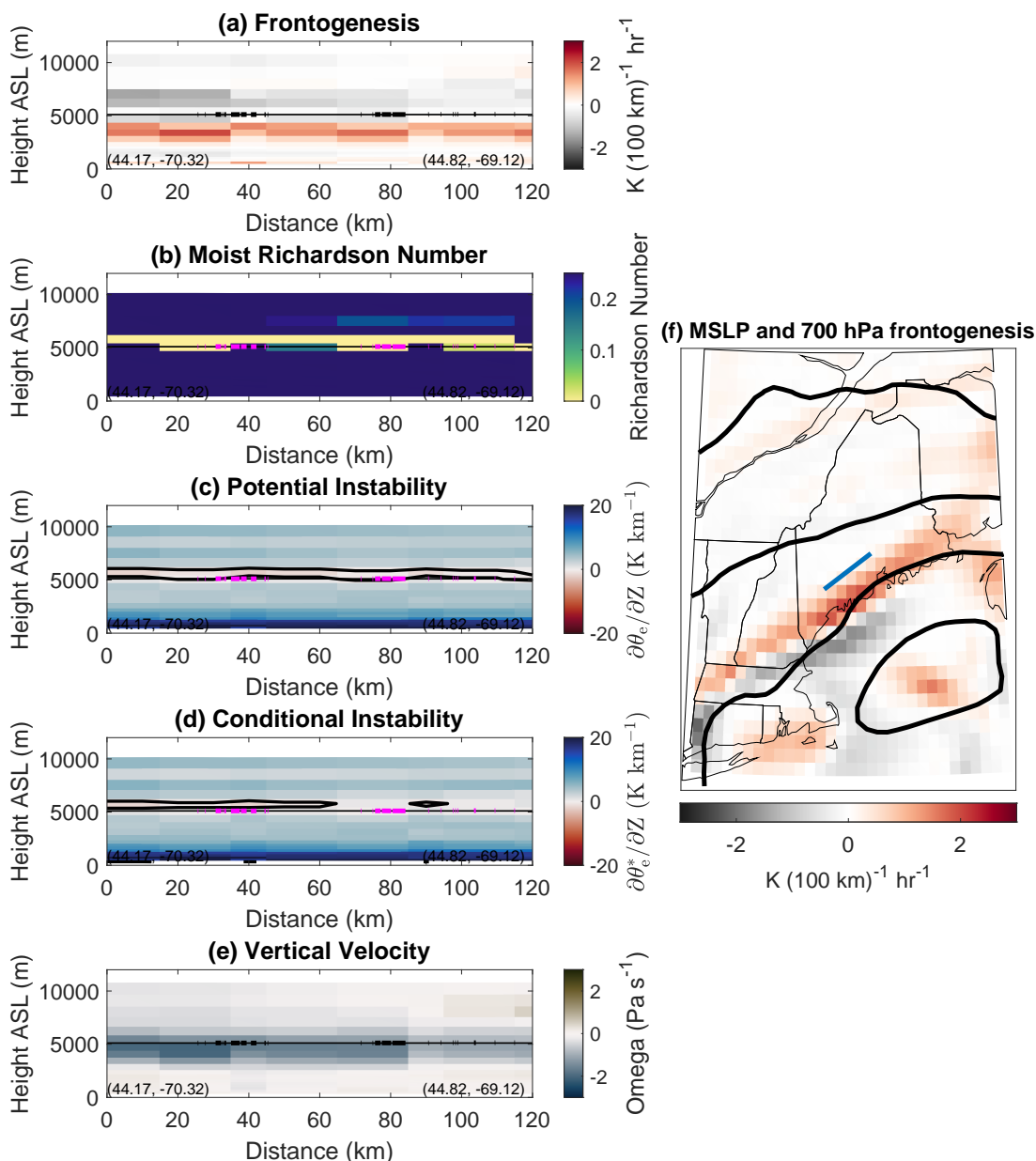


Figure 5.1: **(a)** 2D Frontogenesis [ $K(100\text{ km})^{-1}\text{ hr}^{-1}$ ], **(b)**  $Ri_m$  (unitless), **(c)**  $\frac{\partial\theta_e}{\partial Z}$  ( $K\text{ km}^{-1}$ ), **(d)**  $\frac{\partial\theta_e^*}{\partial Z}$  ( $K\text{ km}^{-1}$ ), and **(e)** vertical velocity ( $\text{Pa s}^{-1}$  where upward motion is negative) obtained or calculated from ERA5 data along a cross-section corresponding to the flight leg shown in Fig. 4.3, in which the P-3 flew through a layer of cloud-top generating cells. In panels **(c)** and **(d)**, the zero contour is shown, and red shading indicates potential and conditional instability, respectively. In **(a)-(e)**, the P-3 flight level is indicated by a thin line, and observed in-cloud updrafts  $\geq 0.5\text{ m s}^{-1}$  are indicated by thick lines. Aspect ratio is 3:1. **(f)** Map of the flight leg (blue), MSLP (contoured in black every 5 hPa), and 700 hPa frontogenesis [shaded,  $K(100\text{ km})^{-1}\text{ hr}^{-1}$ ].

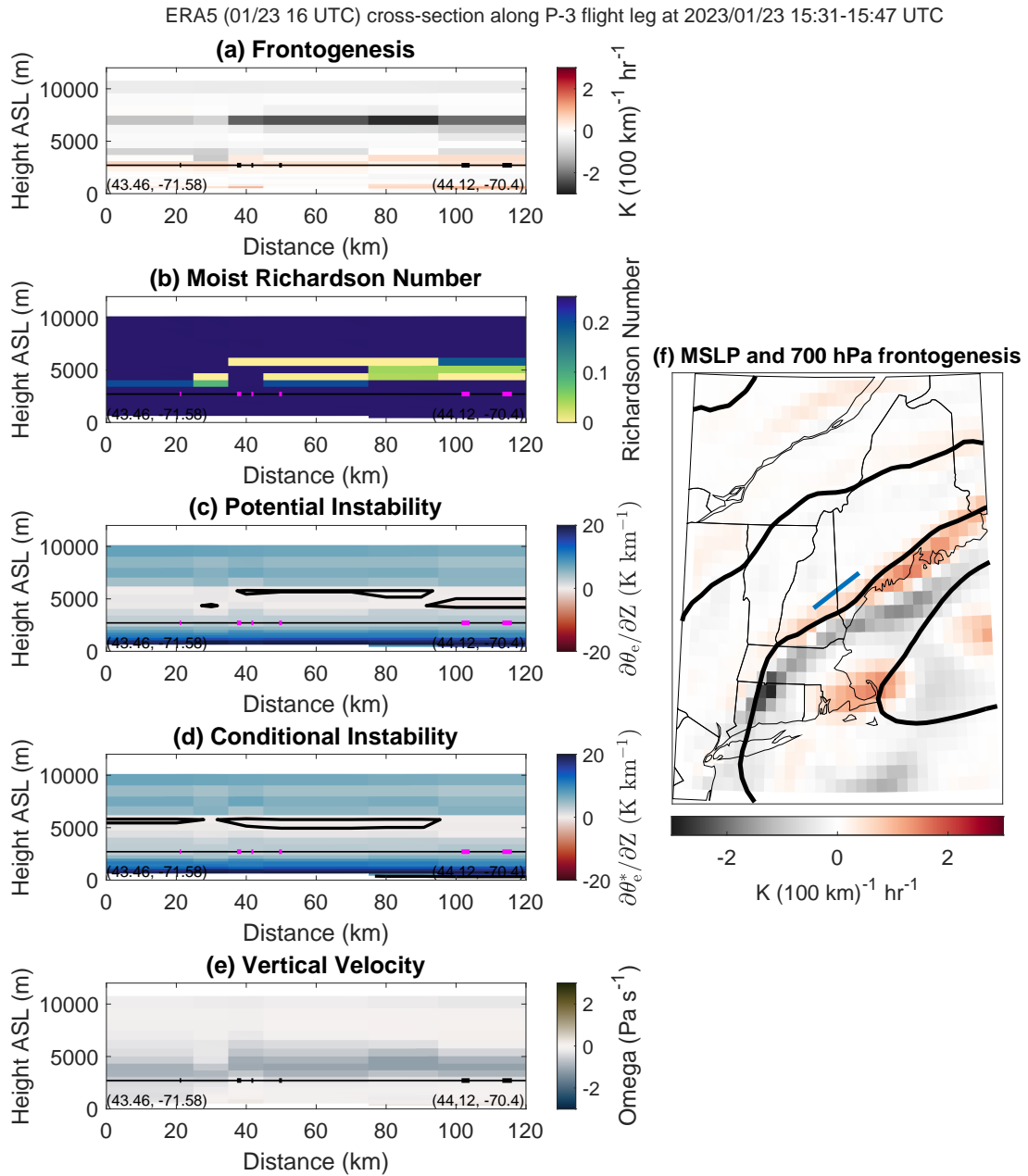


Figure 5.2: As in Fig. 5.1, but for the flight leg shown in Fig. 4.4, in which the P-3 flew below a layer of cloud-top generating cells.

(Fig. 5.1c-d). This all suggests that the updrafts encountered by the P-3 during this flight leg are associated with release of some type of local instability, rather than any larger-scale or persistent upward motion.

The IMPACTS flight leg on 23 January 2023 1535-1546 UTC was entirely within cloud (Fig. 4.4) and had cloud particle concentrations near  $10^{-2} \text{ cm}^{-3}$ . Cloud top was close to 7.5 km for most of the leg. The P-3's flight altitude (3 km) was at least 1 km below the layer with generating cells. At this altitude, the P-3 encountered few updraft envelopes stronger than  $0.5 \text{ m s}^{-1}$ . Based on ERA5 reanalysis (Fig. 5.2bcd), 3 km altitude was stable for shear, potential, and conditional instabilities. Weak frontogenesis was present (Fig. 5.2a) yielding vertical velocity  $\geq 0.5 \text{ m s}^{-1}$  only within a few small segments of the flight leg.

In Appendix A, we present several more examples of cross-sections of frontogenesis, moist Richardson number, potential instability, conditional instability, and vertical velocity from ERA5 data along P-3 flight legs. We include in-cloud flight legs where the minimum ERA5 2-meter temperature was  $> 0^\circ\text{C}$  and where there the P-3 either sampled relatively strong frontogenesis [ $\sim 2 \text{ K}(100 \text{ km})^{-1} \text{ hr}^{-1}$  or more] or sampled several updrafts  $\geq 0.5 \text{ m s}^{-1}$ . Overall, IMPACTS did not sample the type of extreme frontogenesis [ $> 5 \text{ K}(100 \text{ km})^{-1} \text{ hr}^{-1}$ ] found in, e.g., the cases analyzed by Novak et al. (2008) or Lackmann and Thompson (2019). Such cases are difficult to sample because of their rarity and aircraft flight level restrictions.

### 5.1.2 Distributions of vertical velocity measurements

IMPACTS primarily sampled snow-producing storms in the Northeast United States, with a few flights sampling over the Midwest, while PLOWS primarily sampled over the Midwest United States (Fig. 5.3a-b). These two field projects are the primary research aircraft in situ data sets for flat-land winter storms with snow reaching the surface in the US. The vertical air motion distributions sampled during these projects are the best evidence of natural conditions within these winter storms available.

Overall, the in-cloud vertical velocity distributions show mean and median values of a few  $\text{cm s}^{-1}$  and less than 10% of the measurements are capable of lofting snow ( $\geq 0.5 \text{ m s}^{-1}$ ). The distribution of in-cloud vertical velocity measurements during IMPACTS was centered near  $0 \text{ m s}^{-1}$  (mean:  $0.04 \text{ m s}^{-1}$ , median:  $0.03 \text{ m s}^{-1}$ ), while the distribution for PLOWS was centered at slightly higher values (mean:  $0.12 \text{ m s}^{-1}$ , median:  $0.09 \text{ m s}^{-1}$ ). It is likely that the slightly higher mean and median values in PLOWS as compared to IMPACTS relate to PLOWS aircraft specifically targeting altitudes with generating cells whereas IMPACTS had an observation strategy that included sampling at multiple altitudes and temperatures. We found a broader distribution of in-cloud vertical velocities sampled during IMPACTS than during PLOWS (stan-

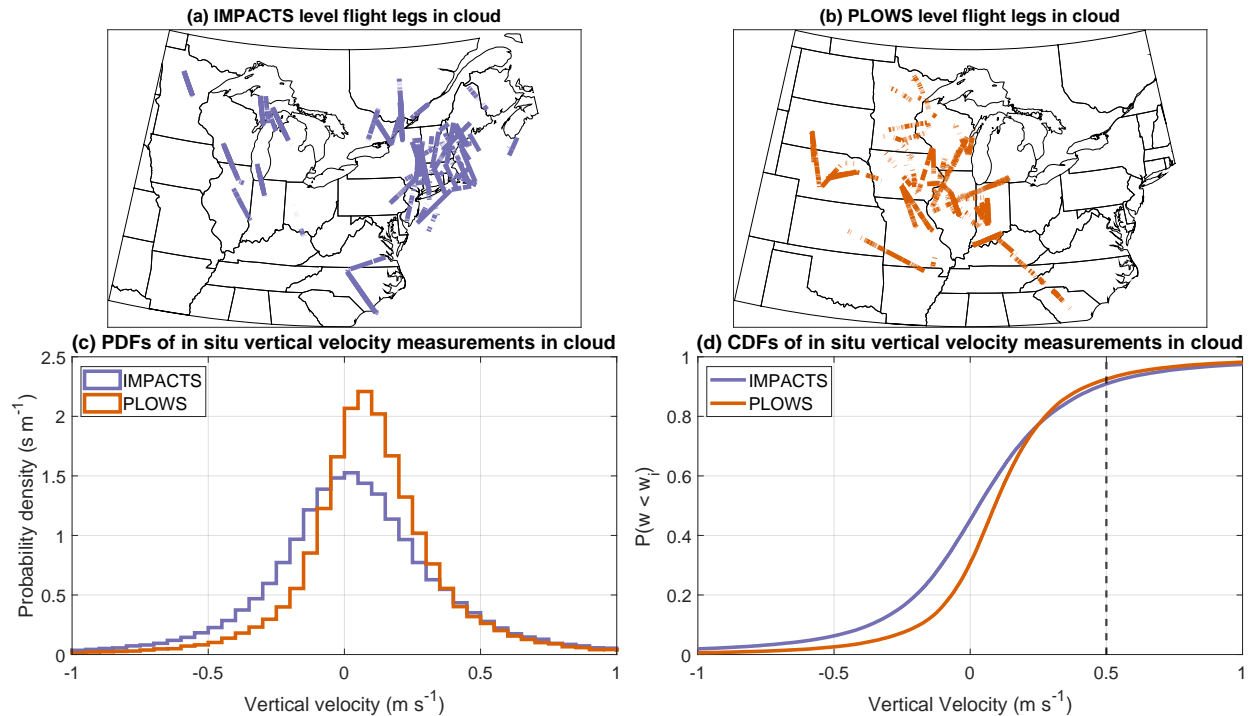


Figure 5.3: Top row: Maps of level flight legs in cloud with air temperature  $< 0^\circ\text{C}$  sampled during (a) IMPACTS and (b) PLOWS. Bottom row: In-cloud vertical velocity measurements taken on level flight legs during IMPACTS and PLOWS, (c) probability density function (PDF) and (d) cumulative density function (CDF).

standard deviations of  $0.56$  and  $0.38 \text{ m s}^{-1}$ , respectively; Fig. 5.3c). Only 9.1% of all in-cloud vertical velocity measurements during IMPACTS, and 7.5% during PLOWS, were  $\geq 0.5 \text{ m s}^{-1}$  (Fig. 5.3d). In-cloud downdrafts were less common than in-cloud updrafts, especially during PLOWS. Just 6.3% of in-cloud vertical velocity measurements during IMPACTS, and 2.6% during PLOWS, were  $\leq -0.5 \text{ m s}^{-1}$ .

In analysis of winter storm aircraft in situ data, there are several ways to sort the data: by air temperature, by altitude above the surface, or by altitude below cloud top. Since cloud top altitudes can vary by several km even within the same storm, and the layer with generating cells tends to follow the cloud top, we have found that sorting by distance from cloud top to be more useful in interpreting physical processes than sorting by air temperature (Fig. 5.4). Points sampled  $< 3 \text{ km}$  below CRS cloud echo top were about twice as likely to have vertical air motion  $\geq 0.5 \text{ m s}^{-1}$ , either upward or downward, than points sampled farther below cloud echo top (Fig. 5.4). Within 3 km of CRS echo top, 13.8% of the points sampled during IMPACTS had upward vertical velocity  $\geq 0.5 \text{ m s}^{-1}$ , compared to 6.5% of the points sampled  $> 3 \text{ km}$  below CRS echo top. For downdrafts, 8.9% of points  $< 3 \text{ km}$  below echo top had vertical velocity  $\leq -0.5 \text{ m s}^{-1}$ , compared to 4.1% of points  $> 3 \text{ km}$  below echo top.

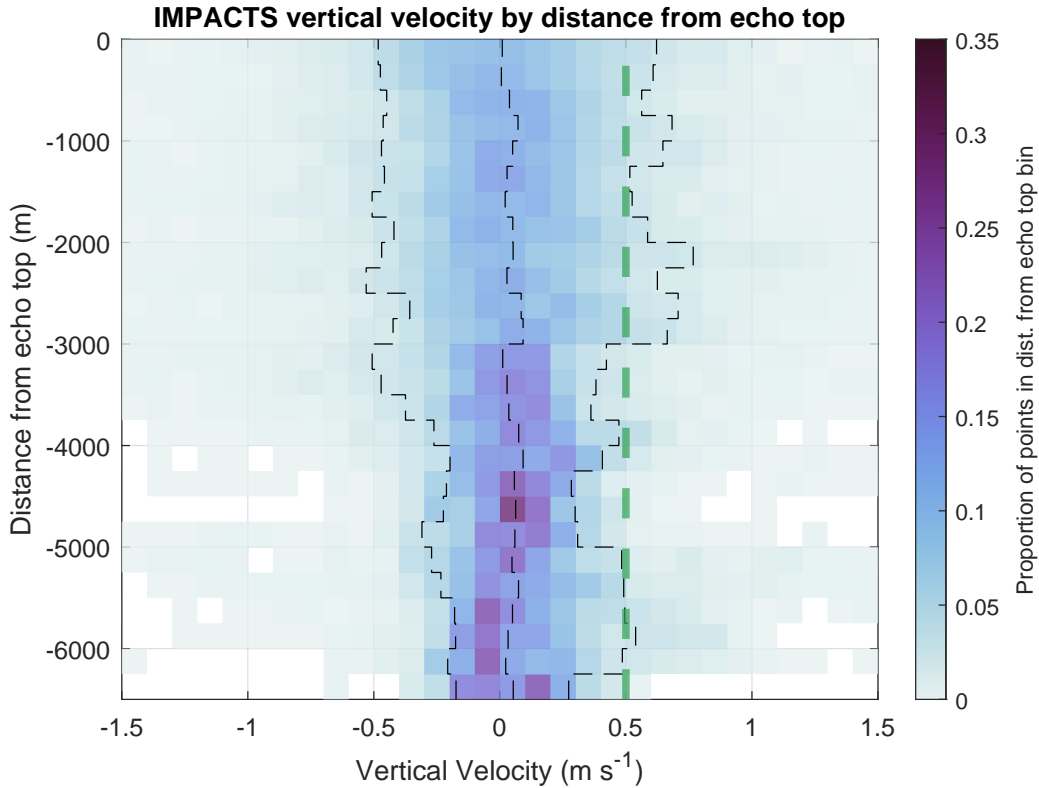


Figure 5.4: 2D histogram of in situ vertical velocity against the P-3 distance below CRS echo top height for in-cloud samples with air temperature  $< 0^{\circ}\text{C}$  during IMPACTS only. The number of points in each bin is normalized by the total number of samples taken at a given distance below echo top. Black dashed lines indicate the 10th, 50th, and 90th percentile of vertical velocity as a function of distance below echo top height. Vertical green dashed line is at  $0.5 \text{ m s}^{-1}$  vertical velocity.

Sorting the vertical velocity data by air temperature mainly illustrates the different sampling strategies and environmental settings between the projects. The vertical velocity distributions sorted by temperature categories are very similar to the overall project distribution for IMPACTS and vary slightly among temperatures for PLOWS (Fig. 5.5). The PLOWS near-cloud top storm environments tended to be colder than those for IMPACTS. As a consequence, PLOWS had more flight legs than IMPACTS at temperatures  $\leq -22^{\circ}\text{C}$ , corresponding to polycrystalline and multiple ice growth modes (Hueholt et al. 2022). The vertical velocity distribution for PLOWS was shifted slightly higher for this low temperature category as compared to PLOWS samples obtained at higher temperatures. Samples at air temperatures between  $-22^{\circ}\text{C}$  and  $-8^{\circ}\text{C}$  represent more than half the samples from both IMPACTS and PLOWS. In this temperature range, ice growth mode is a function of both temperature and relative humidity, with multiple growth mode at low supersaturations with respect to ice, tabular growth for  $RH_{\text{water}} < 100\%$

and branched growth for  $RH_{water} > 100\%$ . The 140 IMPACTS flight legs between  $-8^{\circ}\text{C}$  and  $0^{\circ}\text{C}$  corresponding to tabular and columnar ice growth modes, have about 7% of samples capable of lofting snow. The PLOWS data for these temperatures is based on only 2485 100-m horizontal scale samples and shows a distribution shifted toward lower vertical velocity values with only 1% capable of lofting snow. Because of the small sample size, the PLOWS data at these temperatures may not be representative.

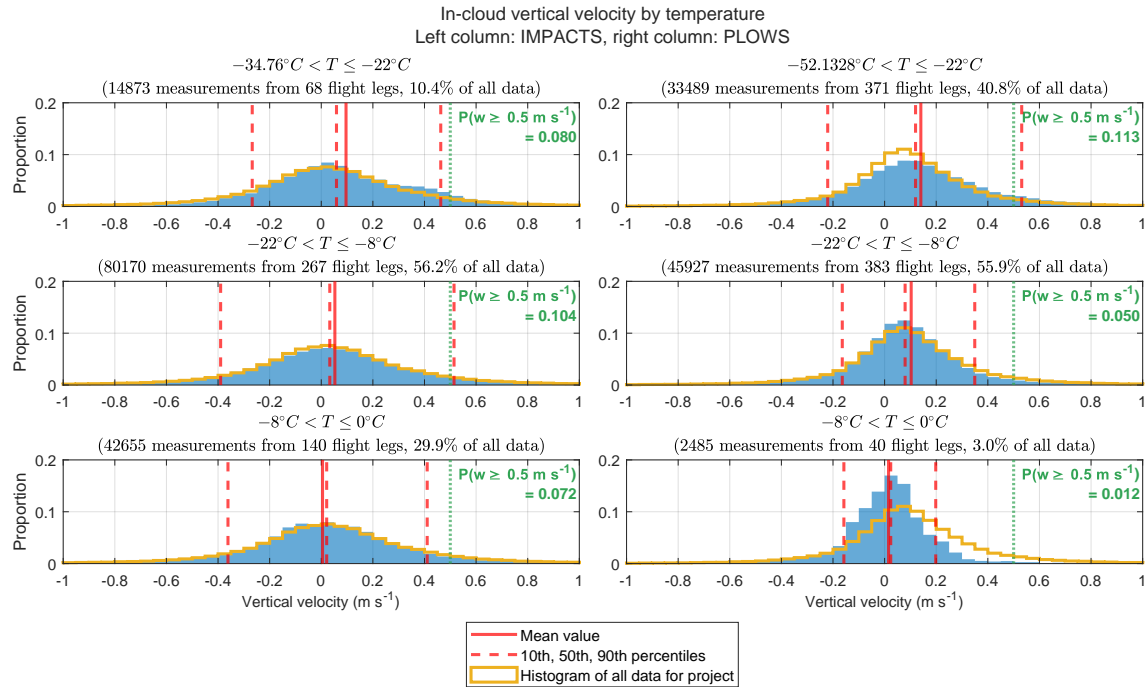


Figure 5.5: Histograms of in-cloud vertical velocity measurements taken on level flight legs at different temperature ranges, from colder temperatures at the top to warmer temperatures at the bottom, as indicated in subplot titles along with the sample size at each temperature range. Data are averaged over 1 s corresponding to about 100 m based on typical air speeds. Distributions from IMPACTS are shown in the left column, and distributions from PLOWS are shown in the right column. Temperature ranges were chosen to correspond with different ice growth modes (Hueholt et al. 2022). Overlays on each panel are as in Fig. 5.4. Gold lines show the distribution for all IMPACTS and PLOWS data in straight and level legs from Fig. 5.3c.

Of the IMPACTS in-cloud vertical velocity data sampled at times when a low pressure center can be tracked using ERA5 data (Tomkins et al. 2024a), most of the sampling was done in the northwest quadrant of cyclones (Fig. 5.6). When the data are subset by quadrant, higher proportions of in-cloud vertical velocity measurements  $\geq 0.5 \text{ m s}^{-1}$  are found in the northwest (0.108) and northeast (0.105) quadrants. Air mass boundaries (warm and/or occluded fronts)

**IMPACTS in-cloud level flight legs relative to cyclone**

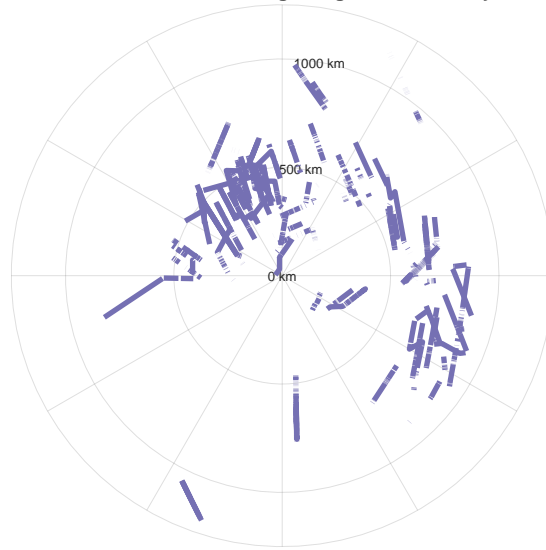


Figure 5.6: In-cloud level flight legs sampled during IMPACTS, shown in a Lagrangian framework relative to the low pressure center as determined using ERA5 data (Tomkins et al. 2024a). The origin of this figure represents the location of the low pressure center.

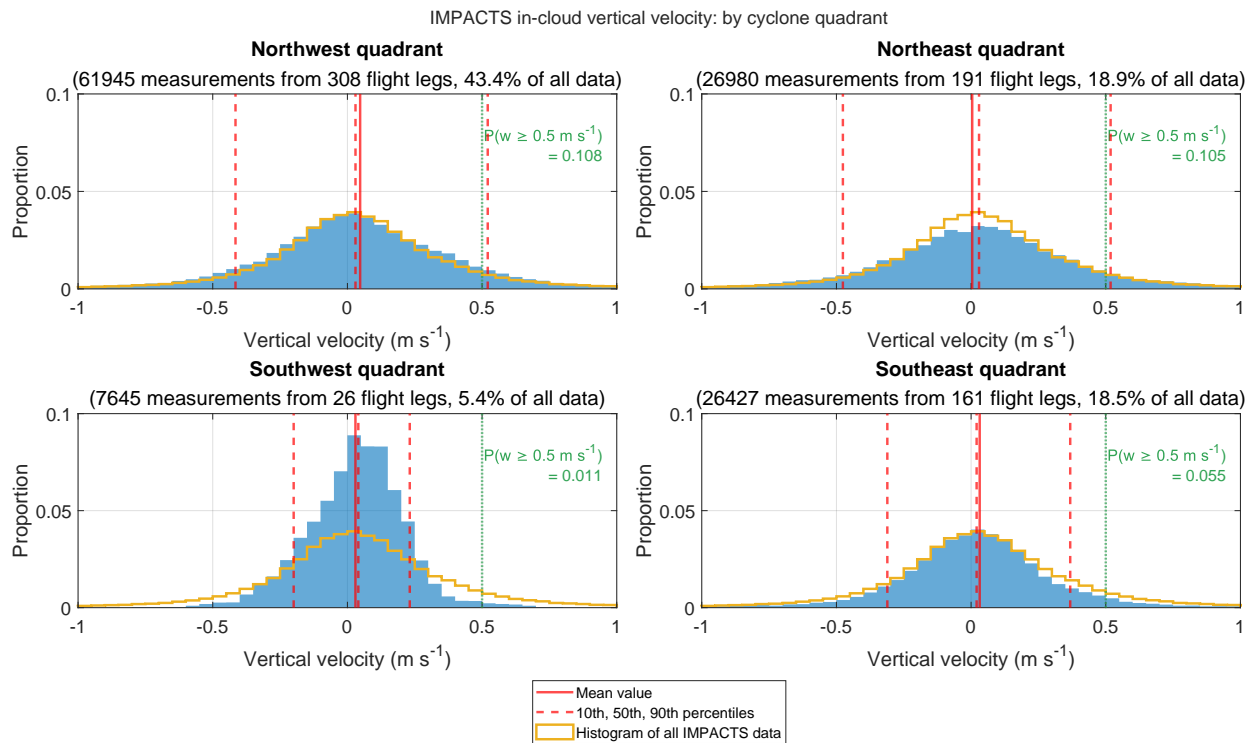


Figure 5.7: Distribution of in-cloud vertical velocity sampled during IMPACTS by cyclone quadrant. Overlays in each subplot are as in Fig. 5.5.

are often found in the northwest and northeast quadrants, which are generally associated with frontogenesis and strong vertical wind shear (which may be sufficient for Kelvin-Helmholtz instability). The warmer air mass above warm fronts also often contains local potential instability (Markowski and Richardson 2010, p. 132). Release of instability near warm and occluded frontal surfaces likely results in a broader distribution of vertical velocity in the northwest and northeast quadrants.

Because the research flights during IMPACTS and PLOWS targeted regions of likely snow growth, we expect the proportion of aircraft samples with vertical velocity  $\geq 0.5 \text{ m s}^{-1}$  to be an overestimate compared to the proportion of the entire storm volume with vertical velocity  $\geq 0.5 \text{ m s}^{-1}$ . Therefore, the IMPACTS and PLOWS velocity distributions (Fig. 5.3) showing less than  $\sim 10\%$  of in-cloud measurements of upward air velocity  $\geq 0.5 \text{ m s}^{-1}$  represent an upper bound, so strong enough upward motions to loft precipitation-size ice particles are only present in a small portion of winter storms. We found vertical velocity measurements  $\geq 0.5 \text{ m s}^{-1}$  more frequently when subsetting to measurements taken  $< 3 \text{ km}$  below CRS echo top (Fig. 5.4). The preferred locations of stronger upward motions near cloud top relates to the frequent occurrence of generating cells at these locations. It is also inconsistent with the locations of frontal surfaces which tend to be in the lower portions of the storm (Wallace and Hobbs 2006).

### 5.1.3 Updraft envelope properties

We identified 2253 updraft envelopes during IMPACTS and 1079 updraft envelopes during PLOWS. Many of those updraft envelopes were narrow and weak, i.e., the updraft envelope threshold ( $0.5 \text{ m s}^{-1}$ ) was only barely met for a brief time period (few hundred m distance). The mean length of updraft envelopes observed during both IMPACTS and PLOWS was  $0.53 \text{ km}$ , while the median updraft envelope length was  $0.27 \text{ km}$  for IMPACTS and  $0.24 \text{ km}$  for PLOWS. Overall,  $90\%$  of updrafts envelopes were shorter than  $1.2 \text{ km}$ . The median value of the updraft envelope mean vertical velocity was  $0.75 \text{ m s}^{-1}$  for IMPACTS and  $0.72 \text{ m s}^{-1}$  for PLOWS. There does not appear to be a correlation between updraft envelope length and mean vertical velocity, i.e., wider updrafts are not necessarily stronger (Fig. 5.8a). Keeping in mind that updraft envelopes are defined as contiguous spans along flight track with  $w > 0.5 \text{ m s}^{-1}$ , median envelope mean vertical velocity values are only slightly higher,  $0.74 \text{ m s}^{-1}$  for IMPACTS and  $0.72 \text{ m s}^{-1}$  for PLOWS. In aggregate, the more numerous narrower updraft envelopes contributed more of the upward mass flux than the more sparse wider envelopes (Fig. 5.8b). During IMPACTS,  $65\%$  of the upward mass flux (Eq. 4.1) within envelopes meeting our criteria was contributed by updraft envelopes shorter than  $2 \text{ km}$ . For PLOWS, this value was  $64\%$ .

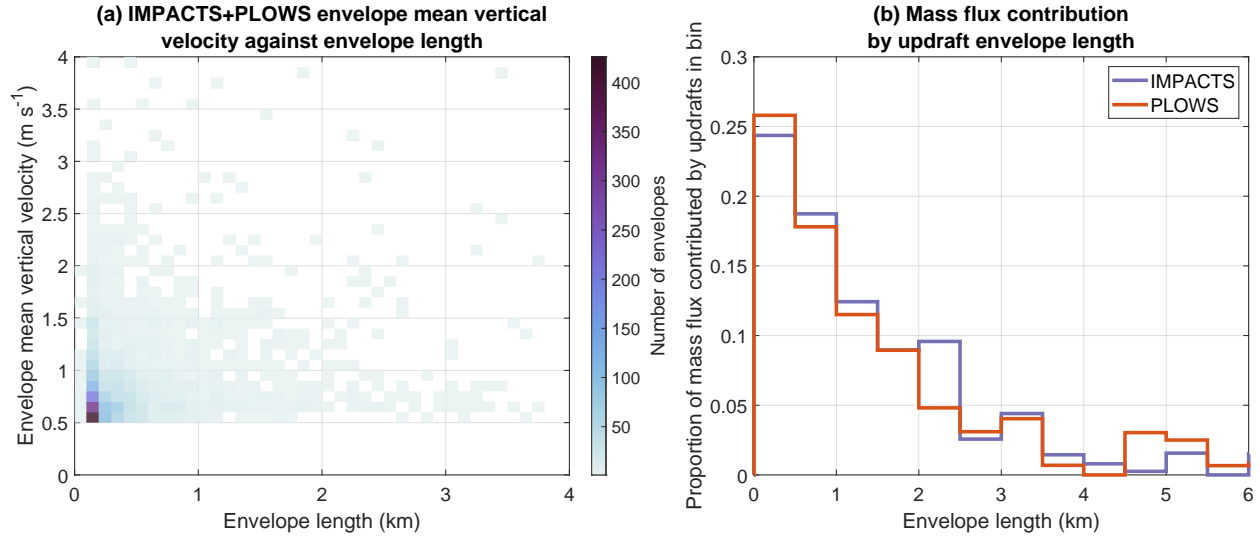


Figure 5.8: **(a)** 2-D histogram of updraft envelope mean vertical velocity against updraft envelope length, for IMPACTS and PLOWS combined. **(b)** The proportion of total upward mass flux contributed by updraft envelopes within 0.5-km length bins for IMPACTS and PLOWS separately.

## 5.2 Modeled distributions of in-cloud vertical velocity in winter storms

As a rough prototype of a potential future line of inquiry, we compare our observed distributions of vertical velocity to model output from colleagues who used the Weather Research and Forecasting Model (WRF) to simulate winter storms. One of the simulated cases was a snow storm that occurred on 1-3 February 2016 in the Midwest United States (Lackmann and Thompson 2019, Gary Lackmann, personal communication), the other case occurred on 7 February 2020 in the Northeast United States (this storm was sampled during IMPACTS; Brian Colle, personal communication). Both simulations used Thompson microphysics (Thompson et al. 2004) and other key parameterization settings were similar. For both simulations we focus on a time interval during the mature stage of the storm. For the 1-3 February 2016 case, we examine four output time steps at 3 km horizontal grid spacing, each 15 min apart. For the 7 February 2020 case, we examine nine output time steps at 2 km horizontal grid spacing, also with 15 min between each output time step.

We define in-cloud grid points in the model output as those with a total cloud water and cloud ice mixing ratio ( $q_c + q_i$ ) of at least  $10^{-3}$  g kg<sup>-1</sup>. We also subset to grid points with a temperature between  $-40^{\circ}\text{C}$  and  $0^{\circ}\text{C}$ . Across all of the time steps, there was a total of roughly 2.6 million grid points meeting these conditions in the 2016 case simulation, and roughly 4.1

Observed and modeled in-cloud vertical velocity distributions for winter storms ( $-40^{\circ}\text{C} \leq T < 0^{\circ}\text{C}$ )

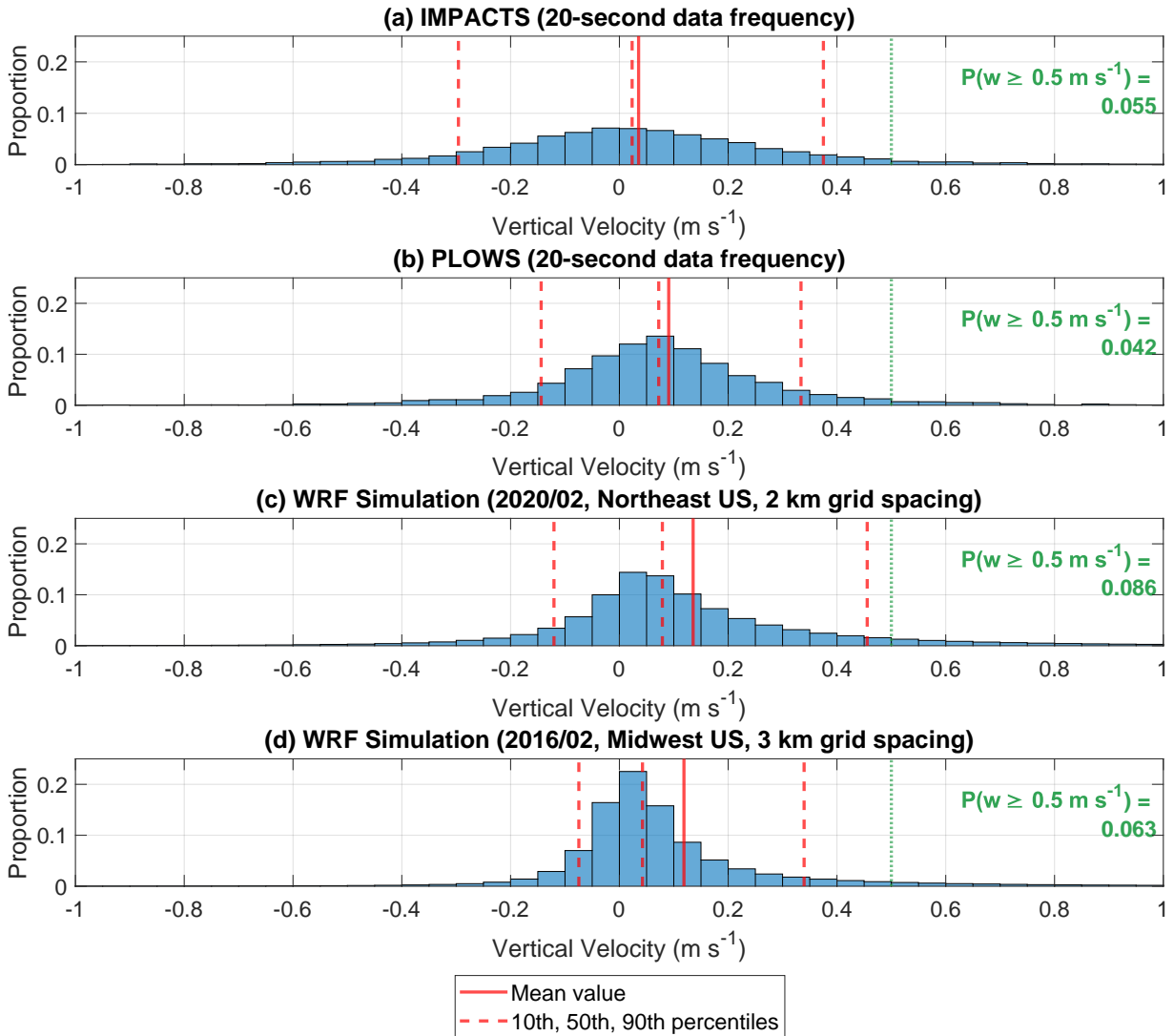


Figure 5.9: Histograms of in-cloud vertical velocity, in terms of the proportion of data within each bin, for **(a)** IMPACTS, **(b)** PLOWS, and WRF simulations of **(c)** the 1-3 February 2016 case and **(d)** the 7 February 2020 case. In this figure, the data from IMPACTS and PLOWS are smoothed and subsampled to 20-second averages (based on typical airspeeds, approximately 2 km spatial scale). In each panel, the proportion of points where vertical velocity  $\geq 0.5 \text{ m s}^{-1}$  is annotated in green, and the mean, 10th percentile, 50th percentile, and 90th percentile of the vertical velocity are shown using vertical lines as indicated by the legend.

million grid points meeting these conditions in the 2020 case simulation.

Because vertical velocity is scale-variant as discussed in Sect. 4.1, we compare the simulated distributions of in-cloud vertical velocity to observed data which are smoothed and subsampled to 20-second averages (Fig. 5.9). As the aircraft ground speed was typically around  $100 \text{ m s}^{-1}$ , 20 s represents about 2 km-resolution data. Averaging and subsampling in this way reduces the proportion of observed in-cloud vertical velocities  $\geq 0.5 \text{ m s}^{-1}$  during IMPACTS and PLOWS to 5.5% and 4.2%, respectively.

The distributions of in-cloud vertical velocity for the two simulated cases have some notable discrepancies compared to the observed data sets from IMPACTS and PLOWS (Fig. 5.9). Although this comparison is not "apples to apples," as it is between the entire in-cloud volumes at altitudes above  $0^\circ\text{C}$  for the model output versus along the flight tracks for the observations, some information relevant to motivating future work can be gleaned. Given that PLOWS in particular, and IMPACTS to an extent, targeted regions where upward motions and ice growth were expected, their observed updraft distributions are likely upper bounds on what would be present over the entire storm volume. Yet, the models show substantially higher proportions of values  $> 0.5 \text{ m s}^{-1}$  (WRF Northeast case 8.6%, WRF Midwest case 6.3%) as compared to IMPACTS (5.5%) and PLOWS (4.2%). In-cloud downdrafts are noticeably more rare in the model output compared to the observations, as indicated by the 10th percentile of vertical velocity ( $-0.30 \text{ m s}^{-1}$  for IMPACTS,  $-0.14 \text{ m s}^{-1}$  for PLOWS,  $-0.12 \text{ m s}^{-1}$  for the WRF Northeast case, and  $-0.07 \text{ m s}^{-1}$  for the WRF Midwest case). Numerical models with grid spacing  $> 1 \text{ km}$  do not resolve turbulence and mixing well, which can lead to updrafts that are too strong, even compared to observed data at the same scale (Bryan et al. 2003). Detailed comparisons with model output are beyond the scope of this study. Future work can improve the comparison methods and address whether there is a systemic overestimate in modeled vertical velocity distributions toward stronger values at 2 km scales typical of mesoscale model simulations.

### 5.3 Observed in-cloud relative humidity distribution in winter storms

As another prototype for future work, we examine the in situ-observed distribution of  $RH_{ice}$  from IMPACTS as a function of the distance from CRS echo top height (Fig. 5.10).  $RH_{ice}$  was measured using a chilled mirror hygrometer on the P-3, which has a measurement uncertainty of  $\sim 5\%$ . Therefore, points with measured  $RH_{ice} < 95\%$  are points with ice shrinkage, points with measured  $RH_{ice} > 105\%$  are points with ice growth, and points in between are uncertain.

This preliminary analysis suggests that regions within 2 km of cloud top height are the

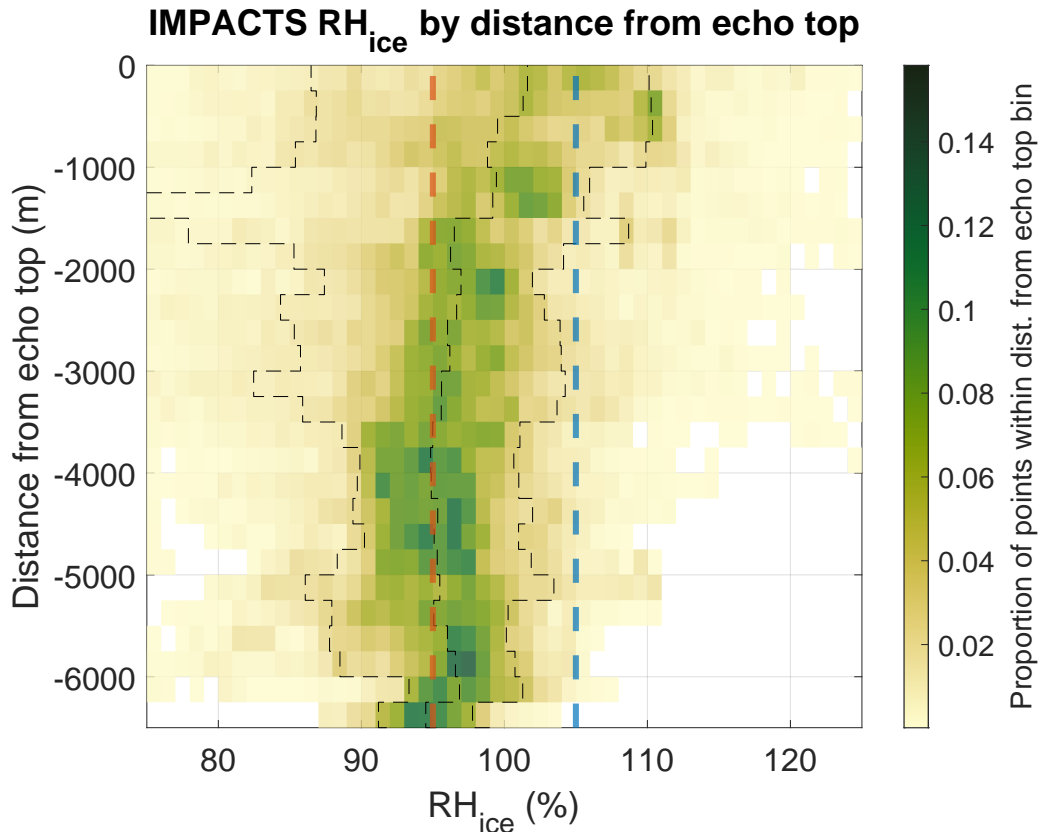


Figure 5.10: 2D histogram of  $RH_{ice}$  against distance below echo top height for IMPACTS in-cloud samples with air temperature  $< 0^{\circ}\text{C}$ . The number of points in each bin is normalized by the total number of samples taken at a given distance from echo top. Black dashed lines indicate the 10th, 50th, and 90th percentile of  $RH_{ice}$  as a function of distance from echo top height. Vertical brown line is at 95%  $RH_{ice}$ , and vertical blue line is at 105%  $RH_{ice}$ .

primary regions of ice mass increases in winter storms. The distribution of  $RH_{ice}$  broadens closer to echo top, and the mode of the  $RH_{ice}$  distribution shifts to higher values at altitudes closer to echo top. Points with  $RH_{ice} > 105\%$  were observed less than one-tenth of the time at all altitudes more than 2 km below echo top height. The median  $RH_{ice}$  value increases from  $\sim 95\%$  at 2 km below echo top height to nearly 105% in the closest 0.5 km below echo top height (Fig. 5.10). Lower regions of cloud ( $> 2$  km below cloud top) are more likely to be regions where ice mass is constant or decreasing.

## 5.4 Conclusions

We used in situ measurements of vertical velocity obtained during winter storms from the IMPACTS (Fig. 5.3a) and PLOWS (Fig. 5.3b) field campaigns to characterize the distributions of

vertical velocity by distance from cloud radar echo top and temperature, and tabulated the horizontal breadth of updrafts. Based on straight and level flight leg data corresponding to about 100-m spatial scale, our key results are:

- Upward motions capable of lofting precipitation-sized ice were often associated with cloud-top generating cells, while regions below generating cell layers typically had much fewer updrafts.
- Vertical velocity exceeded  $0.5 \text{ m s}^{-1}$  in less than 10% of the samples (9.1% of 100-m scale measurements during IMPACTS and 7.5% during PLOWS).
- Most (57%) updraft envelopes exceeding a threshold of  $0.5 \text{ m s}^{-1}$  were less than 300 m in breadth (median envelope lengths of 0.27 km for IMPACTS and 0.24 km for PLOWS). 90% of updraft envelopes were less than 1.2 km in breadth.
- The more numerous narrower updrafts ( $< 2 \text{ km}$ ) contributed more upward mass flux within updraft envelopes than the scarcer wider updrafts.

These results show that the types of winter storms sampled by IMPACTS and PLOWS (extratropical cyclones, e.g., Nor'easters, Alberta clippers, and Great Plains cyclones) contain mostly weak vertical motions incapable of lofting precipitation-size ice. Our findings are not applicable to orographic or lake-effect snow storms which superimpose additional forcings on extratropical cyclones. The findings that upward motions ( $\geq 0.5 \text{ m s}^{-1}$ ) are present in only small portions of the cloud volume and are most common in regions near cloud top generating cells extends and confirms the work of Rosenow et al. (2014) who used airborne radar data obtained during PLOWS. In addition to generating cells, Kelvin-Helmholtz waves also yield upward motions  $\geq 0.5 \text{ m s}^{-1}$  in some regions of winter storms but these also manifest as sporadic, small convective scale updrafts ( $< 2 \text{ km}$  across; e.g., Rauber et al. 2017).

Even when one overcompensates for the sampling bias of updraft envelopes size by multiplying aircraft measured length by 3.2 (Sect. 4.2.6), the vast majority of updrafts potentially capable of lofting snow are  $< 1 \text{ km}$ . There is *a lack of observational evidence supporting the existence of  $> 25 \text{ km}$  broad areas of uplift capable of lofting precipitation-sized ice in flat-land winter storms*. The strengths and sizes of actual updrafts within these storms bear little resemblance to the conceptual model of a 25+ km wide updraft regions with vertical air motions  $> 0.5 \text{ m s}^{-1}$  in Lackmann and Thompson (2019). Lackmann and Thompson (2019) mistakenly cited broad-scale lofting as a primary factor in residence time. They ignored other factors in residence time including the altitudes where precipitation-size ice first forms and begins to fall. Convective-scale overturning motions are important to produce upward air motion  $\geq 0.5 \text{ m s}^{-1}$ . Gradual

large-scale layer lifting within winter storms may contribute to the destabilization of the environment and to the subsequent release of instability allowing for cloud-top generating cells to form, as discussed in previous work on conditional symmetric instability and slant-wise convection (e.g., Xu 1992; Schultz and Schumacher 1999; Morcrette and Browning 2006).

Generating cells near the top of winter storms are key regions where cloud ice can grow to precipitation size by vapor deposition and riming. The precipitation particles falling from cloud top are then advected horizontally by the mean flow. Convergent flow may result in locally higher precipitation particle concentrations (Janiszewski et al. 2023), or sheared flow may "smear" ice streamers together (Tomkins 2024). To maintain conditions of supersaturation with respect to water requires stronger updrafts than it does to maintain supersaturation with respect to ice. Below the layer of generating cells, vertical motions are weaker, the air is less likely to be supersaturated with respect to ice, and ice mass shrinkage via sublimation is more likely. Sublimation can be a self-limiting process, as it increases the ambient relative humidity which later particles fall through. But, vertical air motions and ambient RH do not completely describe the conditions immediately adjacent (few microns) to the surface of individual ice particles. When there is nonzero airflow around an ice crystal (such as when it is falling and/or advected by horizontal winds), ventilation can enhance vapor density at an ice particle's corners, increasing RH immediately adjacent to the particle above ambient values (Hallett and Mason 1958; Keller and Hallett 1982; Takahashi et al. 1991; Fukuta and Takahashi 1999). Quantitative ventilation effects for the complex shapes of natural snow are poorly understood and hence often not accounted for in numerical models but may well turn out to be an important process in ice mass growth (Wang 2002; Bailey and Hallett 2002).

Surface snowfall rates and accumulations depend on where within the storm precipitation-size particles form and conditions along their trajectories to the ground. Precipitation-sized ice that forms at higher altitudes has more time to be horizontally advected and dispersed than ice particles that only grow to sufficient size and begin to fall at lower altitudes. Preliminary analysis of in situ-observed  $RH_{ice}$  data from IMPACTS lends evidence that regions within  $\sim 2$  km of cloud top are where most ice growth occurs in winter storms (Fig. 5.10). During the 2023 IMPACTS deployment, two laser diode hygrometers (DLHs; Diskin et al. 2002) were used in addition to the chilled mirror hygrometer to measure humidity. These independent measurements of  $RH_{ice}$  allow for improved evaluation of data quality. Future analysis of in situ RH data from IMPACTS in the context of in situ vertical air motions and coordinated cloud radar data is likely to yield further insights into ambient conditions and processes associated with ice mass growth and shrinkage.

## CHAPTER

# 6

# CONCLUSIONS

## 6.1 Summary of key findings

We utilized two recent and unique observational data sets to:

1. Investigate the occurrence of gravity waves and their co-occurrence with enhanced reflectivity features and Doppler velocity waves in winter storms in the Toronto, ON, Canada, and New York, NY, USA, metro areas.
2. Characterize the distribution of in-cloud vertical velocity in winter storms and evaluate where and in what portion of winter storms there is strong enough upward motion to loft precipitation-size ice particles.

We used data from networks of high-precision pressure sensors in Toronto and New York to objectively identify pressure wave events with wavelengths  $\leq 170$  km, wave periods  $\leq 67$  min, and amplitudes between 0.45 hPa and 5.5 hPa. Context from reanalysis, radar, and surface weather station data helped determine which of these pressure wave events were gravity waves, as opposed to surface fronts, outflow boundaries, or a wake low. We found only 23 coherent gravity wave events meeting our criteria across 40 months of data. Only 6 gravity wave events co-occurred with surface snowfall. We found no instances of enhanced reflectivity bands in

snow being collocated with gravity waves, and only 3 instances of enhanced reflectivity bands in rain being collocated with gravity waves.

In situ aircraft data from 42 research flights into winter storms during the PLOWS and IMPACTS field campaigns revealed an in-cloud 100-m scale vertical velocity distribution centered near  $0 \text{ m s}^{-1}$  and with  $< 10\%$  of in-cloud measurements having upward motion  $\geq 0.5 \text{ m s}^{-1}$ . Most updrafts were small in spatial scale. 90% of the updraft envelopes we identified were  $< 1.2 \text{ km}$  long. We found upward motions  $\geq 0.5 \text{ m s}^{-1}$  to be more common closer to cloud radar echo top, where there are cloud-top generating cells and colder temperatures. Our results reaffirm the conclusions of previous studies (e.g., Rosenow et al. 2014) which found stronger vertical motions associated with cloud-top generating cells and wave motions. Nearly everywhere else in winter storms vertical motions capable of lofting snow are scarce.

## 6.2 Implications

### 6.2.1 On gravity waves in winter storms

While there are individual cases in the literature indicating that gravity waves are an important contributor to heavy snowfall rates, our findings suggest that gravity waves do not commonly yield enhanced reflectivity features in flat-land winter storms. For example, the gravity wave case presented by Bosart et al. (1998) and Zhang et al. (2002) was unusual in many ways. That gravity wave underwent a resonant interaction with an upper-level front leading to its amplification to roughly 10 hPa peak-to-trough (we did not detect any pressure wave events with a peak-to-trough amplitude  $> 5.5 \text{ hPa}$ ). The gravity wave also became "inseparable" from the upper-level front in this process (Zhang et al. 2002), obfuscating the degree to which the gravity wave and the front respectively contributed to the heavy snow event. Other cases have been recorded of terrain-generated gravity waves contributing to heavy snowfall events (e.g., Gaffin et al. 2003). Orographic processes are not relevant in our study regions along the Northeast US coastline or in Southern Ontario.

The surface cyclone-relative locations of gravity waves in our results and in the literature, as well as the typical surface cyclone track associated with snow events in the Northeast US also seem to imply that gravity waves would be uncommon during snow storms in the Northeast US. Gravity waves are most often found east of cyclones, ahead of warm fronts (Table 3.3 and Uccellini and Koch 1987). Cyclone tracks during Northeast US snow events are often offshore (Fig. 3.11), meaning that gravity waves would be expected even farther offshore. Hence, we only detected one gravity wave event during a snow storm in the New York City metro area.

## 6.2.2 On winter storm in-cloud vertical velocities

Smaller-scale updrafts associated with cloud-top generating cells appear to be the main region of ice growth in winter storms. Regions of relatively high precipitation ice mass per unit volume could form in cloud-top generating cells, then the resulting ice streamers are tilted and smeared during their descent through layers with wind shear (Tomkins 2024). Numerical weather models need to reasonably represent the distributions of naturally-occurring vertical velocity magnitudes and updraft sizes in order to improve prediction of snowfall rates and accumulations.

The hypothesis that broad-scale (25+ km) lofting of precipitation-size ice particles is commonly of importance to generating locally-enhanced surface snowfall rates (Lackmann and Thompson 2019) likely originated in part from mistaken interpretations of previous work that did not account for the scales of the observations cited and the scale variance of vertical air motions (Section 4.1.2). Broad-scale upward motion strong enough to loft snow particles appears to be rare in flat-land winter storms. Additionally, common practice in plotting vertical cross-sections with high vertical to horizontal aspect ratios yields vertically exaggerated plots and distorts features such as sloping fronts making them appear much more upright than they actually are.

## 6.3 Future work

There are still remaining questions on the nature of Doppler velocity waves in winter storms and their relevance (or lack thereof) to increased snow rates. We found in a few cases that gravity waves co-occurred with Doppler velocity waves in the New York City and Toronto metro areas (Table 3.4). Since gravity waves during surface snow were rare at our locations, we do not have a sufficient sample to draw conclusions about the relationship among gravity waves, Doppler velocity waves, and snow rates. Tomkins (2024) found that time periods with Doppler velocity waves were associated with slightly higher snow rates than time periods without Doppler velocity waves in the New York City and Boston metro areas. Future work could examine if there is a causal relationship between Doppler velocity waves and enhanced snow rates, or if this is coincidence or caused by a different physical mechanism (i.e., if both Doppler velocity waves and enhanced snow rates are both commonly present in similar environments but otherwise unrelated). Other possible mechanisms should be explored as potential primary causes for the Doppler velocity waves, such as flow anomalies associated with potential vorticity dipoles (Leonardo and Colle 2023). Kelvin-Helmholtz waves may also produce Doppler velocity waves on scales of  $\sim 3$  km Houser and Bluestein (2011); Barnes et al. (2018) but most Kelvin-Helmholtz

waves are at smaller horizontal scales (e.g., Browning 1971b; Plant and Keith 2007). To determine if the shear instability required for Kelvin-Helmholtz waves is present, information on the wind and thermodynamic profile are required. Either weather balloon or vertical wind profiler data can provide the wind profile. Weather balloon data or other in situ measurements such as from a drone or aircraft are needed to provide the thermodynamic profile within cloud.

There are many potential avenues for future work with the data collected during IMPACTS. In order to further explore the ambient environmental conditions associated with ice particle growth and shrinkage, in situ humidity data need to be analyzed (Hueholt et al. 2022). In the 2023 IMPACTS deployment, two diode laser hygrometers (DLH; Diskin et al. 2002) with different laser path lengths were used to precisely measure in situ humidity on the P-3, in addition to a standard chilled mirror hygrometer which was used during all three winter seasons of IMPACTS deployments. The Particle Habit Imaging and Polar Scattering (PHIPS) probe (Abdelmonem et al. 2011) provided high-resolution particle images during each IMPACTS deployment. The PHIPS images are of adequate resolution to discern ice particle shapes and degrees of riming, which will inform on the sequences of growth modes of the ice particles (Hueholt et al. 2022). Corresponding humidity data will indicate whether ice particles are actively growing where they were observed ( $RH_{ice} > 100\%$ ) or not. Subsequent analysis of ambient environmental properties examined in this study with corresponding RH will address basic questions regarding the conditions associated with ice mass increases and decreases. If there is substantial ice shrinkage in winter storms below generating cell layers, then the ground-relative height of generating cells may be relevant to snow rate. For example, if generating cells are present at 7 km altitude, then more of the falling snow could sublimate than if generating cells were present at 5 km altitude.

Current conceptual models assume  $RH_{ice} > 100\%$  in radar echo and that precipitation-size ice grows gradually and relatively continuously as it descends from generating cells near cloud top to the surface (e.g., Plummer et al. 2014, 2015; Rosenow et al. 2014). In contrast, IMPACTS data sets on vertical air motions suggest that ice growth is likely to be more episodic than continuous. Most updrafts stronger than  $0.5 \text{ m s}^{-1}$  were  $< 300 \text{ m}$  across, with regions of weak or downward vertical motion in between. Ice particles likely grow within these narrow updrafts for a brief period of time (on the order of minutes) relative to their overall residence time in cloud (on the order of 1 hr to fall 4 km). Our findings are consistent with a conceptual model for flat-land winter storms in which most ice growth occurs near cloud top in overturning generating cells associated with some combination of conditional, potential, and/or shear instability. While the large-scale, weak vertical motions associated with synoptic-scale forcing in winter storms likely do not directly yield or maintain supersaturation with respect to ice over a large portion of cloud volume, they may be relevant to yielding, maintaining, and/or

releasing the instability which leads to overturning cloud-top generating cells. Weather balloon observations in regions of winter storms with and without conditional, potential, and shear instability would be needed to examine this idea, along with context on large-scale forcing for ascent which would likely come from reanalysis model output. A modelling approach would require careful analysis of the large scale forcing for vertical air motion along with the change in local stability with time in advance of generating cell formation over a given area.

Gravity waves appear unlikely to be a primary process for enhancing snowfall in typical flat-land winter storms. Further improvements in understanding the physical processes associated with ice mass increases will benefit from filling two major gaps in current knowledge. While ground-based and airborne observations have yielded many snapshots of winter storm generating cell structures, we lack key information on their life cycles. Do typical generating cells persist for 10 minutes or an hour? How does the distribution of cell duration relate to the sources of instability? Observation platforms that can follow a set of generating cells are needed to address these questions. The small spatial scales of updrafts (often  $< 300$  m) suggests that numerical model grid spacing  $\geq 1$  km may be inadequate for realistically simulating cloud processes in winter storms (as found by Bryan et al. 2003, for deep convection). To date, quantitative estimates of ventilation effects come from a few laboratory studies (e.g., Bailey and Hallett 2002) and modelling of idealized ice shapes (e.g., Wang 2002). More laboratory work is needed for both idealized and more realistic ice shapes while varying  $RH_{ice}$  within naturally occurring ambient values.

## REFERENCES

- Abdelmonem, A., M. Schnaiter, P. Amsler, E. Hesse, J. Meyer, and T. Leisner, 2011: First correlated measurements of the shape and light scattering properties of cloud particles using the new Particle Habit Imaging and Polar Scattering (PHIPS) probe. *Atmospheric Measurement Techniques*, **4** (10), 2125–2142, <https://doi.org/10.5194/amt-4-2125-2011>.
- Adam, D., 2022: TONGA VOLCANO CREATED PUZZLING ATMOSPHERIC RIPPLES. *Nature*, **602**, 497.
- Adams-Selin, R. D., 2020: Impact of Convectively Generated Low-Frequency Gravity Waves on Evolution of Mesoscale Convective Systems. *Journal of the Atmospheric Sciences*, **77** (10), 3441–3460, <https://doi.org/10.1175/JAS-D-19-0250.1>.
- Adams-Selin, R. D., and R. H. Johnson, 2010: Mesoscale Surface Pressure and Temperature Features Associated with Bow Echoes. *Monthly Weather Review*, **138** (1), 212–227, <https://doi.org/10.1175/2009MWR2892.1>.
- Allen, G., and Coauthors, 2013: Gravity-wave-induced perturbations in marine stratocumulus: Gravity-Wave-Induced Perturbations in Marine Stratocumulus. *Quarterly Journal of the Royal Meteorological Society*, **139** (670), 32–45, <https://doi.org/10.1002/qj.1952>.
- Allen, L., 2024: Data for "Objectively identified mesoscale surface air pressure waves in the context of winter storm environments and radar reflectivity features: a 3+ year analysis". Zenodo, [Dataset], <https://doi.org/10.5281/zenodo.11373040>.
- Allen, L., L. Tomkins, and S. Yuter, 2023a: 04 Feb 2022 KOKX Reflectivity and Doppler Velocity Waves. Series: Supplemental videos of the paper "Objective identification of pressure wave events from networks of 1-Hz, high-precision sensors", TIB AV-Portal [video], <https://doi.org/10.5446/62540>.
- Allen, L., L. Tomkins, and S. Yuter, 2023b: 14 Sep 2021 KOKX Reflectivity and Doppler Velocity Waves. Series: Supplemental videos of the paper "Objective identification of pressure wave events from networks of 1-Hz, high-precision sensors", TIB AV-Portal [video], <https://doi.org/10.5446/62542>.
- Allen, L., L. Tomkins, and S. Yuter, 2023c: 15 Nov 2020 KBUF Reflectivity and Doppler Velocity Waves. Series: Supplemental videos of the paper "Objective identification of pressure wave events from networks of 1-Hz, high-precision sensors", TIB AV-Portal [video], <https://doi.org/10.5446/62541>.
- Allen, L., L. Tomkins, and S. Yuter, 2023d: 25 Feb 2022 KBUF Reflectivity and Doppler Velocity Waves. Series: Supplemental videos of the paper "Objective identification of pressure wave events from networks of 1-Hz, high-precision sensors", TIB AV-Portal [video], <https://doi.org/10.5446/62539>.
- Allen, L., and S. E. Yuter, 2024: ERA5 Cross-Sections for NASA IMPACTS P-3 Flight Legs. <https://doi.org/10.17605/OSF.IO/J9VWY>, [Analysis], Publisher: OSF.

- Allen, L. R., and M. A. Miller, 2023: lralen34/pressure-wave-detection-public: Code for Objective identification of pressure wave events from networks of 1-Hz, high-precision sensors. Zenodo [code], <https://doi.org/10.5281/zenodo.10150876>.
- Allen, L. R., L. M. Tomkins, and S. E. Yuter, 2024a: 2021/02/18 KOKX radar 4-panel animation. Copernicus Publications, series: Video Supplement to "Objectively identified mesoscale surface air pressure waves in the context of winter storm environments and radar reflectivity features: a 3+ year analysis", TIB AV-Portal [video], <https://doi.org/10.5446/67765>.
- Allen, L. R., L. M. Tomkins, and S. E. Yuter, 2024b: 2023/04/01 KBUF radar 4-panel animation. Series: Video Supplement to "Objectively identified mesoscale surface air pressure waves in the context of winter storm environments and radar reflectivity features: a 3+ year analysis", TIB AV-Portal [video], <https://doi.org/10.5446/67635>.
- Allen, L. R., L. M. Tomkins, and S. E. Yuter, 2024c: 2023/04/05 KBUF radar 4-panel animation. Series: Video Supplement to "Objectively identified mesoscale surface air pressure waves in the context of winter storm environments and radar reflectivity features: a 3+ year analysis", TIB AV-Portal [video], <https://doi.org/10.5446/67633>.
- Allen, L. R., S. E. Yuter, M. A. Miller, and L. M. Tomkins, 2024d: Objective identification of pressure wave events from networks of 1 Hz, high-precision sensors. *Atmospheric Measurement Techniques*, **17** (1), 113–134, <https://doi.org/10.5194/amt-17-113-2024>.
- American Meteorological Society, 2022: Standard atmosphere - Glossary of Meteorology. URL [https://glossary.ametsoc.org/wiki/Standard\\_atmosphere](https://glossary.ametsoc.org/wiki/Standard_atmosphere).
- American Meteorological Society, 2024: Pseudoadiabatic lapse rate - Glossary of Meteorology. URL [https://glossary.ametsoc.org/wiki/Pseudoadiabatic\\_lapse\\_rate](https://glossary.ametsoc.org/wiki/Pseudoadiabatic_lapse_rate).
- Amores, A., S. Monserrat, M. Marcos, D. Argüeso, J. Villalonga, G. Jordà, and D. Gomis, 2022: Numerical Simulation of Atmospheric Lamb Waves Generated by the 2022 Hunga-Tonga Volcanic Eruption. *Geophysical Research Letters*, **49** (6), <https://doi.org/10.1029/2022GL098240>.
- Anthony, R. E., A. T. Ringler, D. C. Wilson, and E. Wolin, 2018: Do Low-Cost Seismographs Perform Well Enough for Your Network? An Overview of Laboratory Tests and Field Observations of the OSOP Raspberry Shake 4D. *Seismological Research Letters*, **90** (1), 219–228, <https://doi.org/10.1785/0220180251>.
- Bailey, M., and J. Hallett, 2002: Nucleation effects on the habit of vapour grown ice crystals from 18 to 42C. *Quarterly Journal of the Royal Meteorological Society*, **128** (583), 1461–1483, <https://doi.org/10.1002/qj.200212858304>.
- Barnes, H. C., J. P. Zagrodnik, L. A. McMurdie, A. K. Rowe, and R. A. Houze, 2018: Kelvin–Helmholtz Waves in Precipitating Midlatitude Cyclones. *Journal of the Atmospheric Sciences*, **75** (8), 2763–2785, <https://doi.org/10.1175/JAS-D-17-0365.1>.
- Barrick, J. D. W., J. A. Ritter, C. E. Watson, M. W. Wynkoop, J. K. Quinn, and D. R. Norfolk, 1996: Calibration of NASA Turbulent Air Motion Measurement System. URL <https://ntrs.nasa.gov/citations/19970010469>.

- Baxter, M. A., and P. N. Schumacher, 2017: Distribution of Single-Banded Snowfall in Central U.S. Cyclones. *Weather and Forecasting*, **32** (2), 533–554, <https://doi.org/10.1175/WAF-D-16-0154.1>.
- Bedard, A. J., 1978: Infrasound Originating Near Mountainous Regions in Colorado. *Journal of Applied Meteorology and Climatology*, **17** (7), 1014–1022, [https://doi.org/10.1175/1520-0450\(1978\)017<1014:IONMRI>2.0.CO;2](https://doi.org/10.1175/1520-0450(1978)017<1014:IONMRI>2.0.CO;2).
- Bhatia, A., and H. Fountain, 2022: ‘It’s Super Spectacular.’ See How the Tonga Volcano Unleashed a Once-in-a-Century Shockwave. *The New York Times*, URL <https://www.nytimes.com/interactive/2022/04/14/upshot/tonga-pressure-wave.html>.
- Bolton, D., 1980: The Computation of Equivalent Potential Temperature. *Monthly Weather Review*, **108** (7), 1046–1053, [https://doi.org/10.1175/1520-0493\(1980\)108<1046:TCOEPT>2.0.CO;2](https://doi.org/10.1175/1520-0493(1980)108<1046:TCOEPT>2.0.CO;2).
- Bonilla, M. G., R. K. Mark, and J. J. Lienkaemper, 1984: Statistical relations among earthquake magnitude, surface rupture length, and surface fault displacement. *Bulletin of the Seismological Society of America*, **74** (6), 2379–2411, <https://doi.org/10.1785/BSSA0740062379>.
- Bosart, L. F., W. E. Bracken, and A. Seimon, 1998: A Study of Cyclone Mesoscale Structure with Emphasis on a Large-Amplitude Inertia–Gravity Wave. *Monthly Weather Review*, **126** (6), 1497–1527, [https://doi.org/10.1175/1520-0493\(1998\)126<1497:ASOCMS>2.0.CO;2](https://doi.org/10.1175/1520-0493(1998)126<1497:ASOCMS>2.0.CO;2).
- Bosch, 2020: BMP388 Data Sheet. URL <https://www.bosch-sensortec.com/products/environmental-sensors/pressure-sensors/bmp388/>.
- Bosch, 2022: BME280 Data Sheet. URL <https://www.bosch-sensortec.com/products/environmental-sensors/humidity-sensors-bme280/>.
- Browning, K. A., 1971a: Radar measurements of air motion near fronts. *Weather*, **26** (8), 320–340, <https://doi.org/10.1002/j.1477-8696.1971.tb04211.x>.
- Browning, K. A., 1971b: Structure of the atmosphere in the vicinity of large-amplitude Kelvin-Helmholtz billows. *Quarterly Journal of the Royal Meteorological Society*, **97** (413), 283–299, <https://doi.org/10.1002/qj.49709741304>.
- Bryan, G. H., J. C. Wyngaard, and J. M. Fritsch, 2003: Resolution Requirements for the Simulation of Deep Moist Convection. *Monthly Weather Review*, **131** (10), 2394–2416, [https://doi.org/10.1175/1520-0493\(2003\)131<2394:RRFTSO>2.0.CO;2](https://doi.org/10.1175/1520-0493(2003)131<2394:RRFTSO>2.0.CO;2).
- Burt, S., 2022: Multiple airwaves crossing Britain and Ireland following the eruption of Hunga Tonga–Hunga Ha’apai on 15 January 2022. *Weather*, **77** (3), 76–81, <https://doi.org/10.1002/wea.4182>.
- Canavero, F. G., and F. Einaudi, 1987: Time and Space Variability of Spectral Estimates of Atmospheric Pressure. *Journal of the Atmospheric Sciences*, **44** (12), 1589–1604, [https://doi.org/10.1175/1520-0469\(1987\)044<1589:TASVOS>2.0.CO;2](https://doi.org/10.1175/1520-0469(1987)044<1589:TASVOS>2.0.CO;2).

- Carr, J. L., Horváth, D. L. Wu, and M. D. Friberg, 2022: Stereo Plume Height and Motion Retrievals for the Record-Setting Hunga Tonga-Hunga Ha'apai Eruption of 15 January 2022. *Geophysical Research Letters*, **49** (9), e2022GL098131, <https://doi.org/10.1029/2022GL098131>.
- Christie, D. R., K. J. Muirhead, and A. L. Hales, 1978: On Solitary Waves in the Atmosphere. *Journal of the Atmospheric Sciences*, **35** (5), 805–825, [https://doi.org/10.1175/1520-0469\(1978\)035<0805:OSWITA>2.0.CO;2](https://doi.org/10.1175/1520-0469(1978)035<0805:OSWITA>2.0.CO;2).
- Coffer, B. E., and M. D. Parker, 2022: Infrasound signals in simulated nontornadic and pre-tornadic supercells. *The Journal of the Acoustical Society of America*, **151** (2), 939–954, <https://doi.org/10.1121/10.0009400>.
- Colle, B. A., 2004: Sensitivity of Orographic Precipitation to Changing Ambient Conditions and Terrain Geometries: An Idealized Modeling Perspective. *Journal of the Atmospheric Sciences*, **61** (5), 588–606, [https://doi.org/10.1175/1520-0469\(2004\)061<0588:SOOPTC>2.0.CO;2](https://doi.org/10.1175/1520-0469(2004)061<0588:SOOPTC>2.0.CO;2).
- Colle, B. A., M. F. Garvert, J. B. Wolfe, C. F. Mass, and C. P. Woods, 2005: The 13–14 December 2001 IMPROVE-2 Event. Part III: Simulated Microphysical Budgets and Sensitivity Studies. *Journal of the Atmospheric Sciences*, **62** (10), 3535–3558, <https://doi.org/10.1175/JAS3552.1>.
- Colle, B. A., and C. F. Mass, 2000: The 5–9 February 1996 Flooding Event over the Pacific Northwest: Sensitivity Studies and Evaluation of the MM5 Precipitation Forecasts. *Monthly Weather Review*, **128** (3), 593–617, [https://doi.org/10.1175/1520-0493\(2000\)128<0593:TFFEOT>2.0.CO;2](https://doi.org/10.1175/1520-0493(2000)128<0593:TFFEOT>2.0.CO;2).
- Colle, B. A., and Y. Zeng, 2004: Bulk Microphysical Sensitivities within the MM5 for Orographic Precipitation. Part I: The Sierra 1986 Event. *Monthly Weather Review*, **132** (12), 2780–2801, <https://doi.org/10.1175/MWR2821.1>.
- Connelly, R., and B. A. Colle, 2019: Validation of Snow Multibands in the Comma Head of an Extratropical Cyclone Using a 40-Member Ensemble. *Weather and Forecasting*, **34** (5), 1343–1363, <https://doi.org/10.1175/WAF-D-18-0182.1>.
- Connolly, P. J., G. Vaughan, P. Cook, G. Allen, H. Coe, T. W. Choullarton, C. Dearden, and A. Hill, 2013: Modelling the effects of gravity waves on stratocumulus clouds observed during VOCALS-UK. *Atmospheric Chemistry and Physics*, **13** (14), 7133–7152, <https://doi.org/10.5194/acp-13-7133-2013>.
- Crawford, A. D., E. A. P. Schreiber, N. Sommer, M. C. Serreze, J. C. Stroeve, and D. G. Barber, 2021: Sensitivity of Northern Hemisphere Cyclone Detection and Tracking Results to Fine Spatial and Temporal Resolution Using ERA5. *Monthly Weather Review*, **149** (8), 2581–2598, <https://doi.org/10.1175/MWR-D-20-0417.1>.
- Cronce, M., R. M. Rauber, K. R. Knupp, B. E. Jewett, J. T. Walters, and D. Phillips, 2007: Vertical Motions in Precipitation Bands in Three Winter Cyclones. *Journal of Applied Meteorology and Climatology*, **46** (10), 1523–1543, <https://doi.org/10.1175/JAM2533.1>.

- de Groot-Hedlin, C. D., M. A. H. Hedlin, and K. T. Walker, 2014: Detection of gravity waves across the USArray: A case study. *Earth and Planetary Science Letters*, **402**, 346–352, <https://doi.org/10.1016/j.epsl.2013.06.042>.
- Del Pezzo, E., and F. Giudicepietro, 2002: Plane wave fitting method for a plane, small aperture, short period seismic array: a MATHCAD program. *Computers & geosciences*, **28** (1), 59–64.
- Diskin, G. S., J. R. Podolske, G. W. Sachse, and T. A. Slate, 2002: Open-path airborne tunable diode laser hygrometer. *Diode Lasers and Applications in Atmospheric Sensing*, SPIE, Seattle, WA, Vol. 4817, 196–204, <https://doi.org/10.1117/12.453736>.
- Doyle, J. D., and D. R. Durran, 2007: Rotor and Subrotor Dynamics in the Lee of Three-Dimensional Terrain. *Journal of the Atmospheric Sciences*, **64** (12), 4202–4221, <https://doi.org/10.1175/2007JAS2352.1>.
- Eaton, S. W., and Coauthors, 2022: An algorithmic approach to predicting mechanical draft cooling tower fan speeds from infrasound signals. *Applied Acoustics*, **199**, 109 015, <https://doi.org/10.1016/j.apacoust.2022.109015>.
- Einaudi, F., A. J. Bedard, and J. J. Finnigan, 1989: A Climatology of Gravity Waves and Other Coherent Disturbances at the Boulder Atmospheric Observatory during March–April 1984. *Journal of the Atmospheric Sciences*, **46** (3), 303–329, [https://doi.org/10.1175/1520-0469\(1989\)046<0303:ACOGWA>2.0.CO;2](https://doi.org/10.1175/1520-0469(1989)046<0303:ACOGWA>2.0.CO;2).
- Fitch, K. E., C. Hang, A. Talaei, and T. J. Garrett, 2021: Arctic observations and numerical simulations of surface wind effects on Multi-Angle Snowflake Camera measurements. *Atmospheric Measurement Techniques*, **14** (2), 1127–1142, <https://doi.org/10.5194/amt-14-1127-2021>.
- Fovell, R. G., G. L. Mullendore, and S.-H. Kim, 2006: Discrete Propagation in Numerically Simulated Nocturnal Squall Lines. *Monthly Weather Review*, **134** (12), 3735–3752, <https://doi.org/10.1175/MWR3268.1>.
- Fritts, D. C., and M. J. Alexander, 2003: Gravity wave dynamics and effects in the middle atmosphere. *Reviews of Geophysics*, **41** (1), <https://doi.org/10.1029/2001RG000106>.
- Fritz, J., 2023: Evaluating Weather Forecasts of Winter Precipitation Start Times and End Times. Denver, CO.
- Fukuta, N., and T. Takahashi, 1999: The Growth of Atmospheric Ice Crystals: A Summary of Findings in Vertical Supercooled Cloud Tunnel Studies. *Journal of the Atmospheric Sciences*, **56** (12), 1963–1979, [https://doi.org/10.1175/1520-0469\(1999\)056<1963:TGOAIC>2.0.CO;2](https://doi.org/10.1175/1520-0469(1999)056<1963:TGOAIC>2.0.CO;2).
- Gaffin, D. M., S. S. Parker, and P. D. Kirkwood, 2003: An Unexpectedly Heavy and Complex Snowfall Event across the Southern Appalachian Region. *Weather and Forecasting*, **18** (2), 224–235, [https://doi.org/10.1175/1520-0434\(2003\)018<0224:AUHACS>2.0.CO;2](https://doi.org/10.1175/1520-0434(2003)018<0224:AUHACS>2.0.CO;2).
- Ganetis, S. A., B. A. Colle, S. E. Yuter, and N. P. Hoban, 2018: Environmental Conditions Associated with Observed Snowband Structures within Northeast U.S. Winter Storms. *Monthly Weather Review*, **146** (11), 3675–3690, <https://doi.org/10.1175/MWR-D-18-0054.1>.

- Garrett, T. J., and S. E. Yuter, 2014: Observed influence of riming, temperature, and turbulence on the fallspeed of solid precipitation. *Geophysical Research Letters*, **41** (18), 6515–6522, <https://doi.org/10.1002/2014GL061016>.
- Garvert, M. F., C. P. Woods, B. A. Colle, C. F. Mass, P. V. Hobbs, M. T. Stoelinga, and J. B. Wolfe, 2005: The 13–14 December 2001 IMPROVE-2 Event. Part II: Comparisons of MM5 Model Simulations of Clouds and Precipitation with Observations. *Journal of the Atmospheric Sciences*, **62** (10), 3520–3534, <https://doi.org/10.1175/JAS3551.1>.
- Global Volcanism Program, 2022: Report on Hunga Tonga-Hunga Ha'apai (Tonga). In: Sennert, S K (ed.), Weekly Volcanic Activity Report, 12 January-18 January 2022, URL <https://volcano.si.edu/showreport.cfm?doi=GVP.WVAR20220112-243040>.
- Gossard, E. E., 1988: Measuring drop-size distributions in clouds with a clear-air-sensing Doppler radar. *Journal of Atmospheric and Oceanic Technology*, **5** (5), 640–649.
- Gossard, E. E., 1994: Measurement of cloud droplet size spectra by Doppler radar. *Journal of Atmospheric and Oceanic Technology*, **11** (3), 712–726.
- Gossard, E. E., and W. H. Hooke, 1975: *Waves in the Atmosphere: Atmospheric Infrasound and Gravity Waves - Their Generation and Propagation*. No. 2, Developments in Atmospheric Science, Elsevier.
- Gossard, E. E., R. O. Strauch, and R. R. Rogers, 1990: Evolution of droplet size distributions in liquid precipitation observed by ground-based Doppler radar. *Journal of Atmospheric and Oceanic Technology*, **7** (6), 815–828.
- Gray, S. L., O. Martínez-Alvarado, L. H. Baker, and P. A. Clark, 2011: Conditional symmetric instability in sting-jet storms. *Quarterly Journal of the Royal Meteorological Society*, **137** (659), 1482–1500, <https://doi.org/10.1002/qj.859>.
- Greybush, S. J., S. Saslo, and R. Grumm, 2017: Assessing the Ensemble Predictability of Precipitation Forecasts for the January 2015 and 2016 East Coast Winter Storms. *Weather and Forecasting*, **32** (3), 1057–1078, <https://doi.org/10.1175/WAF-D-16-0153.1>.
- Grivet-Talocia, S., and F. Einaudi, 1998: Wavelet analysis of a microbarograph network. *IEEE Transactions on Geoscience and Remote Sensing*, **36** (2), 418–432, <https://doi.org/10.1109/36.662727>.
- Grivet-Talocia, S., F. Einaudi, W. L. Clark, R. D. Dennett, G. D. Nastrom, and T. E. VanZandt, 1999: A 4-yr Climatology of Pressure Disturbances Using a Barometer Network in Central Illinois. *Monthly Weather Review*, **127** (7), 1613–1629, [https://doi.org/10.1175/1520-0493\(1999\)127<1613:AYCOPD>2.0.CO;2](https://doi.org/10.1175/1520-0493(1999)127<1613:AYCOPD>2.0.CO;2).
- Hallett, J., and B. J. Mason, 1958: The influence of temperature and supersaturation on the habit of ice crystals grown from the vapour. *Proceedings of the Royal Society of London. Series A. Mathematical and Physical Sciences*, **247** (1251), 440–453, <https://doi.org/10.1098/rspa.1958.0199>.

- Herrmann, R. B., 1975: The use of duration as a measure of seismic moment and magnitude. *Bulletin of the Seismological Society of America*, **65** (4), 899–913, <https://doi.org/10.1785/BSSA0650040899>.
- Hersbach, H., and Coauthors, 2020: The ERA5 global reanalysis. *Q.J.R. Meteorol. Soc.*, **146** (730), 1999–2049, <https://doi.org/10.1002/qj.3803>.
- Hersbach, H., and Coauthors, 2023a: ERA5 hourly data on pressure levels from 1940 to present. Copernicus Climate Change Service (C3S) Climate Data Store (CDS), [Dataset], <https://doi.org/10.24381/CDS.BD0915C6>.
- Hersbach, H., and Coauthors, 2023b: ERA5 hourly data on single levels from 1940 to present. Copernicus Climate Change Service (C3S) Climate Data Store (CDS), [Dataset], <https://doi.org/10.24381/CDS.ADBB2D47>.
- Heymsfield, G. M., L. Li, M. L. W. McLinden, L. Liao, C. N. Helms, and S. Guimond, 2024: Chapter 8: NASA Airborne Radars for Studying Clouds and Precipitation. *Advances in Weather Radar, Volume 1: Precipitation sensing platforms*, V. N. Bringi, Ed., Institute of Engineering and Technology, 450.
- Hoban, N. P., 2016: Observed Characteristics of Mesoscale Banding in Coastal Northeast U.S. Snow Storms. M.S. thesis, North Carolina State University, Raleigh, NC, URL <http://www.lib.ncsu.edu/resolver/1840.20/33405>.
- Holton, J. R., and G. J. Hakim, 2013: *An Introduction to Dynamic Meteorology*. 5th ed., Academic Press.
- Houser, J. L., and H. B. Bluestein, 2011: Polarimetric Doppler Radar Observations of Kelvin–Helmholtz Waves in a Winter Storm. *Journal of the Atmospheric Sciences*, **68** (8), 1676–1702, <https://doi.org/10.1175/2011JAS3566.1>.
- Houze, R. A., 2012: Orographic effects on precipitating clouds. *Reviews of Geophysics*, **50** (1), <https://doi.org/10.1029/2011RG000365>.
- Houze, R. A., 2014: Chapter 12 - Clouds and Precipitation Associated with Hills and Mountains. *International Geophysics*, R. A. Houze, Ed., Cloud Dynamics, Vol. 104, Academic Press, 369–402, <https://doi.org/10.1016/B978-0-12-374266-7.00012-3>.
- Hueholt, D. M., S. E. Yuter, and M. A. Miller, 2022: Revisiting Diagrams of Ice Growth Environments. *Bulletin of the American Meteorological Society*, **103** (11), E2584–E2603, <https://doi.org/10.1175/BAMS-D-21-0271.1>.
- Janiszewski, A., R. M. Rauber, B. F. Jewett, G. M. McFarquhar, T. J. Zaremba, and J. E. Yorks, 2023: A Kinematic Modeling Study of the Reorganization of Snowfall between Cloud-Top Generating Cells and Low-Level Snowbands in Midlatitude Winter Storms. *Journal of the Atmospheric Sciences*, **80** (11), 2729–2745, <https://doi.org/10.1175/JAS-D-23-0024.1>.

- Johnson, R. H., and P. J. Hamilton, 1988: The Relationship of Surface Pressure Features to the Precipitation and Airflow Structure of an Intense Midlatitude Squall Line. *Monthly Weather Review*, **116** (7), 1444–1473, [https://doi.org/10.1175/1520-0493\(1988\)116<1444:TROSPF>2.0.CO;2](https://doi.org/10.1175/1520-0493(1988)116<1444:TROSPF>2.0.CO;2).
- Keeler, J. M., B. F. Jewett, R. M. Rauber, G. M. McFarquhar, R. M. Rasmussen, L. Xue, C. Liu, and G. Thompson, 2016: Dynamics of Cloud-Top Generating Cells in Winter Cyclones. Part I: Idealized Simulations in the Context of Field Observations. *Journal of the Atmospheric Sciences*, **73** (4), 1507–1527, <https://doi.org/10.1175/JAS-D-15-0126.1>.
- Keeler, J. M., R. M. Rauber, B. F. Jewett, G. M. McFarquhar, R. M. Rasmussen, L. Xue, C. Liu, and G. Thompson, 2017: Dynamics of Cloud-Top Generating Cells in Winter Cyclones. Part III: Shear and Convective Organization. *Journal of the Atmospheric Sciences*, **74** (9), 2879–2897, <https://doi.org/10.1175/JAS-D-16-0314.1>.
- Keller, V. W., and J. Hallett, 1982: Influence of air velocity on the habit of ice crystal growth from the vapor. *Journal of Crystal Growth*, **60** (1), 91–106, [https://doi.org/10.1016/0022-0248\(82\)90176-2](https://doi.org/10.1016/0022-0248(82)90176-2).
- Kingsmill, D. E., P. O. G. Persson, S. Haimov, and M. D. Shupe, 2016: Mountain waves and orographic precipitation in a northern Colorado winter storm. *Quarterly Journal of the Royal Meteorological Society*, **142** (695), 836–853, <https://doi.org/10.1002/qj.2685>.
- Kjelaas, A. G., D. W. Beran, W. H. Hooke, and B. R. Bean, 1974: Waves Observed in the Planetary Boundary Layer using an Array of Acoustic Sounders. *Journal of the Atmospheric Sciences*, **31** (8), 2040–2045, [https://doi.org/10.1175/1520-0469\(1974\)031<2040:WOITPB>2.0.CO;2](https://doi.org/10.1175/1520-0469(1974)031<2040:WOITPB>2.0.CO;2).
- Koch, S. E., and P. B. Dorian, 1988: A Mesoscale Gravity Wave Event Observed during CCOPE. Part III: Wave Environment and Probable Source Mechanisms. *Monthly Weather Review*, **116** (12), 2570–2592, [https://doi.org/https://doi.org/10.1175/1520-0493\(1988\)116%3C2570:AMGWEO%3E2.0.CO;2](https://doi.org/https://doi.org/10.1175/1520-0493(1988)116%3C2570:AMGWEO%3E2.0.CO;2).
- Koch, S. E., and C. O’Handley, 1997: Operational Forecasting and Detection of Mesoscale Gravity Waves. *Weather and Forecasting*, **12** (2), 253–281, [https://doi.org/10.1175/1520-0434\(1997\)012<0253:OFADOM>2.0.CO;2](https://doi.org/10.1175/1520-0434(1997)012<0253:OFADOM>2.0.CO;2).
- Koch, S. E., and S. Saleeby, 2001: An Automated System for the Analysis of Gravity Waves and Other Mesoscale Phenomena. *Weather and Forecasting*, **16** (6), 661–679, [https://doi.org/10.1175/1520-0434\(2001\)016<0661:AASFTA>2.0.CO;2](https://doi.org/10.1175/1520-0434(2001)016<0661:AASFTA>2.0.CO;2).
- Koch, S. E., and L. M. Siedlarz, 1999: Mesoscale Gravity Waves and Their Environment in the Central United States during STORM-FEST. *Monthly Weather Review*, **127** (12), 2854–2879, [https://doi.org/10.1175/1520-0493\(1999\)127<2854:MGWATE>2.0.CO;2](https://doi.org/10.1175/1520-0493(1999)127<2854:MGWATE>2.0.CO;2).
- Kocin, P. J., and L. W. Uccellini, 2004: A Snowfall Impact Scale Derived from Northeast Storm Snowfall Distributions. *Bulletin of the American Meteorological Society*, **85** (2), 177–194, <https://doi.org/10.1175/BAMS-85-2-177>.

- Lackmann, G. M., 2011: *Midlatitude Synoptic Meteorology*. American Meteorological Society.
- Lackmann, G. M., and G. Thompson, 2019: Hydrometeor Lofting and Mesoscale Snowbands. *Monthly Weather Review*, **147** (11), 3879–3899, <https://doi.org/10.1175/MWR-D-19-0036.1>.
- Lance, S., C. A. Brock, D. Rogers, and J. A. Gordon, 2010: Water droplet calibration of the Cloud Droplet Probe (CDP) and in-flight performance in liquid, ice and mixed-phase clouds during ARCPAC. *Atmospheric Measurement Techniques*, **3** (6), 1683–1706, <https://doi.org/10.5194/amt-3-1683-2010>.
- Lawson, R. P., D. O'Connor, P. Zmarzly, K. Weaver, B. Baker, Q. Mo, and H. Jonsson, 2006: The 2D-S (Stereo) Probe: Design and Preliminary Tests of a New Airborne, High-Speed, High-Resolution Particle Imaging Probe. *Journal of Atmospheric and Oceanic Technology*, **23** (11), 1462–1477, <https://doi.org/10.1175/JTECH1927.1>.
- LeMone, M. A., and E. J. Zipser, 1980: Cumulonimbus Vertical Velocity Events in GATE. Part I: Diameter, Intensity and Mass Flux. *Journal of the Atmospheric Sciences*, **37** (11), 2444–2457, [https://doi.org/10.1175/1520-0469\(1980\)037<2444:CVVEIG>2.0.CO;2](https://doi.org/10.1175/1520-0469(1980)037<2444:CVVEIG>2.0.CO;2).
- Leonardo, N. M., and B. A. Colle, 2023: The Development of Snow Multi-Bands in High-Resolution Idealized Baroclinic Wave Simulations. *American Meteorological Society 20th Conference on Mesoscale Processes*, Madison, WI, USA, URL <https://ams.confex.com/ams/WAFNWPMS/meetingapp.cgi/Paper/425221>.
- Leonardo, N. M., and B. A. Colle, 2024: Analysis of Snow Multibands and Their Environments with High-Resolution Idealized Simulations. *Monthly Weather Review*, **152** (4), 925–943, <https://doi.org/10.1175/MWR-D-23-0211.1>.
- Lilly, J., 2021: jLab: A data analysis package for Matlab, v.1.7.1. URL <https://doi.org/10.5281/zenodo.4547006>.
- Lilly, J. M., and S. C. Olhede, 2012: Generalized Morse Wavelets as a Superfamily of Analytic Wavelets. *IEEE Transactions on Signal Processing*, **60** (11), 6036–6041, <https://doi.org/10.1109/TSP.2012.2210890>.
- Lindzen, R. S., and K.-K. Tung, 1976: Banded Convective Activity and Ducted Gravity Waves. *Monthly Weather Review*, **104** (12), 1602–1617, [https://doi.org/10.1175/1520-0493\(1976\)104<1602:BCAADG>2.0.CO;2](https://doi.org/10.1175/1520-0493(1976)104<1602:BCAADG>2.0.CO;2).
- Ma, S., L. Ran, J. Cao, B. Jiao, and K. Zhou, 2023: Characteristics for the sources and sinks of gravity waves in an orographic heavy snowfall event. *Front. Earth Sci.*, **17** (2), 604–619, <https://doi.org/10.1007/s11707-021-0961-2>.
- Mapes, B. E., 1993: Gregarious Tropical Convection. *Journal of the Atmospheric Sciences*, **50** (13), 2026–2037, [https://doi.org/10.1175/1520-0469\(1993\)050<2026:GTC>2.0.CO;2](https://doi.org/10.1175/1520-0469(1993)050<2026:GTC>2.0.CO;2).
- Markowski, P., and Y. Richardson, 2010: *Mesoscale Meteorology in Midlatitudes*. Wiley-Blackwell, URL <http://doi.wiley.com/10.1002/9780470682104>.

- Matoza, R. S., and Coauthors, 2022: Atmospheric waves and global seismoacoustic observations of the January 2022 Hunga eruption, Tonga. *Science*, **377** (6601), 95–100, <https://doi.org/10.1126/science.abo7063>.
- McAnelly, R. L., J. E. Nachamkin, W. R. Cotton, and M. E. Nicholls, 1997: Upscale Evolution of MCSs: Doppler Radar Analysis and Analytical Investigation. *Monthly Weather Review*, **125** (6), 1083–1110, [https://doi.org/10.1175/1520-0493\(1997\)125<1083:UEOMDR>2.0.CO;2](https://doi.org/10.1175/1520-0493(1997)125<1083:UEOMDR>2.0.CO;2).
- McLinden, M. L. W., L. Li, G. M. Heymsfield, M. Coon, and A. Emory, 2021: The NASA GSFC 94-GHz Airborne Solid-State Cloud Radar System (CRS). *Journal of Atmospheric and Oceanic Technology*, **38** (5), 1001–1017, <https://doi.org/10.1175/JTECH-D-20-0127.1>.
- McMurdie, L. A., and Coauthors, 2022: Chasing Snowstorms: The Investigation of Microphysics and Precipitation for Atlantic Coast-Threatening Snowstorms (IMPACTS) Campaign. *Bulletin of the American Meteorological Society*, **103** (5), E1243–E1269, <https://doi.org/10.1175/BAMS-D-20-0246.1>.
- Meyer, F., 1994: Topographic distance and watershed lines. *Signal Processing*, **38** (1), 113–125, [https://doi.org/10.1016/0165-1684\(94\)90060-4](https://doi.org/10.1016/0165-1684(94)90060-4).
- Miller, J. E., 1948: ON THE CONCEPT OF FRONTOGENESIS. *Journal of the Atmospheric Sciences*, **5** (4), 169–171, [https://doi.org/10.1175/1520-0469\(1948\)005<0169:OTCOF>2.0.CO;2](https://doi.org/10.1175/1520-0469(1948)005<0169:OTCOF>2.0.CO;2).
- Miller, M. A., and L. R. Allen, 2023: Data for Objective identification of pressure wave events from networks of 1-Hz, high-precision sensors. Zenodo, [Dataset], <https://doi.org/10.5281/zenodo.8136536>.
- Miller, M. A., S. E. Yuter, N. P. Hoban, L. M. Tomkins, and B. A. Colle, 2022: Detecting wave features in Doppler radial velocity radar observations. *Atmos. Meas. Tech.*, **15** (6), 1689–1702, <https://doi.org/10.5194/amt-15-1689-2022>.
- Morcrette, C. J., and K. A. Browning, 2006: Formation and release of symmetric instability following Delta-M adjustment. *Quarterly Journal of the Royal Meteorological Society*, **132** (617), 1073–1089, <https://doi.org/10.1256/qj.04.108>, URL <https://onlinelibrary.wiley.com/doi/abs/10.1256/qj.04.108>, \_eprint: <https://onlinelibrary.wiley.com/doi/pdf/10.1256/qj.04.108>.
- Nappo, C. J., 2002: *An introduction to atmospheric gravity waves*, International Geophysics Series, Vol. 85. Academic press.
- National Weather Service, 2018: Communicating Probabilistic Information for Decision-Makers: A Case Study Using Experimental Snow Forecast Products. NOAA NWS Final Rep. Tech. rep., 48 pp. URL <https://vlab.noaa.gov/web/nws-social-science/past-projects>.
- Nicholls, M. E., R. A. Pielke, and W. R. Cotton, 1991: Thermally Forced Gravity Waves in an Atmosphere at Rest. *Journal of the Atmospheric Sciences*, **48** (16), 1869–1884, [https://doi.org/10.1175/1520-0469\(1991\)048<1869:TFGWIA>2.0.CO;2](https://doi.org/10.1175/1520-0469(1991)048<1869:TFGWIA>2.0.CO;2).

- NOAA National Centers for Environmental Information, 2021a: Automated Surface/Weather Observing Systems (ASOS/AWOS). URL <https://www.ncei.noaa.gov/products/land-based-station/automated-surface-weather-observing-systems>, [Dataset].
- NOAA National Centers for Environmental Information, 2021b: Global BUFR Data Stream: Upper Air Reports from the National Weather Service Telecommunications Gateway (NWS TG). URL <https://www.ncei.noaa.gov/access/metadata/landing-page/bin/iso?id=gov.noaa.ncdc:C01500>, [Dataset].
- NOAA National Centers for Environmental Information, 2024: U.S. Billion-dollar Weather and Climate Disasters, 1980 - present. [Dataset], <https://doi.org/10.25921/STKW-7W73>.
- NOAA National Weather Service Radar Operations Center, 1991: NOAA Next Generation Radar (NEXRAD) Level II Base Data. NOAA National Centers for Environmental Information, [Dataset], <https://doi.org/10.7289/V5W9574V>.
- Novak, D. R., L. F. Bosart, D. Keyser, and J. S. Waldstreicher, 2004: An Observational Study of Cold Season–Banded Precipitation in Northeast U.S. Cyclones. *Weather and Forecasting*, **19** (6), 993–1010, <https://doi.org/10.1175/815.1>.
- Novak, D. R., K. F. Brill, and W. A. Hogsett, 2014: Using Percentiles to Communicate Snowfall Uncertainty. *Weather and Forecasting*, **29** (5), 1259–1265, <https://doi.org/10.1175/WAF-D-14-00019.1>.
- Novak, D. R., B. A. Colle, and A. R. Aiyyer, 2010: Evolution of Mesoscale Precipitation Band Environments within the Comma Head of Northeast U.S. Cyclones. *Monthly Weather Review*, **138** (6), 2354–2374, <https://doi.org/10.1175/2010MWR3219.1>.
- Novak, D. R., B. A. Colle, and S. E. Yuter, 2008: High-Resolution Observations and Model Simulations of the Life Cycle of an Intense Mesoscale Snowband over the Northeastern United States. *Monthly Weather Review*, **136** (4), 1433–1456, <https://doi.org/10.1175/2007MWR2233.1>.
- Novak, D. R., and Coauthors, 2023: Innovations in Winter Storm Forecasting and Decision Support Services. *Bulletin of the American Meteorological Society*, **104** (3), E715–E735, <https://doi.org/10.1175/BAMS-D-22-0065.1>, publisher: American Meteorological Society Section: Bulletin of the American Meteorological Society.
- Olhede, S., and A. Walden, 2002: Generalized Morse wavelets. *IEEE Transactions on Signal Processing*, **50** (11), 2661–2670, <https://doi.org/10.1109/TSP.2002.804066>.
- Oue, M., B. A. Colle, S. E. Yuter, P. Kollias, P. Yeh, and L. M. Tomkins, 2024: Microscale Updrafts Within Northeast U.S. Coastal Snowstorms Using High-Resolution Cloud Radar Measurements. *Monthly Weather Review*, <https://doi.org/10.1175/MWR-D-23-0055.1>.
- Pierce, A. D., and J. W. Posey, 1971: Theory of the Excitation and Propagation of Lamb’s Atmospheric Edge Mode from Nuclear Explosions. *Geophysical Journal International*, **26** (1-4), 341–368, <https://doi.org/10.1111/j.1365-246X.1971.tb03406.x>.

- Plant, R. S., and G. J. Keith, 2007: Occurrence of Kelvin-Helmholtz Billows in Sea-breeze Circulations. *Boundary-Layer Meteorol*, **122** (1), 1–15, <https://doi.org/10.1007/s10546-006-9089-x>.
- Plummer, D. M., G. M. McFarquhar, R. M. Rauber, B. F. Jewett, and D. C. Leon, 2014: Structure and Statistical Analysis of the Microphysical Properties of Generating Cells in the Comma Head Region of Continental Winter Cyclones. *Journal of the Atmospheric Sciences*, **71** (11), 4181–4203, <https://doi.org/10.1175/JAS-D-14-0100.1>.
- Plummer, D. M., G. M. McFarquhar, R. M. Rauber, B. F. Jewett, and D. C. Leon, 2015: Microphysical Properties of Convectively Generated Fall Streaks within the Stratiform Comma Head Region of Continental Winter Cyclones. *Journal of the Atmospheric Sciences*, **72** (6), 2465–2483, <https://doi.org/10.1175/JAS-D-14-0354.1>.
- Proud, S. R., A. T. Prata, and S. Schmauß, 2022: The January 2022 eruption of Hunga Tonga-Hunga Ha’apai volcano reached the mesosphere. *Science*, **378** (6619), 554–557, <https://doi.org/10.1126/science.abo4076>.
- Qin, Z., and Coauthors, 2023: Vertical transport of water in isolated convective clouds in the interior western United States as observed using airborne in-situ measurements. *Atmospheric Research*, **285**, 106 629, <https://doi.org/10.1016/j.atmosres.2023.106629>.
- Radford, J. T., G. M. Lackmann, and M. A. Baxter, 2019: An Evaluation of Snowband Predictability in the High-Resolution Rapid Refresh. *Weather and Forecasting*, **34** (5), 1477–1494, <https://doi.org/10.1175/WAF-D-19-0089.1>.
- Rauber, R. M., S. M. Ellis, J. Vivekanandan, J. Stith, W.-C. Lee, G. M. McFarquhar, B. F. Jewett, and A. Janiszewski, 2017: Finescale Structure of a Snowstorm over the Northeastern United States: A First Look at High-Resolution HIAPER Cloud Radar Observations. *Bulletin of the American Meteorological Society*, **98** (2), 253–269, <https://doi.org/10.1175/BAMS-D-15-00180.1>.
- Rauber, R. M., and Coauthors, 2014: Stability and Charging Characteristics of the Comma Head Region of Continental Winter Cyclones. *Journal of the Atmospheric Sciences*, **71** (5), 1559–1582, <https://doi.org/10.1175/JAS-D-13-0253.1>.
- ReVelle, D. O., 2008: Acoustic-Gravity Waves from Bolide Sources. *Earth Moon Planet*, **102** (1), 345–356, <https://doi.org/10.1007/s11038-007-9181-3>.
- Rosenow, A. A., D. M. Plummer, R. M. Rauber, G. M. McFarquhar, B. F. Jewett, and D. Leon, 2014: Vertical Velocity and Physical Structure of Generating Cells and Convection in the Comma Head Region of Continental Winter Cyclones. *Journal of the Atmospheric Sciences*, **71** (5), 1538–1558, <https://doi.org/10.1175/JAS-D-13-0249.1>.
- Ruppert, J. H., S. E. Koch, X. Chen, Y. Du, A. Seimon, Y. Q. Sun, J. Wei, and L. F. Bosart, 2022: Mesoscale Gravity Waves and Midlatitude Weather: A Tribute to Fuqing Zhang. *Bulletin of the American Meteorological Society*, **103** (1), E129–E156, <https://doi.org/10.1175/BAMS-D-20-0005.1>.

- Schultz, D. M., and P. N. Schumacher, 1999: The Use and Misuse of Conditional Symmetric Instability. *Monthly Weather Review*, **127** (12), 2709–2732, [https://doi.org/10.1175/1520-0493\(1999\)127<2709:TUAMOC>2.0.CO;2](https://doi.org/10.1175/1520-0493(1999)127<2709:TUAMOC>2.0.CO;2).
- Schultz, D. M., and Coauthors, 2019: Extratropical Cyclones: A Century of Research on Meteorology's Centerpiece. *Meteorological Monographs*, **59**, 16.1–16.56, <https://doi.org/10.1175/AMSMONOGRAPHS-D-18-0015.1>.
- Seifert, A., and T. Heus, 2013: Large-eddy simulation of organized precipitating trade wind cumulus clouds. *Atmospheric Chemistry and Physics*, **13** (11), 5631–5645, <https://doi.org/10.5194/acp-13-5631-2013>.
- Smith, R. B., 1979: The Influence of Mountains on the Atmosphere. *Advances in Geophysics*, B. Saltzman, Ed., Vol. 21, Elsevier, 87–230, [https://doi.org/10.1016/S0065-2687\(08\)60262-9](https://doi.org/10.1016/S0065-2687(08)60262-9).
- Stull, R. B., 1993: Review of non-local mixing in turbulent atmospheres: Transient turbulence theory. *Boundary-Layer Meteorol*, **62** (1), 21–96, <https://doi.org/10.1007/BF00705546>.
- Takahashi, T., T. Endoh, G. Wakahama, and N. Fukuta, 1991: Vapor Diffusional Growth of Free-Falling Snow Crystals between -3 and -23°C. *Journal of the Meteorological Society of Japan. Ser. II*, **69** (1), 15–30, [https://doi.org/10.2151/jmsj1965.69.1\\_15](https://doi.org/10.2151/jmsj1965.69.1_15).
- Thompson, G., R. M. Rasmussen, and K. Manning, 2004: Explicit Forecasts of Winter Precipitation Using an Improved Bulk Microphysics Scheme. Part I: Description and Sensitivity Analysis. *Monthly Weather Review*, **132** (2), 519–542, [https://doi.org/10.1175/1520-0493\(2004\)132<0519:EFOWPU>2.0.CO;2](https://doi.org/10.1175/1520-0493(2004)132<0519:EFOWPU>2.0.CO;2).
- Tomkins, L., S. E. Yuter, and M. Miller, 2024a: Low pressure tracks for northeast US winter storms from 1996-2023. OSF, [Dataset], <https://doi.org/10.17605/OSF.IO/AZ5W2>.
- Tomkins, L. M., 2024: Synthesis of Radar-Observed Characteristics, Storm Structures, and Surface Snowfall Rates in 10+ Years of Northeast US Winter Storms. Ph.D. Dissertation, North Carolina State University, Raleigh, NC, URL <https://repository.lib.ncsu.edu/items/e59f0b8b-1a9a-4119-b155-bfa58ab694e7>.
- Tomkins, L. M., D. B. Mechem, S. E. Yuter, and S. R. Rhodes, 2021: Regional Flow Conditions Associated with Stratocumulus Cloud-Eroding Boundaries over the Southeast Atlantic. *Monthly Weather Review*, **149** (6), 1903–1917, <https://doi.org/10.1175/MWR-D-20-0250.1>.
- Tomkins, L. M., S. E. Yuter, and M. A. Miller, 2024b: Dual adaptive differential threshold method for automated detection of faint and strong echo features in radar observations of winter storms. *Atmospheric Measurement Techniques*, <https://doi.org/10.5194/egusphere-2023-2888>, [accepted, in press].
- Tomkins, L. M., S. E. Yuter, M. A. Miller, and L. R. Allen, 2022: Image Muting of Mixed Precipitation to Improve Identification of Regions of Heavy Snow in Radar Data. *Atmospheric Measurement Techniques*, 1–15, <https://doi.org/10.5194/amt-2022-160>.

- Torrence, C., and G. P. Compo, 1998: A Practical Guide to Wavelet Analysis. *Bulletin of the American Meteorological Society*, **79** (1), 61–78, [https://doi.org/10.1175/1520-0477\(1998\)079<0061:APGTWA>2.0.CO;2](https://doi.org/10.1175/1520-0477(1998)079<0061:APGTWA>2.0.CO;2).
- Trifunac, M. D., and A. G. Brady, 1975: A study on the duration of strong earthquake ground motion. *Bulletin of the Seismological Society of America*, **65** (3), 581–626, <https://doi.org/10.1785/BSSA0650030581>.
- UCAR/NCAR - Earth Observing Laboratory, 2024: Two-Dimensional Optical Array Cloud Probe. URL <https://www.eol.ucar.edu/instruments/two-dimensional-optical-array-cloud-probe>.
- Uccellini, L. W., and S. E. Koch, 1987: The synoptic setting and possible energy sources for mesoscale wave disturbances. *Monthly weather review*, **115** (3), 721–729.
- Vergoz, J., and Coauthors, 2022: IMS observations of infrasound and acoustic-gravity waves produced by the January 2022 volcanic eruption of Hunga, Tonga: A global analysis. *Earth and Planetary Science Letters*, **591**, 117–139, <https://doi.org/10.1016/j.epsl.2022.117639>.
- Wallace, J. M., and P. V. Hobbs, 2006: *Atmospheric Science: An Introductory Survey*, International Geophysics Series, Vol. 92. 2nd ed., Elsevier.
- Wang, P. K., 2002: *Ice microdynamics*. Academic Press.
- Wells, D. L., and K. J. Coppersmith, 1994: New empirical relationships among magnitude, rupture length, rupture width, rupture area, and surface displacement. *Bulletin of the Seismological Society of America*, **84** (4), 974–1002, <https://doi.org/10.1785/BSSA0840040974>.
- Xu, Q., 1992: Formation and Evolution of Frontal Rainbands and Geostrophic Potential Vorticity Anomalies. *Journal of the Atmospheric Sciences*, **49** (8), 629–648, [https://doi.org/10.1175/1520-0469\(1992\)049<0629:FAEOFR>2.0.CO;2](https://doi.org/10.1175/1520-0469(1992)049<0629:FAEOFR>2.0.CO;2).
- Yang, J., Z. Wang, A. J. Heymsfield, and J. R. French, 2016: Characteristics of vertical air motion in isolated convective clouds. *Atmospheric Chemistry and Physics*, **16** (15), 10 159–10 173, <https://doi.org/10.5194/acp-16-10159-2016>.
- Yuter, S. E., J. D. Hader, M. A. Miller, and D. B. Mechem, 2018: Abrupt cloud clearing of marine stratocumulus in the subtropical southeast Atlantic. *Science*, **361** (6403), 697–701, <https://doi.org/10.1126/science.aar5836>.
- Zhang, F., 2004: Generation of Mesoscale Gravity Waves in Upper-Tropospheric Jet–Front Systems. *Journal of the Atmospheric Sciences*, **61** (4), 440–457, [https://doi.org/10.1175/1520-0469\(2004\)061<0440:GOMGWI>2.0.CO;2](https://doi.org/10.1175/1520-0469(2004)061<0440:GOMGWI>2.0.CO;2).
- Zhang, F., C. A. Davis, M. L. Kaplan, and S. E. Koch, 2001: Wavelet analysis and the governing dynamics of a large-amplitude mesoscale gravity-wave event along the East Coast of the United States. *Quarterly Journal of the Royal Meteorological Society*, **127** (577), 2209–2245.
- Zhang, F., S. E. Koch, C. A. Davis, and M. L. Kaplan, 2000: A survey of unbalanced flow diagnostics and their application. *Advances in Atmospheric Sciences*, **17** (2), 165–183, <https://doi.org/10.1007/s00376-000-0001-1>.

Zhang, F., C. Snyder, and R. Rotunno, 2002: Mesoscale Predictability of the “Surprise” Snowstorm of 24–25 January 2000. *Monthly Weather Review*, **130** (6), 1617–1632, [https://doi.org/10.1175/1520-0493\(2002\)130<1617:MPOTSS>2.0.CO;2](https://doi.org/10.1175/1520-0493(2002)130<1617:MPOTSS>2.0.CO;2).

## APPENDIX

## APPENDIX

### A

# ERA5 FORCING AND INSTABILITY METRICS FOR SELECTED P-3 FLIGHT LEGS DURING IMPACTS

In this appendix, selected cross-sections of ERA5 forcing (frontogenesis and vertical velocity) and instability (Kelvin-Helmholtz instability, potential instability, and conditional instability) are shown for P-3 in-cloud flight legs during IMPACTS which were  $\geq 50$  km long and which likely had frozen precipitation at the surface (ERA5 2-meter temperature  $< 0^{\circ}\text{C}$ ). The cross-sections shown in this appendix are for flight legs either through relatively strong frontogenesis or in which several in-cloud updrafts were sampled. The full set of cross-sections can be found at <https://doi.org/10.17605/OSF.IO/J9VWY> (Allen and Yuter 2024).

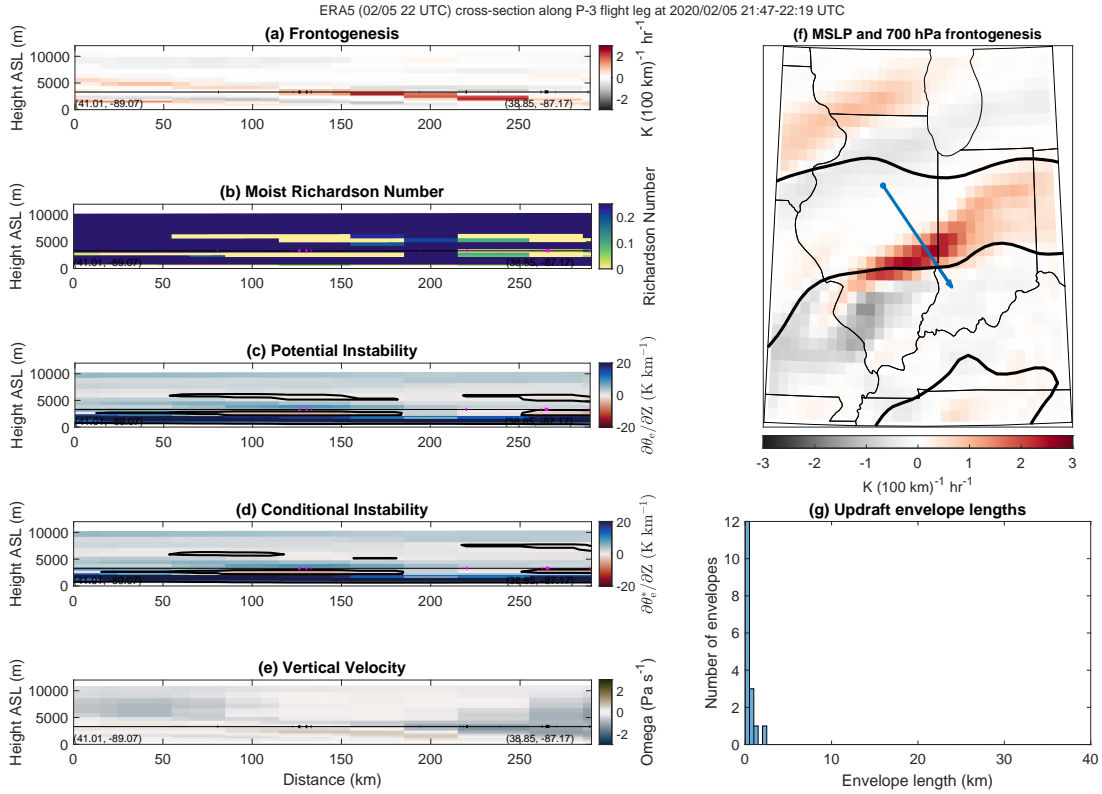


Figure A.1: Cross-sections (3:1 aspect ratio) of **(a)** frontogenesis [ $\text{K}(100 \text{ km})^{-1} \text{ hr}^{-1}$ ], **(b)** moist Richardson number (unitless), **(c)** the vertical gradient in  $\theta_e$  ( $\text{K km}^{-1}$ ), **(d)** the vertical gradient in  $\theta_e^*$  ( $\text{K km}^{-1}$ ), and **(e)** vertical velocity ( $\text{Pa s}^{-1}$ , where negative values indicate upward motion) from ERA5 data along the P-3 flight leg from 21:47 to 22:19 UTC 05 February 2020. In **(a)-(e)**, the P-3 flight track is shown by thin black lines and in-cloud updraft observations  $\geq 0.5 \text{ m s}^{-1}$  are shown by thicker black (**(a)** and **(e)**) or magenta (**(b)-(d)**) lines. **(f)** Map of the P-3 flight track (blue), with MSLP (black contours every 5 hPa) and 700 hPa frontogenesis [ $\text{K}(100 \text{ km})^{-1} \text{ hr}^{-1}$ ] from ERA5 data at the time corresponding to the cross-sections. **(g)** Histogram of in-cloud updraft envelope lengths for the flight leg shown.

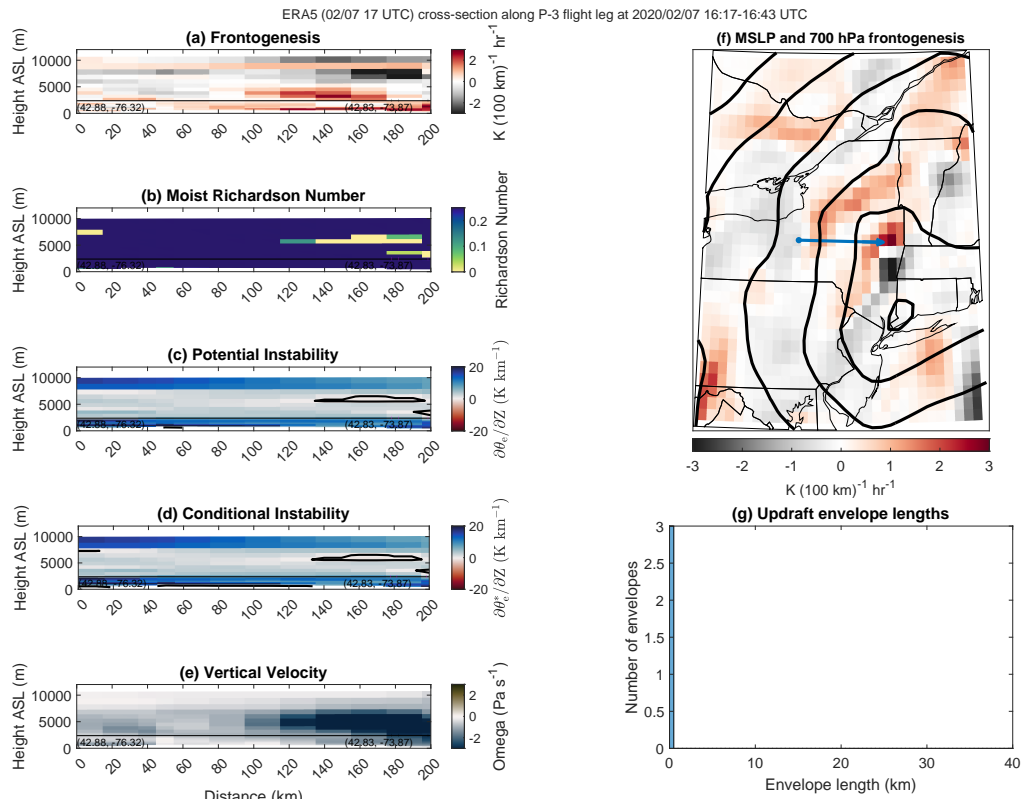


Figure A.2: As in Fig. A.1, but for the P-3 flight leg from 16:17 UTC 07 February 2020 to 16:43 UTC 07 February 2020.

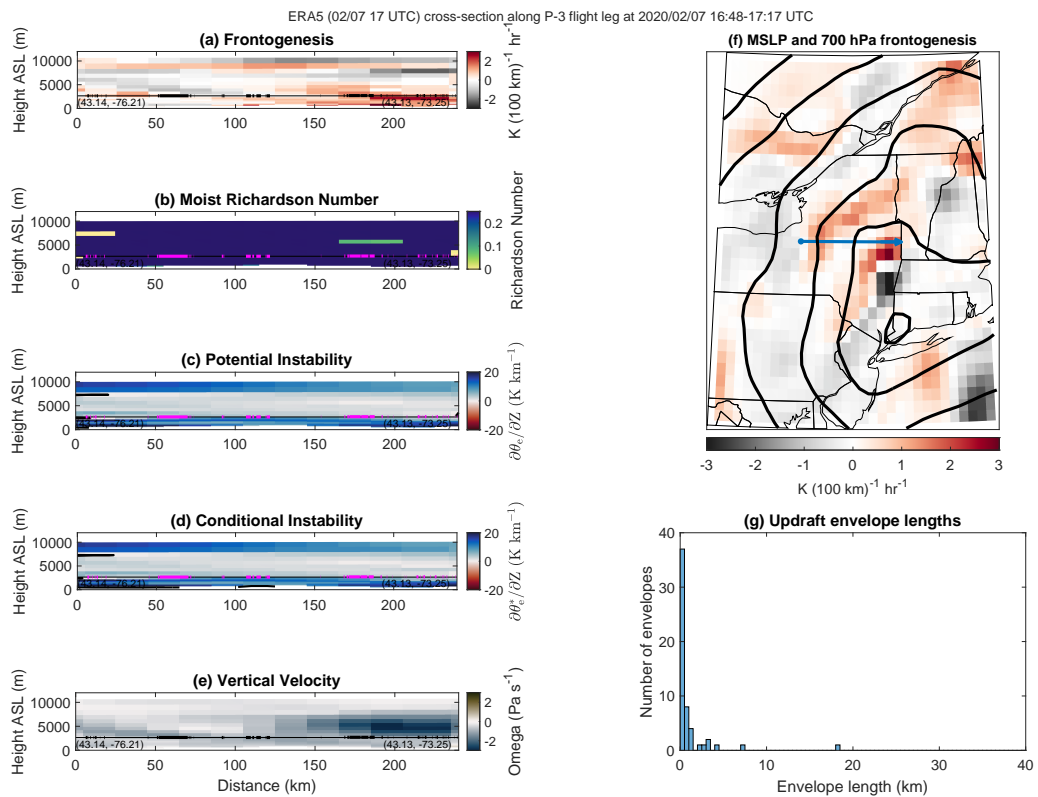


Figure A.3: As in Fig. A.1, but for the P-3 flight leg from 16:48 UTC 07 February 2020 to 17:17 UTC 07 February 2020.

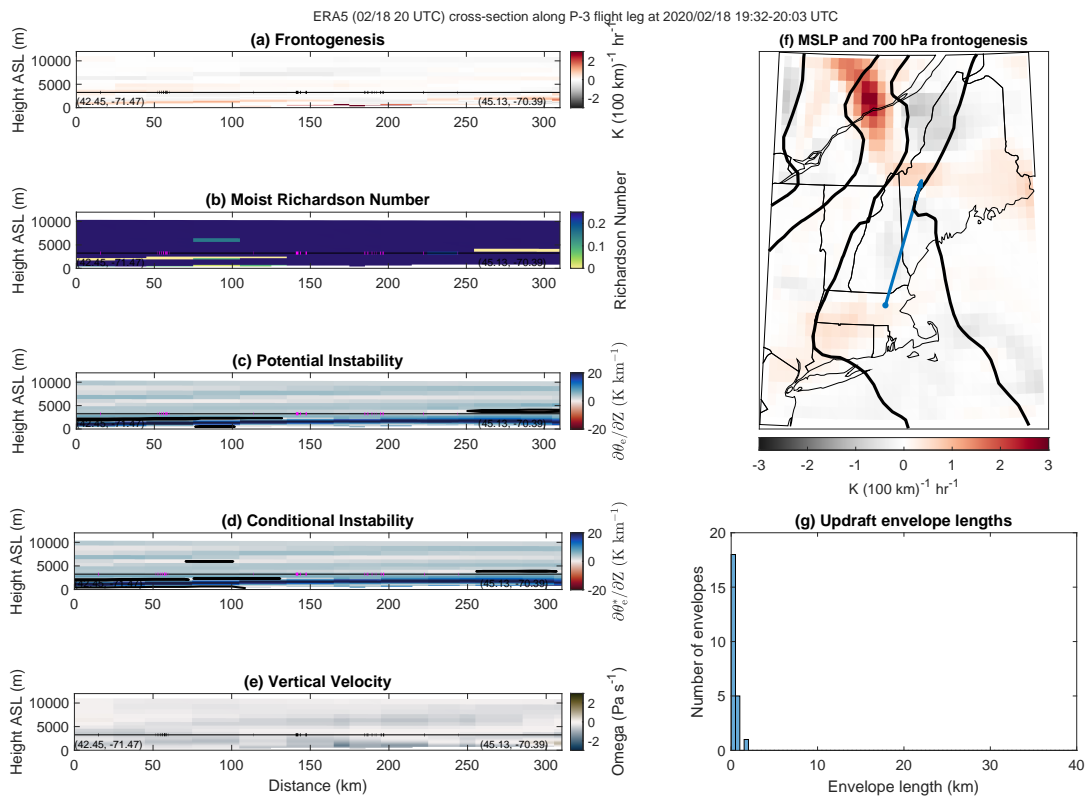


Figure A.4: As in Fig. A.1, but for the P-3 flight leg from 19:32 UTC 18 February 2020 to 20:03 UTC 18 February 2020.

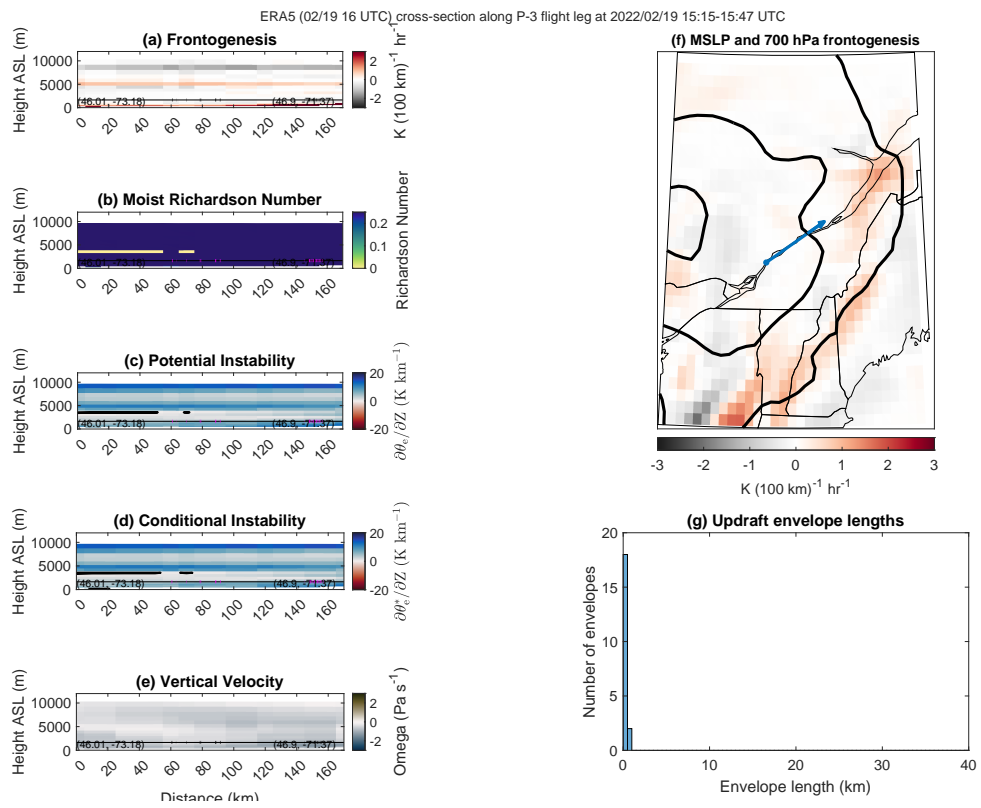


Figure A.5: As in Fig. A.1, but for the P-3 flight leg from 15:15 UTC 19 February 2022 to 15:47 UTC 19 February 2022.

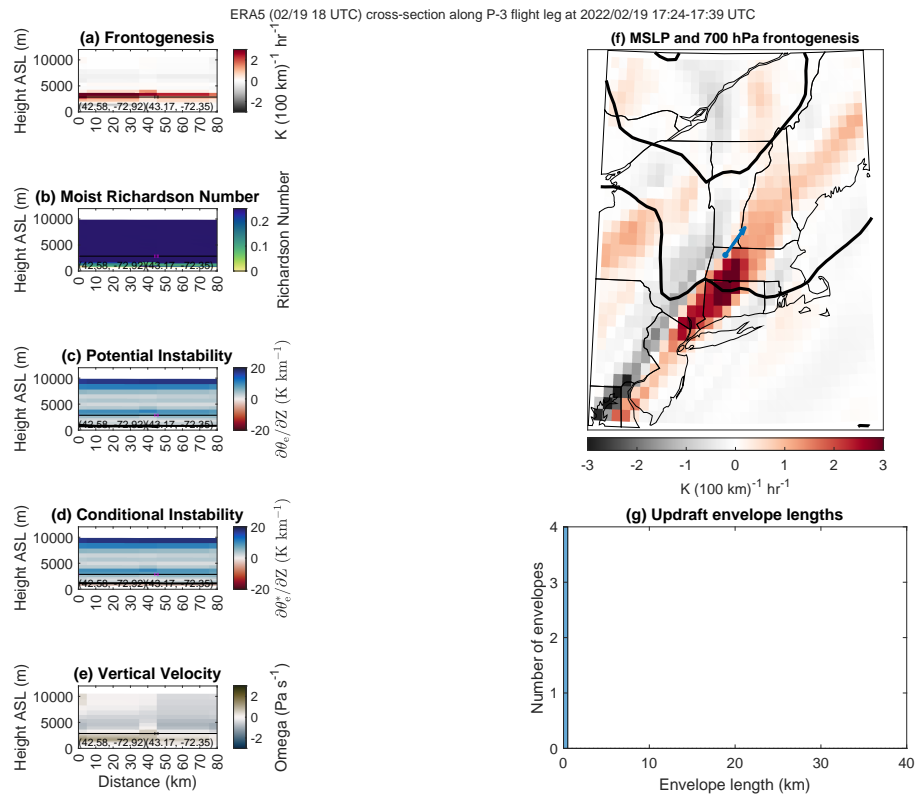


Figure A.6: As in Fig. A.1, but for the P-3 flight leg from 17:24 UTC 19 February 2022 to 17:39 UTC 19 February 2022.

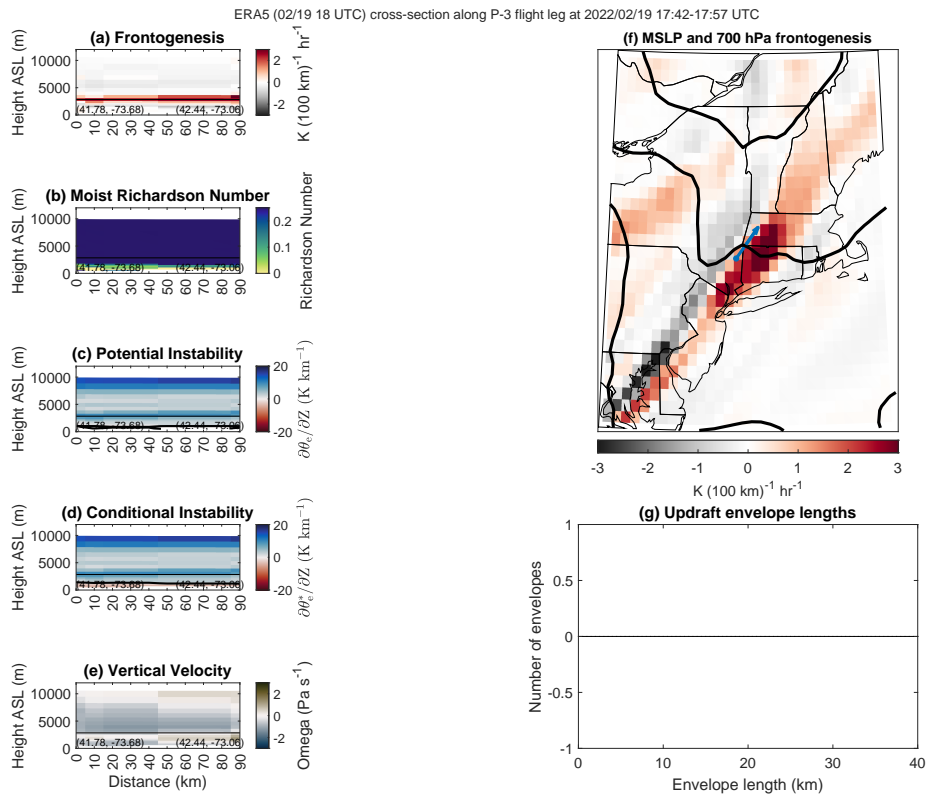


Figure A.7: As in Fig. A.1, but for the P-3 flight leg from 17:42 UTC 19 February 2022 to 17:57 UTC 19 February 2022.

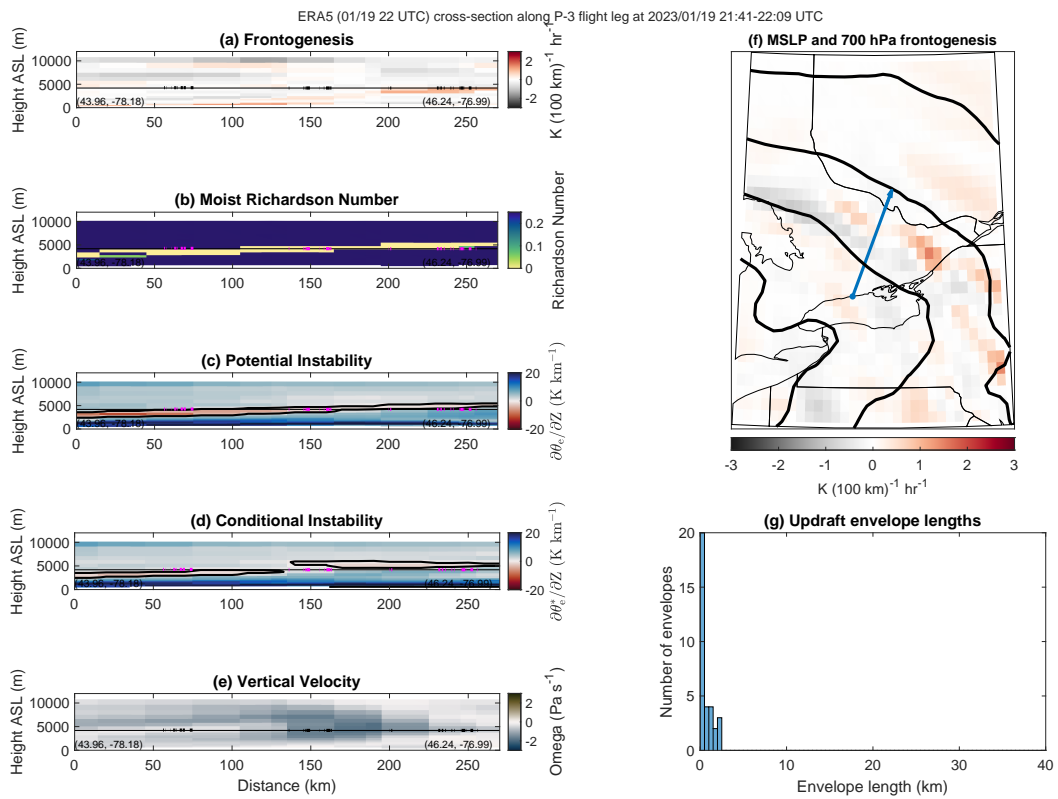


Figure A.8: As in Fig. A.1, but for the P-3 flight leg from 21:41 UTC 19 January 2023 to 22:09 UTC 19 January 2023.

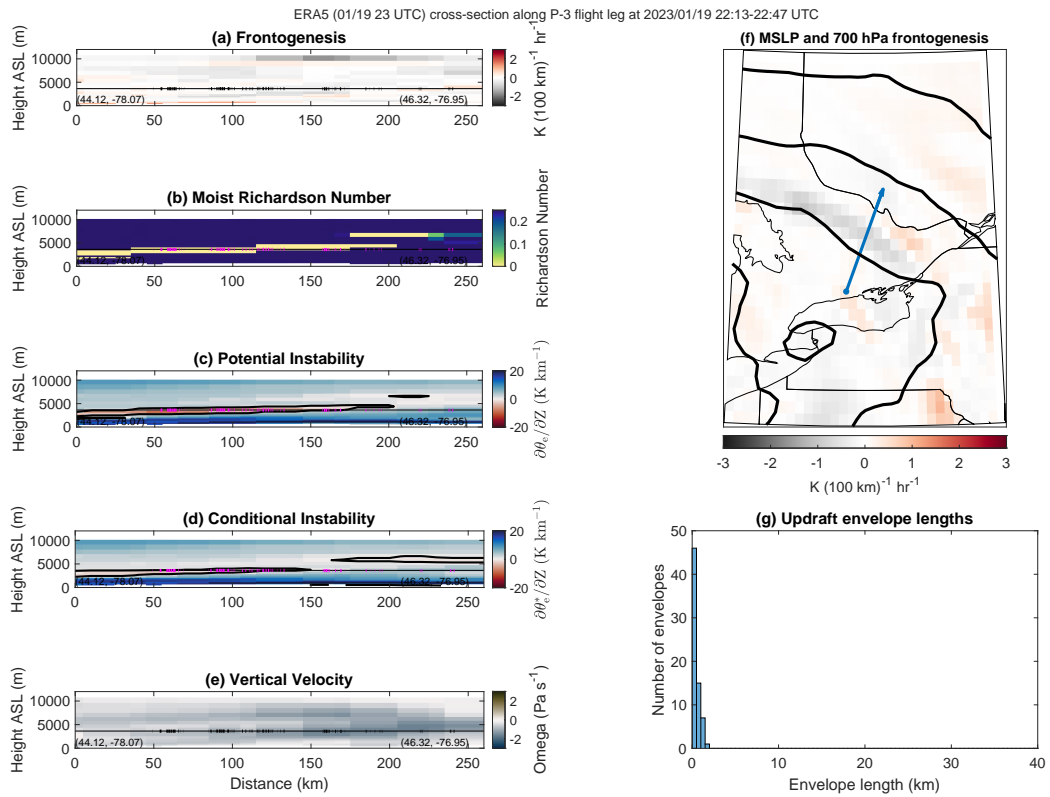


Figure A.9: As in Fig. A.1, but for the P-3 flight leg from 22:13 UTC 19 January 2023 to 22:47 UTC 19 January 2023.

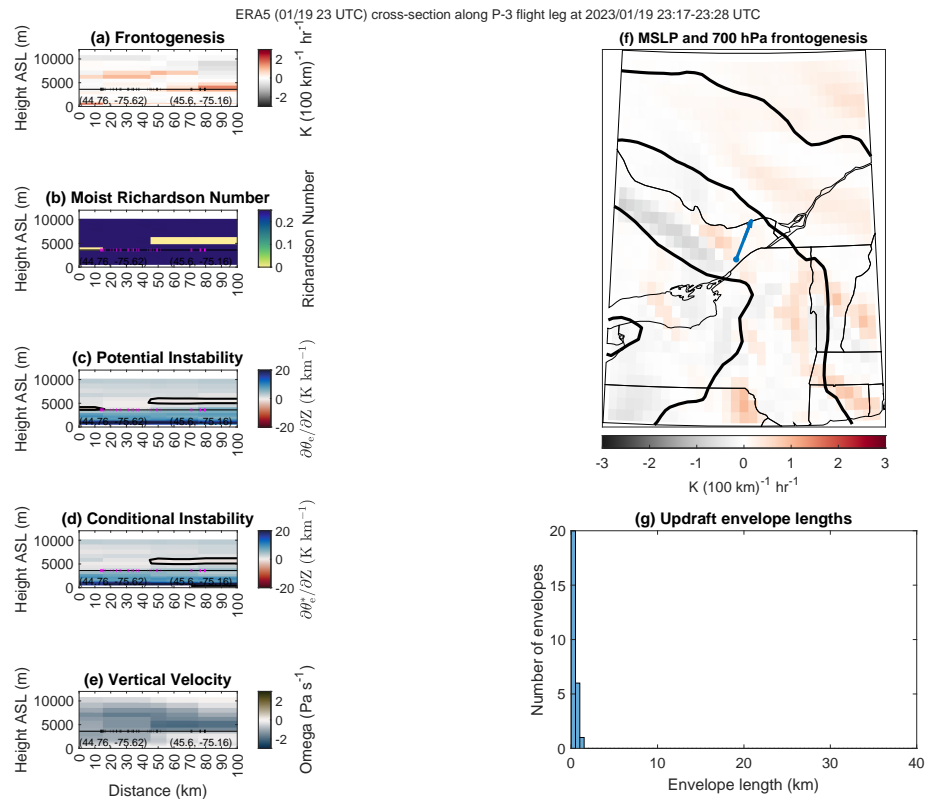


Figure A.10: As in Fig. A.1, but for the P-3 flight leg from 23:17 UTC 19 January 2023 to 23:28 UTC 19 January 2023.

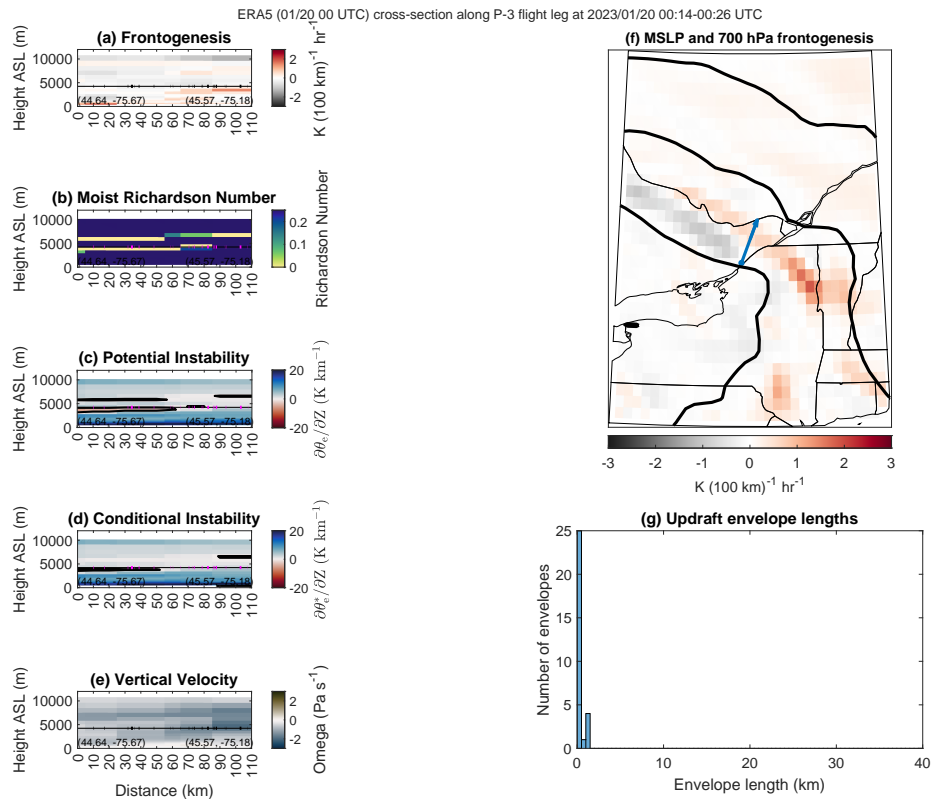


Figure A.11: As in Fig. A.1, but for the P-3 flight leg from 00:14 UTC 20 January 2023 to 00:26 UTC 20 January 2023.

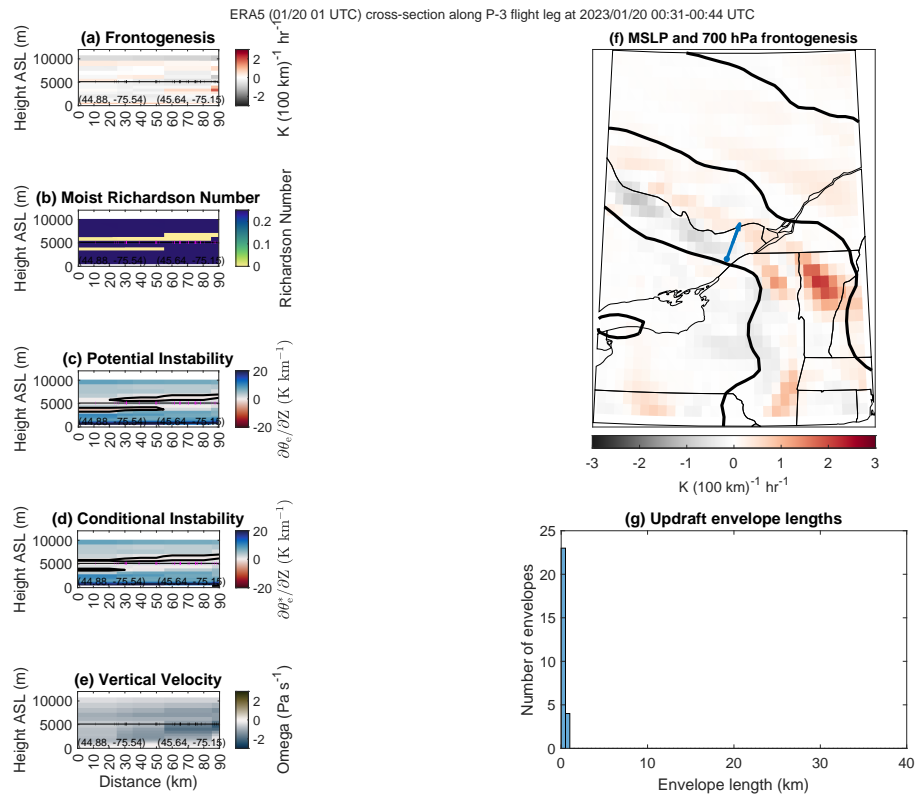


Figure A.12: As in Fig. A.1, but for the P-3 flight leg from 00:31 UTC 20 January 2023 to 00:44 UTC 20 January 2023.

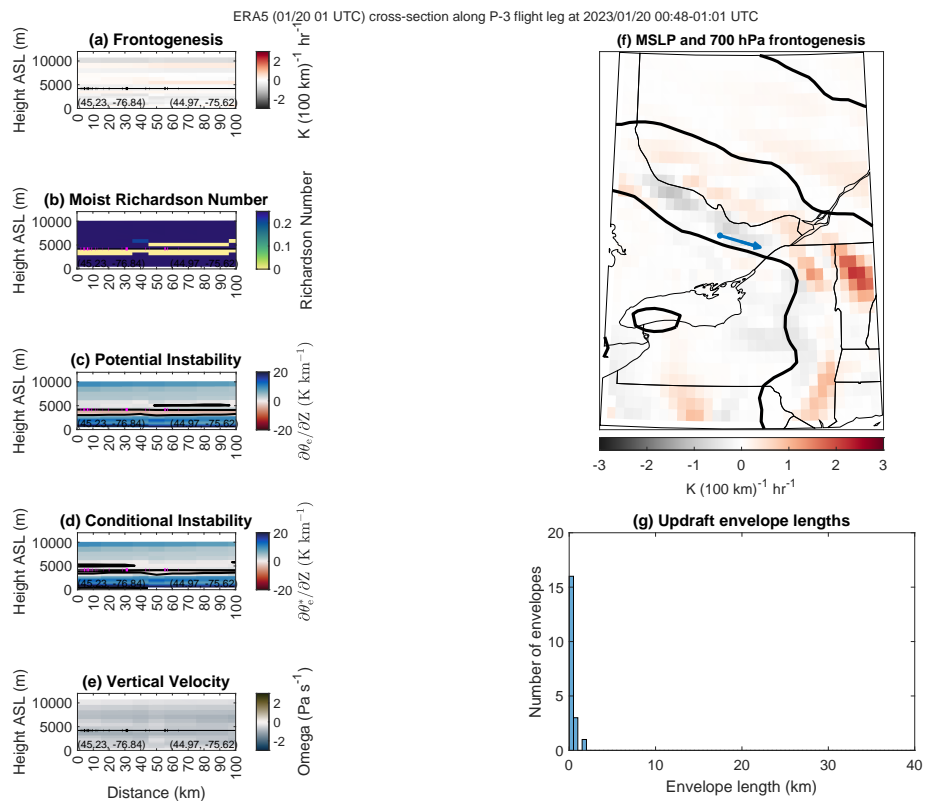


Figure A.13: As in Fig. A.1, but for the P-3 flight leg from 00:48 UTC 20 January 2023 to 01:01 UTC 20 January 2023.

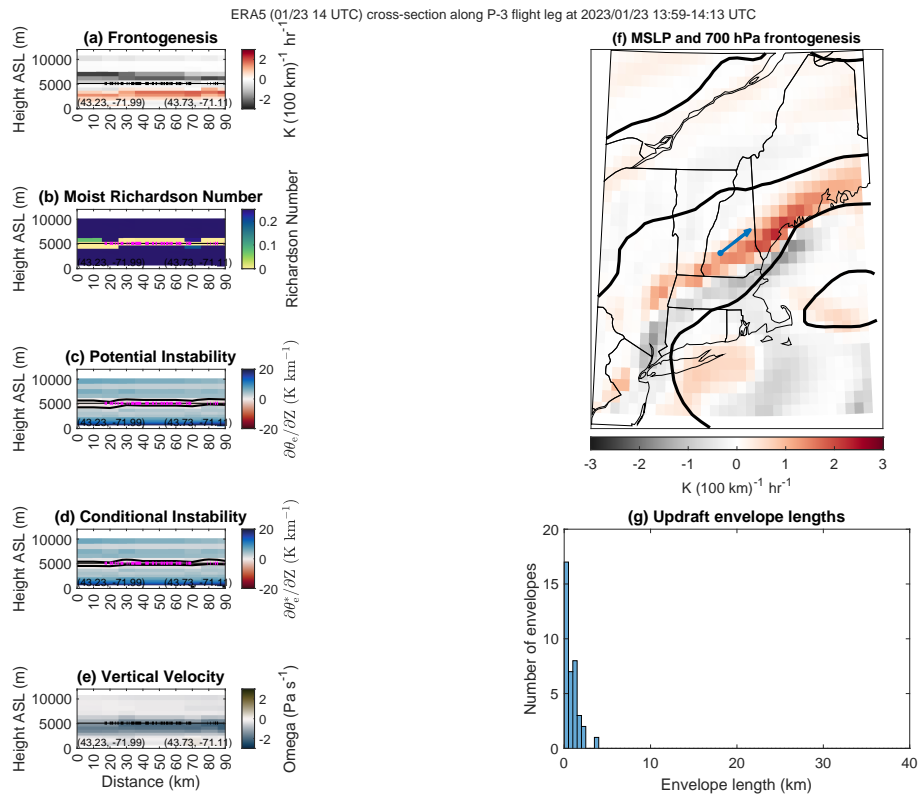


Figure A.14: As in Fig. A.1, but for the P-3 flight leg from 13:59 UTC 23 January 2023 to 14:13 UTC 23 January 2023.

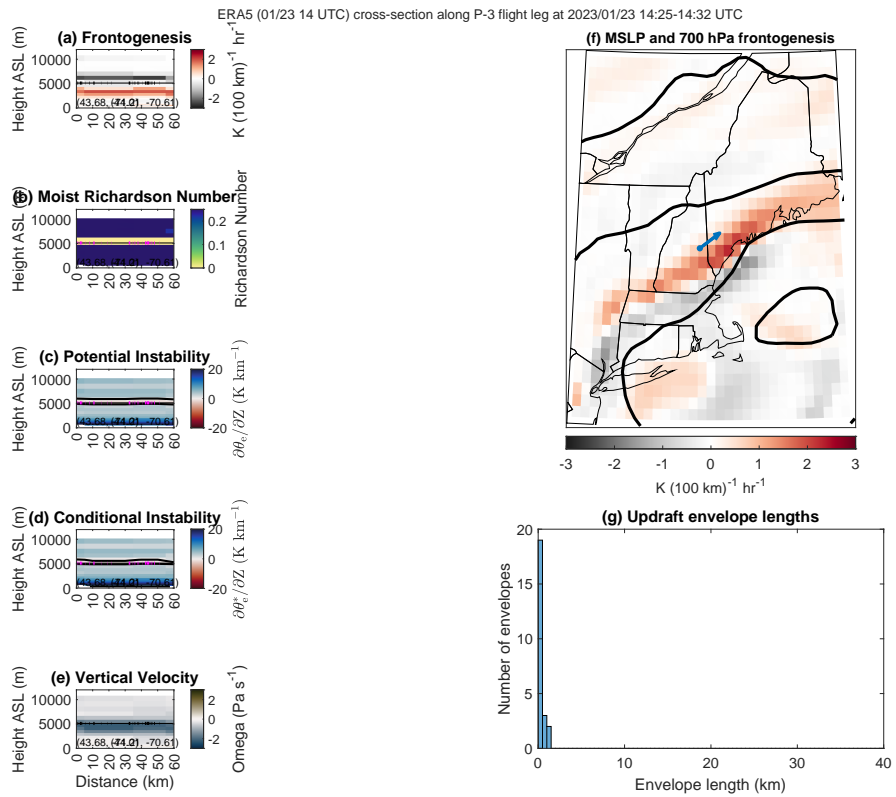


Figure A.15: As in Fig. A.1, but for the P-3 flight leg from 14:25 UTC 23 January 2023 to 14:32 UTC 23 January 2023.

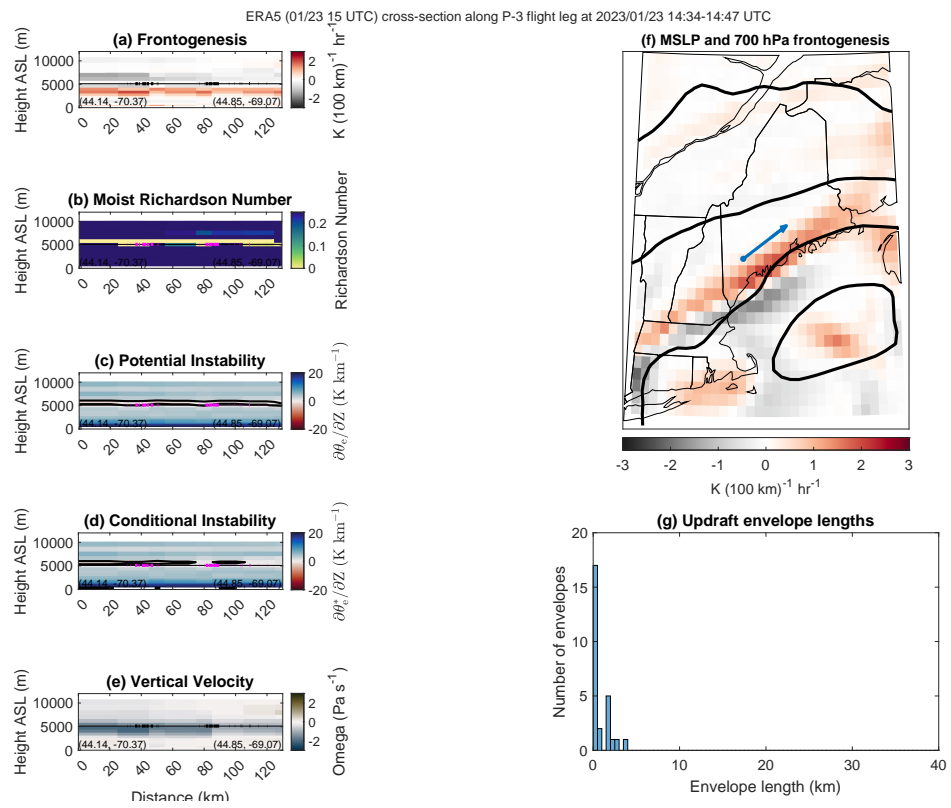


Figure A.16: As in Fig. A.1, but for the P-3 flight leg from 14:34 UTC 23 January 2023 to 14:47 UTC 23 January 2023.

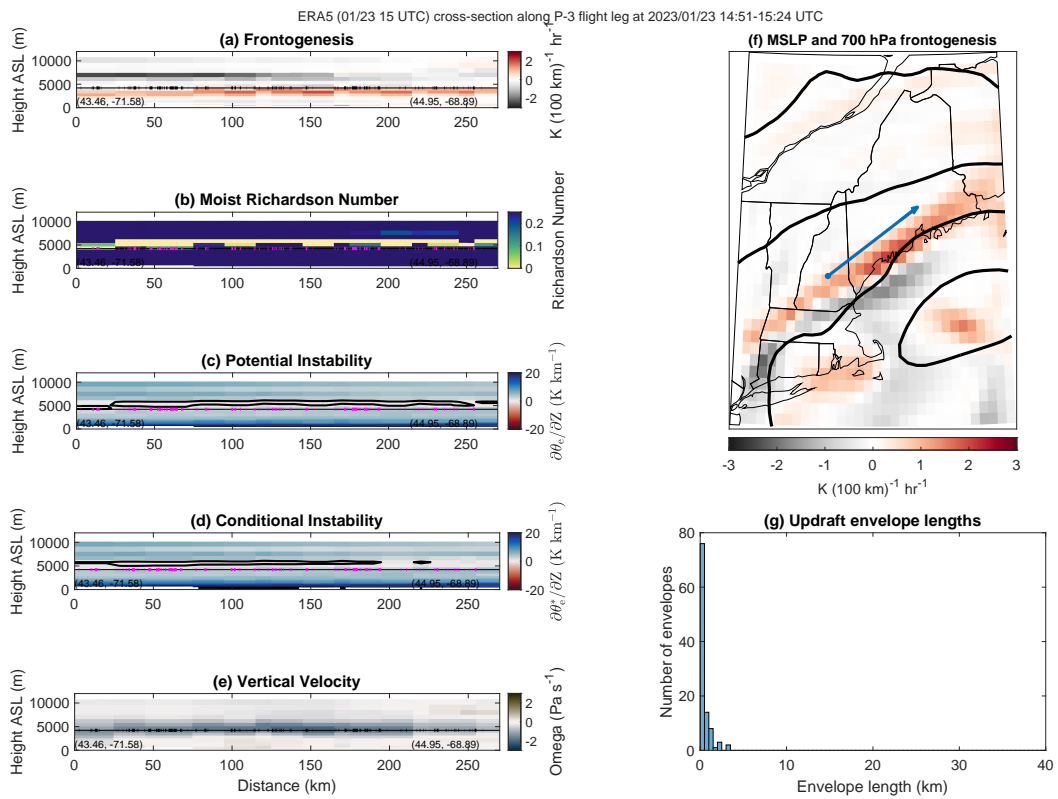


Figure A.17: As in Fig. A.1, but for the P-3 flight leg from 14:51 UTC 23 January 2023 to 15:24 UTC 23 January 2023.

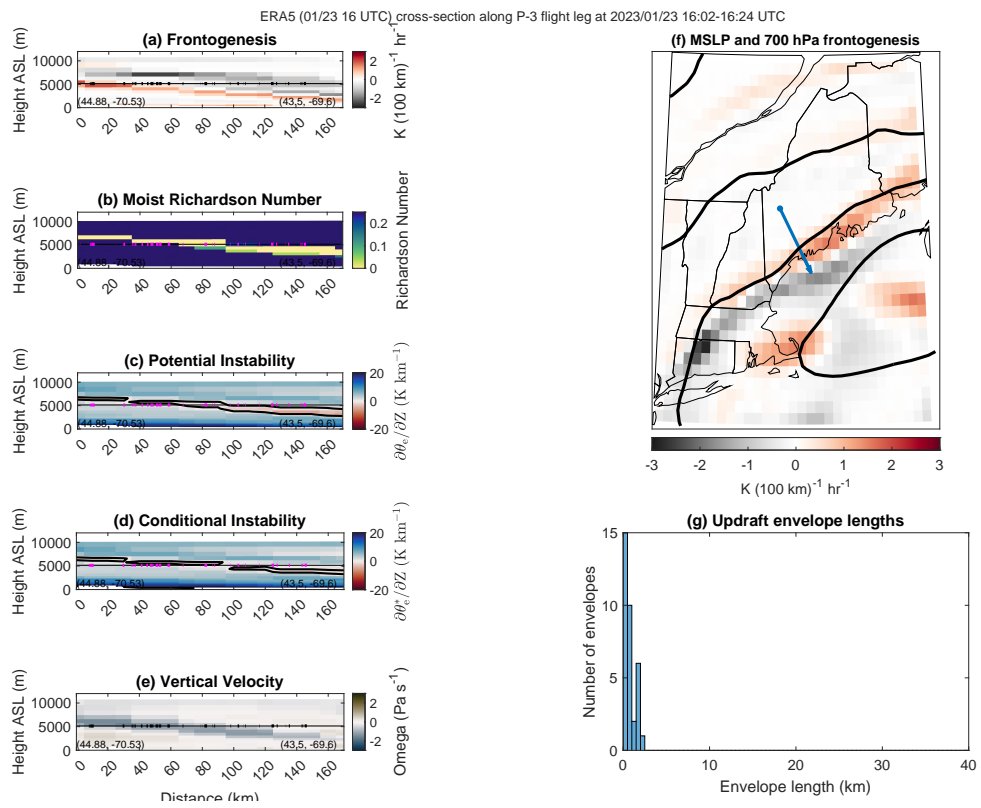


Figure A.18: As in Fig. A.1, but for the P-3 flight leg from 16:02 UTC 23 January 2023 to 16:24 UTC 23 January 2023.

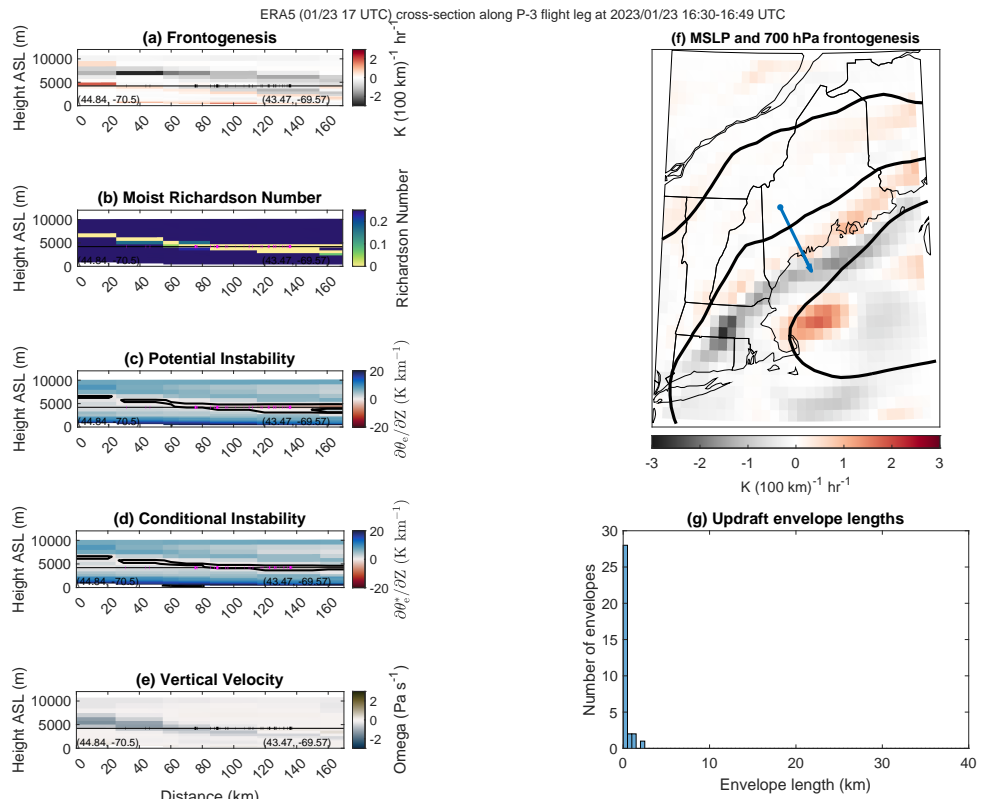


Figure A.19: As in Fig. A.1, but for the P-3 flight leg from 16:30 UTC 23 January 2023 to 16:49 UTC 23 January 2023.

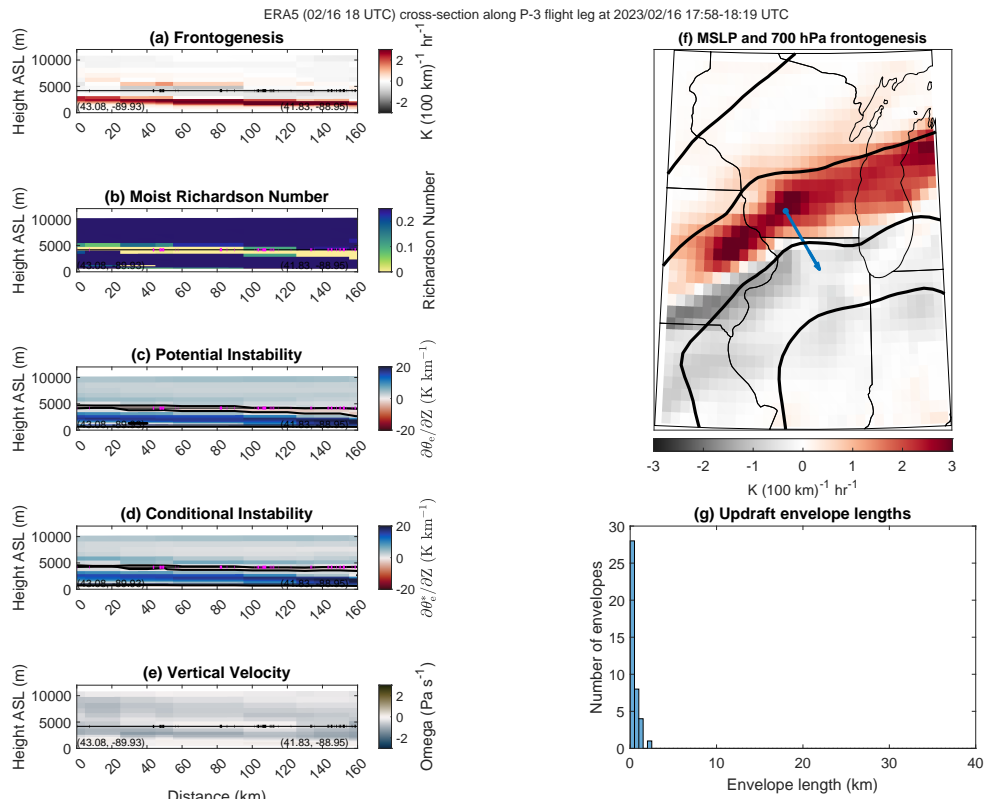


Figure A.20: As in Fig. A.1, but for the P-3 flight leg from 17:58 UTC 16 February 2023 to 18:19 UTC 16 February 2023.

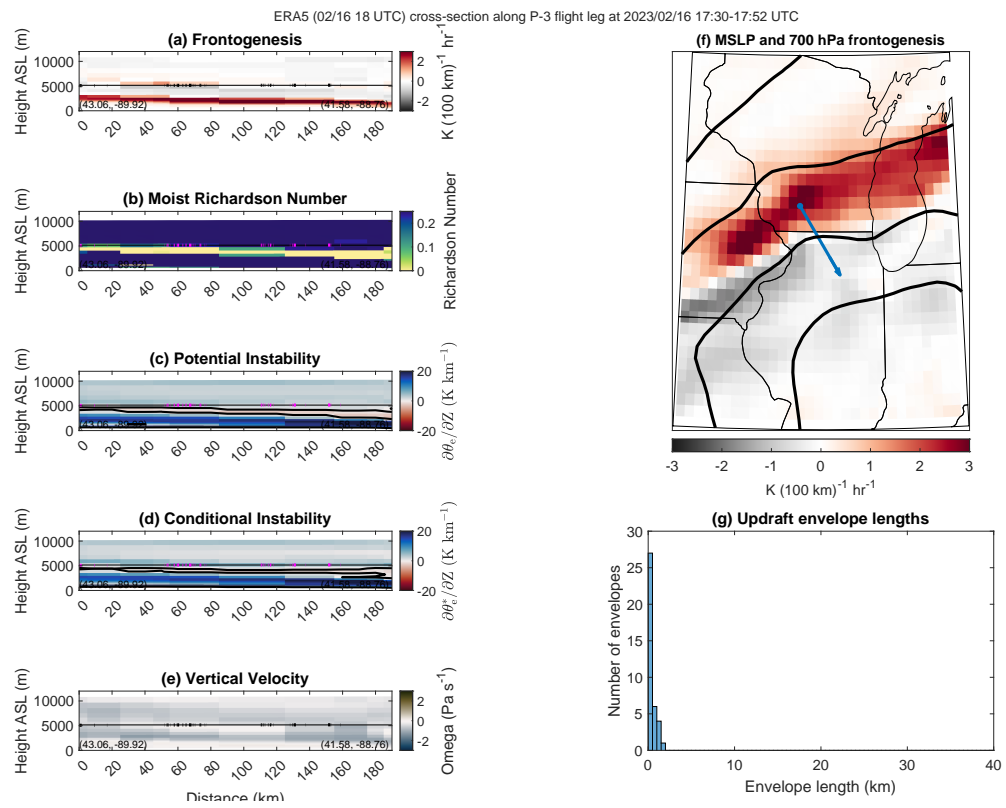


Figure A.21: As in Fig. A.1, but for the P-3 flight leg from 17:30 UTC 16 February 2023 to 17:52 UTC 16 February 2023.

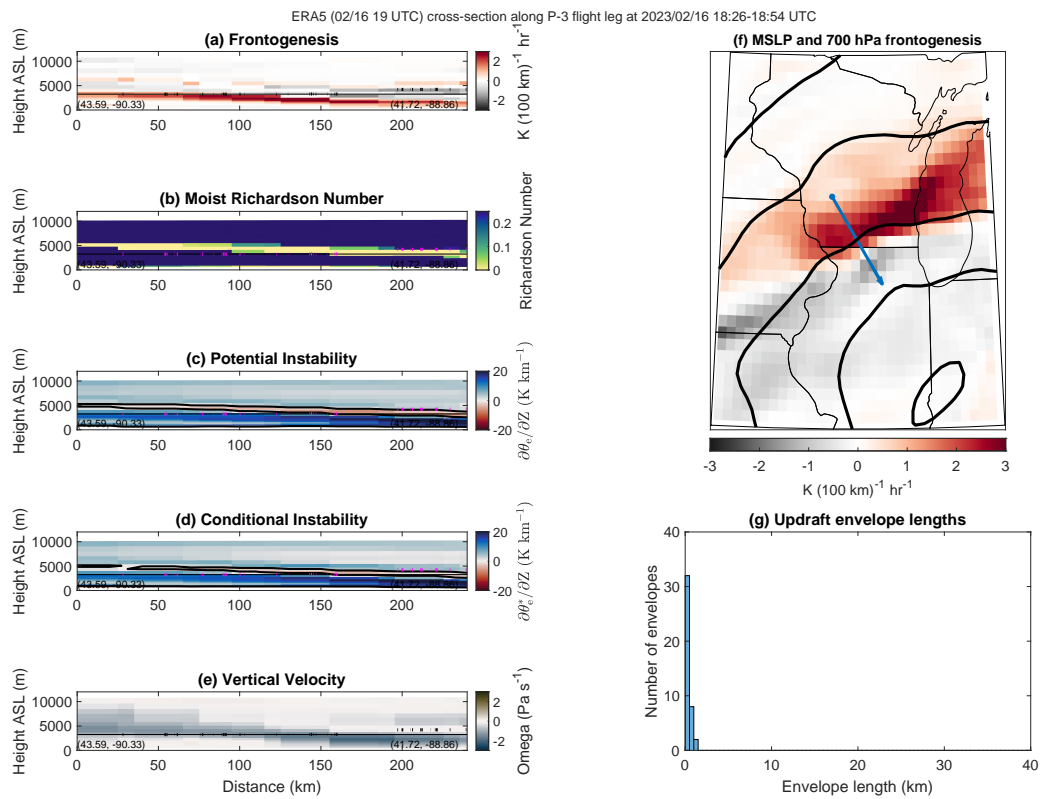


Figure A.22: As in Fig. A.1, but for the P-3 flight leg from 18:26 UTC 16 February 2023 to 18:54 UTC 16 February 2023.

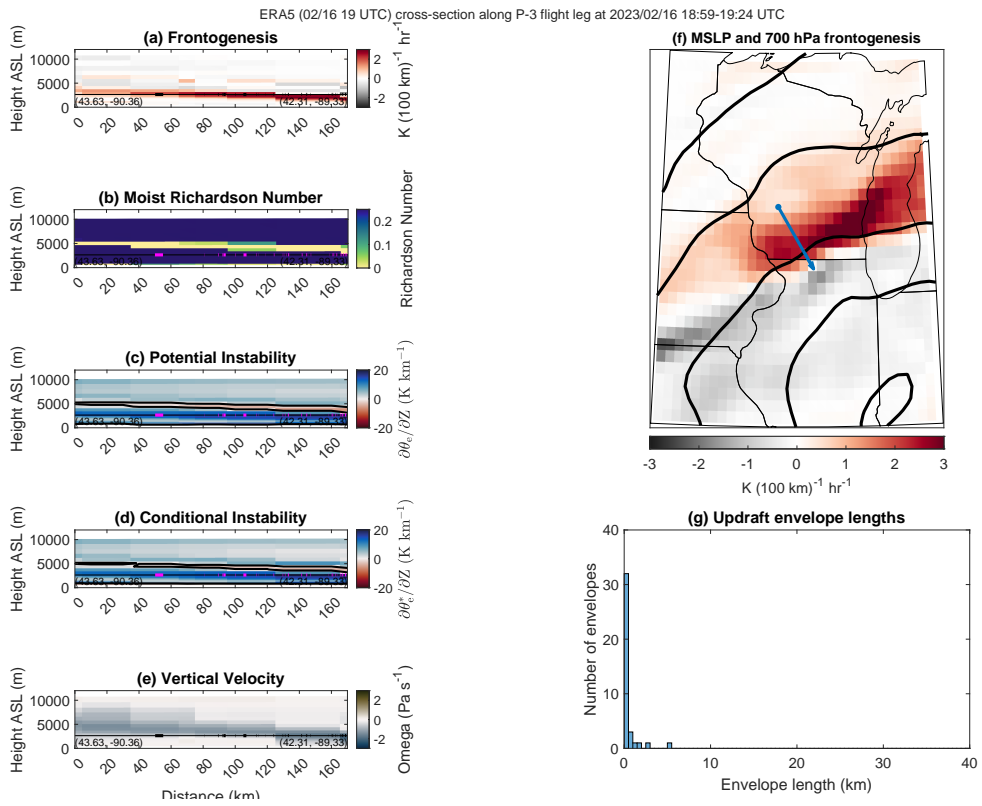


Figure A.23: As in Fig. A.1, but for the P-3 flight leg from 18:59 UTC 16 February 2023 to 19:24 UTC 16 February 2023.

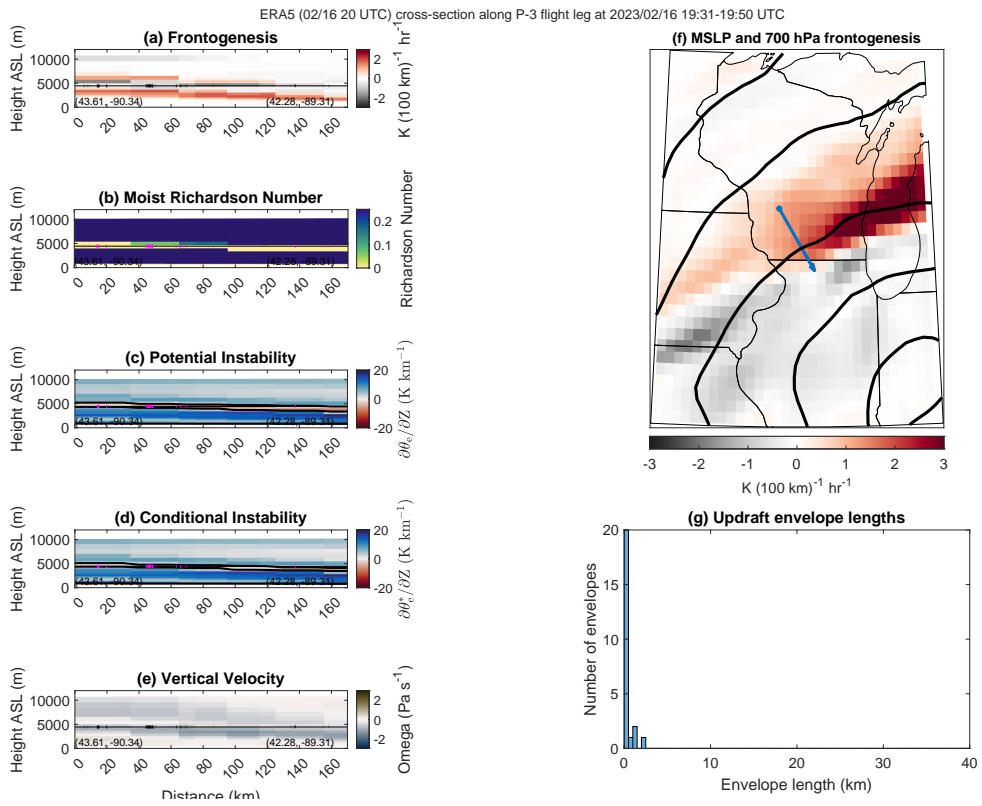


Figure A.24: As in Fig. A.1, but for the P-3 flight leg from 19:31 UTC 16 February 2023 to 19:50 UTC 16 February 2023.

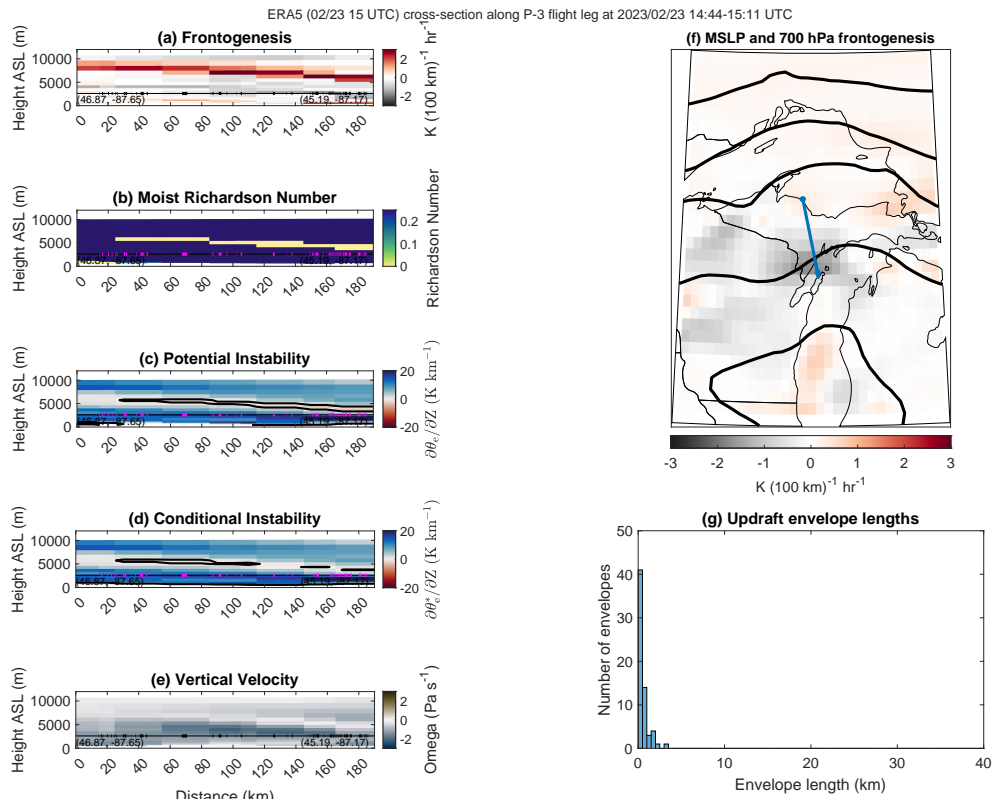


Figure A.25: As in Fig. A.1, but for the P-3 flight leg from 14:44 UTC 23 February 2023 to 15:11 UTC 23 February 2023.

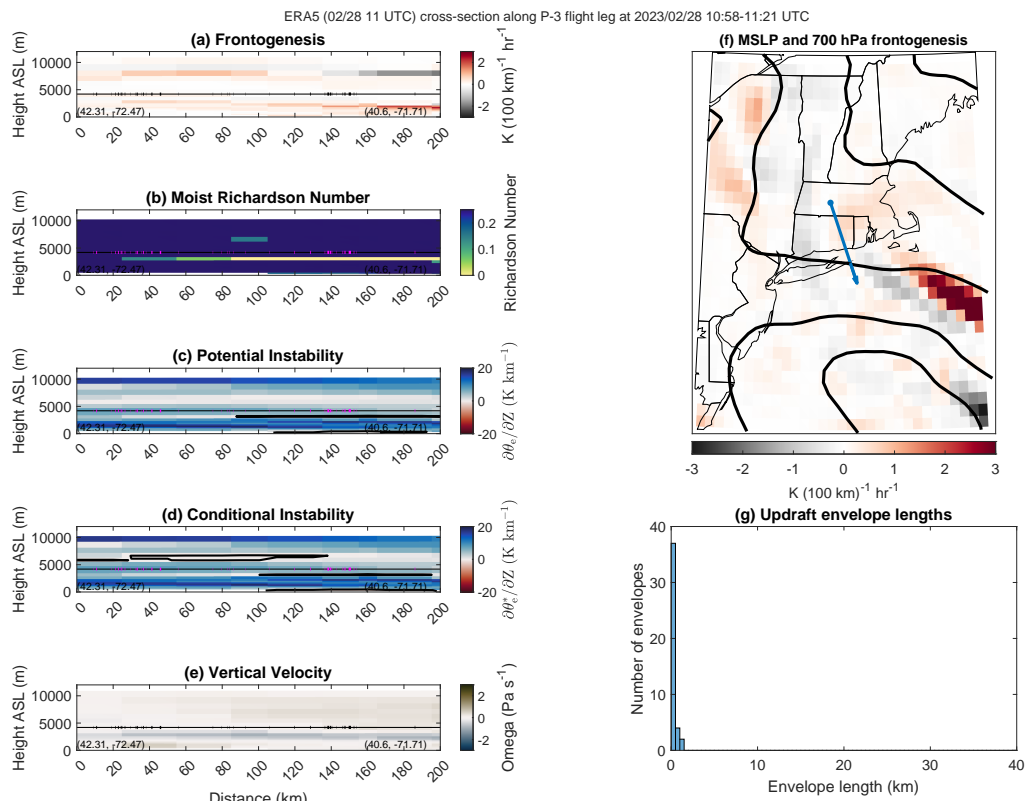


Figure A.26: As in Fig. A.1, but for the P-3 flight leg from 10:58 UTC 28 February 2023 to 11:21 UTC 28 February 2023.